

**Exotic binaries in Galactic globular clusters: identification,
classification, and their formation**

by

Yue Zhao

A thesis submitted in partial fulfillment of the requirements for the degree of

Doctor of Philosophy

Department of Physics
University of Alberta

© Yue Zhao, 2021

Abstract

Globular clusters (GCs) are dense and massive stellar populations, which provide a unique environment where the high stellar density facilitates frequent dynamical encounters, creating many exotic binaries. These exotic binaries generally have short orbits and often harbour compact objects, namely neutron stars (NSs), black holes (BHs), and white dwarfs (WDs). With the unprecedented sensitivity and angular resolution of the *Chandra X-ray Observatory*, GCs are found to host an overabundance of X-ray binaries.

This thesis contains chapters that identify and classify exotic binaries in multiple GCs and presents their relation to cluster dynamics, incorporating X-ray, UV, optical, and radio observations. In the GC M3 (NGC 5272), we discovered 16 X-ray sources within the half-light radius (r_h), where the second brightest source (M3-CX2) is a newly discovered low-mass X-ray binary candidate. In a study of NGC 6397, we incorporate deep radio imaging observations from the MAVERIC radio survey and find a strong “hidden” millisecond pulsar candidate. A deep observation of M30 reveals 10 new X-ray sources within r_h and suggests a difference between the radial distributions of bright and faint X-ray sources. Finally, a census of radio sources in multiple GCs indicates that they are likely a mixture of millisecond pulsars (the numbers of which, per

cluster, scale with the rate of stellar encounters in each cluster) and quiescent black hole binaries (which do not show a simple scaling with the number of stellar encounters per cluster).

Preface

This thesis is original work by Yue Zhao, conducted under supervision by Craig Heinke.

Chapter 2 of this thesis has been published in Zhao et al. 2019, titled “Identifications of faint Chandra sources in the globular cluster M3”, *MNRAS*, 483, 4560. This work presents analyses of X-ray, UV, and optical observations of the Galactic globular cluster M3 (NGC 5272). We compile a catalogue of 16 X-ray sources, and discovered optical/UV counterparts to 10 of the X-ray sources. Additionally, we model spectral energy distribution of the known cataclysmic variable 1E1339.8+2837, the best fit of which suggests a hotter (blue) spectral component from an accretion disc and a cooler spectral component potentially from a subgiant donor star. I performed all the X-ray data analyses, WFC3 photometry, ACS/HRC photometry (for SED modelling), and wrote the paper. My supervisor C. Heinke helped me with the introduction and discussion sections of the paper and provided guidance on data processing and analysis. H. Cohn and P. Lugger performed the ACS/WFC photometry which provides useful information that complements the identified optical/UV counterparts. A. Cool contributed helpful discussions and comments.

Chapter 3 of this thesis has been published in Zhao et al. 2020a, titled “The MAVERIC survey: a hidden pulsar and a black hole candidate in ATCA radio imaging of the globular cluster NGC 6397”, *MNRAS*, 493, 6033. This work presents combined radio and X-ray imaging observations of the Galactic globular cluster NGC 6397, where we find a “hidden” pulsar and a black hole candidate. This work is based on radio observations proposed by J. Strader, and radio data analyses were performed by V. Tudor, who was supervised by J. C.

A. Miller-Jones. I performed all X-ray data analyses and wrote the paper. My supervisor C. Heinke helped me with the introduction (particularly the sections about GC radio sources and eclipsing millisecond pulsars) and discussion. The other co-authors of the paper contributed greatly to discussions and comments on paper structure, technical details, and scientific discussion.

Chapter 4 of this thesis has been published in Zhao et al. 2020b, titled “A deep *Chandra* survey for faint X-ray sources in the core-collapsed globular cluster M30, and searches for optical and radio counterparts”, *MNRAS*, 499, 3338. This work presents X-ray, UV, optical, and radio analyses of the Galactic globular cluster M30, compiling an X-ray catalogue of 23 sources. We also find optical counterparts to 18 of the 23 sources, and a radio counterpart to a known millisecond pulsar. An comparison between radial distribution of bright and faint X-ray sources suggests that bright sources are more centrally concentrated, which is consistent with observations of other core-collapsed GCs. This work is based on a set of Cycle 18 *Chandra* X-ray observations, which were proposed by S. Guillot. I performed all X-ray analyses and optical/UV photometry in this work, and wrote the paper. My supervisor C. Heinke assisted with discussions on individual sources. H. Cohn and P. Lugger performed the statistical comparison of radial distributions of different bright and faint X-ray sources. S. Guillot and C. Echiburú provided the best fit model parameters to A1 (the quiescent low-mass X-ray binary) which was presented in the discussion and the X-ray luminosity vs. hardness ratio plot (see Figure 4.4 in Chapter 4). The detailed spectral analysis of A1 has been published in a separate paper (Echiburú et al., 2020). The other co-authors are all from the MAVERIC collaboration, who provided informative discussions and technical details of the radio data (proposed by J. Strader) used in this work.

Chapter 5 of this thesis has been published in Zhao et al. 2021b, titled “The MAVERIC Survey: Dynamical Origin of Radio Sources in Galactic Globular Clusters”, *ApJ*, 914, 77. In this work, we present an analysis of how

globular cluster radio source numbers are dependent on cluster mass and stellar encounter rate (Γ) using a maximum likelihood method. We find a significant dependence (at the 99% confidence level) on mass and/or Γ , while excluding dependence on Γ alone at 90% confidence. Some of the cluster radio sources are therefore of dynamical origin, while others have a more complicated dependence on cluster parameters. The catalogue used in this work has been published in Shishkovsky et al. (2020). I prepared the modelling script, performed the simulations, and wrote the paper. C. Heinke planned the project and supervised my analyses, contributing greatly to technical details of the modelling script. The other co-authors contributed informative comments that help me refine the paper.

A significant part of the results presented in this thesis are based on new observations obtained from the following instruments: the *Chandra X-ray Observatory* (Chapter 2, 3, 4); the *Hubble Space Telescope* (Chapter 2, 3, 4); the *Australia Telescope Compact Array* (Chapter 3); and the *Karl G. Jansky Very Large Array* (Chapter 4, 5).

“The eternal mystery of the world is its comprehensibility ...

The fact that it is comprehensible is a miracle.”

— Albert Einstein

Acknowledgements

I would like to first thank my supervisor and my mentor, Craig Heinke, for all the supports to my coursework and research as well as for all the valuable discussions from which I have benefited greatly. My accomplishments, my growing interest in high-energy astrophysics, and every step of progress would not have been possible without your guidance.

I would also like to thank my wonderful collaborators that I have worked with over the past several years. Thank you to Haldan Cohn and Phyllis Lugger from Indiana University for all the informative discussions on our collaborative work and for all the help with optical/UV data analyses, thank you to Adrienne Cool from San Francisco State University for all the constructive comments and suggestions on our work, and thank you to Sebastien Guillot from Institut de Recherche en Astrophysique et Planétologie and Constanza Echiburú from McGill University for the collaboration on X-ray and optical analyses. Thank you to people from the MAVERIC collaboration including Jay Strader, Laura Chomiuk, Laura Shishkovsky, and Ryan Urquhart from Michigan State University; Tom Maccarone from Texas Tech University; Arash Bahramian, James Miller-Jones, Vlad Tudor from the International Centre for Radio Astronomy Research (ICRAR); and Gregory Sivakoff from University of Alberta. I would like to thank them for their instruction on working with and proposing for radio observations. I would also like to give my thanks to Sergey Tsygankov from University of Turku, Wynn Ho from Haverford College, and Alexander Y. Potekhin from Ioffe Institute for important theoretical support.

Thank you to members of the Astrophysics Group at the University of Alberta. My committee members consist of Gregory Sivakoff and Rodrigo

Fernández, who have been offering valuable instruction and guidance on my thesis research. Thank you also to graduate students working in similar fields including Asma Hattawi, Pavan Hebbar, and Jiaqi Zhao for their support; thanks to my office mates Kenny X. Van, Roger Hatfull, and Dinesh Kandel for helpful discussions; thanks to post-doc Aarran Shaw for many valuable instructions.

Finally, thank you to my family members. My decision of staying in academia has been consistently encouraged by you, and I am sincerely grateful for all the love and supports.

Contents

1	Introduction	1
1.1	Globular Clusters	1
1.2	Exotic binaries in globular clusters	2
1.2.1	Low-mass X-ray binaries	4
1.2.2	Millisecond pulsars	6
1.2.3	Cataclysmic variables	8
1.2.4	Chromospherically active binaries	10
1.3	Identification of X-ray sources	11
1.4	Why study GC exotic binaries?	11
2	Identification of Faint Chandra Sources in the Globular Cluster	
	M3	13
2.1	Introduction	14
2.2	Observations	17
2.2.1	<i>Chandra</i> Observations	17
2.2.2	<i>HST</i> Observations	17
2.3	Analyses	19
2.3.1	Merging Chandra Observations	19
2.3.2	Source Detection	19
2.3.3	Source counts	20
2.3.4	Optical Photometry	20
2.3.5	Astrometry	23

2.3.6	Counterpart search	25
2.3.7	Cluster Subpopulations and Chance Coincidences	27
2.3.8	Optical Variability	29
2.3.9	SED-Modelling of 1E1339	30
2.3.10	X-ray spectral analysis	32
2.4	Individual Sources & Discussions	33
2.4.1	CX1/1E1339	33
2.4.2	CX2: a quiescent low-mass X-ray binary (qLMXB)?	35
2.4.3	CX6	37
2.4.4	CX8, CX12 and CX16	38
2.4.5	CX7 and CX13	39
2.4.6	CX9 and CX14	39
2.4.7	Estimate of XRBs and AGNs	40
2.5	Conclusions	42

3 The MAVERIC survey: A hidden pulsar and a black hole candidate in ATCA radio imaging of the globular cluster NGC 6397 **52**

3.1	Introduction	54
3.1.1	Radio sources in globular clusters	54
3.1.2	Eclipsing millisecond pulsars	56
3.1.3	NGC 6397	58
3.2	Observations & Analyses	59
3.2.1	Radio Observations	59
3.2.2	X-ray Observations	60
3.2.3	<i>HST</i> observations and Astrometry	62
3.3	Results	65
3.3.1	U12, PSR J1740-5340	65
3.3.2	U18: A hidden MSP?	66

3.3.3	U24—radio related to a quiescent LMXB?	68
3.3.4	U97	69
3.3.4.1	A chromospherically active binary?	69
3.3.4.2	A quiescent black hole (BH) X-ray binary	70
3.3.4.3	A white dwarf system?	71
3.3.5	U108, W127, W129 and W135	72
3.4	Discussion	73
3.5	Conclusions	74
4	A deep <i>Chandra</i> survey for faint X-ray sources in the Galactic globular cluster M30, and searches for optical and radio counterparts	80
4.1	Introduction	82
4.2	Observations and data reduction	84
4.2.1	<i>Chandra</i> observations	84
4.2.2	<i>HST</i> observations	85
4.2.3	<i>VLA</i> observations	86
4.3	Data analyses	87
4.3.1	Merging the X-ray observations	87
4.3.2	Source detection	88
4.3.3	Source counts	89
4.3.4	X-ray spectral analyses	91
4.3.5	X-ray variability	92
4.3.6	Astrometry	93
4.3.6.1	Co-adding images	93
4.3.6.2	Absolute Astrometry	93
4.3.6.3	<i>Chandra</i> boresight correction	94
4.3.7	Optical photometry	95
4.3.7.1	UV variability	97

4.3.8	Counterpart search and source identification	97
4.3.8.1	Basic methodologies	97
4.3.8.2	Radio counterparts	99
4.3.8.3	Chance coincidence	100
4.4	Results and Discussion	101
4.4.1	A1—a qLMXB	101
4.4.2	Known CVs: B and C	106
4.4.3	New faint CVs and candidates	107
4.4.3.1	A3	107
4.4.3.2	Sources 8, 9, 12, W15, W19, and W21	108
4.4.4	Previously suggested ABs: sources 7 and 10	109
4.4.5	New ABs and candidates	110
4.4.5.1	A2	110
4.4.5.2	W16	110
4.4.5.3	W17	111
4.4.5.4	W20	112
4.4.6	MSP A	113
4.4.7	Unclassified sources and likely AGN	114
4.4.8	Spatial distribution of different source classes	116
4.5	Conclusions	120
5	The MAVERIC Survey: Dynamical Origin of Radio Sources in Galactic Globular Clusters	130
5.1	Introduction	132
5.2	Observations and Method	135
5.3	Results and Discussion	138
5.4	Conclusion	147
6	Conclusions	151

Bibliography	154
Appendices	176
A Renormalization of SED models with χ^2 minimization method .	176
B An updated X-ray source catalogue and tentative identification of new sources in NGC 6397	177
C All finding charts for M30 X-ray sources	188

List of Tables

2.1	<i>Chandra</i> Observations of M3	17
2.2	<i>HST</i> Observations of M3	19
2.3	Summary on resulting χ^2 from fitting constants to light curves in different filters.	30
2.4	Calibrated specific fluxes (F_λ) of CX1 in different filters from the 2004 ACS observation.	31
2.5	A catalogue of X-ray sources in M3.	49
2.6	Magnitudes and colours of identified optical counterparts.	50
2.7	Summary of X-ray spectral analyses.	51
3.1	Positional information of radio-X-ray cross-matched sources	78
3.2	Radio and X-ray properties of sources in Tab. 3.1.	79
4.1	<i>Chandra</i> observations of M30.	85
4.2	<i>HST</i> observations of M30	86
4.3	M30 X-ray source catalogue.	121
4.4	Results of spectral fitting to the Cycle 18 spectra.	123
4.5	Parameters used in DOLPHOT.	125
4.6	Optical counterparts	126
4.7	Cored-Power-Law Model Fit Results	129
5.1	Radio source counts in different GCs.	148
5.2	Radio sources in the core with $L_{\text{low}} > 5 \times 10^{27}$ erg s $^{-1}$	150

1	X-ray catalogue of source within the 2'9 half-light radius.	181
2	Optical counterparts to the new sources.	187

List of Figures

- 1.1 Dynamical formation channels of close exotic binaries in GCs. Compact objects are indicated with filled black circles. The compact stellar core of the red giant is represented with a filled cyan circle. 3
- 1.2 *Left:* Optical/near-IR image of the globular cluster NGC 6440 (PanSTARRS DR1, Chambers et al. 2016). *Right:* *Chandra*/ACIS X-ray image zoomed in on the half-light radius of NGC 6440; the different colours in the *Chandra* image represent the energies of X-ray sources: low-energy (soft) sources are in red, intermediate-energy sources are in green, and high-energy sources are in blue. The red dashed circle indicates the size of the core, while the green solid circle demarcates the half-light radius (Harris, 1996, 2010 edition). 4
- 1.3 Rotation period derivative (\dot{P}) vs. rotation period (P) plotted for pulsars from the ATNF catalogue. Blue dashed lines mark surface magnetic field strengths; red dotted lines mark different spin-down powers; green dashed-dotted lines mark characteristic ages. MSPs are at the lower-left of the plot, roughly below the 10^{10} G line. 7

2.1	Merged 0.5 – 7 keV <i>Chandra</i> exposure-corrected ACIS-S X-ray image of the central $4'.8 \times 4'.8$ region of M3. The dashed blue circle shows the $0'.37$ core region; the solid blue circle shows the $2'.31$ half-light radius (Harris, 1996, 2010 edition). Sources detected by <i>wavdetect</i> are marked with solid black circles. The size of each pixel is $0'.492$	18
2.2	<i>Left:</i> $UV_{275} - NUV_{336}$ CMD generated by stars within a region of $140'' \times 140''$ centered on the cluster core. <i>Middle:</i> $UV_{336} - B_{438}$ CMD generated by stars within the same region. Both left and middle panels were generated using DAOPHOT results. <i>Right:</i> $V_{606} - I_{814}$ CMD from the catalogue of the <i>ACS Globular Cluster Treasury Program</i> . Optical counterparts are shown with red circles and annotated with their CX IDs (two potential counterparts are shown for CX9, though we find the brighter, redder one more likely). The error bars of CX8 and CX13 were indicated to show the uncertainty of their blue excesses.	23
2.3	$B_{435} - V_{555}$ CMD from the 2004 ACS/WFC observation. Optical counterparts are annotated by red circles. The large photometric errors of CX16 are indicated with error bars.	24
2.4	A histogram showing the distribution of offsets for the 10 identified counterparts. Each offset was normalised to the corresponding 95% error radius (P_{err}). The dashed line marks edges of the error circles.	27

2.5	Proper motion distribution of stars with at least one good photometric measurement in each filter from the Padova Catalogue plotted in 4 V_{606} magnitude bins. The cluster's average proper motion corresponds to the zero point. The proper motion of background galaxies, obtained from GAIA DR2's estimate of the cluster motion, is marked with a red cross. Counterparts are shown with red points. The orange dashed circle in each panel shows the 3 rms radius within which stars are considered as likely cluster members. The red dotted-dashed circle in each panel shows the corresponding 3σ composite error radius of the AGN proper motion.	28
2.6	Proper motion cleaned $UV_{275} - NUV_{336}$ CMD overplotted with different subpopulations.	29
2.7	Finding charts for 7 identified optical counterparts in 5 different bands (UV bands are from the 2012 WFC3/UVIS observations; V_{606} and I_{814} bands are from the 2006 ACS/WFC observations) made from drizzle-combined images. North is up and east is to the left. The green solid circles represent the 95% <i>Chandra</i> error circles as calculated in Hong et al. (2005). Identified counterparts are annotated with red arrows. Note that the counterparts to CX12 was only found in the two UV filters (UV_{275} , NUV_{336}); similarly, the counterparts to CX2 and CX13 were only detected in the two ACS/WFC bands, so the red arrows on the other finding charts only point to their nominal positions. The counterpart to CX8 appears to be a faint extension in V_{606} and I_{814} . Also, notice that a cosmic ray on the UV_{275} finding chart of CX8 has been excluded to avoid confusion. The red straggler (RS) and subgiant (SG) potential counterparts to CX9 are annotated with arrows and texts.	43

2.8	Optical/UV light curves of the identified counterparts that have detections in multiple exposures in the WFC3/UVIS observations (2012) and/or the ACS/WFC observations (2006). Photometric errors are from DAOPHOT software. The best fit constants are indicated with a solid green line.	45
2.9	Best fit SED models and data from the 2004 observations. <i>Left panel</i> shows the best fit single-component model (solid black) overplotted with the data (red). <i>Right panel</i> shows the same data (red) and the best fit two-component model (solid black), composed of a renormalised B2 component (blue dashed-dotted) and an renormalised M0 component (orange dashed).	46
2.10	<i>Chandra</i> spectra of CX2. The top panel shows the rebinned (only for plotting purpose) data (black) with the best fit POWERLAW model and BBODYRAD model overplotted with a solid red line and a solid blue line, respectively. The bottom panel shows the same data, but overplotted with the best fit VMEKAL model (blue) and NSATMOS model (red). The yellow dashed line indicates the energy limit at 0.5 keV, below which channels were ignored during the fits. Ratio = data/model.	46

2.11 0.5 – 2.5 keV L_X vs. absolute V band magnitudes (using V_{555} for CX7 and CX16, and V_{606} for others). L_X of CX1 is from Stacey et al. (2011). The dashed line corresponds to the $L_X = 34.0 - 0.4M_V$ separatrix from Bassa et al. (2004), dividing cluster CVs and ABs. The dotted-dashed line corresponds to the $L_X = 32.3 - 0.27M_V$ separatrix from Verbunt et al. (2008), marking the upper limit of L_X for nearby ABs. CV candidates with confirmed cluster memberships are marked with filled blue squares. Possible CV/AGN candidates are marked with filled blue diamonds. The red filled circle marks the location of CX2 if we were to adopt the suggested counterpart. For comparison, the red open circle indicates the location of CX2 on the plot if we adopt the bright MS star mentioned in Sec. 2.4.2 as the counterpart. 47

2.12 $V_{555} - I_{814}$ CMD from the 2004 ACS/WFC observations. The red circle marks the location of the CX6 counterpart. 47

2.13 Number of non-AGN X-ray sources (N_X) in multiple GCs v.s. renormalised stellar encounter rates (Γ) from Bahramian et al. (2013). Γ s have been renormalised such that NGC 6266 has a Γ of 100. The lower limit inferred from our results of M3 is indicated with an orange square. The dashed line indicates the linear regression fit from Lugger et al. (2017). 48

3.1	<i>Left:</i> 0.5-7 keV X-ray image of a $6'.6 \times 6'.6$ square region centered on the cluster. North is up and east is to the left. New sources detected by <code>wavdetect</code> (blue) and sources from Bogdanov et al. (2010) (red) are marked by circles that enclose 90% of their PSFs. The solid black circle shows the $2'.9$ half-light radius (r_h), while the dashed black circle depicts the $2'.33$ searching radius used in Bogdanov et al. (2010). <i>Right:</i> a zoomed-in $45'' \times 45''$ square region centered on the cluster. The solid black circle shows the $0.05'$ core radius (r_c).	63
3.2	Colour-magnitude diagrams (CMDs) of stars from the HUGS catalogue. Locations and errors of optical/UV counterparts to X-ray sources with radio counterparts are indicated with red points and bars. We also present the photometry of 3 objects that lie within the 95% error circle of W134, a new X-ray source with HUGS data available (see also Appendix B).	64
3.3	X-ray (0.5-7 keV), radio (5.5 GHz and 9 GHz) and optical (F625W) finding charts for U12, U18, U24, U97 and U108. North is up and east is to the left. The X-ray and radio charts are all $14'' \times 14''$ in size while the F625W finding charts are $2''.8 \times 2''.8$. We show the 95% <i>Chandra</i> error region with red circles. Since the radio sources have relatively small positional uncertainties, we only show their nominal positions with green crosses in the X-ray and radio images, while in the somewhat zoomed-in F625W charts, we show radio error regions with green ellipses (the sizes of which are described in Sec. 3.2) and indicate the optical counterparts with black arrows. The radio beams in the radio charts are shown with blue ellipses on the bottom right of the 5.5 and 9 GHz images.	75

3.4 5 GHz radio luminosities plotted vs. 1-10 keV X-ray luminosities for different classes of accreting compact objects. X-ray sources in NGC 6397 associated with radio counterparts are shown with filled pentagons. The radio luminosities are calculated assuming flat ($\alpha = 0$) spectra. The deep-green circles represent known quiescent black holes (Soleri et al., 2010; Miller-Jones et al., 2011; Gallo et al., 2012; Ratti et al., 2012; Corbel et al., 2013; Rushton et al., 2016; Plotkin et al., 2017). The dashed grey line shows the L_R - L_X correlation for black holes from Gallo et al. (2014). The larger purple circles are radio-selected black hole candidates (Strader et al., 2012; Chomiuk et al., 2013; Miller-Jones et al., 2015; Tetarenko et al., 2016; Bahramian et al., 2017; Shishkovsky et al., 2018). The light-green triangles mark known transitional millisecond pulsars (Hill et al., 2011; Papitto et al., 2013; Deller et al., 2015; Bogdanov et al., 2018). The deep-blue squares and pink stars show quiescent/hard-state NSs and accreting millisecond X-ray pulsars (AMXPs), respectively (Migliari & Fender, 2006; Tudor et al., 2017). The yellow triangles show upper limits of L_R of two X-ray transients (Tetarenko et al., 2016; Ludlam et al., 2017). The orange diamonds mark radio detected bright white dwarfs (WDs), including AE Aqr (Eracleous et al., 1991; Abada-Simon et al., 1993), SS Cyg (at flare peak; Russell et al. 2016) and AR Sco (a radio-pulsating white dwarf; Marsh et al. 2016). The hollow markers indicate upper limits. For script and data used to generate the plot, see Bahramian et al. (2018). . . 77

4.1 0.5–7 keV X-ray image of M30. The left panel shows a $2'.5 \times 2'.5$ square region centered on the cluster. All sources are indicated with circles that enclose 90% of their PSFs, with new sources in blue and previously reported sources (Lugger et al., 2007) in red. The solid black circle indicates the $1'.03$ half-light radius of the cluster and the dashed black circle represents the $0'.06$ core region according to Harris (1996, 2010 edition). The right panel shows a zoomed-in view of the central $28'' \times 28''$ square region. 90

4.2 *Top:* $UV_{275} - U_{336}$ (top left) and $U_{336} - B_{438}$ (top right) CMDs plotted for stars with errors in magnitudes ≤ 0.1 (black). *Bottom:* $V_{606} - I_{814}$ CMD plotted for stars with errors in magnitudes ≤ 0.1 (black). The locations of the counterparts are marked with red dots. Counterparts with uncertainties in magnitudes greater than 0.1 (intrinsic error calculated by DOLPHOT) are plotted together with error bars. 102

4.3 UV_{275} and U_{336} rms variability plotted against UV_{275} (left) and U_{336} (right) magnitudes. The locations of counterparts are indicated with filled red circles annotated with the corresponding source IDs. The majority of stars lie on a sequence, while stars with variability appear to be outliers. 103

- 4.4 X-ray colour-magnitude diagram plotting X-ray hardness ratios defined in eq.(4.1) vs. unabsorbed model fluxes (luminosities calculated assuming the cluster distance of 8.1 kpc) from Table 4.4. Different source classes are indicated with different markers, and open markers are less certain identifications. The lines indicate locations on this plot derived from models: power-law, `vapec`, NS hydrogen atmosphere (H-Atm) of different temperatures (using a 12 km, $1.4 M_{\odot}$ NS while assuming emission from the whole NS), and blackbody `bodyrad` of different temperatures assuming emission region of 120 m. For better readability, we only plot error bars for sources with $F(0.5 - 7 \text{ keV}) \gtrsim 1.3 \times 10^{-15} \text{ erg s}^{-1} \text{ cm}^{-2}$. Averaged uncertainties of the fainter sources are indicated by a capped error bar on the lower left of the plot. The fluxes of A1 are from the best-fitting atmospheric model in Echiburú et al. (2020). 104
- 4.5 0.5–2.5 keV X-ray luminosities vs. absolute V -band magnitudes (M_V), assuming an 8.1 kpc distance. Note that V_{555} magnitudes from Lugger et al. (2007) are used for A2 and B to derive M_V s. The short-dashed line indicates the separatrix $\log_{10} L_X[0.5 - 2.5 \text{ keV}] = -0.4M_V + 34$ from Bassa et al. (2004); the dashed-dotted line marks the upper limit of L_X for nearby ABs, which was derived by Verbunt et al. (2008) as $\log_{10} L_X[0.5 - 2.5 \text{ keV}] = 32.3 - 0.27M_V$. Open symbols are less certain identifications. 105
- 4.6 HUGS $UV_{275} - U_{336}$ CMD plotting U_{336} magnitudes vs. $U_{336} - UV_{275}$ colours for cluster members. Different subpopulations are plotted with different markers. 106

4.7	Number of chance coincidences (N_c) as defined in eq. (4.2) vs. distance from the cluster centre (in arcmin) for different sub-populations (Section 4.3.8.3). The vertical dashed and dashed-dotted lines indicate the core radius (r_c) and half-light radius (r_h). The probability of a chance coincidence with a main sequence star is significant throughout the half-light radius. . . .	107
4.8	WFPC2 V_{555} rms plotted versus V_{555} magnitudes. W17-1 and W17-2 are apparently outliers to the bulk of stars, indicating marked variability.	112
4.9	<i>Top</i> : X-ray spectrum of source 6 fitted with a vappec model (the spectrum is rebinned for better readability). <i>Bottom</i> : fitting residuals; a likely emission feature is present around 1.9 keV. . .	116
4.10	Binned radial profile of MSTO sample with a cored power law fit out to the half-light radius.	119
4.11	Cumulative radial distributions for selected stellar groups. Fitting information and K-S sample comparisons for these stellar groups are given in Table 4.7.	119
5.1	68% (solid red), 90% (dashed green), and 99% (dashed-dotted grey) contours in the ab plane for fits to radio source counts in cluster cores (left) and half-light regions (right). The best-fitting values of a and b are indicated with a black cross in each panel. The colorbar presents intensity of Z . For source counts in the core, $a \neq 0$ or $b \neq 0$ at the 90% level, while $a = b = 0$ is consistent with the data for sources within the half-light regions.	139
5.2	The marker and the contours are the same as those of Figure 5.1, but this fit required N_c to be equal to or greater than the number of confirmed members in the core (left) or within the half-light region (right).	139

5.3 Observed core source counts (black empty squares) and observed half-light region source counts (red empty diamonds) vs. predicted source counts in the core (black filled squares) and in the half-light region (red filled diamonds) based on the constrained fits plotted for all 22 GCs. The error bars on the observed numbers indicate 84% confidence upper and lower limits (Gehrels, 1986); for GCs with zero counts, we only plot the upper bar. The uncertainties in predicted numbers are propagated from uncertainties in Γ and M , and the 68% confidence ranges of a and b . The black dashed and red dotted lines in each panel marks the number of expected background sources in the core ($\mu_{b,\text{core}}$) and in the half-light region ($\mu_{b,\text{half}}$), respectively. 141

5.4 *Top:* A histogram showing distribution of spectral index (α) for core radio sources with constrained α values as listed in Table 5.2 (orange). *Bottom:* Histograms of α for pulsars from the ATNF catalog (hatched green), AGNs (hatched red), pulsar and AGN combined (solid black contour). The counts in each bin is normalized by dividing the total counts of each sample and the bin width. The core sources divide into steep-index and flatter-index groups; the flatter group is more numerous than expected from a pulsar-only distribution. Despite that the AGNs can partly account for the flatter group, there is an overabundance of core sources around $-0.5 \lesssim \alpha \lesssim -0.2$ 145

1	<p>X-ray colour-magnitude diagram plotting 0.5-6 keV fluxes (left scale) and luminosities (right scale) vs. hardness ratio (X_C, defined in eq.(6)) for known (red) and new (blue) sources. X_Cs and fluxes of the known sources are adapted from Bogdanov et al. (2010), while were calculated by <code>srcflux</code> (Sec. 3.2.2) for the new sources. For better readability, we only labelled the relevant known sources and the new sources, and put error bars on several sources to represent uncertainties at different flux levels. Upper/lower limits and errors in X_C are at the 90% confidence as derived according to methods in Gehrels (1986). We also indicate the locations of power-law models with different photon indices (Γs).</p>	180
2	<p><i>Chandra</i> ACIS-S spectra of W129 (top) and W145 (bottom) overplotted with best-fitting power-law (W129) and <code>vmekal</code> (W145) model. The bottom panel of each plot shows the fitting residuals. The spectra are re-binned only for plotting purpose.</p>	184
3	<p>Proper motions (PMs) from <i>Gaia</i> DR2 of stars within a 3' searching radius. The plot is centered on the cluster proper motion at $\mu_\alpha = 3.2908 \pm 0.0026 \text{ mas yr}^{-1}$, $\mu_\delta = -17.5908 \pm 0.0025 \text{ mas yr}^{-1}$. PM of each counterpart is indicated with red dot and 1 σ error bars.</p>	185
4	<p><i>Gaia</i> CMD plotting $G_{BP} - G_{RP}$ colours vs. G_{BP} band magnitudes. The counterparts are indicated with red filled circles.</p>	185
5	<p><i>HST/ACS</i> R625W finding chart for W134 showing a $2''.1 \times 2''.1$ region centered on the nominal X-ray position of W134, north is up and east is to the left. The red circle indicates the <i>Chandra</i> 95% error region while likely counterparts are indicated with yellow circles.</p>	186

- 6 UV₂₇₅, U₃₃₆, B₄₃₈, V₆₀₆, and I₈₁₄ finding charts for 23 X-ray sources; north is up and east is to the left. The green circle in each finding chart marks the 95% *Chandra* error circle as per Hong et al. (2005), and identified counterparts are indicated with red cross hairs. In the charts for source 13 and MSP A, the ellipses in cyan marks the 1 σ radio positional uncertainty. . . . 188

List of Abbreviations

AB	Active Binary
ACIS	Advanced CCD Imaging Spectrometer
AGN	Active Galactic Nuclei
ATNF	Australia Telescope National Facility
ATCA	Australia Telescope Compact Array
BH	Black Hole
BY Dra	BY Draconis
CV	Cataclysmic variable
GC	Globular Cluster
HMXB	High-mass X-ray binary
HST	The Hubble Space Telescope
LMXB	Low-mass X-ray binary
MSP	Millisecond Pulsar
NS	Neutron Star
RS CVn	RS Canum Venaticorum variable
VLA	the Karl G. Jansky Very Large Array
WD	White Dwarf
XRB	X-ray Binary

Chapter 1

Introduction

1.1 Globular Clusters

Globular clusters (GCs) are old stellar populations that harbour $\sim 10^{4-6}$ stars. These stars are gravitationally bound and grouped to form very dense cores. Stellar densities in the core can be as high as $10^{4-6} M_{\odot} \text{pc}^{-3}$, which, by contrast, significantly exceeds that of the solar neighborhood (~ 1 star per cubic parsec¹). The dense nature of the cores leads to a number of dynamical features of GCs, which greatly affect how GCs evolve over time.

GCs also represent the oldest stellar populations, with measured ages ~ 10 Gyr (VandenBerg et al., 2013). It is generally believed that, at the beginning, stars with varying masses were formed at nearly the same epoch, which then evolve at different rates (massive stars evolve faster than low-mass stars); present-day GCs therefore consist of stars at different stages of evolution, of which the most massive stars have become compact stellar remnants (or compact objects) including white dwarfs, neutron stars, and black holes.

¹1 parsec (pc) is approximately 3.26 light years.

1.2 Exotic binaries in globular clusters

Harbouring compact objects and being dynamically active mark the importance of GCs in the field of high-energy astrophysics. In particular, GCs are considered “breeding grounds” of many exotic binaries. These binaries are exotic in that (1) they typically contain a compact object, and/or (2) they have very close orbits (orbital periods of days, to as short as tens of minutes). Extreme physical properties of the compact objects in combination with close orbits facilitate interaction between the compact object and the secondary star — manifested as X-ray sources that have been revealed in almost all GCs.

In the 70s, X-ray missions like *Uhuru* and OSO 7 discovered X-ray sources in the direction of GCs (Giacconi et al., 1974; Clark, 1975; Canizares & Neighbours, 1975). The relatively low instrument sensitivities limited the detection to bright ($L_X \geq 10^{36}$ erg s⁻¹) sources, but it was soon realised, even with the limited angular resolution of the early missions, that the number of X-ray sources per unit mass is ~ 100 times greater in GCs than for the whole Galaxy (Katz, 1975). The identification of X-ray bursts as thermonuclear burning on the neutron star surface (Lewin & Joss, 1981) identified these bright X-ray sources as accreting neutron stars in close orbits with ordinary stars, where X-rays are emitted through accretion of matter onto the neutron stars.

The discovery of GC X-ray sources promoted studies of dynamical processes in GCs, particularly discussions of possible formation mechanism of these exotic binaries. Fabian et al. (1975) suggested that tidal capture of main sequence stars by neutron stars in dense GC cores can reproduce the observed X-ray sources in GCs. Sutantyo (1975) proposed that X-ray emitting close binaries can be formed by direct collisions between neutron stars/black holes and giant branch stars; the direct collision would completely disrupt the giant’s envelope, leaving behind a stellar core (a helium white dwarf) in very close orbit with the neutron star/black hole (Rasio & Shapiro, 1991). It was then shown by (Hills,

1976) that exchange interactions can also produce close binaries that emit X-rays; in this scenario, a neutron star or a black hole undergoes a close encounter with an already-existing (“primordial”) binary, which ejects one of the stars from the primordial binary, forming an exotic binary containing a neutron star or a black hole. A schematic of these formation channels is presented in Figure 1.1.

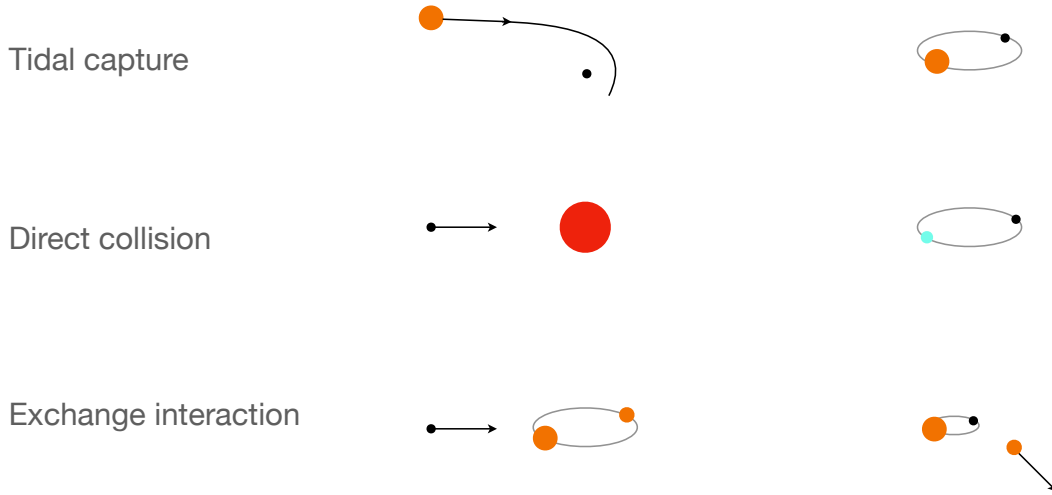


Figure 1.1: Dynamical formation channels of close exotic binaries in GCs. Compact objects are indicated with filled black circles. The compact stellar core of the red giant is represented with a filled cyan circle.

With the advent of *Einstein* and *ROSAT*, faint ($L_X \lesssim 10^{35}$ erg s $^{-1}$) X-ray sources were also found to be overabundant in GCs (Hertz & Grindlay, 1983a; Verbunt, 2001). The unprecedented angular resolution and sensitivity of the *Chandra X-ray Observatory (Chandra)* revealed a plethora of faint sources in many GCs (e.g., Grindlay et al., 2001a,b; Pooley et al., 2002a,b; Bassa et al., 2004; Heinke et al., 2005b, 2006; Lu et al., 2009; Zhao et al., 2019). The faint sources are a mix of multiple types of exotic binaries, which will be introduced in the following sections.

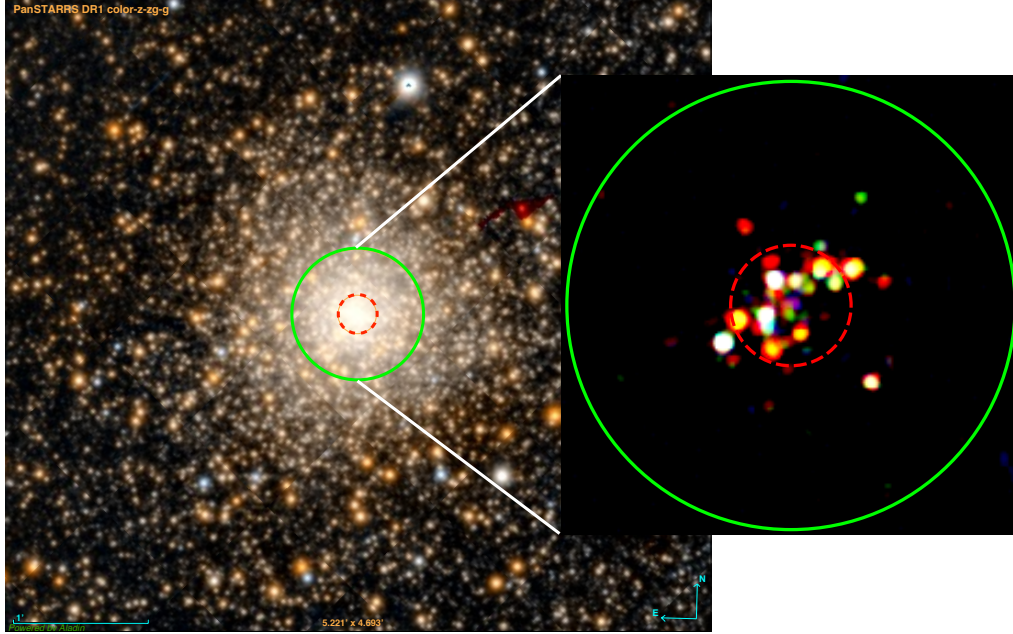


Figure 1.2: *Left:* Optical/near-IR image of the globular cluster NGC 6440 (PanSTARRS DR1, Chambers et al. 2016). *Right:* *Chandra*/ACIS X-ray image zoomed in on the half-light radius of NGC 6440; the different colours in the *Chandra* image represent the energies of X-ray sources: low-energy (soft) sources are in red, intermediate-energy sources are in green, and high-energy sources are in blue. The red dashed circle indicates the size of the core, while the green solid circle demarcates the half-light radius (Harris, 1996, 2010 edition).

1.2.1 Low-mass X-ray binaries

A low-mass X-ray binary (LMXB) is a binary harbouring a neutron star or a black hole in orbit with a low-mass ($\lesssim M_{\odot}$) secondary star (usually a main sequence star). The secondary star is also known as the donor star, from which matter is accreted onto the neutron star or the black hole via Roche-lobe overflow, emitting observable X-rays. For accretion onto a neutron star, the accretion luminosity (L_{acc}) is directly related to the mass transfer rate (\dot{M}) and the mass (M) and radius (R) of the neutron star:

$$L_{\text{acc}} = \frac{GM\dot{M}}{R} = 1.3 \times 10^{36} \left(\frac{\dot{M}}{10^{16} \text{ g s}^{-1}} \right) \left(\frac{M}{M_{\odot}} \right) \left(\frac{R}{10 \text{ km}} \right)^{-1} \text{ erg s}^{-1}. \quad (1.1)$$

For a typical neutron star with a mass of $1.4 M_{\odot}$ and a radius of 12 km, $L_{\text{acc}} \approx 1.5 \times 10^{36} \text{ erg s}^{-1}$ at an accretion rate of 10^{16} g s^{-1} (or $\approx 1.5 \times 10^{-10} M_{\odot} \text{ yr}^{-1}$). LMXBs accreting at a stationary rate are known as “persistent” LMXBs, whose L_{acc} ’s are persistently above $\sim 10^{36} \text{ erg s}^{-1}$, manifested as bright X-ray sources as discovered by the early missions. In contrast to the persistent systems, the majority of LMXBs have been discovered as transient X-ray sources, which stay mostly in a quiescent state but undergo occasional “outbursts” that are $\sim 10^4$ times brighter. Quiescent LMXBs, or qLMXBs, have been identified in the field (following bright outbursts), and in GCs. Accretion in qLMXBs is believed to be halted or at least greatly suppressed (Campana et al., 1998; Rutledge et al., 2002; Heinke et al., 2003b), so their spectra are often characterized by a thermal component consistent with emission from the heated neutron star surface, and/or a hard (power-law) component from continued low-level accretion (Chakrabarty et al., 2014; Wijnands et al., 2015).

So far, all known LMXBs containing black holes (BH LMXBs) are transient systems. They undergo occasional bright outbursts, during which they transition through different accretion states (see e.g., Done et al., 2007, for a review), but spend most of the time in quiescence (Corbel et al., 2006; Plotkin et al., 2013). The associated accretion luminosity (typically between $10^{30-34} \text{ erg s}^{-1}$) does not simply follow eq.(1.1), as the situation is more complicated in that black holes, unlike neutron stars, do not have a hard surface. As a result, the gravitational energy might not be radiated (in the form of X-rays) as efficiently as for NS LMXBs. Observations of BH LMXBs have shown that X-ray spectra of quiescent BH LMXBs are characterised by a power-law model ($N_E \propto E^{-\Gamma}$, where Γ is called the “photon index”, and N_E the number of photons at a specific energy E), with photon indices $\Gamma \approx 2$ (Reynolds et al., 2014)². The exact origin of X-rays is still under debate; the consensus is that the efficiency of radiating gravitational energy is low (as low as $\sim 10^{-7} c^2 \approx 10^{14} \text{ erg g}^{-1}$), which

²Note that Γ is used to denote stellar encounter rates in Chapter 5.

is broadly attributed to radiatively inefficient accretion flow (Narayan & Yi, 1994, 1995a,b; Narayan & McClintock, 2008; Yuan & Narayan, 2014) and/or outflowing material in the form of winds or collimated jets (e.g., Blandford & Begelman, 1999; Markoff et al., 2003, 2005; Yuan & Cui, 2005; Corbel et al., 2008; Plotkin et al., 2012).

1.2.2 Millisecond pulsars

Millisecond pulsars (MSPs) are radio pulsars rotating with periods of a few to tens of milliseconds, which generally have low inferred surface magnetic fields ($\lesssim 10^{10}$ G; see Figure 1.3). MSPs are the descendants of LMXBs where the accreted matter spins up the neutron star (Bhattacharya & van den Heuvel, 1991). Indeed, this connection between LMXBs and MSPs has been confirmed by three cases of transitional millisecond pulsars (tMSPs), that switch back and forth between radio pulsations and accretion, discovered over the past decade: XSS J1227-4853 (Bassa et al., 2014; Bogdanov et al., 2014; Roy et al., 2015), IGR J1824-2452 in the globular cluster M28 (Papitto et al., 2013), and PSR J1023+0038 (Archibald et al., 2009).

MSPs are found in binaries (binary MSPs) or isolated (isolated MSPs). Binary MSPs usually host low-mass degenerate (e.g., white dwarfs) or non-degenerate companions; the latter systems are also known as “spider” pulsars, where the companion is continuously ablated by pulsar wind. Spider pulsars are further categorised, based on the companion masses, into reback and black widow systems: rebacks have non-degenerate companions with mass between 0.1-0.4 M_{\odot} (e.g., Lyne et al., 1990; Ferraro et al., 2001), and can reach up to 0.7-0.9 M_{\odot} (Strader et al., 2019), while black widows are MSPs that host extremely exhausted companions that have masses $\lesssim 0.02 M_{\odot}$ (e.g., Fruchter et al., 1988; Stovall et al., 2014).

MSPs are usually identified with faint ($L \lesssim 10^{33}$ erg s $^{-1}$) X-ray sources. Spectra of isolated MSPs are well-described by blackbody-like emission from

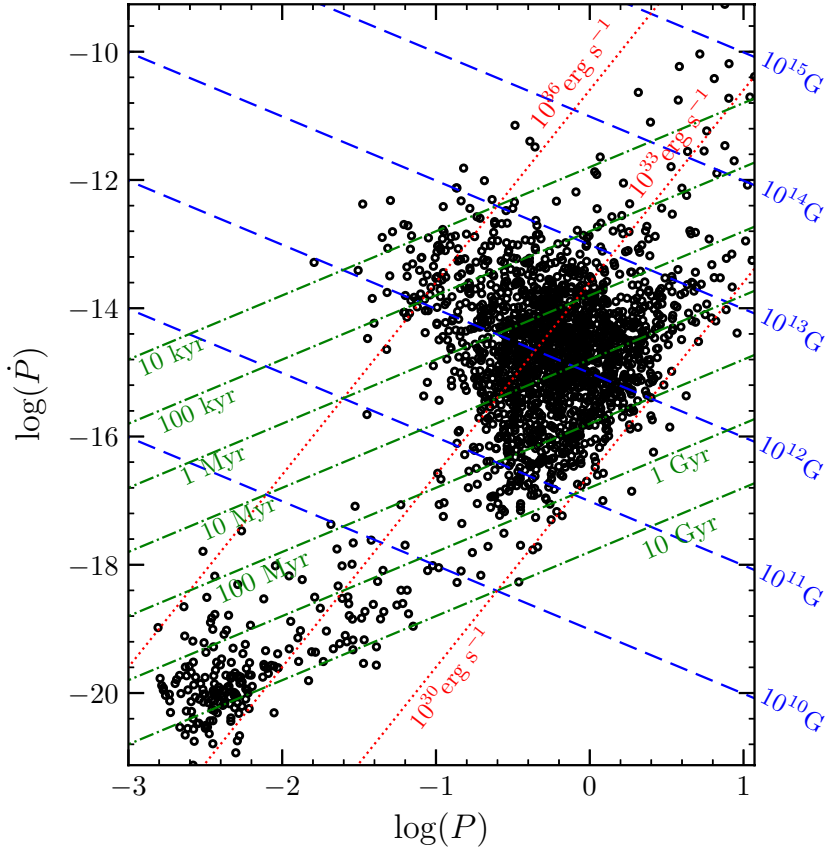


Figure 1.3: Rotation period derivative (\dot{P}) vs. rotation period (P) plotted for pulsars from the ATNF catalogue. Blue dashed lines mark surface magnetic field strengths; red dotted lines mark different spin-down powers; green dashed-dotted lines mark characteristic ages. MSPs are at the lower-left of the plot, roughly below the 10^{10} G line.

hot magnetic polar caps (Bogdanov et al., 2011; Forestell et al., 2014; Zhao et al., 2021a; Bogdanov et al., 2020), while spectra of binary MSPs, such as redbacks and black widows, are often characterised by a hard power-law component (typical Γ between 1.0 and 1.5; see e.g., Bogdanov et al. 2010), which can be attributed to either pulsed pulsar magnetospheric emission (e.g., Rutledge et al., 2004), or the unpulsed intra-binary shock created by the interacting pulsar wind and companion material (e.g., Bogdanov et al., 2005). The intra-binary shock might also lead to eclipses of X-rays, which has been observed in some binary MSPs as X-ray variability modulated on the binary period (Roberts, 2013; Wadiasingh et al., 2018; Kandel et al., 2019).

It has been shown that the numbers of both MSPs and their progenitors, LMXBs, are correlated with the encounter rates of their GCs (Pooley et al., 2002b; Hui et al., 2010; Bahramian et al., 2013), indicating a dynamical origin of GC MSP populations. Indeed, at the time of writing, the dense and massive GC Terzan 5 hosts the largest number of MSPs known (a total of 39 MSPs; Ransom et al. 2005; Lyne et al. 2000; Prager et al. 2017; Cadelano et al. 2018; Andersen & Ransom 2018; Ridolfi et al. 2021), while the second and third places go to 47 Tuc (25; Camilo et al. 2000; Ridolfi et al. 2016; Pan et al. 2016) and M28 (14; Bégin 2006; Lyne et al. 1987).

More MSPs in GCs are being discovered by future radio timing surveys with enhanced sensitivity (e.g., the TRIUMPH project³; FAST⁴). More pulsar candidates have recently been revealed by deep and high-angular-resolution radio imaging surveys as steep-spectrum radio sources (Zhao et al., 2020a; Urquhart et al., 2020), and may be further confirmed with observations at other wavelengths. A strong case of an MSP discovered by a deep radio imaging observation of NGC 6397 is presented in Chapter 3, and a compilation of more steep-spectrum radio sources in globular clusters will be a focus of my future work.

1.2.3 Cataclysmic variables

Cataclysmic variables (CVs) are white dwarfs accreting from low-mass companions. Assuming a typical GC white dwarf mass of $0.5 M_{\odot}$, a surface gravitational acceleration of $\log_{10} g = \log_{10}(GM/R^2) = 7.84$ (Moehler et al., 2004), and a mass accretion rate of $\approx 10^{-10} M_{\odot} \text{ yr}^{-1}$ in eq.(1.1), one gets the accretion luminosity of $L_{\text{acc}} \approx 4.0 \times 10^{32} \text{ erg s}^{-1}$. Following the discussion in Frank et al. (1992), one expects the radiated photons have a characteristic temperature ($T_{\text{rad}} \equiv h\nu/k$) between a blackbody (T_b) and a thermal temperature (T_{th}).

³<http://trapum.org/discoveries.html>

⁴<https://fast.bao.ac.cn/cms/article/65/>

On the one hand, T_b is calculated assuming that the radiation reaches an equilibrium with the accreted material before being radiated (optically thick limit), so

$$L_{\text{acc}} = 4\pi R^2 \sigma_{\text{SB}} T_b^4, \quad (1.2)$$

where σ_{SB} is the Stefan-Boltzmann constant. On the other hand, T_{th} defines another limit at which gravitational energy is converted directly to thermal energy of accreted material, after which emergent radiation has no further interaction with accreted material (optically thin limit) — the radiated photons then have $T_{\text{rad}} \sim T_{\text{th}}$. For each accreted pair of proton and electron, the released gravitational energy is $GM(m_p + m_e)/R \approx GMm_p/R$; and if we assume energy equipartition at thermal equilibrium, the total thermal (kinetic) energy of the electron-proton pair is $2 \times 3kT_{\text{th}}/2$. Equating gravitational energy and thermal energy gives

$$T_{\text{th}} = \frac{GMm_p}{3kR}, \quad (1.3)$$

where m_p is the proton mass. T_{rad} should lie between T_b and T_{th} . Now, if one adopts the typical mass and surface gravitational acceleration as mentioned, one gets a range for photon energies emerging from an accreting white dwarf in a CV:

$$2.4 \text{ eV} \lesssim h\nu \lesssim 23.6 \text{ keV}. \quad (1.4)$$

CVs are therefore potential UV and/or faint ($\lesssim 10^{33} \text{ erg s}^{-1}$) X-ray sources.

CVs in GCs contain low-mass late-type donors that overflow their Roche lobes and transfer mass to white dwarfs. Based on the magnetic field strength, mass from the companion can transfer to the white dwarf in different ways. Non-magnetic CVs have white dwarf magnetic field $\lesssim 10^4 \text{ G}$ (see Warner, 1995, for a review), where an accretion disc reaches down to the white dwarf

surface. Magnetic CVs generally have magnetic fields above $\sim 10^6$ G, and can be further divided into two sub-classes: polars and intermediate polars. Polars have magnetic fields between $2 \times 10^{7-8}$ G, strong enough to directly channel the accretion flow onto the white dwarf’s magnetic poles (see e.g., Cropper, 1990). Intermediate polars have truncated accretion discs, and accretion flow is channeled from the inner disc to the white dwarf magnetic poles (see e.g., Patterson & Skillman, 1994).

Many studies have shown that CVs can be effectively identified using UV and optical photometry. Accreting white dwarfs emit mostly at UV wavelengths, while the companion star dominates emission at longer wavelengths, and $H\alpha$ photometry is effective at identifying emission from accretion discs (e.g., Grindlay et al., 2001b; Pooley et al., 2002a; Knigge et al., 2002; Edmonds et al., 2003a,b; Cohn et al., 2010; Dieball et al., 2010; Lugger et al., 2017). More details are presented in Chapters 2, 4.

1.2.4 Chromospherically active binaries

Binaries containing ordinary or evolved stars in close orbits (orbital periods ranging from less than a day to several days) can also be active X-ray emitters, and are known as chromospherically active binaries, or simply active binaries (ABs; Baily et al. 1990). Stars in ABs are tidally locked to each other, so are forced to rotate at fast rates. This induces strong chromospheric and coronal activity that emits X-rays.

In GCs, it is possible to form ABs that contain only late-type main sequence stars (BY Draconis); or ABs that host at least one evolved component, a sub-giant or a red giant, which are known as RS Canum Venaticorum variables (RS CVn). ABs make up the majority of the faintest ($L_X \lesssim 10^{31}$ erg s $^{-1}$) X-ray sources. X-ray flux associated with coronal activity scales with rotation rate (Ω): $F_X \propto \Omega^2$ (Pallavicini et al., 1981), and the corresponding X-ray luminosity scales with the surface area of the stars.

Unlike LMXBs and MSPs, ABs are not dynamical in origin. AB populations scale with mass, as opposed to stellar encounter rates, which suggests that ABs are more likely formed by evolution of primordial binaries (Bassa et al., 2004).

1.3 Identification of X-ray sources

Identification of X-ray sources involves combining photometric, temporal, spectroscopic, and kinematic information of counterparts at multiple wavelengths. While *Chandra* has revealed a plethora of X-ray sources with sub-arcsecond localisation, the dense nature of GCs requires additional information to more confidently identify counterparts. Typically, optical/UV photometry is a very powerful tool in distinguishing CVs and ABs. Furthermore, deep radio imaging observations can provide additional information that is useful in finding potential MSPs and LMXBs, especially accreting stellar mass black holes in LMXBs. Chapter 2, 3, 4 demonstrate detailed processes of distinguishing between different source classes using *Hubble Space Telescope (HST)* imaging observations and deep radio observations by the *Very Large Array (VLA)* and the *Australia Telescope Compact Array (ATCA)*.

1.4 Why study GC exotic binaries?

Studies of different types of exotic binaries address some of the most exciting topics in modern astrophysics. In addition to understanding relevant GC dynamics, observations of X-ray binaries probe extreme physics of the compact objects. For example, the physics of extremely dense matter can be studied by observing neutron stars in LMXBs, the density of which is impossible to reach in experiments on Earth. LMXBs are also great objects for the study of black hole accretion, partly because the black hole masses are better constrained in stellar-mass black holes compared to super-massive black holes and, pragmati-

cally, because the associated viscous time scale is shorter (\lesssim a year) than that for super-massive black holes (McHardy et al., 2006; Kelly et al., 2009). Furthermore, the extreme gravity around neutron stars provides a testing ground for general relativity, which is made possible in observations of binary pulsars (Hulse & Taylor, 1975; Weisberg & Taylor, 2005) thanks to the very high timing accuracy. Finally, numerical simulations have been suggesting that the dense GC cores can produce gravitational wave sources like black hole mergers (Fragione et al., 2020), shedding light on our understanding of black hole formation and growth processes.

Chapter 2

Identification of Faint Chandra Sources in the Globular Cluster M3

Yue Zhao¹, Craig O. Heinke¹, Haldan N. Cohn², Phyllis M. Lugger², Adrienne M. Cool³

¹ Department of Physics, CCIS 4-183, University of Alberta, Edmonton, AB, T6G 2E1, Canada. ² Department of Astronomy, Indiana University, 727 E. Third St. Bloomington, IN 47405, USA. ³ Department of Physics and Astronomy, San Francisco State University, 1600 Holloway Avenue, San Francisco, CA 94132, USA.

This chapter details the work published in Zhao et al. 2019, “Identification of Faint Chandra Sources in the Globular Cluster M3”, *MNRAS*, 483, 4560, DOI: 10.1093/mnras/sty3384, where we use archival *Chandra* X-ray observations and imaging observation by the *Hubble Space Telescope* to identify a total of 16 X-ray sources in the globular cluster M3 (Zhao et al., 2019).

Abstract

We report a 30 ks *Chandra* ACIS-S survey of the globular cluster M3. Sixteen

X-ray sources were detected within the half-light radius ($2.3'$) with $L_X \gtrsim 2.3 \times 10^{31} \text{ erg s}^{-1}$. We used *Hubble Space Telescope* WFC3/UVIS and ACS/WFC images to find 10 plausible optical/UV counterparts. We fit the spectral energy distribution of the known cataclysmic variable 1E1339.8+2837 with a blue ($T_{\text{eff}} = 2.10_{-0.58}^{+1.96} \times 10^4 \text{ K}$, 90% conf.) spectral component from an accretion disc, plus a red component ($T_{\text{eff}} = 3.75_{-0.15}^{+1.05} \times 10^3 \text{ K}$) potentially from a subgiant donor. The second brightest source (CX2) has a soft blackbody-like spectrum suggesting a quiescent low-mass X-ray binary (qLMXB) containing a neutron star. Six new counterparts have obvious UV and/or blue excesses, suggesting a cataclysmic variable (CV) or background active galactic nucleus (AGN) nature. Two (CX6 and CX8) have proper motions indicating cluster membership, suggesting a CV nature. CX6 is blue in UV filters but red in V-I, which is difficult to interpret. Two CV candidates, CX7 and CX13, show blue excesses in B-V colour but were not detected in the UV. The other two CV candidates were only detected in the two UV bands (UV₂₇₅ and NUV₃₃₆), so do not have proper motion measurements, and may well be AGNs. One *Chandra* source can be confidently identified with a red straggler (a star redward of the giant branch).

2.1 Introduction

Galactic globular clusters (GCs) are gravitationally-bound dense and old stellar populations harbouring $\sim 10^4 - 10^6$ stars. The high stellar density in the core region leads to many stellar encounters, and therefore creates a favourable environment to form a variety of close binary systems through dynamical processes (e.g. Fabian et al., 1975; Hills, 1976; Camilo & Rasio, 2005; Ivanova et al., 2006). Bright X-ray binaries ($L_X \sim 10^{36-37} \text{ erg s}^{-1}$) in globular clusters are transient or persistent low-mass X-ray binaries (LMXBs) typically harbouring accreting neutron stars (NSs) with low-mass optical companions (Lewin & Joss, 1983; Grindlay et al., 1984). These LMXBs are clearly produced dy-

namically, based on their association with the densest globular clusters in our Galaxy (Clark, 1975; Verbunt & Hut, 1987; Verbunt, 2003) and in other galaxies (Jordán et al., 2004; Sivakoff et al., 2007; Jordán et al., 2007; Peacock et al., 2009). High angular resolution X-ray observations with *Chandra* have revealed large numbers of faint ($L_X \sim 10^{29-34}$ erg s $^{-1}$) X-ray sources in globular clusters (Verbunt & Lewin, 2006; Heinke et al., 2010). The faint X-ray population is composed of multiple source classes, including: quiescent low-mass X-ray binaries (qLMXBs) in which accretion onto the NS is thought to be stopped or at least largely suppressed (Campana et al., 1998; Rutledge et al., 2002; Heinke et al., 2003b; Chakrabarty et al., 2014) with luminosities typically $\sim 10^4$ times fainter than during outbursts; cataclysmic variables (CVs) where white dwarfs accrete from low-mass companions (Hertz & Grindlay, 1983a; Cool et al., 1995; Pooley et al., 2002b; Cohn et al., 2010; Rivera Sandoval et al., 2018); millisecond pulsars (MSPs), thought to be radio pulsars that have been spun up by accretion (Bhattacharya & van den Heuvel, 1991), which are observed in both X-ray (Saito et al., 1997; Bogdanov et al., 2006) and radio (Ransom et al., 2005; Freire et al., 2017); and chromospherically active binaries (ABs) composed of two tidally-locked non-degenerate stars, wherein fast rotation induces active coronal regions that emit (relatively faint, $L_X < 10^{31}$ erg s $^{-1}$) X-rays (Bailyn et al., 1990; Dempsey et al., 1993; Grindlay et al., 2001a; Heinke et al., 2005b). The qLMXBs and CVs appear to be correlated with encounter rate (Pooley et al., 2003; Heinke et al., 2003b; Pooley & Hut, 2006; Bahramian et al., 2013), while the ABs are expected to be primordial in origin (Bassa et al., 2004; Verbunt et al., 2008; Bassa et al., 2008; Lu et al., 2009; Huang et al., 2010).

The globular cluster M3 (or NGC 5272) is a good target to study for several reasons. First, M3 is massive, but has a relatively low core density (central luminosity $\rho_c \approx 3.7 \times 10^3 L_\odot \text{ pc}^{-3}$ according to Harris 1996, 2010 version), which suggests a relative predominance of primordially, over dynamically, formed X-ray binaries (XRBs). Moreover, a less dense core facilitates the optical iden-

tification of counterparts to X-ray sources, which is difficult in denser clusters due to crowding. The X-ray sources in M3 also show a relatively dispersed distribution, which allows easier identifications and also makes them good targets for future X-ray observations with instruments that have larger collecting area but relatively larger PSFs (e.g. XMM-Newton, and the future telescope Athena). Secondly, M3’s position far from the Galactic Plane means it suffers relatively little reddening, making photometric studies easier and more precise. This will, in turn, support the identification of possible counterparts.

Previous X-ray studies of M3 have focused on the brightest X-ray source, 1E1339.8+2837 (1E1339 hereafter). 1E1339 was first discovered as a faint X-ray source ($L_X \sim 10^{33}$ erg s $^{-1}$) by the *Einstein Observatory* (Hertz & Grindlay, 1983a). It underwent a bright outburst observed by ROSAT in 1991-1992, during which it showed a very soft spectrum ($kT \approx 20 - 45$ eV, $L_X \sim 10^{35}$ erg s $^{-1}$, Hertz & Grindlay 1983a; Verbunt et al. 1995). The source returned back to quiescence with a much harder X-ray spectrum, observed by ASCA (Dotani et al., 1999) and *Chandra* ($\Gamma \sim 1.4$; see Stacey et al. 2011, which used the same *Chandra* observations presented here). The optical counterpart of 1E1339 was identified by Edmonds et al. (2004) as a star with a very blue $U - V$ colour, showing marked variability on timescales of hours.

1E1339 is the only supersoft X-ray source (SSS) identified in a Galactic GC, though three transient SSSs have been identified in M31 GCs (Henze et al., 2009, 2013), two of them clearly identified with nova explosions, which are the most frequent class of transient SSSs in M31 (e.g. Henze et al., 2011). The bright outburst and the supersoft spectrum suggest a physical connection to other galactic supersoft X-ray sources (SSSs). However, 1E1339’s peak observed X-ray luminosity was ~ 100 times fainter than that of standard SSSs, suggesting a much smaller burning area.

The present work focuses on a systematic multiwavelength study of the faint X-ray sources in M3. The paper is organized as follows: in section 2.2,

we report the *Chandra* and *HST* data we used in our studies. In section 2.3, we describe our analyses including data reduction, source detection, and the relevant techniques and methodologies used in astrometry, photometry, and counterpart identifications. In section 2.4, we discuss the possible nature of each X-ray source based on its photometric and spectroscopic properties. Finally, in section 2.5, we summarise our results.

2.2 Observations

2.2.1 *Chandra* Observations

The globular cluster M3 was observed by the Advanced CCD Imaging Spectrometer (ACIS-S) on board the *Chandra X-ray Observatory*, using the *very faint* mode. Three observations, at roughly 6-month intervals, were taken, focused on monitoring 1E1339. A 1/2 subarray was used to reduce the frametime, and thus pileup from this relatively bright source, but the field of view still covers the whole half-light region of the cluster. Observation details are listed in Tab. 2.1.

Table 2.1: *Chandra* Observations of M3

ObsID	Time of observation	Exposure time (ks)	Chip
4542	2003-11-11 16:33:18	9.93	ACIS-S
4543	2004-05-09 17:26:32	10.15	ACIS-S
4544	2005-01-10 08:54:31	9.44	ACIS-S

2.2.2 *HST* Observations

We used *HST* WFC3/UVIS (GO12605, PI: Piotto), ACS/WFC (GO10775, PI: Sarajedini) and ACS/HRC and ACS/WFC (GO10008, PI: Grindlay) imaging data to search for possible optical counterparts. The WFC3 2012 data contained observations in the F275W (\sim UV), F336W (\sim NUV), and F438W (\sim B) filters, while the 2006 ACS data used the F606W (\sim V) and F814W

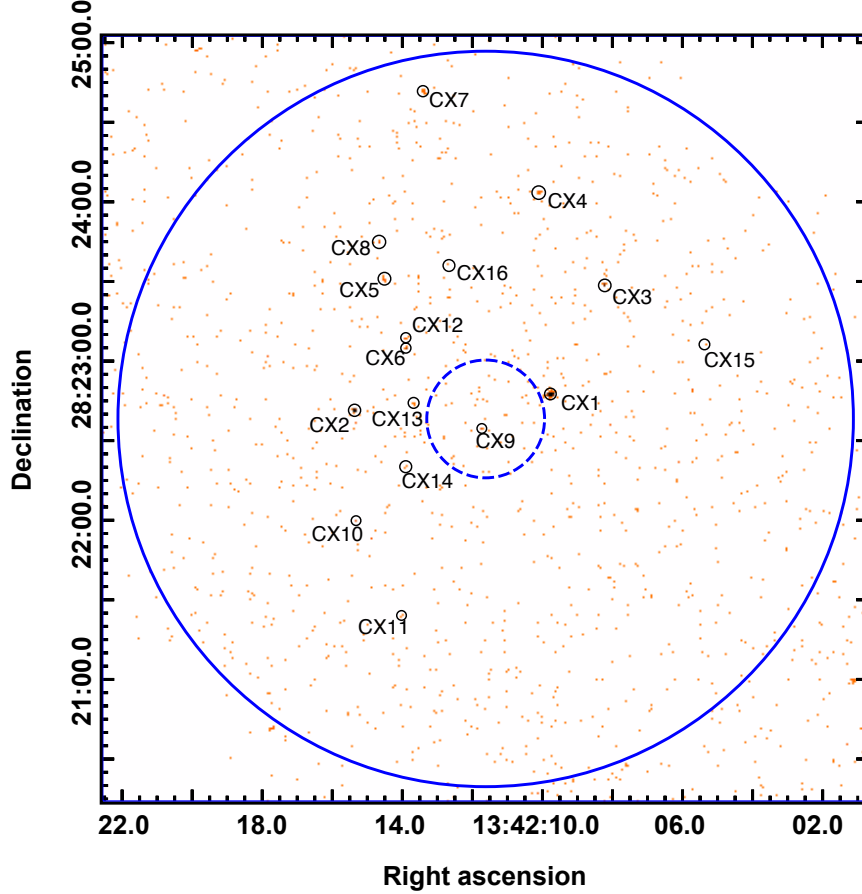


Figure 2.1: Merged 0.5 – 7 keV *Chandra* exposure-corrected ACIS-S X-ray image of the central $4'8 \times 4'8$ region of M3. The dashed blue circle shows the $0'37$ core region; the solid blue circle shows the $2'31$ half-light radius (Harris, 1996, 2010 edition). Sources detected by *wavdetect* are marked with solid black circles. The size of each pixel is $0''.492$.

(\sim I) filters. The ACS/HRC and ACS/WFC 2004 data were taken over a broad range of UV and optical bands, in conjunction with the second *Chandra* observation. This enables us to construct a simultaneous spectral energy distribution (SED) for the supersoft X-ray source 1E1339. Details of these observations are listed in Tab. 2.2.

Table 2.2: *HST* Observations of M3

GO	Time of observation	Exposure time (s)	Camera/Channel	Filter
10008	2004-05-09 17:51:18	620	ACS/HRC	F220W
	2004-05-09 17:41:19	464	ACS/HRC	F250W
	2004-05-09 17:17:33	1200	ACS/HRC	F330W
	2004-05-09 19:05:02	680	ACS/WFC	F435W
	2004-05-09 19:22:02	678	ACS/WFC	F555W
	2004-05-09 18:52:26	290	ACS/WFC	F814W
10775	2006-02-20 11:16:31	532	ACS/WFC	F606W ($\sim V$)
	2006-02-20 12:55:54	612	ACS/WFC	F814W ($\sim I$)
12605	2012-05-15 01:39:53	2490	WFC3/UVIS	F275W ($\sim UV$)
	2012-05-15 01:49:19	1400	WFC3/UVIS	F336W ($\sim NUV$)
	2012-05-15 01:36:38	168	WFC3/UVIS	F438W ($\sim B$)

2.3 Analyses

2.3.1 Merging Chandra Observations

The *Chandra* data were reduced using the *Chandra Interactive Analysis of Observations* software (CIAO) version 4.10¹ and CALDB version 4.7.8. We first reprocessed the data using the CIAO *chandra_repro* script to update the calibration, generating new level-2 event files. We then add the three observations to get a deeper view of the cluster. We first adjust aspect solutions between observations by using the brightest source 1E1339. The new aspect solutions were applied to the event files by using the CIAO *wcs_update* tool. Finally, the combined exposure map and the corresponding exposure-corrected image were generated by using the CIAO *merge_obs* tool. The resulting merged broad-band exposure-corrected (0.5 – 7 keV) X-ray image is shown in Fig. 2.1.

2.3.2 Source Detection

We generated an X-ray source list by running the CIAO *wavdetect*² tool on the combined broad-band X-ray image. The *wavdetect* algorithm correlates possible source pixels with a “Mexican Hat” function with different scale sizes

¹<http://cxc.harvard.edu/ciao/>

²<http://cxc.harvard.edu/ciao/threads/wavdetect/>

and identifies pixels with sufficiently large positive correlation values to further calculate source positions, error circles and other information about the sources. We chose $scales = 2, 4$ to cover the possible sizes of point sources at different off-axis angles, and used $sigthresh = 3 \times 10^{-6}$ (the reciprocal of the area of the region) to limit the expected number of false detections to 1. The detected sources are listed in Tab. 2.5. The right ascensions and declinations are the coordinates as calculated by *wavdetect*. P_{err} is the 95% error circle following the empirical formula from Hong et al. (2005).

2.3.3 Source counts

We used the CIAO *srcflux*³ script to calculate the source counts in 3 energy bands: broad (0.5 – 7.0 keV), soft (0.5 – 2.0 keV), and hard (2.0 – 7.0 keV). The effective energy of each band was calculated as the flux-weighted average using the best-fit models of 1E1339 in Stacey et al. (2011). To calculate the combined counts, we first apply the script to each individual observation, and then add up the counts. For all sources except CX6 and CX12, the extraction region is defined by a circle that encloses 90% of the PSF at 1 keV, and the background region is an annulus with inner radius the same as that of the extraction region and outer radius 5 times the radius of the source region. Because CX6 and CX12 are close to one another, their background regions were defined separately as annuli excluding the other source. In Tab. 2.5, we ordered the sources in descending order of their observed counts in the broad band.

2.3.4 Optical Photometry

We used the wide-field observations from three epochs (2004, 2006, and 2012) to systematically study the photometry of this GC.

³<http://cxc.harvard.edu/ciao/threads/fluxes/>

The 2012 WFC3/UVIS photometry has been analysed as part of the *Hubble Space Telescope UV Legacy Survey of Galactic Globular Clusters* (Piotto et al., 2015, GO-13297), and the reduced data and data products, including magnitudes of detected point sources, are now available to the public (Soto et al., 2017). However, we found that some stars detected on our images, which coincide with X-ray error circles, are not included in the Padova catalogue, though evidence for their presence is visible to the eye. Therefore, we also generated our own photometric catalogue by performing PSF-fitting photometry on the three WFC3/UVIS filters for counterpart searching.

We used *HST* data products that are pipeline-processed, flat-fielded, and with charge transfer efficiency (CTE) trails removed (i.e., FLC images) to get the stacked images for photometry, absolute astrometry, and counterpart searches. We used the *HST* Drizzlepac software version 2.0⁴ for image alignment and combination. For each filter, all FLC frames are first aligned to a reference frame (one of the FLC images) with the Drizzlepac *Tweakreg* tool. The aligned images were then combined using the Drizzlepac *AstroDrizzle* tool with *pixfrac*=1.0. In order to get higher resolution, the drizzle-combined images were oversampled by a factor of two so that their pixel size is half of the original (0'02/pixel for WFC3/UVIS, and 0'025/pixel for ACS/WFC). The drizzle-combined images of ACS/WFC were used for visual inspection of candidates and for making finding charts.

We then performed aperture and PSF-fitting photometry on the drizzle-combined WFC3 images (2012 observation) using the PyRAF⁵ DAOPHOT (Stetson, 1987) package. A star list was first generated for each filter by the *daofind* task with 3 σ detection threshold. We then chose relatively bright and isolated stars to model the PSFs. In order to account for possible spatial variability, at least 100 PSF candidate stars were selected across each image and

⁴http://www.stsci.edu/hst/HST_overview/drizzlepac

⁵http://www.stsci.edu/institute/software_hardware/pyraf

the PSF model was set to be a second-order function of x and y ($varorder = 2$). The best-fit PSF model was then applied to all stars in the field by using *allstar*.

The following three steps were taken to calibrate the DAOPHOT/*allstar* photometry. First, magnitudes corresponding to a finite aperture were calibrated to those corresponding to an infinite aperture using the "curve of growth" method applied to a subset of reasonably isolated bright stars. Second, instrumental magnitudes of infinite aperture were shifted to the VEGAMAG system by using the WFC3 zeropoints from the STScI web page⁶. Finally, PSF-fitting photometry only gives relative magnitudes, so we cross-identified stars between aperture photometry and PSF-fitting photometry, and applied the average offsets to convert magnitudes in PSF photometry to instrumental magnitudes.

The photometry of the 2006 ACS/WFC observations (GO-10775, PI: Sarajedini) has been produced as part of the *ACS Globular Cluster Treasury Program* (Sarajedini et al., 2007; Anderson et al., 2008, GO-10775) which provides V_{606} and I_{814} magnitudes (available at the *Mikulski Archive for Space Telescopes* (MAST) website⁷).

We obtained photometry for the 2004 F435W (B) and F555W (V) images (GO-10008, PI: Grindlay) using software based on the program developed for the *ACS Globular Cluster Treasury Program*, described in Anderson et al. (2008) and known as Ksync. We performed photometric calibration to the VEGAMAG system by doing aperture photometry on moderately bright, isolated stars within a 0.15 arcsec radius aperture, finding the aperture correction to an infinite radius aperture from Sirianni et al. (2005), calculating the median offset between the Ksync photometry and the aperture photometry, and applying the calibrations from the HST calibration website.⁸

With the obtained magnitudes for different filters, we constructed colour-

⁶http://www.stsci.edu/hst/wfc3/phot_zp_1bn

⁷<https://archive.stsci.edu/prepds/acsggct/>

⁸<https://acszeropoints.stsci.edu/>

magnitude diagrams (CMDs) by cross-matching catalogues in different filters. In Fig. 2.2 we show the resulting $UV_{275} - NUV_{336}$, the $NUV_{336} - B_{438}$, and the $V_{606} - I_{814}$ CMDs; in Fig. 2.3, we show the $B_{435} - V_{555}$ CMD.

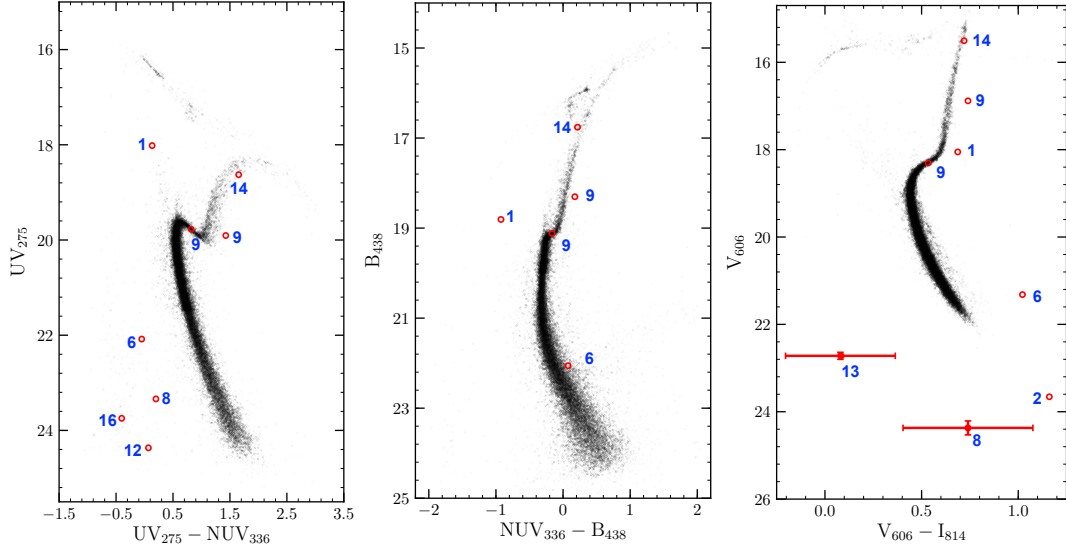


Figure 2.2: *Left:* $UV_{275} - NUV_{336}$ CMD generated by stars within a region of $140'' \times 140''$ centered on the cluster core. *Middle:* $UV_{336} - B_{438}$ CMD generated by stars within the same region. Both left and middle panels were generated using DAOPHOT results. *Right:* $V_{606} - I_{814}$ CMD from the catalogue of the *ACS Globular Cluster Treasury Program*. Optical counterparts are shown with red circles and annotated with their CX IDs (two potential counterparts are shown for CX9, though we find the brighter, redder one more likely). The error bars of CX8 and CX13 were indicated to show the uncertainty of their blue excesses.

2.3.5 Astrometry

The accuracy of *HST* astrometry is limited by at least two error sources. The first type of error comes from the fact that positions of guide stars used to derive the astrometric information are known with some uncertainties ($\lesssim 200$ mas for WFC3; $\lesssim 300$ mas for ACS. See ACS and WFC3 Handbooks; Lucas 2016, Deustua 2016). Secondly, errors are also introduced when the instrument aperture is mapped to the guide stars. The *Chandra* images are not astrometrized at the sub-arcsecond level, and therefore also require astrometric calibrations.

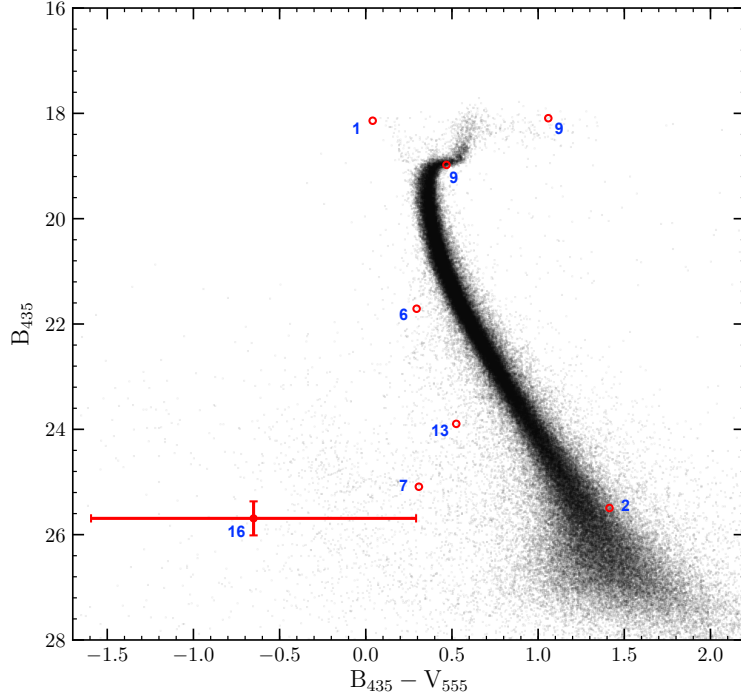


Figure 2.3: $B_{435} - V_{555}$ CMD from the 2004 ACS/WFC observation. Optical counterparts are annotated by red circles. The large photometric errors of CX16 are indicated with error bars.

Our process of calibrating for astrometry includes two steps: 1. Calibrate one of the optical images to a known catalogue that has superior astrometry, and use this image as the reference frame; 2. Align other optical images to the reference frame, and align the *Chandra* catalogue to the reference frame for boresight correction—such that CX1 centres on its known counterpart (Edmonds et al., 2004). To fulfill this, we cross-matched source positions in one of our *daofind* catalogues with those from the Gaia Catalogue (Data Release 2; see Gaia Collaboration et al. 2016, 2018a). We chose the NUV_{336} image as the reference image because it has a sufficiently long exposure, yet not so long to render bright sources saturated. We used a total of 895 Gaia sources that have relatively accurate positions (with errors in RA and DEC both ≤ 0.5 mas) found within a $1'$ search radius centred on the cluster core. Cross-matching resolved a total of 868 matches. We calculated the average offsets ($Gaia - NUV_{336}$) in RA and DEC, finding an average $\Delta RA \sim -0.384'' \pm 0.004''$ and an average

$\Delta\text{DEC} \sim 0.254'' \pm 0.003''$ (1σ errors). For boresight correction, we found the Gaia – *Chandra* offsets of CX1 to be $\Delta\text{RA} \sim -0.22''$ and $\Delta\text{DEC} \sim 0.10''$.

2.3.6 Counterpart search

The principle of hunting for optical counterparts to XRBs more or less depends on the source class. For example, CVs typically have a strong UV excess that originates from the shock-heated region on the WD surface and/or the accretion disc, so they usually appear as blue outliers on UV – NUV or NUV – B CMDs. ABs are either K/M type main sequence stars (BY Draconis, or BY Dra) or F/K type subgiants (RS Canum Venaticorum or RS CVn). Examples of works using these classifications include Cohn et al. (2010) and Cool et al. (2013). Using these criteria, we searched possible counterparts primarily in the 95% error circles. If no interesting object was found within the 95% error circle, we also applied a somewhat larger searching region ($\leq 1.8P_{\text{err}}$), recognising that this procedure incurs a higher risk of spurious coincidences.

We also have to consider possible confusion from foreground stars and background AGNs. Foreground stars usually appear redder, while background AGNs appear bluer, than cluster members. To exclude non-members, we check the proper motion (PM) of each counterpart candidate and compare that with the PM of the GC. The cluster membership can be confirmed if the star moves in accordance with the cluster’s systematic PM, and in disagreement with the PM of other possibilities. The enhanced angular resolution of HST cameras (e.g. ACS and WFC3) has made proper motion measurement possible over a relatively short span of time. Therefore, as part of the *Hubble Space Telescope UV Legacy Survey of Galactic Globular Clusters*, Piotto et al. (2015) includes a PM study of M3 by cross-matching the WFC3 source list with the ACS source list obtained 6.2 years earlier. Using the ACS(2006) and WFC3(2012) x and y positions from the Padova catalogue, we first calculated the displacements in x and y for each counterpart. The displacement can then be converted to proper

motions with $v_i = \Delta x_i \times 50/\text{Epoch}$ (see Soto et al. 2017), where Epoch = 6.2 yr is the time interval between the ACS and the WFC3 observations. As another check on cluster membership, we incorporated the membership probability (P_μ) from the 2018 release of the public catalogue (see Nardiello et al. 2018).

We used stars that have at least one good photometric measurement in all three UV filters from the Padova catalogue as the sample for our PM check. We first computed PMs for each candidate counterpart and then compare them with the PM rms of the sample. A star is accepted as a cluster member if both its v_α and v_δ are smaller than 3 times the PM rms ($\approx 1.779 \text{ mas yr}^{-1}$). Fig. 2.5 shows the PM distribution of the selected sample plotted in 4 separate magnitude bins, with candidate counterparts marked with red circles. The 3-rms limit of each bin is indicated with a dashed circle. Because the first bin is made of bright stars that are close to saturation, it has a relatively large rms. To exclude background AGN, we used the proper motion measurement of the cluster from GAIA DR2 (Gaia Collaboration et al., 2018b, see Table C.1.), from which we found $v_\alpha = 0.1127 \pm 0.0029 \text{ mas yr}^{-1}$ and $v_\delta = 2.6274 \pm 0.0022 \text{ mas yr}^{-1}$ for background AGN (marked with a red cross in Fig. 2.5).

Relying purely on photometric properties, we found potential counterparts to 10 of 16 *Chandra* sources. 8 of these are located within the corresponding 95% error circles, all except for the possible counterparts to CX7 and CX16. Fig. 2.4 shows a histogram of offsets for 10 identified counterparts in unit of their 95% error radii. PMs for our proposed counterparts to CX2, CX7, CX12, CX13 and CX16 are not available due to their nondetections in either 2006 or 2012, or both (see Tab. 2.6). However, the counterparts to CX1, CX6, CX8, CX9 and CX14 all have PMs less than 3 rms different from M3 (both in the α and δ directions), and are inconsistent with the expected location of AGN, outside the expected 3σ PM radius expected for background sources. The cluster memberships of the counterparts to CX1, CX6, CX9 and CX14 are confirmed by the calculated membership probability (P_μ). The counterpart to

CX8 was detected as a very faint extension to a relatively bright star in the 2006 ACS/WFC observations (see Fig. 2.7), which might cause ambiguity in measuring the positions, so the PM information should be taken with care. Fig. 2.7 shows a mosaic of finding charts, wherein the most likely counterpart to each *Chandra* source is annotated with a red arrow. The corresponding optical colours and magnitudes of these stars are marked with red circles in Fig. 2.2. The magnitudes used for identification are summarised in Tab. 2.6.

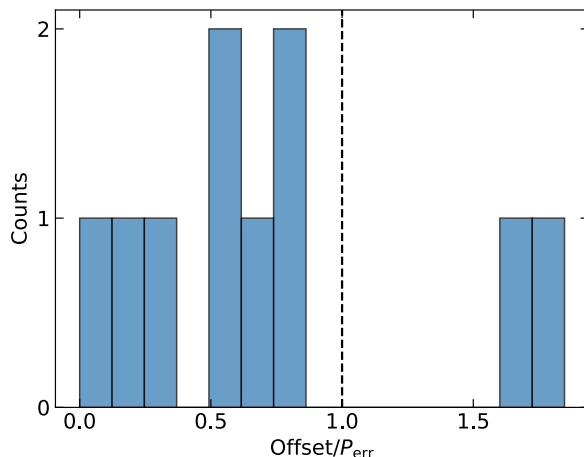


Figure 2.4: A histogram showing the distribution of offsets for the 10 identified counterparts. Each offset was normalised to the corresponding 95% error radius (P_{err}). The dashed line marks edges of the error circles.

2.3.7 Cluster Subpopulations and Chance Coincidences

In crowded regions (e.g. the cluster core), the chance of a potential counterpart being a coincidence is significant, so it is important to estimate the number of chance coincidences for different cluster subpopulations. To get a census of cluster members, we used the PM information in the Padova catalogue to remove the non-members. We found ≈ 45554 cluster members detected in the WFC3 FOV. We applied polygonal selection areas on the UV – NUV CMD to divide members into different subpopulations (see Fig. 2.6). We found ≈ 2592 evolved stars, including ≈ 967 subgiants, and ≈ 1625 red giants. 108 stars were identified as (moderately) blue stars. Finally, we found a population of

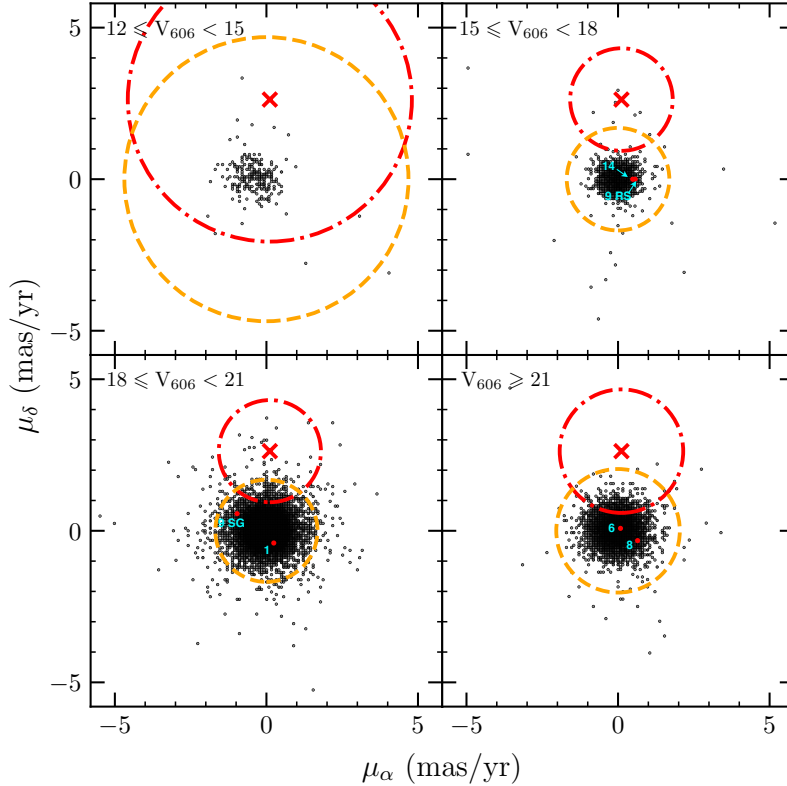


Figure 2.5: Proper motion distribution of stars with at least one good photometric measurement in each filter from the Padova Catalogue plotted in 4 V_{606} magnitude bins. The cluster’s average proper motion corresponds to the zero point. The proper motion of background galaxies, obtained from GAIA DR2’s estimate of the cluster motion, is marked with a red cross. Counterparts are shown with red points. The orange dashed circle in each panel shows the 3 rms radius within which stars are considered as likely cluster members. The red dotted-dashed circle in each panel shows the corresponding 3σ composite error radius of the AGN proper motion.

169 blue stragglers and a population of only 9 red stragglers. The predicted number of chance coincidences per error circle was estimated by multiplying the number of stars in each subpopulation by the ratio of the average area of the error circles ($\approx 0.72 \text{ arcsec}^2$) to the WFC3 FOV. We found that the average error circle contains ≈ 1.25 normal cluster stars, though this varies somewhat by location in the cluster (see Fig. 2.7). Among evolved members, an average error circle contains ≈ 0.04 red giants and ≈ 0.03 subgiants, so there is a substantial chance of finding a giant and/or subgiant star within an error circle. However, the probability of finding a blue star in an error circle

is quite small ($\approx 3.01 \times 10^{-3}$), as is the probability of a red straggler star ($\approx 2.47 \times 10^{-4}$) or a blue straggler star ($\approx 4.63 \times 10^{-3}$). Thus, the probability of finding a blue star in any of the 16 error circles by chance is only 5%, and that of finding a red straggler is only 0.4%. The probability of finding a blue straggler by chance coincidence is comparable to that of finding a blue star ($\approx 7\%$).

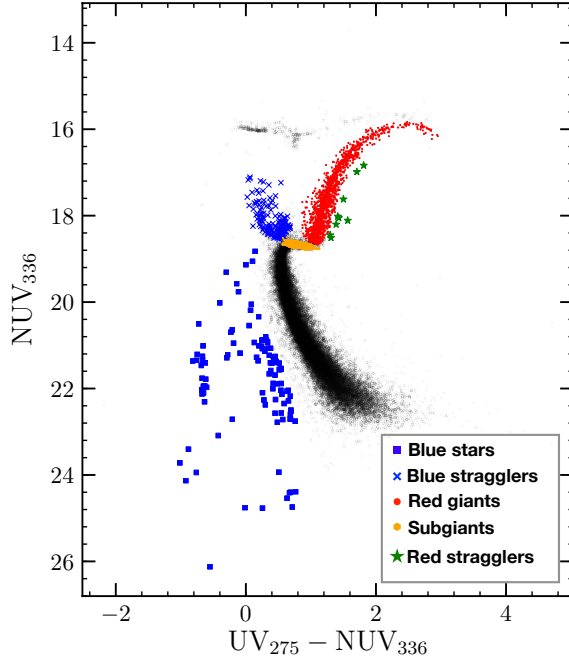


Figure 2.6: Proper motion cleaned $UV_{275} - NUV_{336}$ CMD overplotted with different subpopulations.

2.3.8 Optical Variability

Signs of optical/UV variability can be helpful to further confirm the nature of the source, especially for CV identifications, since most CVs appear as blue variable stars (see e.g. Cool et al. 1998; Edmonds et al. 2003b; Dieball et al. 2017; Rivera Sandoval et al. 2018).

For the new counterparts that were detected in multiple exposures, we constructed *HST* light curves in the 2012 WFC3/UVIS and the 2006 ACS/WFC

bands by doing DAOPHOT photometry (aperture photometry if the surrounding field of the counterpart is relatively uncrowded, e.g. CX16. Otherwise, PSF-fitting photometry was applied, e.g. CX9) on individual CR-removed, distortion-corrected FLC frames. The resulting light curves are shown in Fig. 2.8. We then used least-square fitting to fit each light curve to a constant and used the resulting reduced χ^2 (on Fig. 2.8) as a measure of variability. The resulting χ^2 are summarised in Tab. 2.3.

CX	Filters				
	2012			2006	
	UV ₂₇₅	NUV ₃₃₆	B ₄₃₅	V ₆₀₆	I ₈₁₄
1	183.1	578.9	149.8	24.4	29.6
6	27.0	14.9	8.9	6.1	1.2
9	7.7	17.2	46.0	544.3	53.3
12	0.6	0.3	-	-	-
14	296.9	93.7	313.4	-	-
16	0.6	2.0	-	-	-

Table 2.3: Summary on resulting χ^2 from fitting constants to light curves in different filters.

2.3.9 SED-Modelling of 1E1339

As mentioned above, the 2004 ACS data for 1E1339 (see Tab. 2.2) were taken over a broad range of filters, which yielded a dataset that can be used to construct and analyse the spectral energy distribution (SED). The target is well resolved and isolated in the three HRC filters, so that we can obtain photometric results with relatively high accuracy. However, the source is affected by saturation blemish from a nearby bright star on the B₄₃₅, V₅₅₅ and I₈₁₄ images. We, therefore, performed photometry with relatively small apertures (radius of 0.05'' or 1 ACS/WFC pixel) for these three filters. To calculate fluxes, we first calculated count rates from instrumental magnitudes. These count rates were then calibrated to infinite apertures by dividing the corresponding encircled energy (EE) fractions from Sirianni et al. (2005). Finally, count rates

were converted to specific fluxes (F_λ) by multiplying the corresponding inverse sensitivities (PHOTFLAM⁹), i.e.

$$F_\lambda = \frac{\text{Count rate in a small aperture}}{\text{EE}} \times \text{PHOTFLAM}. \quad (2.1)$$

The specific fluxes in different filters are summarised in Tab. 2.4. The calibrated B_{435} and V_{555} magnitudes are also summarised in Tab. 2.6.

Table 2.4: Calibrated specific fluxes (F_λ) of CX1 in different filters from the 2004 ACS observation.

Filters	ACS/HRC			ACS/WFC		
	F220W	F250W	F330W	F435W	F555W	F814W
Flux ($\times 10^{-16}$ erg s ⁻¹ cm ⁻² Å ⁻¹)	6.62(43)	7.92(53)	7.36(50)	4.07(30)	2.83(14)	2.02(10)

We used tabulated stellar SED models from the Pickles library, an atlas of 131 stellar spectral models, (Pickles, 1998) to model the SED. Spectra were convolved with the filter bandpasses and corrected for the expected extinction using PySynphot package¹⁰. The model spectra were then renormalised with a χ^2 minimization process (see Appendix). We first tried χ^2 fits with one-component models. The minimum of χ^2 was obtained with a type B5I spectrum, but still a bad fit ($\chi^2 \approx 153.89$). This was mainly caused by an obvious excess in the data (vs. the models) in the I_{814} band ($\log(F_{\lambda,\text{data}}) - \log(F_{\lambda,\text{model}}) \approx 0.37$, corresponding to a difference in magnitude of ≈ 0.92), requiring a second cooler component to compensate for the excess. We, therefore, tried with two-component composite models. This is done by looping over all possible combinations of two components drawn from the Pickles library and picking out the combination with the smallest χ^2 . The best fit was obtained with a B2 + M0 model, which is a greatly improved fit ($\chi^2 \approx 3.42$). The M0 component now accounts for the V and I excesses relative to the B2 component. To constrain the spectral types of each component, we stepped one component at a time through differ-

⁹<http://www.stsci.edu/hst/acs/analysis/>

¹⁰<http://pysynphot.readthedocs.io/en/latest/>

ent spectral types, allowing the other fit parameters to vary. We found a 90% confidence interval of K3-M2 or $T_{\text{eff}} = 3.75_{-0.15}^{+1.05} \times 10^3$ K for the redder component. For the bluer component, we found O8-B5 or $T_{\text{eff}} = 2.10_{-0.58}^{+1.96} \times 10^4$ K. The data overplotted with the best fit models are shown in Fig. 2.9.

Care should be taken, however, that the above spectral types do not necessarily reflect the actual traits of the accretor or the donor. Typically in CVs, the O or B type spectral components are ascribed to the combined light from the accretion disc and/or the WD surface, while the M type component might be caused by binary interactions. We will further discuss this in Sec. 2.4.1

2.3.10 X-ray spectral analysis

We performed detailed X-ray spectral analysis for sources with >100 counts that have not previously been published; only one source in our *Chandra* catalogue fits this description, CX2. For other sources with >10 counts, we perform simplified spectral analyses. We used the CIAO *specextract*¹¹ script to extract spectra of these sources from each of the 3 observations. Because these observations do not span a very long time, to get better statistics, we combined the 3 spectra and their responses using FTOOLS/ADDSPEC¹² before doing the analysis. The combined spectra were then re-binned using the CIAO *dmgroup*¹³ tool to at least 1 count per bin. Spectral analysis was then performed on the combined spectra with HEASoft/Xspec version 12.9.1 using C-statistics (Cash, 1979). Because the accuracy of the *Chandra* response matrix file falls off at low energies, we ignored energy channels below 0.5 keV during the fits. (These channels are included in the plots just to demonstrate the obvious excess at low energies.) We fixed the absorption hydrogen column density at the cluster value $\sim 8.7 \times 10^{19} \text{ cm}^{-2}$, which is derived by applying the conversion factor

¹¹<http://cxc.cfa.harvard.edu/ciao/threads/pointlike/>

¹²<https://heasarc.gsfc.nasa.gov/ftools/caldb/help/addspec.txt>

¹³<http://cxc.harvard.edu/ciao/ahelp/dmgroup.html>

($\sim 2.81 \pm 0.13 \times 10^{21}$) from Bahramian et al. (2015) and using $E(B - V) = 0.01$ from Harris (1996, 2010 edition).

We tried fits to CX2 with multiple models including an empirical power law (POWERLAW), a blackbody (BBODYRAD), a neutron star atmosphere (NSATMOS), and a hot plasma model (VMEKAL). For sources with more than 10 counts but fainter than CX2, we fit an individual power law to each source. We combined the spectra of sources with less than 10 counts (CX7-CX16) and fit a power law to the combined spectrum to get an average photon index. We obtained an average index of $\Gamma \approx 1.3$, which was then applied to the spectra of CX7-CX16 to calculate fluxes (fluxes of sources fainter than CX9 were calculated with *srcflux*, so no C-statistic or goodness calculation is available). All fitting results are summarised in Tab. 2.7.

2.4 Individual Sources & Discussions

2.4.1 CX1/1E1339

The optical counterpart of 1E1339 was first identified by Edmonds et al. (2004), using WFPC2 data, to be a star with a very blue $U - V$ colour (but lying on the subgiant branch in a $V - I$ CMD), showing marked variability on timescales of hours. Our photometry confirms its blue $U - V$ excess. Though 1E1339 lies on the blue straggler region in $UV-NUV$ and $B - V$ CMDs, it does not lie in the blue straggler region in other CMDs (see Figures 2.2, 2.3). This illustrates that multiple emission components are required, as expected in cataclysmic variables; examples of real blue straggler counterparts, and another CV that only appears to lie on the blue straggler sequence in some CMDs, can be found in Edmonds et al. (2003a). The ACS photometry from the *ACS Globular Cluster Treasury Program* revealed a red excess in $V - I$ colour ($E(V - I) \approx 0.09$ with respect to the red giant branch), suggesting a red straggler (RS) secondary (Mathieu et al., 2003; Geller et al., 2017b). Unusually red secondaries in XRBs

have been observed in some CVs in 47 Tuc (Edmonds et al., 2003a), M30 (Lugger et al., 2007), and NGC 6752 (Thomson et al., 2012). Such bloating may be due to irradiation, or more likely due to continued mass loss from the donor, as expected under standard CV evolutionary theory (Knigge et al., 2011). Using the correspondences between T_{eff} and $V - I$ colours from Cox (2000), we found that the envelope of 1E1339’s companion should have expanded by roughly 3% in order to have the observed red excess. Leiner et al. (2017) and Ivanova et al. (2017) show evolutionary models for binary mass-transferring systems that indeed demonstrate optical colours like these. This star also varies by ≈ 0.2 mags in the UV and B filters on timescales of hours. Fitting its lightcurves to a constant gives a poor reduced χ^2 (e.g. reduced $\chi^2 \approx 183$ for the UV_{275} filter, see Fig. 2.8).

Our SED fitting result corroborates this observed red excess (≈ 0.92 mags as mentioned in Sec. 2.3.9), since a second, cooler component is required to get a satisfactory fit. The red excess might be partly due to variability, either long term or short term, of CX1. However, the presence of this red excess in two independent *HST* epochs (2004 and 2006 $V - I$ CMDs) indicates its extreme colour is likely real. The 0.92-mag difference between the observed and expected I magnitudes is larger than can reasonably be explained by the observed short-term variability, of typically 0.2 magnitudes (Edmonds et al., 2004).

The cooler spectral component suggests an M0-type subgiant, while the bluer component has a spectral type for a B2-type giant, which is likely to represent the combined light from the WD and the accretion disc. We note that the extreme UV brightness indicates a high rate of mass transfer through the accretion disc. Should the accretor be a neutron star or black hole, a very high X-ray luminosity ($> 10^{36}$ erg s $^{-1}$) would be expected; the lack of such bright X-rays indicates that the accretor is almost certainly a white dwarf.

2.4.2 CX2: a quiescent low-mass X-ray binary (qLMXB)?

To model CX2's X-ray spectrum, we first tried a simple absorbed power-law model (TBabs*POWERLAW) and found a rather soft photon index ($\Gamma = 3.6_{-0.3}^{+0.4}$). The soft nature of this source was further confirmed by the low kT (≈ 0.2 keV) from a blackbody fit (TBabs*BBODYRAD). We then tried fits with more physically motivated models. A thermal plasma fit (TBabs*VMEKAL) yielded a slightly worse fit (Goodness = 92.9%) with a $kT \sim 0.4$ keV. A neutron star atmosphere model (TBabs*NSATMOS, Heinke et al. 2006) consistently yielded a low $kT_{\text{eff}} \approx 0.10$ keV (typical for a quiescent low-mass X-ray binary (qLMXB)) with an NS radius $R_{\text{NS}} \approx 8.6$ km (Goodness = 9.6%), or $kT_{\text{eff}} \approx 0.09$ when R_{NS} was frozen to 10 km (Goodness = 13.2%). The models and best fit parameters are summarised in Tab. 2.7. Fig. 2.10 shows the spectrum overplotted with the best fit models (see Tab. 2.7). Below 0.5 keV, the data are poor fits, but we attribute this to the difficulty of calibrating this portion of the X-ray spectrum.

We identify a potential optical counterpart to this source, a star that lies on the red side of the main sequence in the $B_{435} - V_{555}$ CMD (Fig. 2.3). This star shows a relatively large photometric error in the B_{435} band (see Tab. 2.6), which makes its CMD position uncertain. However, as this counterpart is not clearly off the main sequence, Sec. 2.3.6 suggests that this star may well be a chance coincidence.

We consider several possible natures for CX2; quiescent LMXB, MSP, CV, or AB in the cluster, or a background or foreground source. The NS atmosphere fit is consistent with a qLMXB nature, with a radius consistent with emission from a full NS surface. However, it is inconsistent with the expectation of emission from NS polar caps as seen in typical MSPs (Zavlin et al., 2002; Bogdanov et al., 2006). Although the VMEKAL fit is statistically reasonable, the implied temperature is low. If CX2 is a member of M3, its X-ray luminosity of 2×10^{32} erg/s is at the very high end of X-ray luminosities for globular

cluster CVs, and all known CVs in globular clusters with $L_X > 10^{31}$ erg/s have much harder X-ray spectra (e.g. Heinke et al., 2005b; Pooley & Hut, 2006), so a CV nature can be ruled out empirically. Verbunt et al. (2008) showed that nearby chromospherically active stars are limited in their X-ray luminosity, with $\log L_X < 32.3 - 0.27M_V$, while active binaries in globular clusters are limited by $\log L_X < 34.0 - 0.4M_V$ (Bassa et al., 2004). CX2’s suggested counterpart has $M_V = 8.6$ (Tab. 2.6) and $L_X = 2 \times 10^{32}$ erg/s (Tab. 2.7), so CX2 lies well above both limits (see Fig. 2.11), strongly suggesting that it is not an AB. If CX2 were instead a foreground AB, the optical counterpart to CX2 should be brighter than $M_V = -0.3$; however, no bright cluster non-members were found within the error circle of CX2, arguing against a foreground system. A bright cluster MS star ($P_\mu = 98.1\%$) is located NW of the error circle (Fig.2.7), but is still too faint (by 0.6 mags, $V \approx 19.7 \pm 0.03$; see Fig. 2.11). Furthermore, X-ray bright cluster ABs generally have harder X-ray spectra than fainter ones (e.g. Heinke et al. 2005b), which contradicts the soft nature of the source. We therefore conclude that CX2 is most likely to be a qLMXB.

Considering the relatively low central density and large mass of M3, it is interesting to consider whether this quiescent LMXB is more likely to be generated from a primordial binary (that is, via a similar evolutionary path as similar objects outside clusters), or via dynamical encounters (as the majority of quiescent LMXBs and millisecond pulsars in GCs are thought to be produced). To calculate the probability of this quiescent LMXB being a primordial binary, we use estimates of the total number of quiescent neutron star LMXBs in the Milky Way, which center around 10^3 to 10^4 systems (Heinke et al., 2020; Pfahl et al., 2003; Kiel & Hurley, 2006; Jonker et al., 2011; Britt et al., 2014). We use the Milky Way’s stellar mass of $5 \times 10^{10} M_\odot$ (Cox, 2000), and an estimate of M3’s stellar mass of $6 \times 10^5 M_\odot$ (adjusting the calculations of Gnedin et al. 2002¹⁴ to use the average mass-to-light ratio of 1.86 from Watkins et al. 2015),

¹⁴<http://www-personal.umich.edu/~ognedin/gc/vesc.dat>

to predict 0.01 to 0.1 quiescent LMXBs in M3. Some population syntheses (e.g. Pfahl et al., 2003) do generate up to 10^5 LMXBs in the current Milky Way, which would predict of order 1 quiescent LMXB in M3. However, such a large number of quiescent LMXBs, in a Galaxy with of order 100 persistently bright LMXBs, is strongly empirically disfavored by the observed ratio of ~ 10 -20 quiescent LMXBs per persistently bright LMXB in globular clusters (Heinke et al., 2003b, 2005a), and by the other empirical estimates cited above. From the dynamical side, 5 quiescent LMXBs are observed in 47 Tuc (Heinke et al., 2005a), and M3 has a stellar interaction rate 19% that of 47 Tuc (Bahramian et al., 2013), so 0.97 dynamically-formed quiescent LMXBs are predicted in M3. Thus, we find it 10-100 times more likely that this quiescent LMXB was formed dynamically, rather than primordially.

As a point of interest, performing the same calculation for the quiescent LMXB in ω Centauri (Rutledge et al., 2002) indicates a prediction of 0.04-0.4 primordial systems, vs. 0.45 dynamically formed systems, suggesting that the ω Centauri quiescent LMXB has a decent chance to be a primordial system.

2.4.3 CX6

A power-law fit to CX6's X-ray spectrum produces a negative photon index ($\Gamma = -0.7_{-0.7}^{+0.8}$) if we freeze the N_{H} at the cluster value. However, Γ becomes more physically reasonable when N_{H} is allowed to float to a higher value. For example, at $N_{\text{H}} = 6.0 \times 10^{22} \text{ cm}^{-2}$, $\Gamma = 1.2_{-1.3}^{+1.1}$.

The optical counterpart to this source is very blue in UV colours ($E(UV - NUV) \approx -0.85$), but the $V - I$ colour indicates a very large red excess in visible light, $E(V - I) \approx 0.37$, compared to the main sequence. This red excess was confirmed in the 2004 ACS/WFC $V_{555} - I_{814}$ CMD (see Fig. 2.12) with $E(V - I) \approx 0.43$ with respect to the MS; however, using the B_{435} and V_{555} magnitudes from the same epoch, the star shows moderate blue excess relative to the MS (see Fig. 2.3). Assuming the same V magnitude as CX6, the $V - I$

colour on the main sequence ($V - I \approx 0.65$) corresponds to an F9V-G0V dwarf with $T_{\text{eff}} \approx 5900$ K, whereas CX6 corresponds to a K3V-K3.5V dwarf with $T_{\text{eff}} \approx 4800$ K (spectral types and T_{eff} 's are from Pecaut & Mamajek 2013). Again, if we apply the ‘‘bloated envelope’’ scenario as for CX1, the change in T_{eff} requires that the companion to be bloated by a factor of ~ 1.5 , which does not seem physically reasonable. Although high measured N_{H} 's are common among AGNs, both CX6's PM and the associated P_{μ} strongly support its cluster membership. In Sec. 2.3.6, we estimated the number of chance coincidences of blue stars to be minuscule ($\approx 2.14 \times 10^{-3}$), so the suggested counterpart is very unlikely to be spurious. Therefore, the high N_{H} might imply a CV seen edge-on, such as the CVs W8, W15, and AKO9 in 47 Tuc (Heinke et al., 2005b), but the red excess remains unexplained. Optical/UV variability analyses indicate strong UV and B variabilities to this star, suggestive of a CV nature, which might also be the cause of the observed simultaneous blue and red excess. Future spectroscopic study (e.g. with integral field units, such as MUSE) of this object could determine its nature.

2.4.4 CX8, CX12 and CX16

Similar to CX1 and CX6, the counterparts to these sources also show obvious UV excesses. Considering the calculations of Sec. 2.3.7, none of these counterparts are likely to be chance coincidences, so they should be CVs or background AGNs. The 2012 WFC3 observations only detected these three counterparts in the two UV bands (UV_{275} and NUV_{336}). However, the 2004 ACS observations detected the counterpart to CX16, which shows a blue excess in the $B_{435} - V_{555}$ CMD with a relatively larger error bar (see Fig. 2.3). Although CX8 is apparently detected in the ACS GC survey catalogue (and therefore has a measured PM), this detection appears as a faint extension to a nearby bright star, which results in a larger photometric error and makes the blue excess more uncertain. Identifications of the faint optical counterparts to

CX12 and CX16 are even more difficult, due to the lack of both accurate $V - I$ colours, and proper motions.

Another potential issue with these faint sources is that they have poorer localizations than bright sources. The potential counterpart to CX16 is a faint UV source northeast of its error circle with a distance of $\approx 0.98''$ (or $\approx 1.84P_{\text{err}}$) from the nominal *Chandra* position, which suggests that it may be a chance coincidence. However, the *HST* lightcurve for CX16 reveals NUV_{336} variability on hours timescales (reduced $\chi^2 \approx 1.96$), suggesting a faint CV nature, since AGN tend to show less short-term variability. New HST imaging could reveal their PMs, testing an AGN hypothesis.

2.4.5 CX7 and CX13

Our suggested counterparts to CX7 and CX13 show moderately blue colors in $B_{435} - V_{555}$ (2004) and/or $V_{606} - I_{814}$ (2006) CMDs (see Fig. 2.3 and Tab. 2.6). The counterpart to CX13 (within the 95% error circle) was too faint to be detected in the 2012 WFC3 observations, so no proper motion is available for it. The counterpart to CX7 is outside the 95% error circle ($\approx 0.9''$, or $\approx 1.7P_{\text{err}}$, from the nominal *Chandra* position). Because it was only covered by the 2004 ACS/WFC observations, only limited information can be drawn from the photometry. Considering the lack of PM measurements for these sources, we conclude that they could either be CVs or AGNs.

2.4.6 CX9 and CX14

We found evolved stars that coincide with the error circles of CX9 and CX14. A red straggler (lying to the red of the giant branch; see Geller et al. 2017b for the definitions of red stragglers and sub-subgiants) and a subgiant are located in CX9's error circle, while a red giant is in CX14's error circle. The red straggler to CX9 was also detected in the Ksync photometry (2004 ACS/WFC

observations; see Fig. 2.3) to have an obvious red excess. CX9 and CX14 may be RS Canum Venaticorum (RS CVn) variables, which are systems with an evolved primary (e.g. F/K type subgiant or K type giant) in a close binary, where the primary has active chromospheric regions that induce large stellar spots. The observed X-ray emissions in RS CVn stars are thought to originate from active coronal regions on the primary and/or the secondary star.

However, it is also possible that the evolved stars in these error circles are simply chance coincidences, or that the evolved stars have unseen compact companions. Considering the very low number of expected chance coincidences ($\approx 2.58 \times 10^{-4}$) for a red straggler to reside within the *Chandra* error circle, vs. a subgiant (with the number of chance coincidence $\approx 2.77 \times 10^{-2}$), we regard the red straggler as a highly likely optical counterpart of CX9. Red stragglers are rare, may be the product of mass transfer in a binary system, and have often been identified as X-ray sources (Belloni et al., 1998; Mathieu et al., 2003; Leiner et al., 2017). CX9 is a very interesting target for future observations, and fortunately, it is not affected by serious crowding in the core, which makes it resolvable with instruments that have even larger PSFs.

2.4.7 Estimate of XRBs and AGNs

The number of AGN expected within the half-light radius can be estimated using the empirical model with three power-law components from Mateos et al. (2008). Applying a soft (0.5–2.0 keV) flux limit of $S = 5.22 \times 10^{-16} \text{ erg s}^{-1} \text{ cm}^{-2}$, the model predicts that $N_{\text{AGN}}(> S) \approx 2_{-1}^{+3}$ (90% confidence limits are from Gehrels 1986) within the half-light radius. Thus, we expect that 14_{-3}^{+1} of our detected sources are likely members of M3, with CX12, and CX16 being plausible AGN (with no PM or P_{μ} available). CX8 does have a PM suggestive of a cluster member; however, further P_{μ} information is required for more secure identification. There are probably other AGNs among our X-ray sources without optical counterparts, which lie below our optical/UV detection limits.

Three confirmed MSPs (and one candidate) are known in M3, two with timing solutions and thus known positions (Hessels et al., 2007). The two known MSP positions do not correspond to any detected X-ray sources in our data. This is not surprising, since most MSPs observed in globular clusters have $L_X(0.3-8 \text{ keV})$ between 10^{30} – $10^{31} \text{ ergs s}^{-1}$ (e.g. only 1 of 23 MSPs with known positions in 47 Tuc has $L_X > 10^{31} \text{ erg s}^{-1}$; Bogdanov et al. 2006; Ridolfi et al. 2016; Bhattacharya et al. 2017). Due to the larger distance to M3 (10.2 kpc; Harris 1996, 2010 version) and the relatively short exposures here, we do not have X-ray detection below $L_X \sim 1.3 \times 10^{31} \text{ erg s}^{-1}$. However, it is still possible that one of our X-ray sources might be an MSP with an unusually high X-ray luminosity

We compared the number of X-ray sources we found in M3 with those from other GCs, and with the expected numbers of dynamically formed X-ray binaries. We used stellar encounter rates (Γ) from Bahramian et al. (2013), and numbers of non-AGN X-ray sources (N_X) in multiple GCs from Pooley et al. (2003) and Lugger et al. (2007). Since our luminosity limit ($L_{0.5-6.0} \approx 1.1 \times 10^{31} \text{ erg s}^{-1}$) is higher than Pooley’s ($L_{0.5-6} = 4.0 \times 10^{30} \text{ erg s}^{-1}$), the N_X in M3 (14_{-3}^{+1}) reported here should be regarded as a lower limit. We compare our results of M3 with other GCs in Fig. 2.13 (where we have renormalised all Γ s so that Γ for NGC 6266 is 100), together with a linear regression fit ($N_X \propto \Gamma^{0.58 \pm 0.10}$) from Lugger et al. (2007). Deeper *Chandra* and *HST* observations would be helpful to verify the X-ray source content, and source classification, of M3. M3 will be a particularly helpful cluster, along with M13, M5, and ω Cen, in studying how lower-density clusters produce X-ray sources, as these clusters are likely to contain both primordial and dynamically-formed X-ray binaries.

2.5 Conclusions

Using ~ 30 ks of *Chandra* observations, we detected 16 X-ray point sources within the half-light radius of the globular cluster M3. The X-ray sources include the transient supersoft source and CV 1E1339, and a likely quiescent LMXB with a neutron star companion. Our optical/UV identification campaign has identified plausible optical and/or UV counterparts to 10 of 16 sources, including the previously identified 1E1339, a red straggler, a likely CV with unusually red optical colours, a faint red MS star to the qLMXB candidate, a possible giant (perhaps an RS CVn chromospherically active star), and five objects with UV and/or blue excesses, which may be CVs or AGNs.

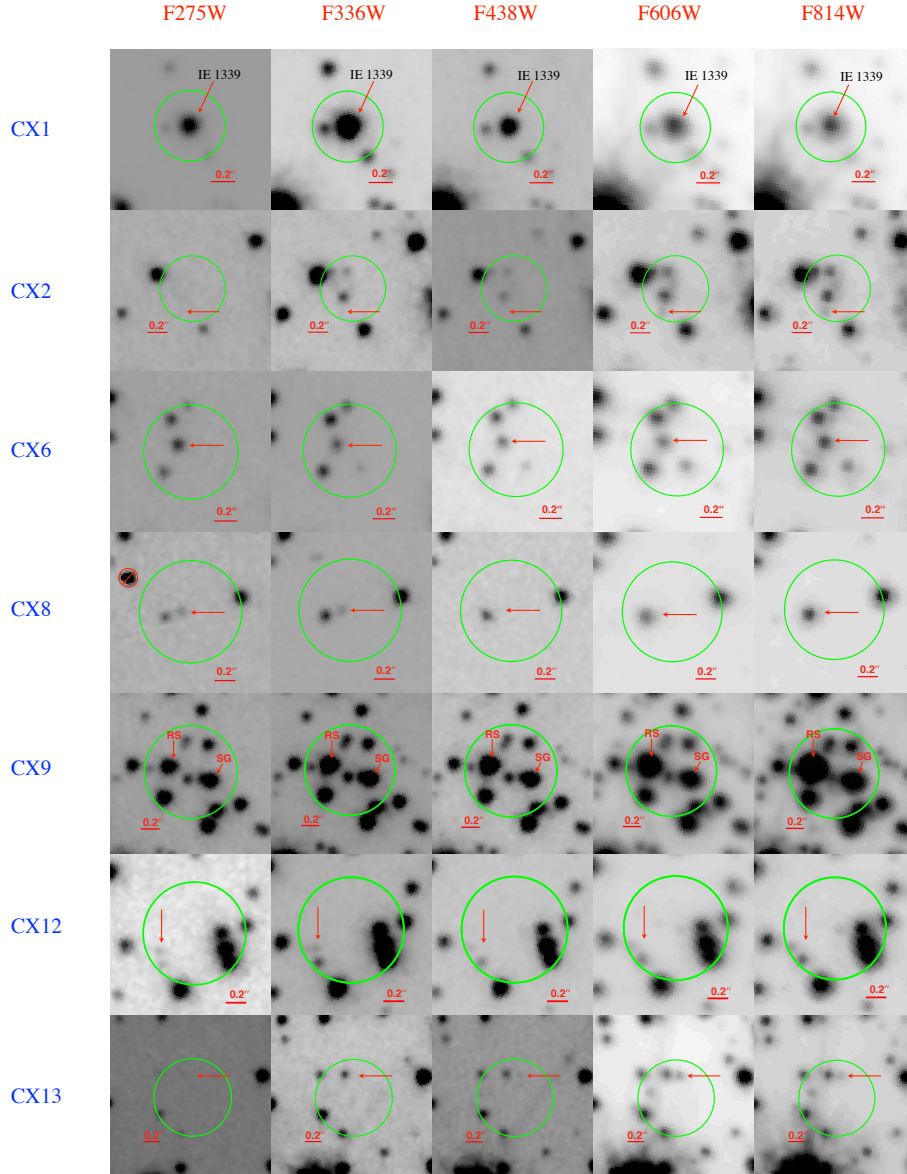


Figure 2.7: Finding charts for 7 identified optical counterparts in 5 different bands (UV bands are from the 2012 WFC3/UVIS observations; V_{606} and I_{814} bands are from the 2006 ACS/WFC observations) made from drizzle-combined images. North is up and east is to the left. The green solid circles represent the 95% *Chandra* error circles as calculated in Hong et al. (2005). Identified counterparts are annotated with red arrows. Note that the counterparts to CX12 was only found in the two UV filters (UV_{275} , NUV_{336}); similarly, the counterparts to CX2 and CX13 were only detected in the two ACS/WFC bands, so the red arrows on the other finding charts only point to their nominal positions. The counterpart to CX8 appears to be a faint extension in V_{606} and I_{814} . Also, notice that a cosmic ray on the UV_{275} finding chart of CX8 has been excluded to avoid confusion. The red straggler (RS) and subgiant (SG) potential counterparts to CX9 are annotated with arrows and texts.

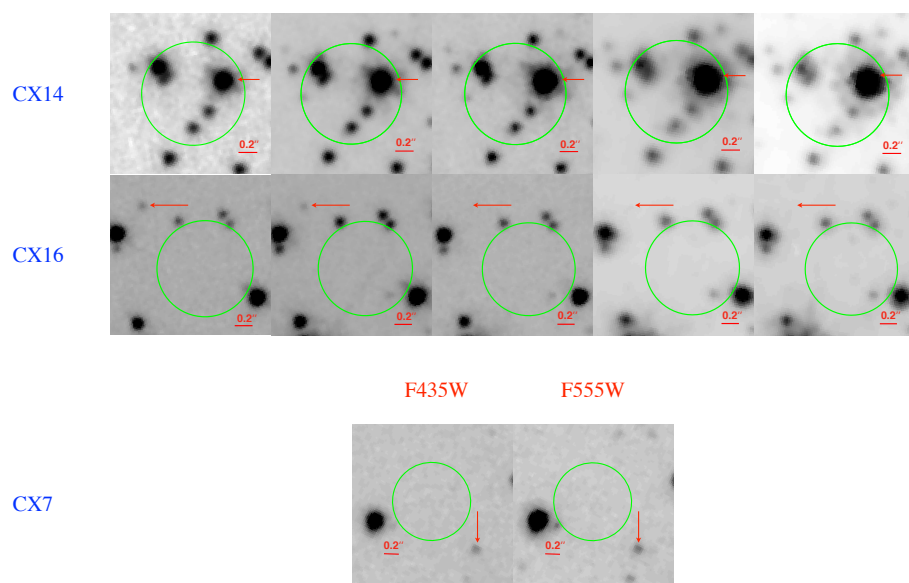


Figure 2.7: (Continued) CX7 was only covered by the 2004 ACS/WFC observations. Plausible counterparts for CX7 and CX16 lie somewhat outside the 95% *Chandra* error circle.

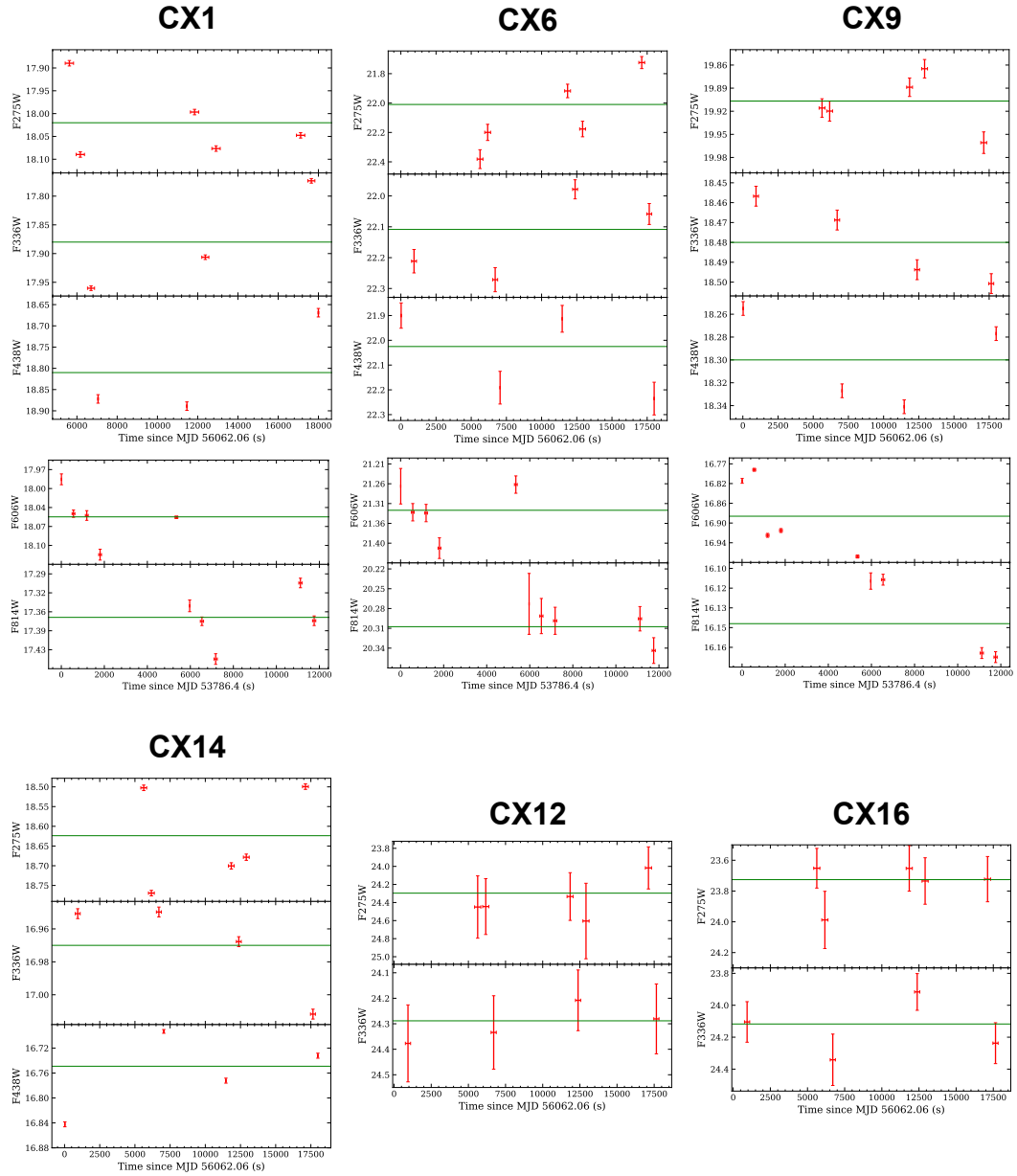


Figure 2.8: Optical/UV light curves of the identified counterparts that have detections in multiple exposures in the WFC3/UVIS observations (2012) and/or the ACS/WFC observations (2006). Photometric errors are from DAOPHOT software. The best fit constants are indicated with a solid green line.

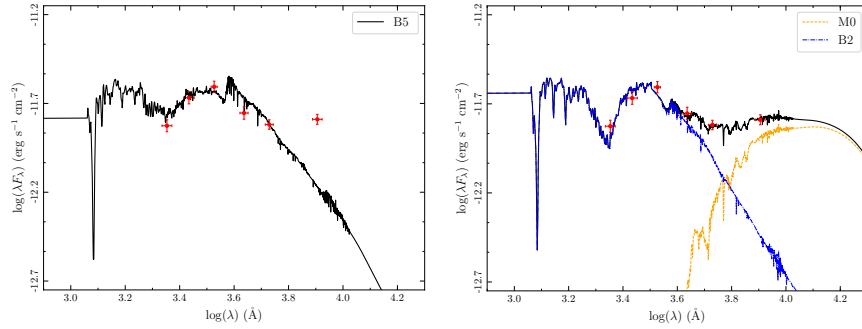


Figure 2.9: Best fit SED models and data from the 2004 observations. *Left panel* shows the best fit single-component model (solid black) overplotted with the data (red). *Right panel* shows the same data (red) and the best fit two-component model (solid black), composed of a renormalised B2 component (blue dashed-dotted) and an renormalised M0 component (orange dashed).

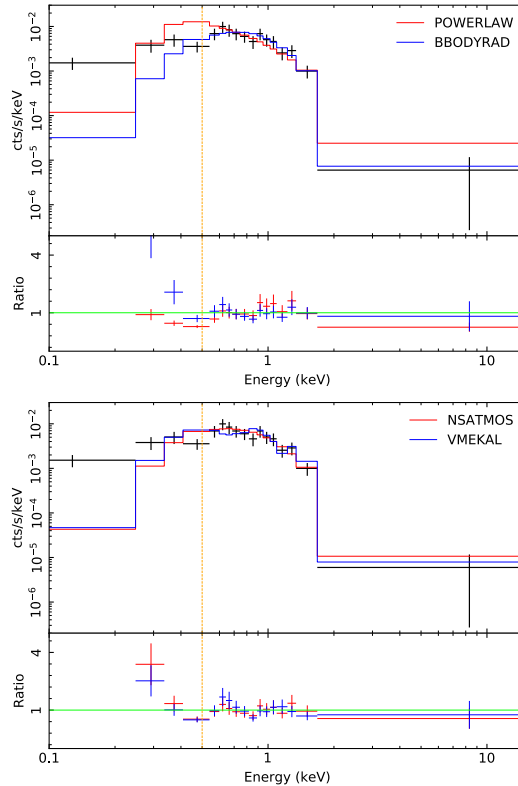


Figure 2.10: *Chandra* spectra of CX2. The top panel shows the rebinned (only for plotting purpose) data (black) with the best fit POWERLAW model and BBODYRAD model overplotted with a solid red line and a solid blue line, respectively. The bottom panel shows the same data, but overplotted with the best fit VMEKAL model (blue) and NSATMOS model (red). The yellow dashed line indicates the energy limit at 0.5 keV, below which channels were ignored during the fits. Ratio = data/model.

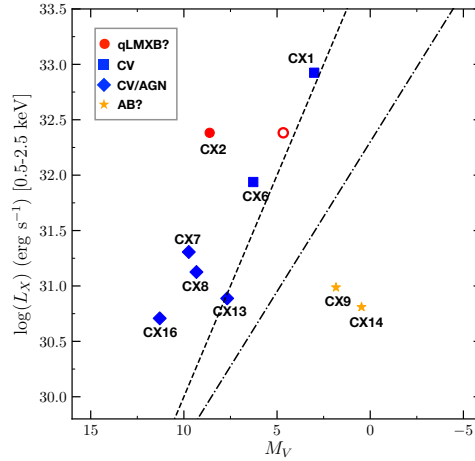


Figure 2.11: $0.5 - 2.5$ keV L_X vs. absolute V band magnitudes (using V_{555} for CX7 and CX16, and V_{606} for others). L_X of CX1 is from Stacey et al. (2011). The dashed line corresponds to the $L_X = 34.0 - 0.4M_V$ separatrix from Bassa et al. (2004), dividing cluster CVs and ABs. The dotted-dashed line corresponds to the $L_X = 32.3 - 0.27M_V$ separatrix from Verbunt et al. (2008), marking the upper limit of L_X for nearby ABs. CV candidates with confirmed cluster memberships are marked with filled blue squares. Possible CV/AGN candidates are marked with filled blue diamonds. The red filled circle marks the location of CX2 if we were to adopt the suggested counterpart. For comparison, the red open circle indicates the location of CX2 on the plot if we adopt the bright MS star mentioned in Sec. 2.4.2 as the counterpart.

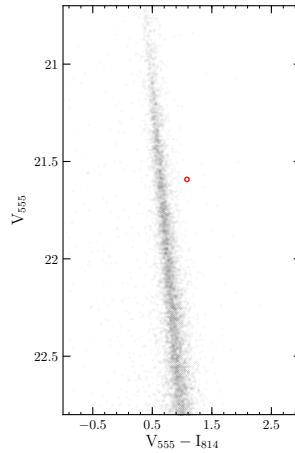


Figure 2.12: $V_{555} - I_{814}$ CMD from the 2004 ACS/WFC observations. The red circle marks the location of the CX6 counterpart.

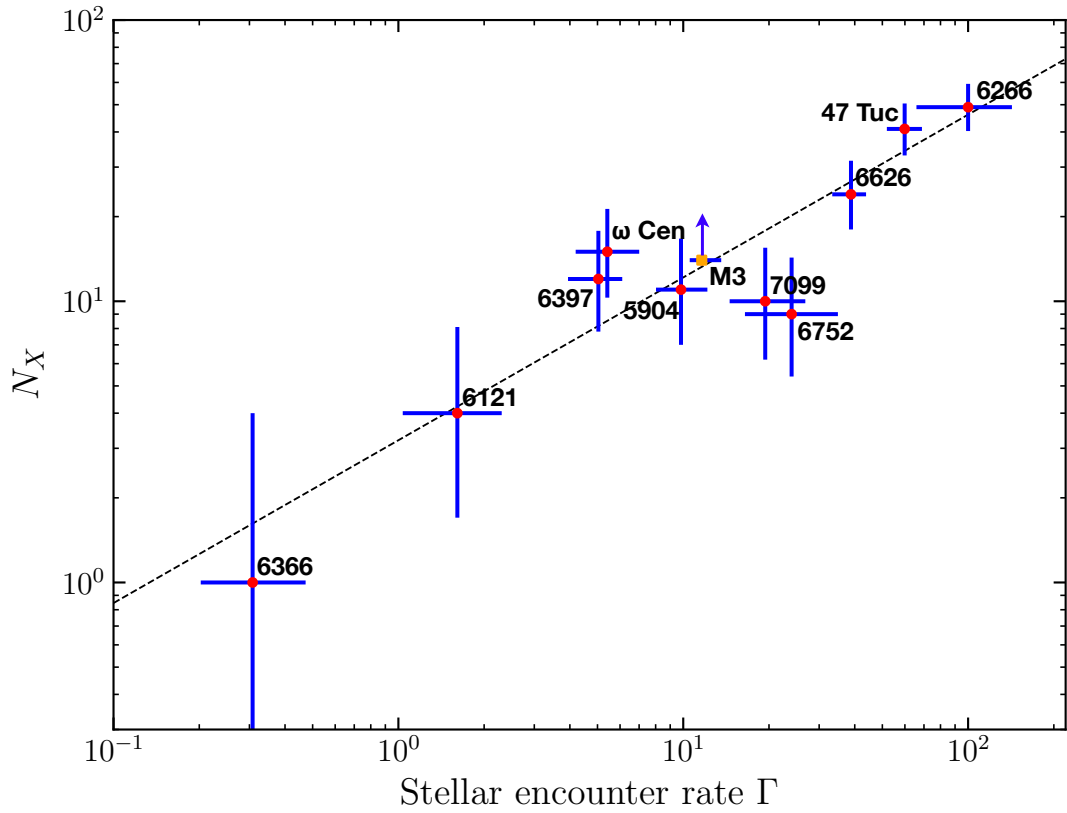


Figure 2.13: Number of non-AGN X-ray sources (N_X) in multiple GCs v.s. renormalised stellar encounter rates (Γ) from Bahramian et al. (2013). Γ s have been renormalised such that NGC 6266 has a Γ of 100. The lower limit inferred from our results of M3 is indicated with an orange square. The dashed line indicates the linear regression fit from Lugger et al. (2017).

Table 2.5: A catalogue of X-ray sources in M3.

Name	α (J2000) (h : m : s)	Positions ^a		Dist. ^b (")	P_{err}^c (")	Net Counts (absorbed)				Notes
		δ (J2000) (° : ' : ")				0.5 – 7.0 keV	0.5 – 2.0 keV counts (err) ^d	2.0 – 7.0 keV		
CX1	13:42:09.771	+28:22:47.618		25.8	0.295	1038.1 (32.3)	738.6(27.2)	299.5 (17.4)		SSS (1E1339)
CX2	13:42:15.364	+28:22:41.458		49.5	0.321	138.4 (11.8)	137.5 (11.7)	1.0 (1.0)		qLMXB
CX3	13:42:08.218	+28:23:28.528		67.5	0.362	41.8 (6.5)	23.9 (4.9)	17.8 (4.2)		-
CX4	13:42:10.105	+28:24:03.498		87.6	0.410	19.8 (4.4)	10.0 (3.2)	9.8 (3.2)		-
CX5	13:42:14.511	+28:23:31.053		64.4	0.382	18.6 (4.5)	13.8 (3.7)	4.8 (2.2)		-
CX6	13:42:13.899	+28:23:04.927		40.2	0.403	16.0 (4.0)	3.0 (1.7)	13.0 (3.6)		CV
CX7	13:42:13.411	+28:24:41.737		125.8	0.519	8.8 (3.0)	5.0 (2.2)	3.9 (2.0)		CV/AGN
CX8	13:42:14.664	+28:23:44.921		78.7	0.482	7.9 (2.5)	4.9 (2.2)	2.9 (1.7)		CV?
CX9	13:42:11.730	+28:22:34.608		3.9	0.490	7.8 (2.8)	5.0 (2.2)	3.0 (1.7)		RS/AB
CX10	13:42:15.322	+28:21:59.867		62.1	0.539	7.0 (2.8)	3.0 (1.7)	4.0 (2.0)		-
CX11	13:42:14.023	+28:21:24.128		80.6	0.620	6.0 (2.6)	5.0 (2.2)	1.0 (1.0)		-
CX12	13:42:13.901	+28:23:08.819		42.9	0.498	5.8 (2.5)	6.0 (2.4)	0.0 (0.0)		CV/AGN
CX13	13:42:13.678	+28:22:44.243		27.8	0.453	5.8 (2.4)	4.9 (2.2)	1.0 (1.0)		CV/AGN
CX14	13:42:13.903	+28:22:20.201		35.1	0.543	4.9 (2.2)	3.9 (2.0)	1.0 (1.0)		AB?
CX15	13:42:05.389	+28:23:06.513		87.0	0.784	4.0 (2.0)	2.0 (1.4)	2.0 (1.4)		-
CX16	13:42:12.668	+28:23:36.034		59.4	0.534	3.9 (2.0)	3.0 (1.7)	1.0 (1.0)		CV/AGN

^a Coordinates from *wandetect*

^b Offsets from the center of the core in arcsec

^c 95% error circles as calculated by Hong et al. (2005)

^d errors generated by CIAO *srcflux* tool

Table 2.6: Magnitudes and colours of identified optical counterparts.

CX	Magnitudes ^a										Notes
	2012			2006			2004				
	UV ₂₇₅	NUV ₃₃₆	B ₄₃₈	V ₆₀₆	I ₈₁₄	B ₄₃₅	V ₅₅₅	P _μ ^b	Comments		
1	18.02 ± 0.01	17.88 ± 0.02	18.81 ± 0.01	18.05 ± 0.03	17.37 ± 0.04	18.14 ± 0.18	18.10 ± 0.18	96.9%	Blue in UV, moderate red excess in V-I		
2	-	-	-	23.66 ± 0.03	22.50 ± 0.05	25.49 ± 0.48	24.08 ± 0.05	-	Faint MS star, small red excess		
6	22.08 ± 0.01	22.13 ± 0.02	22.06 ± 0.02	21.32 ± 0.02	20.30 ± 0.05	21.71 ± 0.22	21.42 ± 0.00	98.0%	Blue in UV, large red excess in V-I		
7 [†]	-	-	-	-	-	25.09 ± 0.33	24.78 ± 0.01	-	Faint blue star outside the error circle		
8	23.34 ± 0.03	23.14 ± 0.03	-	24.37 ± 0.16	23.63 ± 0.29	-	-	-	Faint blue star		
9	19.91 ± 0.02	18.48 ± 0.02	18.30 ± 0.01	16.88 ± 0.00	16.14 ± 0.00	18.09*	17.03 ± 0.06	88.9%	Red straggler		
9	19.78 ± 0.02	18.96 ± 0.02	19.12 ± 0.02	18.31 ± 0.01	17.77 ± 0.01	18.98 ± 0.00	18.51 ± 0.00	97.7%	Subgiant		
12	24.37 ± 0.03	24.30 ± 0.04	-	-	-	-	-	-	Faint blue star, only detected in UV		
13	-	-	-	22.72 ± 0.08	22.64 ± 0.29	23.90*	23.37 ± 0.72	-	Moderately blue star		
14	18.63 ± 0.02	16.97 ± 0.01	16.76 ± 0.01	15.51 ± 0.013	14.79 ± 0.04	-	-	96.6%	Red giant		
16 [†]	23.75 ± 0.02	24.15 ± 0.02	-	-	-	25.69 ± 0.32	26.34 ± 0.89	-	Faint blue star outside the error circle, only detected in UV		

^a Magnitudes are calibrated to VEGAMAG system

^b Probability of being a member of the cluster, from Nardiello et al. (2018)

* superscript indicates that the magnitude has a very large uncertainty and should be taken with care

† superscript indicates that the optical counterpart is outside the 95% Chandra error circle

Table 2.7: Summary of X-ray spectral analyses.

Source	Model	N_{H}^a (10^{19} cm^{-2})	Γ or R_i^b	kT (keV)	$f_{0.5-7.0, \text{unabs}}$ ($10^{-16} \text{ erg cm}^{-2} \text{ s}^{-1}$)	$L_{0.5-7.0, \text{unabs}}$ ($10^{30} \text{ erg s}^{-1}$)	Cstat/dof	Goodness
CX								
	TBabs*POWERLAW		$3.6^{+0.4}_{-0.3}$	-	$206.6^{+30.1}_{-27.4}$	$257.2^{+37.5}_{-34.2}$	53.1/59	66.8%
2	TBabs*BBODYRAD	(8.7)	$1.4^{+0.5}_{-0.3}$	$0.20^{+0.02}_{-0.02}$	$177.4^{+25.9}_{-23.6}$	$220.9^{+32.2}_{-29.4}$	49.3/59	53.8%
	TBabs*VMEKAL		-	$0.42^{+0.11}_{-0.06}$	$184.1^{+26.8}_{-24.5}$	$229.2^{+33.4}_{-30.5}$	60.4/59	92.9%
	TBabs*NSATMOS		$8.6^{+5.7}_{-3.6^*}$	$0.10^{+0.06}_{-0.02}$	$183.3^{+26.7}_{-24.4}$	$228.2^{+33.3}_{-30.3}$	46.2/59	9.6%
3			$0.8^{+0.4}_{-0.4}$		$167.5^{+45.0}_{-38.1}$	$208.6^{+56.1}_{-47.5}$	43.1/34	51.9%
4			$0.8^{+0.6}_{-0.6}$		$63.9^{+27.3}_{-21.4}$	$79.5^{+34.0}_{-26.6}$	11.08/15	3.3%
5	TBabs*POWERLAW	(8.7)	$2.1^{+0.8}_{-0.7}$	-	$43.3^{+14.6}_{-13.8}$	$53.9^{+21.9}_{-16.2}$	21.6/17	29.2%
			$-0.7^{+0.7}_{-0.8}$		$104.9^{+50.2}_{-38.1}$	$130.6^{+62.4}_{-47.5}$	18.1/13	6.7%
6		(6×10^3)	$1.2^{+1.2}_{-1.3}$		$191.2^{+93.0}_{-70.4}$	$238.1^{+115.7}_{-87.7}$	20.1/13	25.8%
7					$41.7^{+22.2}_{-16.5}$	$52.0^{+27.7}_{-20.5}$	10.7/15	66.9%
8			$0.8^{+0.6}_{-0.6}$		$27.5^{+19.5}_{-13.3}$	$34.2^{+24.3}_{-16.6}$	3.4/7	33.1%
9					$20.0^{+16.8}_{-11.0}$	$24.9^{+21.0}_{-13.7}$	1.0/6	8.5%
10					$18.9^{+17.5}_{-8.6}$	$23.5^{+21.7}_{-10.7}$	-	-
11	TBABS*POWERLAW	(8.7)	$1.3^{+0.4}_{-0.4}$	-	$17.0^{+17.3}_{-8.1}$	$21.1^{+21.5}_{-10.1}$	-	-
12					$14.8^{+16.9}_{-7.6}$	$18.4^{+21.0}_{-9.5}$	-	-
13					$15.9^{+16.8}_{-7.5}$	$19.8^{+20.9}_{-9.4}$	-	-
14					$13.3^{+6.2}_{-6.2}$	$16.5^{+20.2}_{-9.2}$	-	-
15					$11.0^{+12.1}_{-6.9}$	$13.6^{+15.0}_{-8.6}$	-	-
16					$10.5^{+13.5}_{-6.2}$	$13.0^{+16.7}_{-7.7}$	-	-

^a Values in the parentheses indicates that the parameter is fixed during the fit

^b R_i is the radius of the emission region for BBODYRAD model, or the neutron star radius for the NSATMOS model, both in km

* indicates that the error extends beyond the hard limit

Chapter 3

The MAVERIC survey: A hidden pulsar and a black hole candidate in ATCA radio imaging of the globular cluster NGC 6397

Yue Zhao¹, Craig O. Heinke¹, Vlad Tudor², Arash Bahramian², James C. A. Miller-Jones², Gregory R. Sivakoff¹, Jay Strader³, Laura Chomiuk³, Laura Shishkovsky³, Thomas J. Maccarone⁴, Manuel Pichardo Marcano⁴, Joseph D. Gelfand^{5,6}

¹ Department of Physics, CCIS 4-183, University of Alberta, Edmonton, AB, T6G 2E1, Canada. ² International Centre for Radio Astronomy Research-Curtin University, GPO Box U1987, Perth, WA 6845, Australia. ³ Department of Physics and Astronomy, Michigan State University, East Lansing, MI 48824, USA. ⁴ Texas Tech University, Dept. of Physics, Box 41051, Lubbock, TX, 79409-1051, USA. ⁵ New York University Abu Dhabi, Abu Dhabi, United Arab

Emirates. ⁶ NYU Center for Cosmology and Particle Physics, New York, NY 10003, USA.

This chapter details the work published in Zhao et al. 2020a, “The MAVERIC survey: A hidden pulsar and a black hole candidate in ATCA radio imaging of the globular cluster NGC 6397”, *MNRAS*, 493, 6033, DOI: 10.1093/mnras/staa631, where we combine X-ray, radio, and UV/optical imaging observations and identify a strong candidate of a “hidden” pulsar.

Abstract

Using a 16.2 hr radio observation by the Australia Telescope Compact Array (ATCA) and archival *Chandra* data, we found $> 5\sigma$ radio counterparts to 4 known and 3 new X-ray sources within the half-light radius (r_h) of the Galactic globular cluster NGC 6397. The previously suggested millisecond pulsar (MSP) candidate, U18, is a steep-spectrum ($S_\nu \propto \nu^\alpha$; $\alpha = -2.0_{-0.5}^{+0.4}$) radio source with a 5.5 GHz flux density of $54.7 \pm 4.3 \mu\text{Jy}$. We argue that U18 is most likely a “hidden” MSP that is continuously hidden by plasma shocked at the collision between the winds from the pulsar and companion star. The nondetection of radio pulsations so far is probably the result of enhanced scattering in this shocked wind. On the other hand, we observed the 5.5 GHz flux of the known MSP PSR J1740-5340 (U12) to decrease by a factor of >2.8 during epochs of 1.4 GHz eclipse, indicating that the radio flux is absorbed in its shocked wind. If U18 is indeed a pulsar whose pulsations are scattered, we note the contrast with U12’s flux decrease in eclipse, which argues for two different eclipse mechanisms at the same radio frequency. In addition to U12 and U18, we also found radio associations for 5 other *Chandra* X-ray sources, four of which are likely background galaxies. The last, U97, which shows strong H α variability, is mysterious; it may be either a quiescent black hole low-mass X-ray binary, or something more unusual.

3.1 Introduction

X-ray observations have revealed that Galactic globular clusters (GCs) host an overabundance of X-ray sources, which are thought to originate from compact binaries formed through close encounters in the dense cluster cores (Fabian et al., 1975; Hills, 1976; Bailyn et al., 1990; Camilo & Rasio, 2005; Ivanova et al., 2006). One class of dynamically formed close binaries consists of low-mass X-ray binaries (LMXBs), where neutron stars (NSs) accrete matter from low-mass companion stars (Lewin & Joss, 1983; Grindlay et al., 1984). These LMXBs are the progenitors of millisecond pulsars (MSPs), radio pulsars with very stable (low \dot{P}) millisecond-scale spin periods ($P \sim 1 - 10$ ms) and low spindown-inferred dipole magnetic fields ($B \sim 10^{8-9}$ G) (Manchester, 2017), which are also abundant in globular clusters (e.g. Camilo & Rasio, 2005). Cataclysmic variables (CVs), white dwarfs (WDs) accreting from low-mass stars, can also be produced dynamically in dense globular clusters (Pooley et al., 2003; Heinke et al., 2003b; Pooley & Hut, 2006; Ivanova et al., 2006), but in many clusters most CVs are primordial in origin (Verbunt & Meylan, 1988; Davies, 1997; Kong et al., 2006; Bassa et al., 2008; Haggard et al., 2009; Cheng et al., 2018; Belloni et al., 2019). Chromospherically active binaries (ABs), which are close binaries involving rapidly rotating late (K-M) type (BY Draconis) or evolved stars (RS CVn), make up the majority of faint X-ray sources below 10^{31} erg s $^{-1}$, and are mostly formed primordially (Grindlay et al., 2001a; Bassa et al., 2004).

3.1.1 Radio sources in globular clusters

Thanks to the increased sensitivity of new *Karl G. Jansky Very Large Array* (VLA) and ATCA receivers, faint radio sources have been detected in a number of GCs (e.g. Strader et al., 2012; Chomiuk et al., 2013; Miller-Jones et al., 2015). There are several possibilities for these sources.

Neutron star LMXBs in the low/hard states produce flat ($-0.5 < \alpha < 0$;

$S_\nu \propto \nu^\alpha$) to inverted ($\alpha \geq 0$) radio spectra, thought to be from jets, correlated with their X-ray luminosity (Migliari & Fender, 2006; Tudor et al., 2017; Gusinskaia et al., 2020). Black hole LMXBs produce jets with similar radio spectra, but the radio luminosity is significantly higher for a given X-ray luminosity (Gallo et al., 2014, 2018; Plotkin et al., 2019a). Millisecond radio pulsars generally show steep spectral indices, with a mean of $\alpha = -1.4$ and unit standard deviation (Bates et al., 2013).

Non-magnetic¹ CVs show flat to inverted radio spectra during accretion episodes, believed to be synchrotron emission from a jet (Benz et al., 1983; Körding et al., 2008; Miller-Jones et al., 2013; Coppejans et al., 2015, 2016; Russell et al., 2016). Numerous magnetic CVs have been detected in the radio, though a number of magnetic CVs show circular polarization indicative of electron-cyclotron maser emission (Abada-Simon et al., 1993; Chanmugam, 1987; Barrett et al., 2017). This maser emission has been suggested to be produced near the companion star (Mason & Gray, 2007), or to be produced near the WD (Kurbatov et al., 2019). Radio luminosities for all CVs tend to be rather low (10s to 100s of μJy at 300 pc; e.g. Coppejans et al. 2016), except during brief flares within dwarf nova outbursts (Mooley et al., 2017). The most radio-luminous WDs known are the extreme magnetic CV AE Aquarii, which is thought to eject much of the infalling matter through a propeller (Wynn et al., 1997; Meintjes & Venter, 2005), and the WD pulsar AR Sco, where the WD does not accrete, but produces nonthermal emission from the radio through X-ray (Marsh et al., 2016).

ABs are also radio sources, though generally they are not luminous enough for detection at kpc distances except during short (hours) flares (Drake et al., 1989; Osten et al., 2000). Tidal interaction in close orbits leads to synchronised rotation with short orbital period and thus strong coronal magnetic ac-

¹CVs are divided into magnetic systems, where the WD magnetic field is strong enough ($B \sim 10^{6-8}$ G) to channel the accretion onto magnetic poles, and non-magnetic systems where an accretion disc reaches the surface.

tivity (Chugainov, 1966; Bailyn et al., 1990; Dempsey et al., 1993). The emission mechanism is generally attributed to gyrosynchrotron radiation of mildly relativistic electrons interacting with photospheric magnetic fields (Hjellming & Gibson, 1980; Feldman, 1983; Gudel, 1992; Kundu & Shevgaonkar, 1985). They are generally observed to be non-thermal, highly variable and circularly polarised with flat or negative spectral indices ($\alpha \lesssim 0$; García-Sánchez et al. 2003). An unusual system, a sub-subgiant² in a binary with either a very low-mass star, or else with a more massive compact object (possibly a BH) in an extremely face-on binary, is a radio and X-ray source in the globular cluster M10 (Shishkovsky et al., 2018).

3.1.2 Eclipsing millisecond pulsars

MSPs are often in close orbits with very low-mass (as low as $\sim 0.02 M_{\odot}$) stars. If the companion is not fully degenerate, it may produce an outflowing wind, which interacts with the pulsar wind to create an intrabinary shock. The pulsar’s radiation and/or accelerated particles may heat the companion’s surface, enhancing the companion’s wind. This enhanced companion wind, and/or the intrabinary shock, may eclipse the radio pulsations. These systems fall into two major categories, “black widow” systems with brown dwarf companions of $\lesssim 0.02 M_{\odot}$ (Fruchter et al., 1988; Stovall et al., 2014), and “redback” systems with main sequence companions of typically $\sim 0.1-0.4 M_{\odot}$ (Lyne et al., 1990; Ferraro et al., 2001; Roberts, 2013), but possibly higher companion masses up to $0.7-0.9 M_{\odot}$ (Strader et al., 2019). The radio eclipses are often seen to encompass 10-25% of the full orbit, but the eclipse lengths can vary between orbits, and at low frequencies some systems appear to be permanently eclipsed (e.g. Camilo et al., 2000; Freire, 2005). There are also MSPs such as 47 Tuc V which show irregular eclipses at all orbital phases and are sometimes not detected for

²A star fainter than subgiants but redder than the main sequence; see Leiner et al. 2017

many orbits, suggesting they are continuously eclipsed (Camilo et al., 2000; Ridolfi et al., 2016). It is speculated that many MSPs may be continuously hidden behind even stronger winds (Tavani, 1991).

The mechanism by which the wind from the companion star causes eclipses in the radio pulsations is not clear. The radio pulses typically show increased dispersion near the eclipse, and/or become substantially fainter (Stappers et al., 2001; Archibald et al., 2009). Thompson et al. (1994) discuss a range of possible mechanisms, including free-free absorption, pulse smearing, scattering due to Langmuir turbulence, stimulated Raman scattering, and cyclotron absorption. Thompson et al. (1994) and later works (Stappers et al., 2001; Polzin et al., 2019) typically favor cyclotron absorption and/or scattering mechanisms, while some works (Broderick et al., 2016; Polzin et al., 2018) strongly favor cyclotron absorption to explain eclipses, especially at low (e.g. 300 MHz) frequencies. Fruchter & Goss (1992) imaged PSR 1957+20 through eclipses at both 20 and 90 cm with the VLA, discovering that the unpulsed flux disappeared during eclipse at 90 cm but was still present at 20 cm, suggesting cyclotron absorption at low frequencies and scattering at higher frequencies (Thompson et al., 1994). The LOFAR array has been used to image pulsars during eclipses, where the disappearance of the flux at e.g. 149 MHz was seen, in agreement with cyclotron absorption scenarios (Roy et al., 2015; Broderick et al., 2016; Polzin et al., 2018).

Observations of lengthy X-ray eclipses in redbacks were initially understood as a direct eclipse by the secondary star of X-ray emission from an intrabinary shock, located close to the secondary (Bogdanov et al., 2005). However, higher S/N orbital X-ray lightcurves of eclipsing pulsars have revealed modulation of the X-rays throughout the orbit, and sharp peaks, often on either side of the inferior conjunction of the NS (e.g. Bogdanov et al., 2011; Romani & Shaw, 2011; Huang et al., 2012; Bogdanov et al., 2014; Hui et al., 2014; de Martino et al., 2015; Hui et al., 2015). This has inspired interpretation of the X-rays

as due to particle acceleration at the interface between the companion and pulsar winds, beamed in the direction of the particle flow (e.g. Harding & Gaisser, 1990; Arons & Tavani, 1993; Romani & Sanchez, 2016; Wadiasingh et al., 2017). The very hard X-ray photon index rules out shock acceleration, suggesting magnetic reconnection in a striped pulsar wind (e.g. Al Noori et al., 2018). It is unclear how the intrabinary shock manages to wrap around the pulsar; suggested scenarios are that the companion wind is highly magnetized (as the companion is likely magnetically active, van Staden & Antoniadis 2016) and thus that the companion wind balances the pulsar’s via magnetic pressure, or that the companion wind is dense enough for its gas pressure to balance the pulsar wind’s magnetic pressure (Wadiasingh et al., 2018). The latter case is inherently unstable to gravity if the intrabinary shock bends around the pulsar, which may explain rapid transitions between accretion and pulsar states (Papitto et al., 2013). We note that Li et al. (2019) place very constraining upper limits on the B field at the interface between the pulsar and companion winds in PSR B1957+20, casting doubt on the cyclotron absorption eclipse scenario and the magnetospheric pressure balance scenario.

3.1.3 NGC 6397

NGC 6397 has been intensively observed by optical, X-ray and radio instruments as a nearby GC with relatively low extinction ($D \approx 2.3$ kpc; $E(B-V) = 0.18$; Harris 1996, 2010 edition). Ferraro et al. (2001) identified an eclipsing MSP, PSR J1740-5340 (aka NGC 6397-A), the second-discovered “redback” MSP, in NGC 6397. Grindlay et al. (2001b) used 49 ks of *Chandra*/ACIS-I observation to reveal 25 X-ray sources within $2'$ of the cluster, and used *Hubble Space Telescope* imaging to identify eight CVs and four ABs. Grindlay et al. (2001b) identified PSR J1740-5340 as an X-ray source (U12), and suggested that the similar (in X-ray and optical properties) source U18 might be a hidden MSP. Bogdanov et al. (2010) performed a much deeper search for X-ray

sources in 350 ks of *Chandra* observations, finding 79 sources. Cohn et al. (2010) used new *Hubble* imaging to increase the totals for NGC 6397 to 15 CVs and 42 ABs.

In this work, we present our detections of radio counterparts to U12, U18, two previously known faint X-ray sources (U97 and U108) and three newly detected X-ray sources (W127, W129 and W135). In Sec. 3.2, we describe the observational data and relevant methodologies of data reduction; in Sec. 3.3, we present results from cross-matching X-ray with radio catalogues and discuss individual matches; in Sec. 3.5, we summarise results and draw conclusions, and in Sec. B, we present an updated X-ray catalogue and tentative identifications of the new sources.

3.2 Observations & Analyses

3.2.1 Radio Observations

NGC 6397 was observed by the Australia Telescope Compact Array (ATCA; PI: Strader) as part of the MAVERIC (Milky Way ATCA and VLA Exploration of Radio sources In Clusters) survey (Project Code: C2877; Tremou et al. 2018; Shishkovsky et al. 2018). The observation started on 2013-11-09 (exact times MJD 56605.94–56606.39, and 56606.96–56607.38) with two radio bands centered at 5.5 and 9 GHz (both with 2 GHz of bandwidth) in the extended 6A configuration, for a total observational time of 20 hr and a total on-source integration time of 16.2 hr. Calibration and image analysis was done with MIRIAD (Sault et al., 1995) and CASA (version 4.2.0; McMullin et al., 2007), rendering radio images at noise levels of 4.22 and 4.81 $\mu\text{Jy beam}^{-1}$. We used the standard source PKS 1934-638 as both bandpass and flux calibrator, and the nearby source 1740-517 as our secondary calibrator, to determine the time-varying amplitude and phase gains that were then linearly interpolated to the target field. To achieve a high sensitivity, we applied the Briggs weighting

scheme, with a robust parameter of 1, resulting in synthesized beamsizes of $1.54'' \times 2.80''$ and $1.03'' \times 1.87''$ at 5.5 GHz and 9 GHz, respectively. Since there was not sufficient flux density in the field, no self-calibration was done. The radio positional accuracy directly obtained from this procedure is overestimated, so we inflate the source position uncertainties to at least 1/10 the 5.5/9 GHz beam sizes.

We derive spectral indices (α), defined by $S_\nu \propto \nu^\alpha$, using a Bayesian approach. We assume a flat prior of α between -3.5 and 1.5 and calculate the posterior distribution for each radio source, from which we derive a median and an associated uncertainty range that covers 68% of the total area. For sources that were not detected at 9 GHz (so only upper limits to the fluxes are available), we report 3σ upperlimits on α derived from the posterior distribution; medians are also calculated for these sources but are very sensitive to the prior, especially to the assumed lower bound (-3.5), so should be interpreted with caution.

More details on the procedure of generating 5σ radio source catalogues will be presented in a separate work (Tudor et al., in prep).

3.2.2 X-ray Observations

We used the same *Chandra* dataset as in Bogdanov et al. (2010), including an ACIS-I observation from Cycle 1 (ObsID: 79; PI: Murray) and ACIS-S observations from Cycle 3 (ObsIDs: 2668, 2669; PI: Grindlay) and Cycle 8 (ObsIDs: 7460, 7461; PI: Grindlay). All level-1 files are first reprocessed to align to the most up-to-date calibrations using the `chandra_repro` script in the Chandra Interactive Analysis of Observations (CIAO; Fruscione et al. 2006)³ software (version 4.11; CALDB 4.8.2). The resulting level-2 event files were used for further analyses. We then chose the longest observation (Obs. ID

³<https://cxc.harvard.edu/ciao/>

7460) as the reference frame, to which we calculated relative offsets for all other observations based on the centroid positions of U17, the brightest source in the catalogue. These offsets were then used as input to the `wcs_update` tool to update aspect solutions for each observation. Finally, all offsetted event files were combined using the `merge_obs` tool, rendering a combined event file. We then rebinned the combined event file to a quarter of an ACIS pixel (0.25") and applied an energy filter of 0.5-7 keV to generate an X-ray image.

To get source positions, we run `wavdetect` on a $400'' \times 400''$ image centered on the cluster. We used size scale parameters of 1, 1.4, 2.0, and 2.8, while setting the threshold significance parameter to 3.9×10^{-7} . This value is the reciprocal of the number of pixels in the image, to minimise misidentifications of background fluctuations as sources⁴. The `wavdetect` positions are then corrected for boresight offsets (Sec. 3.2.3) before being cross-matched with our radio catalogues.

We searched for point sources within the half-light radius ($= 2'.9$) derived by Harris (1996, 2010 edition) which is somewhat greater than that ($= 2'.33$) used by Bogdanov et al. (2010). As a result, our `wavdetect` run revealed a total of 23 point sources that are not previously catalogued, of which 18 are outside the $2'.33$ radius and 5 are inside (Fig. 3.1). Some of these new sources are found to be positionally consistent with our radio sources (Sec. 3.3); moreover, X-ray positions derived from better astrometry with Gaia DR2 result in sub-arcsecond scale offsets (Sec. 3.2.3). We thus report an extended X-ray catalogue with updated source coordinates including both old and new sources (Sec. B). To distinguish from the old sources, the new sources are named with “W” + sequential ID starting from 124, which are all summarised in Tab. 1. For each new X-ray source, we run the CIAO `srcflux` script to calculate the X-ray counts in soft (0.5-1.5 keV) and hard (1.5-6 keV) bands, and based on the total counts, we calculated 95% error radii (P_{err}) using an

⁴<http://cxc.harvard.edu/ciao/threads/wavdetect/>

empirical formula from Hong et al. (2005).

For sources with radio counterparts, we also extracted X-ray spectra using the CIAO `specextract` script and performed analyses using the HEASOFT/XSPEC software (version 12.10.1; Arnaud 1996)⁵. We combined the ACIS-S spectra for each source using the HEASOFT/FTOOLS `addspec` task to maximise spectral counts, and then rebinned the bright ($\gtrsim 700$ counts between 0.5 and 6 keV) source spectra (U12, U18 and U24) to at least 20 counts per energy bin, and faint spectra (U97, U108, W25, W129 and W135) to at least 1 count per bin. The former are then modelled using the χ^2 statistic, and the latter with the C-statistic (Cash, 1979). Since ACIS’s sensitivity falls off at low energies, we only use energy channels between 0.5-10 keV in all of our fits. We note that the spectra of U12 and U18 have been well-analysed by Bogdanov et al. (2010). We thus adopt the corresponding best-fitting models (power-laws for U12 and U18) and calculate X-ray fluxes between 1 and 10 keV, which will be further used in Sec. 3.3. We fit the faint source spectra to absorbed power-law models using `wilms` abundances (Wilms et al., 2000), keeping the absorption column density (N_{H}) fixed at the cluster value ($\approx 1.57 \times 10^{21} \text{ cm}^{-2}$, derived using $E(B - V) = 0.18$ from Harris 1996 and a conversion factor from Bahramian et al. 2015). For W129, we obtained relatively more counts (111 counts between 0.5 and 10 keV), so we fit its spectrum allowing N_{H} to be free.

3.2.3 *HST* observations and Astrometry

For absolute astrometry, we used data from observations by the *Hubble Space Telescope/Advanced Camera for Surveys* (HST/ACS) in the F625W band (R_{625}). The separate exposures are in the form of “FLC” images that are pipe-lined, flat-fielded and cleaned for charge transfer efficiency (CTE) trails. We used the `Tweakreg` and `Astrodrizzle` tasks in the DRIZZLEPAC software package to

⁵<https://heasarc.gsfc.nasa.gov/xanadu/xspec/>

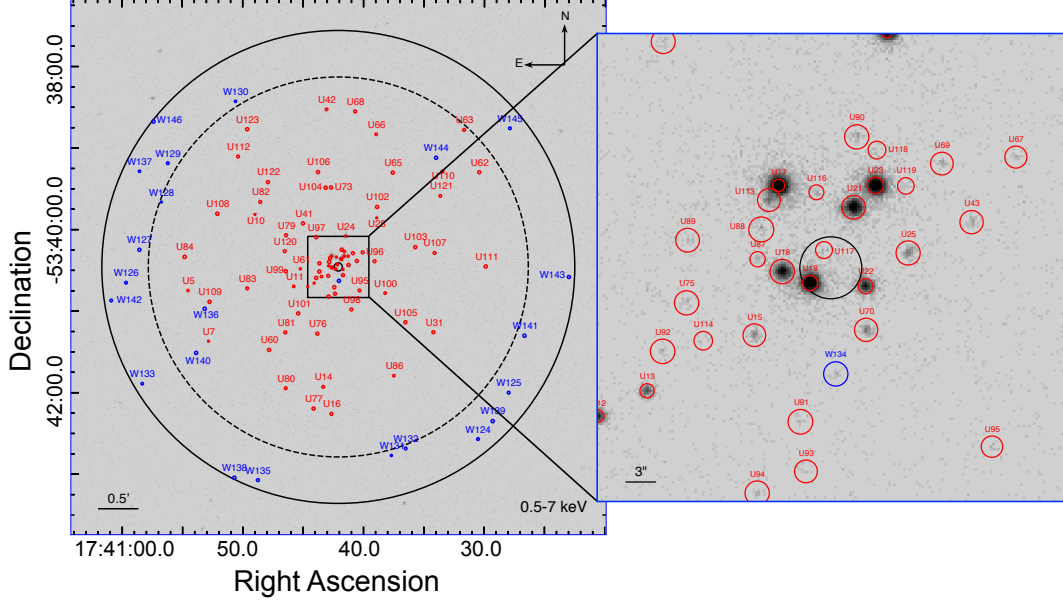


Figure 3.1: *Left*: 0.5-7 keV X-ray image of a $6' \times 6'$ square region centered on the cluster. North is up and east is to the left. New sources detected by `wavdetect` (blue) and sources from Bogdanov et al. (2010) (red) are marked by circles that enclose 90% of their PSFs. The solid black circle shows the 2.9 half-light radius (r_h), while the dashed black circle depicts the 2.33 searching radius used in Bogdanov et al. (2010). *Right*: a zoomed-in $45'' \times 45''$ square region centered on the cluster. The solid black circle shows the $0.05'$ core radius (r_c).

align and combine the individual FLC frames. We set the `pixfrac` to 1.0 and the final pixel size to $0.025''$, oversampling the resulting image by a factor of 2.

We then aligned the resulting “drizzle”-combined image to a catalogue with superior astrometry and used it as the reference frame. For this purpose, we chose stars that have relatively low astrometric uncertainties (with error in RA and DEC ≤ 0.05 mas) from the Gaia Catalogue of Data Release 2 (Gaia Collaboration et al., 2016, 2018a). These stars are matched with stars in the F625W frame so we can calculate averaged relative offsets. We found 50 such stars within a searching radius of $1.2'$ centered on the cluster, resulting in average offsets (Gaia–ACS) of $= 1.53'' \pm 0.03''$ and $= 1.28'' \pm 0.01''$ in RA and DEC (1σ errors), respectively. We consider boresight correction for the catalogue by calculating relative offsets (ACS–*Chandra*) between the X-ray centroids and positions of the identified counterparts for the three brightest

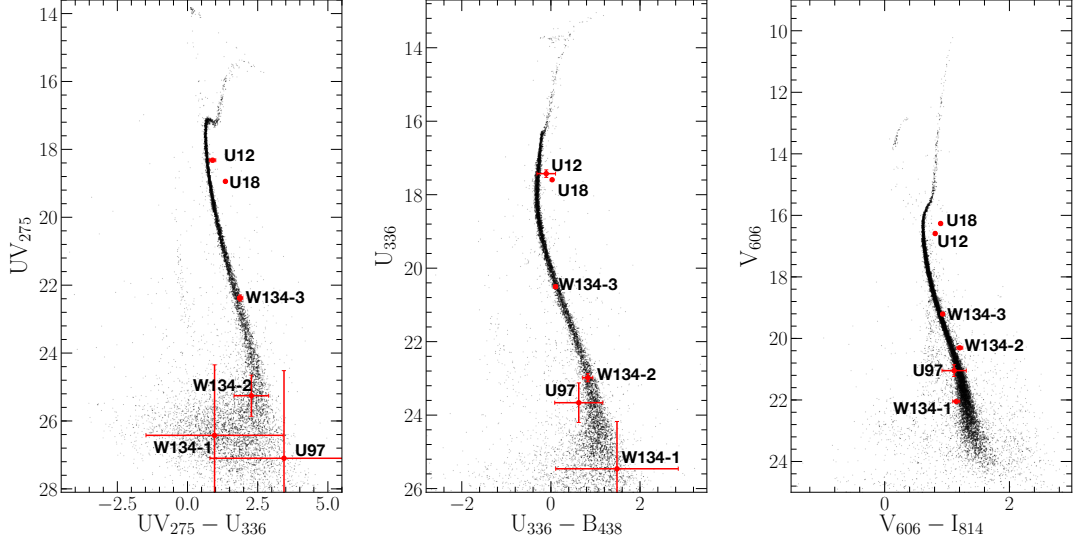


Figure 3.2: Colour-magnitude diagrams (CMDs) of stars from the HUGS catalogue. Locations and errors of optical/UV counterparts to X-ray sources with radio counterparts are indicated with red points and bars. We also present the photometry of 3 objects that lie within the 95% error circle of W134, a new X-ray source with HUGS data available (see also Appendix B).

CVs (U17, U19 and U23), from which we obtained average offsets in RA and DEC of $= -0.09''$ and $-0.13''$, respectively. These offsets are applied to the combined *Chandra* image used for making finding charts.

We also incorporate results from the *HST* *UV Globular Cluster Survey* (“HUGS”; Piotto et al. 2015; Nardiello et al. 2018) into our analyses, which provides photometry in three HST/WFC3 bands: F275W (UV_{275}), F336W (U_{336}), F438W (B_{438}), and two HST/ACS bands: F606W (V_{606}), F814W (I_{814}). The latter are adapted from the *ACS Survey of Galactic Globular Clusters* (ACS GCS; GO-10775, PI: Sarajedini; Sarajedini et al. 2007; Anderson et al. 2008). We plotted 3 colour magnitude diagrams (CMDs) using stars that have good photometric measurements in multiple filters (Fig. 3.2). Locations of interesting sources on the CMDs provide useful information in our further discussions (Sec. 3.3).

3.3 Results

By cross-matching the 5σ radio catalogue with our updated X-ray catalogue, we sought radio sources that lie within P_{err} , and found 7 radio sources positionally coincident with *Chandra* sources, including U12 (PSR 1740-5340), U18, U97, U108 and 3 new sources (W127, W129 and W135) that are likely AGNs. We found U24, the qLMXB, may be associated with a faint extension to a bright source in the 5.5 GHz image, so we also include it in our discussions. In Tab. 3.1, we summarise the positional information of these sources, and in Fig. 3.3, we show the corresponding X-ray, radio and/or optical finding charts. In Tab. 3.2, we present 1-10 keV X-ray fluxes (from spectral fits described in Sec. 3.2.2), and in Fig. 3.4, we plot the 5 GHz radio vs. 1-10 keV X-ray luminosities for cluster sources assuming flat ($\alpha = 0$) radio spectra, together with other classes of accreting compact objects.

3.3.1 U12, PSR J1740-5340

PSR J1740-5340 was discovered by the Parkes telescope as part of a 1.4 GHz radio timing survey for GC MSPs (D’Amico et al., 2001a,b). Irregular radio eclipses were found for more than 40% of its ~ 33 -hr orbit. The X-rays also show a decrease during the radio eclipse, which was interpreted as occultations by the companion star of the shock front produced by interaction between pulsar winds and outflowing mass from the companion (Bogdanov et al., 2010). In the optical, a sub-subgiant with $M \sim 0.3M_{\odot}$ was identified as the counterpart to this MSP (Ferraro et al., 2001; Kaluzny et al., 2003; Orosz & van Kerkwijk, 2003). Further optical spectroscopic studies of this sub-subgiant revealed asymmetric line features and ellipsoidal photometric variations, indicating that the companion fills its Roche lobe (Orosz & van Kerkwijk, 2003), and that it is heated by a beam of radiation from the pulsar (Ferraro et al., 2003; Sabbi et al., 2003). Consistently, we found the optical counterpart to U12 appears

to be in the sub-subgiant region on all three HUGS CMDs (Fig. 3.2). There is no sign of strong UV emission, indicating the absence of a hot disc. This is consistent with the picture suggested by Bogdanov et al. (2010) where matter flows from the companion towards the NS, never reaches the NS, but rather is halted and swept back by the strong pulsar wind, forming an intrabinary shock.

We found an 8σ ATCA source $0.15''$ ($\approx 0.5P_{\text{err}}$) from the nominal X-ray position of U12 (Fig. 3.3), with a 5.5 GHz flux density of $36.7 \pm 4.4 \mu\text{Jy}$. The 9 GHz observation reveals an upper limit of $25 \mu\text{Jy}$, so we obtain a rough 3σ constraint on the spectral index of < 0.5 (see Sec. 3.2.1).

We then imaged the ATCA 5.5 GHz data in two (similar-length) parts, inside and outside the eclipse phases. To calculate the eclipse phases, we used the eclipse phases of 0.05-0.45 quoted in D’Amico et al. (2001a), the orbital period of 1.35405939(5) days from D’Amico et al. (2001b), and a T0 from Mucciarelli et al. (2013) of MJD 52413.22761, to give relevant eclipse times of MJD 56605.44-56605.98 and 56606.79-56607.33. The out-of-eclipse image detects U12 at $58.3 \pm 5.1 \mu\text{Jy}$, while the in-eclipse image does not detect U12, with a 3σ upper limit of $19 \mu\text{Jy}$.

Comparing the out-of-eclipse flux density to the 1.4 GHz flux density of $S_\nu \sim 0.5 - 1.5 \text{ mJy}$ measured by the Parkes radio telescope (D’Amico et al., 2001a, we assume this value is outside the eclipse only) constrains the spectral index $-2.4 \lesssim \alpha \lesssim -1.6$, within the range of steep spectral indices observed in radio pulsars (Bates et al., 2013). We also created images in Q, U, and V Stokes parameters, but did not see evidence of polarised emission. The 3σ upper limit of $16.5 \mu\text{Jy}/\text{beam}$ indicates a polarisation upper limit of 28%.

3.3.2 U18: A hidden MSP?

Grindlay et al. (2001b) discovered the X-ray source U18, associated it with a sub-subgiant counterpart (see also Cohn et al., 2010), and suggested, given the

similarities in X-ray and optical properties to PSR J1740-5340 (U12), that U18 is also a redback MSP, where, in this case, the eclipsing wind completely (or near-completely) blocks the observability of radio pulsations. Bogdanov et al. (2010) confirmed U18’s hard non-thermal spectrum ($\Gamma \approx 1.3$) and variability on timescales from hours to years, which are consistent with a shocked-wind MSP origin for the X-ray emission. Cohn et al. (2010) confirmed that U18’s proper motion marked it as a cluster member, and identified strong optical variability from U18 ($\sigma \sim 0.03$ mags).

U18 has a definite match with an 11.7σ radio source $0.13''$ ($\approx 0.4P_{\text{err}}$) from the nominal X-ray position in our 5.5 GHz radio image (Fig. 3.3). The source was also detected in 9 GHz, allowing us to measure its spectral index, $\alpha = -2.0_{-0.5}^{+0.4}$. The steep radio spectrum is consistent with observations of many MSPs (Sieber, 1973; Lorimer et al., 1995; Bates et al., 2013). Breaking the 5.5 GHz data into two days of similar exposures gives flux densities of 67 ± 5 and $40 \pm 6 \mu\text{Jy}$, confirming variability (at 3.5σ significance), but not indicating extreme flaring. Searching for polarisation gave a 3σ upper limit of 25% polarised emission (similar to U12 above). We also confirm the sub-subgiant position of U18 in all three CMDs, including the UV HUGS data (Fig. 3.2).

Could U18 be something other than an MSP? The radio and X-ray luminosities of U18 are compatible with quiescent black holes (e.g. Gallo et al., 2014). However, the steep radio spectral index of U18 strongly disfavours this scenario, in that quiescent BHs generally have flat to inverted radio spectra.

U18’s steep radio spectral index and high radio luminosity ($L_R \approx 6.9 \times 10^{26} \text{ erg s}^{-1}$ at 5.5 GHz, if one incorrectly assumes a flat radio spectrum) without short, bright flares set its radio emission apart from the CV behaviour discussed in Sec. 3.1.1. Nor do the unusual systems AE Aqr (a propeller system) or AR Sco (a WD pulsar) match U18’s spectral index, or AE Aqr’s flaring behaviour. The optical counterpart to U18 exhibits a moderate $\text{H}\alpha$ excess, and

a relatively low X-ray/optical ratio, which are both consistent with typical globular cluster CVs (e.g. Cohn et al., 2010). However, U18 completely lacks (Fig. 3.2) the UV or blue excesses that originate from the hot accretion disc and/or WD surface in typical CVs. Marked optical/UV variabilities are common in some CVs, which might alter UV flux by up to 1 magnitude on timescales of hours (see e.g., Rivera Sandoval et al. 2018), but cannot be responsible for the strong red excesses of U18 observed in all 3 CMDs. Considering the radio and UV/optical data, we rule out a CV interpretation for U18.

Finally, an AB interpretation cannot be completely ruled out (as the radio spectral index is reasonable; García-Sánchez et al. 2003). The radio luminosity ($L_R = 6.9 \times 10^{26}$ erg s $^{-1}$) can be reached by strong flares in some RS CVn systems (see e.g., García-Sánchez et al., 2003), but is far above the steady radio luminosities seen for known low-mass ABs (see e.g., Guedel & Benz, 1993).

Thus the evidence points to a hidden MSP in U18. Nondetection of pulsations in 1.4 and 3 GHz searches,⁶ if confirmed, generally could imply an unfavorable beaming geometry, but the detection of a bright, steep-spectrum 5.5 GHz source is strong evidence that we are seeing radio pulsar emission from U18. It is possible that U18 shows pulsations at 5.5 GHz while being completely eclipsed at 3 GHz, so we do encourage higher-frequency pulsar searches of NGC 6397. However, this seems unlikely; we conclude that U18 is an MSP whose pulsations may have been completely eclipsed in all observations and frequencies used so far. We discuss the eclipse mechanism further in Sec. 3.4.

3.3.3 U24—radio related to a quiescent LMXB?

U24 is a quiescent low-mass X-ray binary containing a neutron star (Grindlay et al., 2001b; Guillot et al., 2011; Heinke et al., 2014). Detection of radio emission from such an object would be unprecedented. A 6σ flat-to-steep spectrum

⁶Although not published, D’Amico et al. have been timing PSR J1740-5340 at Parkes for a decade at 3 GHz, and their beam includes U18.

($\alpha = -0.7_{-0.6}^{+0.6}$) ATCA source was found $1.2''$ ($\approx 4.3P_{\text{err}}$) northeast of the X-ray position. The relative astrometry indicates that this radio source is not associated with U24, nor with any other detectable X-ray or optical source. However, the radio source appears extended, and may have a faint ($\lesssim 3\sigma$) feature $\sim 1.5''$ south of the radio centroid which may overlap with the position of U24 (displaced by $\approx 0.2''$, Fig. 3.3). This faint extension could be a separate source, though the data is too low-significance to be sure. Deeper radio imaging of NGC 6397 would be needed to verify whether we indeed see radio emission from this quiescent neutron star.

3.3.4 U97

We found a 7.3σ ATCA source $0.13''$ ($0.27P_{\text{err}}$) from the nominal X-ray position of U97, which shows a spectral index of intermediate steepness ($\alpha = -1.3_{-0.7}^{+0.6}$). Assuming the cluster distance and a flat spectrum, we estimate a 5.5 GHz radio luminosity of $4.3 \times 10^{26} \text{ erg s}^{-1}$.

Cohn et al. (2010) found a faint ($V \approx (B + R)/2 \approx 21.9$) and moderately blue counterpart to U97, exhibiting prominent $H\alpha$ variability. Such variation is rare, so the suggested counterpart is highly likely to be the true counterpart. U97 is located fairly close ($\approx 0.5'$ or $\approx 0.2r_h$) to the cluster centre, and the suggested counterpart's proper motion matches the cluster, indicating a high membership probability (Nardiello et al. 2018; Tab. 3.1), so U97 is very likely a cluster member.

3.3.4.1 A chromospherically active binary?

The X-ray/optical ratio of this source overlaps with those of cluster ABs. The HUGS photometry yields a somewhat brighter V_{606} magnitude of 21.0 ± 0.2 , suggesting significant variability. The observed V band magnitude converts to an absolute magnitude (M_V) of 9.2, corresponding to a lower main sequence star of roughly $0.05L_{\odot}$ and $M \approx 0.54M_{\odot}$, according to the stellar models of

Pecaut & Mamajek (2013). This suggests that U97 may be a BY Draconis variable, that is, an AB composed of two MS stars.

Guedel & Benz (1993) found that $\log(L_X/L_R) \lesssim 15.5$ for multiple types of ABs (\approx applies for less luminous objects like BY Dra, while $<$ applies for more luminous classes such as RS CVn), suggesting that the heating of hot coronae (which emit X-rays) and the acceleration of particles (which emit in the radio) are closely related. Given the observed L_X ($\approx 7 \times 10^{29}$ erg s $^{-1}$, see Tab. 3.2) this correlation would predict $L_R(8.5 \text{ GHz}) \approx 2.4 \times 10^{14}$ erg s $^{-1}$ Hz $^{-1}$, which is ~ 3 orders of magnitude fainter than our observed 9 GHz luminosity. The X-ray and radio observations were not simultaneous, so conceivably the high radio luminosity could have been caused by flares at the time of the ATCA observations, while *Chandra* may have observed the source in a quiescent state. However, we found no clear sign of variability from comparing the two separate ATCA images. Furthermore, the radio luminosity ($L_R(5.5 \text{ GHz}) \approx 4.3 \times 10^{26}$ erg s $^{-1}$) we observe would be unparalleled for BY Dra systems. This scenario must be judged extremely unlikely.

3.3.4.2 A quiescent black hole (BH) X-ray binary

The major argument in favour of a BH scenario is that the L_R/L_X ratio is consistent with the scatter of the $L_R - L_X$ correlation for quiescent stellar-mass BHs, from Gallo et al. (2014). The radio spectral index is not well constrained ($\alpha = -1.3_{-0.7}^{+0.6}$) but could be marginally consistent with the flat-to-inverted spectrum observed in quiescent systems (see e.g., Plotkin et al. 2019b), interpreted as self-absorbed synchrotron emission from a collimated jet. The low X-ray luminosity ($L_X(1 - 10 \text{ keV}) = 7.5_{-3.5}^{+4.6} \times 10^{29}$ erg s $^{-1}$; Tab. 3.2) is also consistent with a BH nature.

Although the fit quality is limited by the dearth of counts (27 counts between 0.5 and 10 keV), the (moderately) hard photon index ($\Gamma = 0.5 \pm 1.0$) of U97 could be a counterargument to this scenario. X-ray spectra of quiescent

BHs are usually characterised by softer power-laws ($\Gamma \sim 2.1$; Tomsick et al. 2001; Kong et al. 2002; Corbel et al. 2006; Plotkin et al. 2013; Reynolds et al. 2014). Conceivably a quiescent BH, seen edge-on, would present a harder X-ray spectrum, as the X-rays could be heavily absorbed by part of the accretion disc.

Although the optical counterpart is not obviously blue (as might be expected in an accretion disk scenario), the quiescent nature of the disc at this time could permit the optical/UV light to be dominated by the companion star (e.g., in XTE J1118+480 and A0620-00; see Gallo et al. 2007).

3.3.4.3 A white dwarf system?

As mentioned previously in Sec. 3.1.1, CVs are often observed to be radio sources, but they typically have rather low luminosities ($\lesssim 10^{25}$ erg s⁻¹) in the radio (e.g. Barrett et al., 2017). Two highly magnetic white dwarfs are unusually bright in the radio; AE Aqr (Eracleous et al., 1991) and AR Sco (Marsh et al., 2016). Both lie quite near to U97 in the X-ray/radio luminosity diagram (Fig. 3.4). Note that neither is a standard, accreting CV; AE Aqr is largely in the propeller regime (Eracleous & Horne, 1996), while AR Sco is not thought to be accreting, but to be the first known white dwarf pulsar. The negative radio spectral index of U97 contrasts with the positive radio spectral index of AR Sco, while AE Aqr attains its maximum radio flux density only in short flares, while we measure U97 to have the same radio flux densities (37 and 38 μ Jy, respectively, with noise of 5.5/6.8 μ Jy/beam respectively) in the two halves of our observation. Both AR Sco and AE Aqr are also quite blue, especially in the ultraviolet. This appears not to be the case for U97, according to the HUGS photometry (Fig. 3.2).

3.3.5 U108, W127, W129 and W135

U108 is near an extended object on the optical images, which was interpreted as interacting galaxies by Cohn et al. (2010). We found a 7.7σ radio source $0.57''$ ($1.2P_{\text{err}}$) from the nominal X-ray position, slightly outside the 95% error circle; however, the radio position agrees closely with the optical counterpart, suggesting that the radio and X-ray sources are probably associated with these galaxies (Fig. 3.3).

W127, W129 and W135 are also likely to be extragalactic sources. Arguments for their non-member nature include their large offsets from the cluster centre and, more importantly, their apparently high X-ray absorption (see below), common in AGNs from the obscuring torus. W129 has a relatively “soft” photon index of $\Gamma = 2.7_{-1.2}^{+1.4}$ (Tab. 3.2), but this fit requires heavy absorption of $N_{\text{H}} = 1.2_{-4.7}^{+6.6} \times 10^{23} \text{ cm}^{-2}$ (see Fig. 2). In fact, we searched in the *Mikulski Archive for Space Telescopes* (MAST)⁷ and found that the position of W129 is marginally covered by an *HST* WFC3/IR observation, where we visually identified that W129 is associated with an extended source, likely an early-type galaxy (Fig. 3.3). W127 is deficient of soft X-ray counts, so seems also to be affected by absorption (see Tab.1). A power-law fit to W135 results in a very hard $\Gamma = -0.2_{-1.2}^{+1.0}$. A negative value in this case fits the soft part of the spectrum, since we fixed the N_{H} to the cluster value, which is too low to compensate for the dearth of soft photons. Moreover, searches for possible optical counterparts to either W127 or W135 in the *Gaia* DR2 database did not reveal any objects up to twice the X-ray error radii (Sec. B), suggesting an extragalactic nature.

⁷<http://archive.stsci.edu/>

3.4 Discussion

The identification of U18 as a hidden MSP via its steep-spectrum radio emission is extremely exciting. Its identification in the second-nearest globular cluster (making U18 one of the three nearest MSPs in globular clusters known) suggests that a substantial population of similar systems may exist, with implications for our understanding of the evolution of X-ray binaries into MSPs.

Evidence from previous studies (see Sec. 3.1.2) suggests that more than one mechanism for pulsar eclipses operates, with several works showing that the pulsar signal is absorbed at low frequencies (<1 GHz), but may be scattered at high frequencies. Our current study is unique in indicating that two different eclipse mechanisms appear to be operating in two different MSPs at 5.5 GHz. U12 suffers absorption (dimming by at least a factor of 2.8) during its 5.5 GHz eclipse, while U18 has a similar radio flux as U12 but remains undetected as a radio pulsar. Our detection of the radio counterpart to U18 strongly indicates a scattering process is at work in this system. It is particularly odd that U12 and U18 would show different eclipse mechanisms, as the two systems are remarkably similar in their radio flux, their X-ray flux, and their companion properties (both are sub-subgiants, located a magnitude below the subgiant branch). All three HUGS CMDs show a greater red excess in U18 than U12 (Fig. 3.2). This may suggest that the NS in U18 is in a wider orbit, so that less mass has been stripped away from its companion, leaving it redder (Ivanova et al., 2017). How this could relate to different absorption mechanisms and properties is unclear.

As suggested by Tavani (1991), it may be possible to search for gamma-ray pulsations from U18 to confirm its nature. Blind gamma-ray pulsation searches are only effective for isolated MSPs (Clark et al., 2018), but the example of PSR J1311-3430 (Romani, 2012; Pletsch et al., 2012) shows that gamma-ray pulsations can be uncovered if an optical orbital ephemeris for the counterpart

is available. Indeed, the orbital solution for U18 has recently been uncovered by Pichardo Marcano et al. (2021), suggesting the feasibility of such a search.

3.5 Conclusions

Our studies of the *Chandra* and ATCA observations reveal radio continuum counterparts to 7 X-ray sources including a known MSP (U12; PSR 1740-5340), a “hidden” pulsar (U18) likely obscured by matter stripped from the companion, a BH candidate (U97), a previously identified extragalactic source (U108) and three new sources (W127, W129 and W135), of which two (W127 and W135) are likely to be extragalactic, while the other, W129 has a definite match with a galaxy. The similarities between U12 and U18 and the detection of a steep-spectrum radio counterpart to U18 indicate different eclipsing mechanisms in these two sources, and we suggest that scattering is likely to be the dominant mechanism at high radio frequencies.

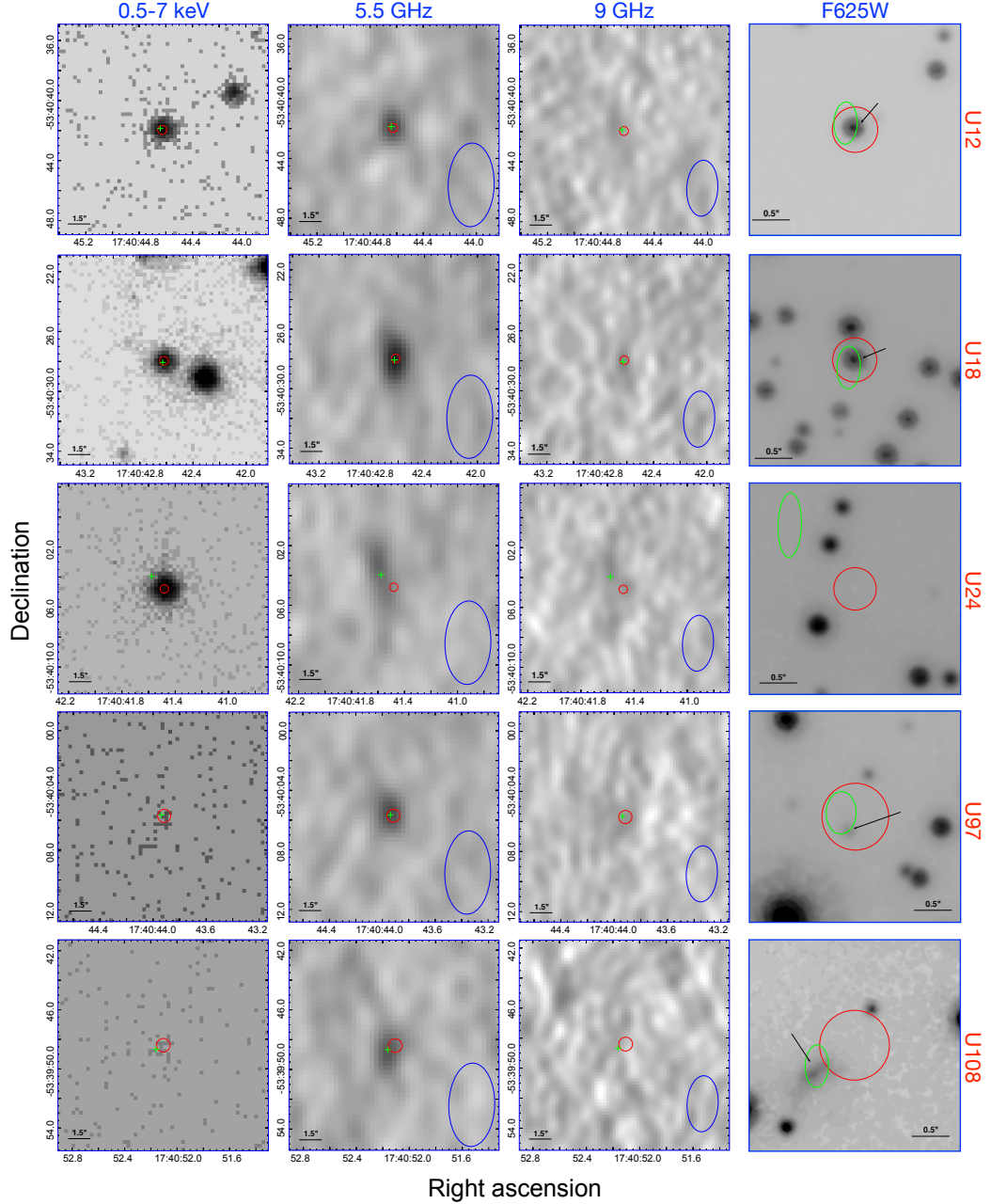


Figure 3.3: X-ray (0.5-7 keV), radio (5.5 GHz and 9 GHz) and optical (F625W) finding charts for U12, U18, U24, U97 and U108. North is up and east is to the left. The X-ray and radio charts are all $14'' \times 14''$ in size while the F625W finding charts are $2''.8 \times 2''.8$. We show the 95% *Chandra* error region with red circles. Since the radio sources have relatively small positional uncertainties, we only show their nominal positions with green crosses in the X-ray and radio images, while in the somewhat zoomed-in F625W charts, we show radio error regions with green ellipses (the sizes of which are described in Sec. 3.2) and indicate the optical counterparts with black arrows. The radio beams in the radio charts are shown with blue ellipses on the bottom right of the 5.5 and 9 GHz images.

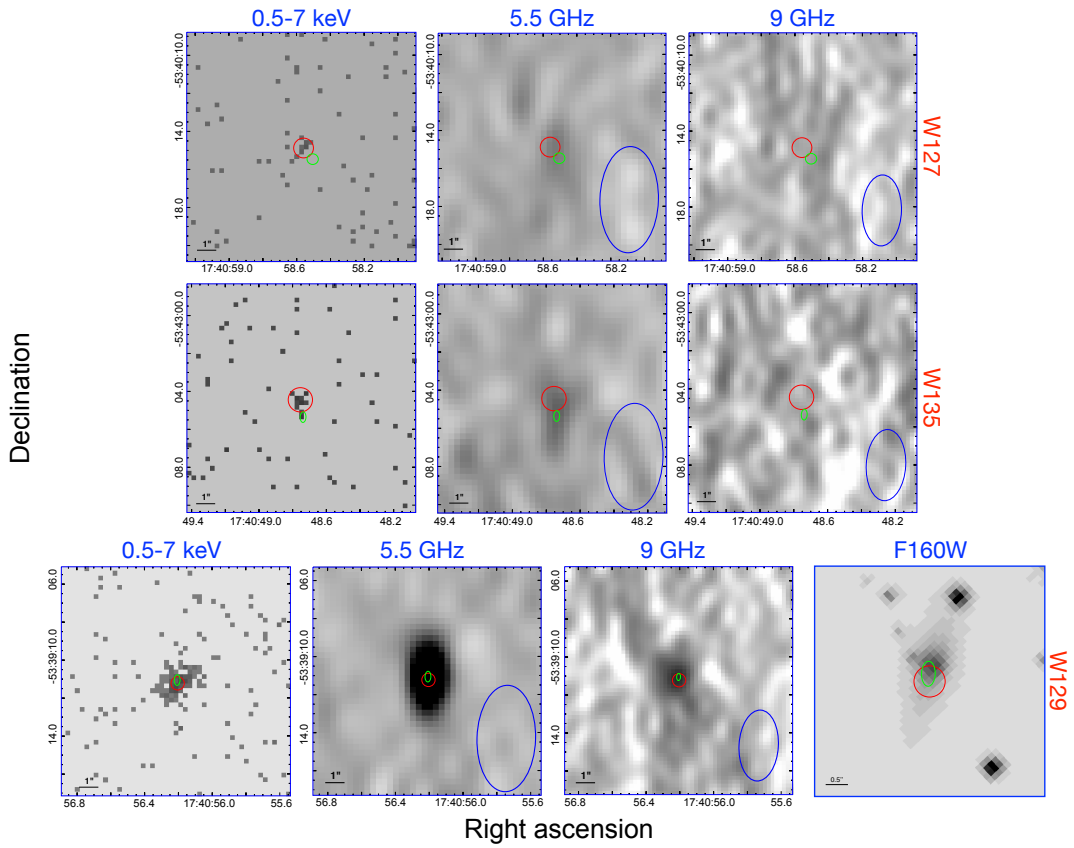


Figure 3.3: (Continued) The top two rows show X-ray (0.5-7 keV) and radio (5.5 GHz and 9 GHz) finding charts for W127 and W135. The last row shows X-ray, radio and infrared (F160W) finding charts for W129. The 5.5/9 GHz and the F160W charts are $12'' \times 12''$ and $5''.5 \times 5''.5$ in size, respectively. Radio error regions are shown with green ellipses.

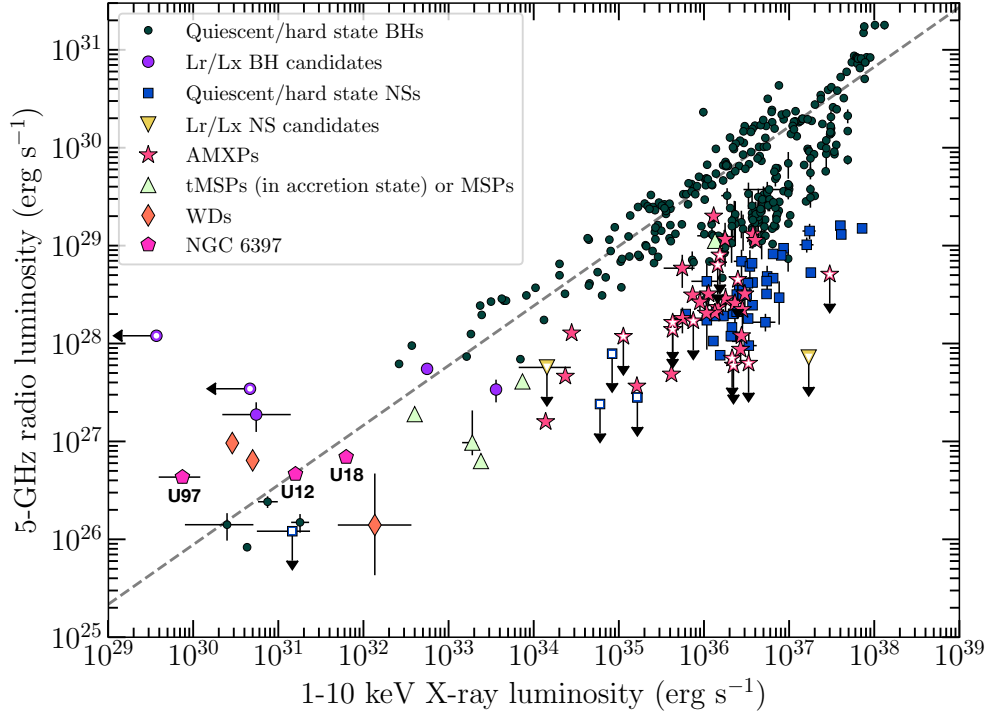


Figure 3.4: 5 GHz radio luminosities plotted vs. 1-10 keV X-ray luminosities for different classes of accreting compact objects. X-ray sources in NGC 6397 associated with radio counterparts are shown with filled pentagons. The radio luminosities are calculated assuming flat ($\alpha = 0$) spectra. The deep-green circles represent known quiescent black holes (Soleri et al., 2010; Miller-Jones et al., 2011; Gallo et al., 2012; Ratti et al., 2012; Corbel et al., 2013; Rushton et al., 2016; Plotkin et al., 2017). The dashed grey line shows the L_R - L_X correlation for black holes from Gallo et al. (2014). The larger purple circles are radio-selected black hole candidates (Strader et al., 2012; Chomiuk et al., 2013; Miller-Jones et al., 2015; Tetarenko et al., 2016; Bahramian et al., 2017; Shishkovsky et al., 2018). The light-green triangles mark known transitional millisecond pulsars (Hill et al., 2011; Papitto et al., 2013; Deller et al., 2015; Bogdanov et al., 2018). The deep-blue squares and pink stars show quiescent/hard-state NSs and accreting millisecond X-ray pulsars (AMXPs), respectively (Migliari & Fender, 2006; Tudor et al., 2017). The yellow triangles show upper limits of L_R of two X-ray transients (Tetarenko et al., 2016; Ludlam et al., 2017). The orange diamonds mark radio detected bright white dwarfs (WDs), including AE Aqr (Eracleous et al., 1991; Abada-Simon et al., 1993), SS Cyg (at flare peak; Russell et al. 2016) and AR Sco (a radio-pulsating white dwarf; Marsh et al. 2016). The hollow markers indicate upper limits. For script and data used to generate the plot, see Bahramian et al. (2018).

Table 3.1: Positional information of radio-X-ray cross-matched sources

Source ID	X-ray position α_X	δ_X	P_{err}^a "	Radio position ^b α_R	δ_R	Optical position ^c α_O	δ_O	P_{μ}^d per cent
U12	17:40:44.63	-53:40:42.0	0.30	17:40:44.64(1)	-53:40:41.9(3)	17:40:44.629	-53:40:41.94	97.9
U18	17:40:42.62	-53:40:28.0	0.29	17:40:42.63(1)	-53:40:28.1(3)	17:40:42.626	-53:40:27.91	98.3
U97	17:40:43.92	-53:40:05.7	0.44	17:40:43.94(1)	-53:40:05.7(3)	17:40:43.927	-53:40:05.89	97.5
U108	17:40:52.11	-53:39:48.4	0.46	17:40:52.16(1)	-53:39:48.7(3)	17:40:52.168	-53:39:48.79	-
W127	17:40:58.56	-53:40:14.9	0.52	17:40:58.51(2)	-53:40:15.5(3)	-	-	-
W129	17:40:56.20	-53:39:11.2	0.35	17:40:56.21(1)	-53:39:11.1(3)	17:40:56.192	-53:39:10.882	-
W135	17:40:48.75	-53:43:04.4	0.64	17:40:48.74(1)	-53:43:05.4(3)	-	-	-

^a95% error radii of X-ray positions; see Hong et al. (2005)

^bThe uncertainties in the α_R and δ_R are derived from projections of the radio error ellipses (Sec. 3.2) to the RA and DEC axes.

^cUncertainties in optical positions are mostly from astrometry (Sec. 3.2.3).

^dMembership probabilities from the HUGS catalogue; see Nardiello et al. (2018).

Table 3.2: Radio and X-ray properties of sources in Tab. 3.1.

ID	F_X ($\times 10^{-16}$ erg s $^{-1}$ cm $^{-2}$)	Photon index (Γ) ^a	S_ν (μ Jy)		Spectral index (α) ^b		Comment
			5.5 GHz	9 GHz	median	3 σ upper limit	
U12	250.4 $^{+14.8}_{-14.8}$	1.7 $^{+0.2}_{-0.2}$	36.7 \pm 4.4	< 25.0	-2.1 $^{+1.1}_{-1.0}$	< 0.5	MSP
U18	990.6 $^{+32.9}_{-33.0}$	1.3 $^{+0.1}_{-0.2}$	54.7 \pm 4.3	21.6 \pm 4.4	-2.0 $^{+0.4}_{-0.5}$	-	MSP?
U97	11.8 $^{+7.3}_{-5.6}$	0.5 $^{+1.0}_{-1.0}$	34.1 \pm 4.7	18.6 \pm 4.5	-1.3 $^{+0.6}_{-0.7}$	-	AB or BH?
U108	5.3 $^{+2.4}_{-1.9}$	1.9 $^{+0.8}_{-0.7}$	34.9 \pm 4.5	< 26.8	-2.0 $^{+1.2}_{-1.0}$	< 0.7	Galaxy
W127	7.2 $^{+4.6}_{-3.3}$	1.1 $^{+1.0}_{-1.0}$	26.9 \pm 5.0	< 35.8	-1.5 $^{+1.5}_{-1.3}$	< 1.0	AGN?
W129	416.8 $^{+72.3}_{-64.9}$	2.7 $^{+1.4}_{-1.2}$	163.0 \pm 5.0	65.0 \pm 8.9	-1.9 $^{+0.3}_{-0.3}$	-	Galaxy
W135	19.8 $^{+11.8}_{-8.7}$	-0.2 $^{+1.0}_{-1.2}$	31.5 \pm 5.8	< 39.4	-1.6 $^{+1.4}_{-1.3}$	< 1.0	AGN?

^aX-ray photon indices derived from spectral fits to a power-law model (Sec. 3.2.2).

^bRadio spectral indices derived using a Bayesian approach; see Sec. 3.2.1.

Chapter 4

A deep *Chandra* survey for faint X-ray sources in the Galactic globular cluster M30, and searches for optical and radio counterparts

Yue Zhao¹, Craig O. Heinke¹, Haldan N. Cohn², Phyllis M. Lugger², Sébastien Guillot^{3,4}, Constanza Echiburú⁵, Laura Shishkovsky⁶, Jay Strader⁶, Laura Chomiuk⁶, Arash Bahramian⁷, James C. A. Miller-Jones⁷, Thomas J. Maccarone⁸, Evangelia Tremou⁹, Gregory R. Sivakoff¹

¹Department of Physics, University of Alberta, CCIS 4-183, Edmonton, AB T6G 2E1, Canada ²Department of Astronomy, Indiana University, 727 E. Third St. Bloomington, IN 47405, USA ³IRAP, CNRS, 9 avenue du Colonel Roche, BP 44346, F-31028 Toulouse Cedex 4, France ⁴Université de Toulouse, CNES, UPS-OMP, F-31028 Toulouse, France ⁵Department of Physics, McGill University, 3600 rue University, Montreal, QC, Canada, H3A 2T8 ⁶Center for Data

Intensive and Time Domain Astronomy, Department of Physics and Astronomy, Michigan State University, East Lansing, MI 48824, USA ⁷International Centre for Radio Astronomy Research-Curtin University, GPO Box U1987, Perth, WA 6845, Australia ⁸Department of Physics & Astronomy, Texas Tech University, Box 41051, Lubbock, TX 79409-1051, USA ⁹LESIA, Observatoire de Paris, CNRS, PSL, SU/UPD, Meudon, France

This chapter details the work published in Zhao et al. 2020b, “A deep *Chandra* survey for faint X-ray sources in the Galactic globular cluster M30, and searches for optical and radio counterparts”, *MNRAS*, 499, 3338, DOI: 10.1093/mnras/staa2927, where we present analyses of a deep X-ray source catalogue of M30; we also incorporate radio and optical/UV imaging data to identify potential counterparts.

Abstract

We present a deep (~ 330 ks) *Chandra* survey of the Galactic globular cluster M30 (NGC 7099). Combining the new Cycle 18 with the previous Cycle 3 observations we report a total of 10 new X-ray point sources within the $1'03$ half-light radius, compiling an extended X-ray catalogue of a total of 23 sources. We incorporate imaging observations by the *Hubble Space Telescope* and the *Karl G. Jansky Very Large Array* from the MAVERIC survey to search for optical and radio counterparts to the new and old sources. Two X-ray sources are found to have a radio counterpart, including the known millisecond pulsar PSR J2140–2310A, the radio position of which also matches a previously reported faint optical counterpart which is slightly redder than the main sequence. We found optical counterparts to 18 of the 23 X-ray sources, identifying 2 new cataclysmic variables (CVs), 5 new CV candidates, 2 new candidates of RS CVn type of active binary (AB), and 2 new candidates of BY Dra type of AB. The remaining unclassified X-ray sources are likely background active galactic nuclei (AGN), as their number is consistent with the expected number of AGN at

our X-ray sensitivity. Finally, our analysis of radial profiles of different source classes suggests that bright CVs are more centrally distributed than faint CVs in M30, consistent with other core-collapsed globular clusters.

4.1 Introduction

Globular clusters (GCs) are old and dense stellar populations and have been intensively studied because of their interesting dynamical features. Specifically, X-ray missions with enhanced angular resolutions and instrumental sensitivity (e.g., *Chandra X-ray Observatory*) have revealed that GCs harbour an overabundance of point-like X-ray sources. Attributed to the very dense core of GCs, these sources are generally thought of as close binaries. Many of these close binaries originate from the close few-body encounters in the dense cores of clusters (e.g., Fabian et al., 1975; Hills, 1976; Camilo & Rasio, 2005; Ivanova et al., 2006, 2008).

The most well-known class of X-ray emitting binaries are low-mass X-ray binaries (LMXBs), which involve neutron stars (NSs) or black holes (BHs) in close orbits with low-mass companions. The NS systems are further classified into systems with relatively persistent X-ray luminosities, vs. transient systems; the latter stay mostly in the quiescent state (with typical $L_X \sim 10^{31-33}$ erg s⁻¹), known as quiescent low-mass X-ray binaries (qLMXBs) and occasionally exhibit outbursts with luminosities typically $\sim 10^4$ times brighter (see Galloway & Keek 2017 for a recent review). LMXBs are considered to be the progenitors of millisecond radio pulsars (MSPs), where the NS has been spun up (“recycled”) to rotate at millisecond periods by accreting matter from the companion, eventually turning on as a radio pulsar (Bhattacharya & van den Heuvel, 1991). Quiescent LMXBs involving BHs, on the other hand, are generally fainter in X-rays ($L_X \sim 10^{30-33}$ erg s⁻¹), but emit strong radio emission via their synchrotron-emitting jets (Fender et al., 2003; Plotkin et al., 2013; Gallo

et al., 2018), enabling identification by their radio-to-X-ray flux ratio (Maccarone, 2005; Strader et al., 2012; Miller-Jones et al., 2015).

Other X-ray emitting close binaries in GCs include cataclysmic variables (CVs) and chromospherically active binaries (ABs), which dominate the faint ($L_X \lesssim 10^{33}$ erg s $^{-1}$) X-ray populations. CVs are white dwarfs (WDs) accreting from low-mass companions, typically seen at $10^{30} < L_X < 10^{33}$ erg s $^{-1}$ in GCs (Hertz & Grindlay, 1983a; Cool et al., 1995; Pooley et al., 2002b); these systems are usually identified through discoveries of optical/UV counterparts or strong optical variability (see e.g., Cohn et al. 2010; Rivera Sandoval et al. 2018). ABs are tidally locked close binaries that involve either main sequence (BY Dra) or evolved (RS CVn) stellar components. Their X-rays are thought to originate from active coronal regions induced by fast rotations as a result of tidal synchronisation; a dozen or more are present in many globular clusters at $L_X \sim 10^{30}$ erg s $^{-1}$ (Bailyn et al., 1990; Dempsey et al., 1993; Grindlay et al., 2001a; Heinke et al., 2005a; Cohn et al., 2010).

Deep radio continuum observations of GCs have recently become possible with bandwidth upgrades to the Australia Telescope Compact Array (*ATCA*) and the Karl G. Jansky Very Large Array (*VLA*). These have enabled the detection of numerous radio point sources in GCs. Many are background active galactic nuclei (AGN), as expected from deep blank-field radio number counts (Kellermann et al., 2008; Padovani et al., 2009). MSPs have steep radio spectra (Kramer et al., 1999), and are seen in large numbers in GCs¹, usually via pulsed emission (Lyne et al., 1987; Camilo et al., 2000; Camilo & Rasio, 2005; Wang et al., 2020), but also in continuum imaging (Hamilton et al., 1985; Fruchter & Goss, 2000; McConnell et al., 2001; Zhao et al., 2020a). Several faint, flat-spectrum radio sources have recently been identified in GCs as black hole candidates (Strader et al., 2012; Chomiuk et al., 2013; Miller-Jones et al., 2015; Bahramian et al., 2017; Tudor et al., 2018), though some may be other

¹For a summary of MSPs in GCs, see <http://www.naic.edu/~pfreire/GCpsr.html>

objects such as unusual NS LMXBs (Bahramian et al., 2018, a candidate transitional millisecond pulsar), or exotic binaries consisting of normal stars and/or white dwarfs (Shishkovsky et al., 2018).

M30 (NGC 7099) is a core-collapsed GC (Djorgovski & King, 1986; Lugger et al., 1995) at a distance of 8.1 kpc (Harris 1996; 2010 edition). A previous study of a 50 ks *Chandra* observation by Lugger et al. (2007) presented a catalogue of 13 ($\lesssim 10^{33}$ erg s $^{-1}$) X-ray sources within M30’s half-mass radius (1'.15), plus optical counterparts identified from observations with the *Hubble Space Telescope* (*HST*). Echiburú et al. (2020) reported analyses of new, deep, Cycle 18 *Chandra* observations of the bright qLMXB in M30, which is dedicated to constraining the mass and radius of the NS. In this work, we incorporate results from X-ray (*Chandra*), radio (*VLA*) and optical (*HST*) observations on M30, cataloguing and identifying faint X-ray sources by searching for possible optical and/or radio counterparts. The paper is organised as follows: In Section 4.2, we describe the observational data used in this work and relevant reduction procedures; in Section 4.3, we present methodologies of our data analyses; in Section 4.4, we provide discussions on individual sources based on our results; and finally, in Section 4.5, we summarise the results and draw conclusions.

4.2 Observations and data reduction

4.2.1 *Chandra* observations

M30 has been visited in Cycle 3 (Obs. ID 2679; PI: Cohn) and Cycle 18 (PI: Guillot) by *Chandra* with the ACIS-S camera, totaling ~ 330 ks of exposure. The Cycle 18 observations were performed in the *very faint* (VFAINT) mode to optimise background cleaning. To reduce frame time, and therefore pileup of the bright qLMXB in the core, a 1/8 subarray centred on the cluster was used. As a result, the Cycle 18 FOV does not add more exposure to most of the cluster outskirts, which were more completely covered by the Cycle 3

Table 4.1: *Chandra* observations of M30.

Cycle	Obs. ID	Exposure (ks)	Start of Obs	Instrument
3	2679	49.43	2001-11-19 02:55:12	ACIS-S
18	20725	17.49	2017-09-04 16:33:05	ACIS-S
18	18997	90.19	2017-09-06 00:05:19	ACIS-S
18	20726	19.21	2017-09-10 02:09:13	ACIS-S
18	20732	47.90	2017-09-14 14:23:17	ACIS-S
18	20731	23.99	2017-09-16 18:04:17	ACIS-S
18	20792	36.86	2017-09-18 04:21:43	ACIS-S
18	20795	14.33	2017-09-22 11:39:56	ACIS-S
18	20796	30.68	2017-09-23 06:09:30	ACIS-S

observation. The analyses in this work thus focus on faint sources within or close to the half-light radius ($1'03$; Harris 1996, 2010 edition). More details of the observations are listed in Table 4.1.

The level-1 ACIS data products are first reprocessed and aligned to the up-to-date calibration (CALDB 4.8.2) using the `chandra_repro` task in the CHANDRA INTERACTIVE ANALYSIS OF OBSERVATIONS (CIAO)² software (Fruscione et al., 2006). This renders level-2 event files that can be used to generate scientific products for further analyses.

4.2.2 *HST* observations

We use imaging data observed by the *HST* Wide-field Camera 3 (WFC3; GO-13297; PI: Piotto) and the Advanced Camera for Surveys (ACS; GO-10775; PI: Sarajedini). These provide images of excellent sub-arcsecond spatial resolution in F275W (UV₂₇₅), F336W (U₃₃₆), and F438W (B₄₃₈) for WFC3, and in F606W (V₆₀₆) and F814W (I₈₁₄) for ACS. All imaging products are composed of single exposures that are pipe-lined, flat-fielded and have charge transfer efficiency (CTE) trails removed (FLC images). The two WFC3 observations are separated roughly by 2 months (Table 4.2), each of which contains one (B₄₃₈) and

²<http://cxc.cfa.harvard.edu/ciao/>

Table 4.2: HST observations of M30

GO	Exposure (s)	Start of Obs	Instrument/Channel	Filter
10775	567	2006-05-02 21:47:08	ACS/WFC	F606W (V_{606})
10775	567	2006-05-02 23:21:19	ACS/WFC	F814W (I_{814})
13297	1450	2014-06-08 22:13:14	WFC3/UVIS	F275W (UV_{275})
13297	1450	2014-08-19 04:53:35	WFC3/UVIS	F275W (UV_{275})
13297	606	2014-06-08 22:05:34	WFC3/UVIS	F336W (U_{336})
13297	606	2014-08-19 05:16:51	WFC3/UVIS	F336W (U_{336})
13297	65	2014-06-08 22:01:50	WFC3/UVIS	F438W (B_{438})
13297	65	2014-08-19 03:56:58	WFC3/UVIS	F438W (B_{438})

two (UV_{275} or U_{336}) dithered exposures. The latter observations are roughly rotated by $\approx 90^\circ$ relative to the earlier observations. Observations by ACS were done roughly 8 years earlier than the WFC3 observations, of which each filter (V_{606} or I_{814}) comprises one short (7 s) and 4 long (140 s each) exposures. A summary of basic information about these *HST* observations is presented in Table 4.2.

These datasets have been fully analysed as part of the *ACS Globular Cluster Treasury Program* (Sarajedini et al. 2007; Anderson et al. 2008)³ and the *Hubble Space Telescope UV Legacy Survey of Galactic Globular Clusters* (HUGS; Piotto et al. 2015), offering a set of kinematic and 5-band photometry information. Although we generate our own photometry catalogues for optical identifications, the HUGS data products provide useful information in cases where stars are missed by our photometry (see Section 4.3.7) and are especially important in determining cluster membership (Nardiello et al., 2018).

4.2.3 VLA observations

M30 was observed by *VLA* as a part of the “*Milky Way ATCA and VLA Exploration of Radio sources In Clusters*” (MAVERIC) survey (Tremou et al. 2018; Shishkovsky et al. 2020). The observations (NRAO/VLA Program IDs: 15A-

³<https://archive.stsci.edu/prepds/acsggct>

100; PI Strader) were performed in three separate blocks, on 2015-06-23, 2015-07-04, and 2015-07-05, totaling 8 hr on source. In each block, M30 was observed with the most extended A configuration, using the C band (4-8 GHz) receivers. The data were taken using the 3-bit mode, with two separate 2048 MHz bands centered on 4.9 and 7 GHz, respectively. Data reduction and imaging were done with AIPS (Greisen, 2003) and CASA (McMullin et al., 2007), rendering root mean square (RMS) values for 4.9 GHz and 7 GHz of $1.7 \mu\text{Jy}/\text{beam}$ and $1.6 \mu\text{Jy}/\text{beam}$, respectively; correspondingly the synthesized beam sizes are $0.74'' \times 0.39''$ and $0.52'' \times 0.28''$ at 4.9 GHz and 7 GHz, respectively.

We then generate radio source catalogue using the processed images. More details on the methodologies and the catalogue are presented in a separate paper (Shishkovsky et al., 2020), while in this work, we only report the radio sources that positionally match sources in our updated X-ray catalogue.

4.3 Data analyses

4.3.1 Merging the X-ray observations

To detect faint X-ray sources, typically to differentiate very faint sources from background fluctuations, it is important to take full advantage of all exposures. Prior to combining the files, we refine the relative WCS information for each event file to account for instrumental offsets. These offsets might be on sub-arcsecond scales, but are crucial for later detections of very faint sources. For this purpose, we chose the longest *Chandra* observation (Obs. ID 18997) as the reference frame, to which we calculate relative offsets for all other observations using the centroid positions of A1, the brightest source. The resulting shifts are then used as input to the CIAO `wcs_update` and the `acis_process_events` tools to update the WCS information for each event file. The latter generates updated event files while preserving the Energy-Dependent Subpixel Event Repositioning (EDSER; Li et al. 2004) pixel adjustment. In a final step, we

run the `merge_obs` script⁴ on the stack of WCS-corrected files. This tool first reprojects all input files to a common tangent point, and then creates a merged event file while generating a combined exposure map and an exposure-corrected X-ray flux image.

We applied a $2'5 \times 2'5$ square spatial filter and energy filters to the merged event file, creating X-ray images binned to a quarter of an arcsec (i.e., half the ACIS pixel size) over a soft (0.5–2 keV), a hard (2–7 keV), and a broad (0.5–7 keV) energy band. Since the on-axis X-ray sources can have PSF sizes under the ACIS pixel scale (0.5"), over-binning the images can better resolve the crowded core, while applying separate energy filters can potentially decompose individual sources that are otherwise blended in the broad-band image (e.g., a soft source in the vicinity of a hard source).

4.3.2 Source detection

We use the CIAO `wavdetect` script⁵ (Freeman et al., 2002) to find and localise possible point sources in the field. `wavdetect` utilises a wavelet-based algorithm which correlates image pixels with the “Mexican Hat” wavelet function at different scales. The tool searches for significant (at a given threshold) correlations and correspondingly centroids the sources, while calculating fluxes and other relevant properties.

We set the `scale` parameter to 1.0, 1.4, 2.0, 2.8, and 4.0 to account for sources of different sizes and use a significance threshold (`sigthresh`) of 1.07×10^{-5} (reciprocal of the number of pixels in the image) to limit false detections. We first generate 3 separate source lists by running `wavdetect` on the extracted soft, hard and broad X-ray images (energy bands defined in Section 4.3.1). These source lists are then cross-matched and concatenated to form a final source catalogue.

⁴http://cxc.harvard.edu/ciao/ahelp/merge_obs.html

⁵<http://cxc.harvard.edu/ciao/ahelp/wavdetect.html>

Besides sources detected by Lugger et al. (2007), our `wavdetect` run yields 9 new sources ($> 3 \sigma$) within the 1'03 half-light radius. To distinguish from previously detected sources, each new source is named as “W” + a sequential number starting from 14. Positional and basic X-ray properties of all old and new sources are summarised in Table 4.3, and in Figure 4.1 we present an X-ray image to show the spatial distribution of these sources.

The known MSP (PSR J2140–2310A; MSP A hereafter), and A3, a previously reported X-ray source, were not detected with the above `wavdetect` parameters. The former has a radio position measured by timing observations as reported by Ransom et al. (2004). The latter is a faint source in close proximity to A1, which was reported as a detection by Lugger et al. (2007). These sources were detected with somewhat higher `sigthresh` values, which might result in more spurious detections elsewhere but still provides good localisation. We found that both MSP A and A3 were detected when `sigthresh`= 0.001, with which `wavdetect` found MSP A and A3 at the 2.9 and 2.6 σ level, respectively. Including MSP A, our X-ray catalogue has 10 new sources, extending the previous catalogue to 23 sources.

The updated half-light radius (1'03) from Harris (1996, 2010 edition) is smaller than the 1'15 search radius used by Lugger et al. (2007), by which sources 12 and 13 are excluded. However, since these two sources were observed both in Cycle 3 and Cycle 18 and were not optically identified, we still include them in our analyses.

4.3.3 Source counts

To calculate total source counts and fluxes, we use the CIAO `srcflux` script. The script cannot be run on merged observations, so we applied the script on individual event files and then summed up the counts and averaged the fluxes. For each source, we compute source counts in the above-defined soft and hard bands, using circular extraction regions with radii that enclose roughly 90%

of the PSF in the broad band image. For each isolated source, we use the default setting where the background is defined by an annulus with inner radius equaling the source radius, and outer radius 5 times that of the inner radius. Sources A1, A2, A3, MSP A, W17, C and W15 are in the close vicinity of another source (Figure 4.1). For these sources, we specify background regions that are outside the core and enclose only source-free fields.

The resulting files from `srcflux` include background-subtracted count rates and model-independent fluxes for individual observations. We convert the former to counts by multiplying by the corresponding exposure time, while the latter were converted to exposure-weighted fluxes. X-ray properties of all sources are summarised in Table 4.3.

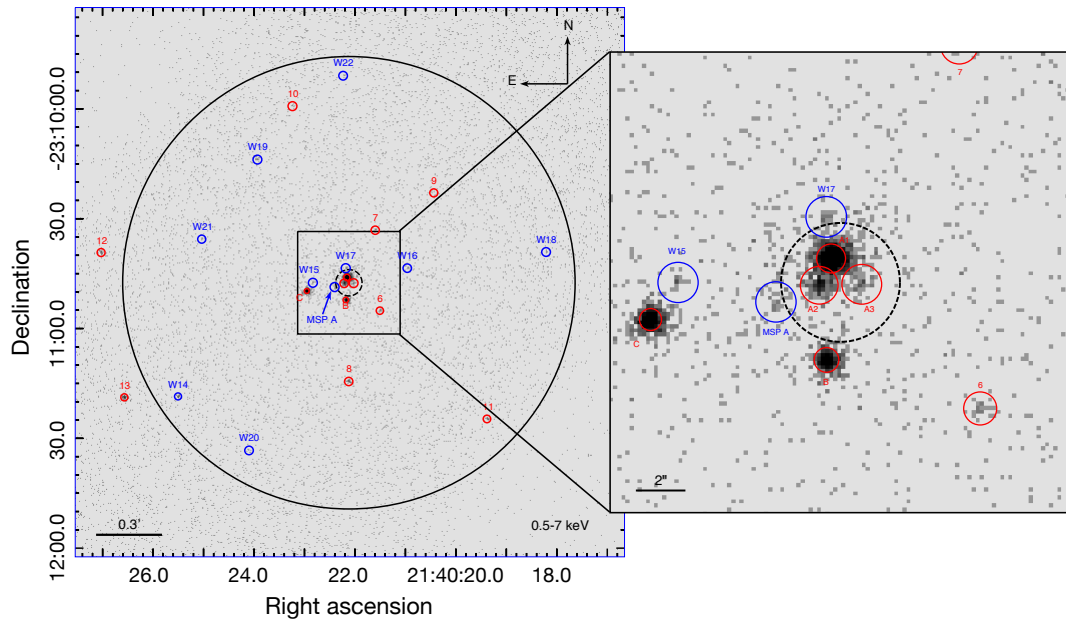


Figure 4.1: 0.5–7 keV X-ray image of M30. The left panel shows a 2.5×2.5 square region centered on the cluster. All sources are indicated with circles that enclose 90% of their PSFs, with new sources in blue and previously reported sources (Lugger et al., 2007) in red. The solid black circle indicates the 1.03 half-light radius of the cluster and the dashed black circle represents the 0.06 core region according to Harris (1996, 2010 edition). The right panel shows a zoomed-in view of the central $28'' \times 28''$ square region.

4.3.4 X-ray spectral analyses

Spectral analyses of the qLMXB A1 to constrain the NS radius and mass are presented in a separate work (Echiburú et al., 2020). The analyses in this paper focus on the other, especially the newly detected, sources, using mostly the Cycle 18 data.

We first extract X-ray spectra using the CIAO `specextract` tool⁶. The source regions are defined as circular regions that enclose roughly 90% of the source PSF, while background regions are chosen as source-free annulus regions around (in cases of sources not affected by crowding) or away from the source (in cases of sources close to the crowded core).

Spectral analyses were performed with the HEASOFT/XSPEC software (version 12.10.1; Arnaud 1996). We combined the Cycle 18 spectra and the corresponding associated files (including response matrices, ancillary response files, and background spectra), using the `addspec` script in HEASOFT/FTOOLS, and properly rebin the co-added spectra using the CIAO `dmgroup` tool. For sources A2, B and C, which have more than 100 counts, we rebinned the spectra to at least 10 counts per bin and analyse them using χ^2 statistics; whereas for sources with fewer than 100 counts, we binned them to contain at least 1 count per bin and use W-statistics (Cash, 1979) in our analyses, while applying the Cramer von Mises (`cvm`) test statistics. We found that source 10 has too few Cycle 18 counts (3 counts between 0.5–10 keV) to properly constrain the spectral flux, so we also incorporated the Cycle 3 data. The fitting quality is therefore evaluated either through the reduced χ^2 ($\chi^2_{\nu} = \chi^2/\text{dof}$) or, for W-statistics, roughly through the `goodness` command in XSPEC, which generates a given number of simulated spectra based on the best-fitting parameters and calculates the fraction of realisations with the fit statistic lower than that for the data. For each W-statistics fit, we generate 1000 realisations and expect percentages below

⁶<http://cxc.harvard.edu/ciao/ahelp/specextract.html>

90% as acceptable. All parameters are reported at the 90% confidence level.

We tried to fit the rebinned spectra to an absorbed power-law (`pow`) or thermal plasma model (`vaptec` in `XSPEC`) between 0.5 and 10 keV, keeping models that better describe the spectra. The Fe abundance in `vaptec` is fixed at the cluster value ($[\text{Fe}/\text{H}] = -2.27$ from Harris 1996). Galactic absorption is accounted for by convolving the models with the `tbabs` model in `XSPEC` using the `wilms` abundance (Wilms et al., 2000). We keep the hydrogen column density (N_{H}) as a free parameter for sources with more than 100 counts, while the N_{H} for fainter sources is fixed at the cluster value ($\approx 2.61 \times 10^{20} \text{ cm}^{-2}$, calculated using the cluster reddening $E(B - V) = 0.03$ from Harris 1996 and a conversion factor from Bahramian et al. 2015). For the faintest spectra that have less than 10 counts (source 10, W17, W18 and W20), constraints on model parameters derived directly from the fits become tenuous, so we only fit the normalisation parameters for these spectra. The plasma temperature (for the `vaptec` model) or photon index (Γ in the `pow` model) are fixed to averaged values obtained by fitting a `vaptec` or `pow` to the co-added spectra of all the faint source spectra ($\Gamma = 2$ for `pow`; $kT = 2.7$ keV for `vaptec`). For the known MSP, MSP A, we fit both a `pow` model and a blackbody model, `bbodyrad`, to its spectrum. We report our results in Table 4.4.

4.3.5 X-ray variability

We run the CIAO `glvary` script to check for variability within each *Chandra* exposure following the instructions in the “Searching for Variability in a Source” thread⁷. The `glvary` script applies the Gregory-Loredo algorithm (Gregory & Loredo, 1992), which divides the event time series into multiple time bins and looks for significant variations between these bins. The degree of variability is indicated with a variability index (VI) between 0 and 10, with values ≥ 6

⁷<https://cxc.cfa.harvard.edu/ciao/threads/variable/>

considered confident variables.

We found variability for A2 and W16 (VI=6) in obsID. 20792 and 18997 (Table 4.1), respectively; likely variability (VI=5) was found in source 8 in obsID. 18997. As expected, we did not find variability for A1 (VI=0) in any of the observations, as emission from qLMXBs are dominated by non-varying thermal X-rays originating from the NS surface.

4.3.6 Astrometry

4.3.6.1 Co-adding images

We used the Python routine `astrodrizzle` from the `DRIZZLEPAC` software package⁸ (version 2.0) to generate combined optical images. The `astrodrizzle` routine takes advantage of the dithering information from the single FLC frames to remove cosmic rays and small-scale detector defects (e.g., hot pixels, bad columns, etc.), while generating co-added images and reconstructing information lost due to undersampling.

For each filter, the individual FLC frames are first aligned with the `Tweakreg` tool, accounting for shifts between the FLC frames. The aligned FLC frames are then combined using `astrodrizzle`. We set the `pixfrac` parameter to 1.0 and use a final pixel size (`final_scale`) half of the native pixel scale (0.02'' for WFC3 and 0.025'' for ACS), oversampling the co-added image by a factor of 2 to mitigate crowding in the core. The “drizzle”-combined images are then used for further astrometric analyses.

4.3.6.2 Absolute Astrometry

There are multiple factors that may affect the accuracy of the *HST* astrometry solution, but the main source of error comes from uncertainties in guide star positions, from which astrometry is derived. As the uncertainties are typically

⁸<http://www.stsci.edu/scientific-community/software/drizzlepac.html>

≈ 200 mas and ≈ 300 mas for WFC3 and ACS, respectively (Lucas, 2016; Deustua, 2016), they might significantly alter our counterpart identifications⁹.

To correct our absolute astrometry, we aligned the *HST* images to the *Gaia* DR2 catalogue (Gaia Collaboration et al., 2016, 2018a), which offers accurate source positions with uncertainties on milliarcsecond (mas) scales. Since most well-localised *Gaia* sources in M30 are bright, we chose the U₃₃₆ image as the reference frame that is sufficiently long in exposure to include many bright objects, but not too deep so as to saturate these stars. In fact, the drizzle-combined dithered images improve spatial sampling of the PSF and therefore provide somewhat improved centroiding.

We found 217 *Gaia* sources within the half-light radius that have superior astrometric solutions (uncertainties in both RA and DEC ≤ 0.2 mas). On the U₃₃₆ image, we obtained centroid positions of stars by running the `daofind` task in the DAOPHOT software package (Stetson, 1987). In the next step, we cross-match the *Gaia* catalogue with the U₃₃₆ image to find counterparts to the *Gaia* sources, finding 217 matches with average offsets in RA and DEC ($Gaia-HST$) = $0.135'' \pm 0.006''$ and $0.123'' \pm 0.004''$ (1σ errors). Finally, the offsets were applied to update the WCS information of the U₃₃₆ image, to which the other *HST* images are aligned.

4.3.6.3 *Chandra* boresight correction

We have applied relative shifts to individual ACIS observations prior to merging (Section 4.3.1); however, the resulting merged event file still requires further astrometric corrections before proceeding with counterpart searches.

For this purpose, we chose the on-axis sources B and C which have rela-

⁹At the time of writing, astrometry of WFC3 and ACS imaging products retrieved from the STSCI archive have been aligned to an updated guide star catalogue, and some have been directly aligned to Gaia catalogue. More details can be found in <https://archive.stsci.edu/contents/newsletters/december-2019/improved-astrometry-for-wfc3-and-ac3?filterName=news-filter&filterPage=news>.

tively well-defined PSFs and possess well-identified counterparts (Lugger et al., 2007). We calculated the corresponding shifts between `wavdetect`-determined X-ray positions and the corresponding counterpart `daofind` positions, yielding average shifts ($Gaia - Chandra$) $\approx -0.279''$ and $\approx 0.107''$ in RA and DEC, respectively, which were then applied to the WCS header information to correct the boresight.

4.3.7 Optical photometry

The photometry of most stars has been fully analysed as a part of the HUGS project (Piotto et al., 2015). The catalogue data products are now available to the public (Nardiello et al., 2018), from which we can readily construct colour-magnitude diagrams (CMDs). However, we noted that some stars (especially the faint ones), though clearly present in the field, do not have HUGS photometry. We therefore also generate our own photometric catalogue as a complement to the HUGS results.

We use the DOLPHOT (version 2.0) photometry package (software based on HSTPHOT; Dolphin 2000) to generate photometry catalogues for individual frames observed by WFC3 and ACS. First, for each camera, we use a drizzle-combined image (U_{336} for WFC3; I_{814} for ACS)¹⁰ as the reference frame, to which coordinates of stars found on individual exposures are transformed. We then applied the `wfc3mask` and the `acsmask` tools to the individual WFC3 and ACS exposures to mask the flagged bad pixels while multiplying the pixel area map by each FLC image. In the next step, we use the `splitgroup` tool to extract 2 individual science extensions from each FLC image, corresponding to separate exposures on the two CCD chips. These CCD-specific images are then fed to the `calcsky` tool to calculate sky levels, generating a sky map for each image.

¹⁰Note that the drizzle-combined images used here are on the original pixel scales, i.e., not oversampled.

The above processes set up the basic input to the final runs. The final step prior to running the `dolphot` task is to determine the proper parameters. We list in Table 4.5 the parameters we used that are not at their default values. We run `dolphot` using the Anderson PSF library (WFC3 ISR 2018-14; ACS ISR 2006-01) by specifying the `ACSpsfType` and `WFC3UVISpsfType` parameters. The software then performs aperture and PSF photometry on the individual FLC frames, calibrates the photometry to big apertures (0.6'' for WFC3; 0.5'' for ACS), and converts the magnitudes to the VEGMAG system using up-to-date zeropoints for ACS (Sirianni et al., 2005) and WFC3¹¹.

The resulting catalogues include the basic positional information and instrumental magnitudes for stars cross-identified on multiple filters. Besides, there are multiple quality parameters that can be used to significantly reduce the raw catalogues and cull for stars with high quality photometry. For each camera, we first extracted a sub-catalogue that contains all star-like objects that have valid instrumental magnitudes in at least one filter. This catalogue is further used for identification of counterparts. We also extract sub-catalogues for making $UV_{275} - U_{336}$, $U_{336} - B_{438}$ and $V_{606} - I_{814}$ colour-magnitude diagrams (CMDs; Figure 4.2). For this purpose, we use stars with relatively low (< 0.1) uncertainties in photometry, which significantly reduced the spread in the faint end of the CMDs. Note that this reduction is only to improve readability of the plot; for faint counterparts that have intrinsically high uncertainties, we keep the error bars when we plot them on the CMDs.

Our photometry catalogue might complement the HUGS photometry in the WFC3 bands (UV_{275} , U_{336} , and B_{438}). However, in the ACS images (V_{606} and I_{814}), magnitudes of some stars were not properly measured by DOLPHOT. Particularly in the core, photometry of some stars is not available due to crowding or bleeding patterns from bright stars, albeit the target is clearly detected.

¹¹<https://www.stsci.edu/hst/instrumentation/wfc3/data-analysis/photometric-calibration/uvis-photometric-calibration>

The HUGS results might also miss some stars but are superior to our photometry in V_{606} and I_{814} . Therefore, for stars not measured by DOLPHOT, we search in the HUGS catalogue and calibrate the magnitudes to align with our photometry (indicated with [†] superscripts in Table 4.6). This conversion was done by calculating average offsets, in V_{606} and I_{814} , using stars with relatively small (≤ 0.05 in DOLPHOT and ≤ 0.01 in HUGS) photometric uncertainties. We found 12086 and 12540 such matches in V_{606} and I_{814} bands and obtained 3 σ -clipped median offsets (DOLPHOT-HUGS) of -0.013 and 0.029 (with 1 σ error of ≈ 0.01 in both bands), respectively.

4.3.7.1 UV variability

The DOLPHOT output also includes frame-specific magnitudes that allow us to check the variability of interesting targets. For this purpose, we collect magnitudes measured on multiple frames and plot their RMS values (σ 's) vs. mean magnitudes. The results are presented in Figure 4.3. While most stars lies on a sequence with increasing RMS towards fainter magnitudes, stars with strong variability should be outliers from the sequence.

4.3.8 Counterpart search and source identification

4.3.8.1 Basic methodologies

Identifying X-ray sources involves incorporation of positional, photometric (both optical and X-ray), temporal, and membership information of each source. Positionally, since bright ($\gtrsim 100$ counts) X-ray sources are more accurately localised, we primarily search within their 95% error circles (Table 4.3), expecting optical counterparts close to the nominal X-ray positions. Faint X-ray sources might have more uncertain X-ray positions, we thus expand the searching region to 1.5 times their 95% error radii. For sources that have *VLA* counterparts and thus somewhat better localisation, we search the radio error regions ($\sim 1/10$

the synthesised beam) for optical counterparts.

The photometric criteria used for identifying optical counterparts depend on the type of the source. For example, we identify CVs with blue outliers on the UV CMDs, as CVs usually manifest strong UV emission thought to originate from a shock-heated region on the white dwarf surface (in the case of magnetic CVs) and/or from the accretion disc; whereas, when observed in optical bands like V_{606} and I_{814} , optical fluxes are dominated by the companion, which has a lower surface temperature, so they may appear to be consistent with, or even slightly redder than, the main sequence (e.g., Edmonds et al., 2003a,b; Lugger et al., 2017; Zhao et al., 2019). On the other hand, ABs often manifest slight red excesses consistent with the binary sequence (BY Dra systems), or they have subgiant or red giant companions (RS CVn systems).

Care should be taken, however, that background AGN can masquerade as CVs with blue excesses on multiple CMDs; whereas foreground stars can be strong X-ray emitters and red outliers. The AGN nature of some sources might be indicated by detections of radio counterparts, yet for most sources that have no radio counterparts, we may rely on the kinematic information of the optical counterpart to check for membership. In this regard, cluster membership probabilities derived from proper motions (PMs) from the HUGS catalogue (Nardiello et al., 2018) are very useful in our analyses.

In X-ray, we define a hardness ratio

$$X_C = 2.5 \log_{10} \left(\frac{F_{0.5-2}}{F_{2-7}} \right), \quad (4.1)$$

where $F_{0.5-2}$ and F_{2-7} are the unabsorbed model fluxes in the soft and hard bands from our spectral fits (Table 4.4), which can roughly separate different source classes. In Figure 4.4, we present an X-ray colour-magnitude diagram, plotting 0.5–7 keV fluxes (and luminosities calculated assuming the cluster distance) vs. X_C . Comparison with e.g. the X-ray hardness diagram of Heinke

et al. (2005b) shows that consistency with a photon index around 1.7 is common for bright ($L_X > 10^{31}$ erg s $^{-1}$) CVs (and, more rarely, bright MSPs and ABs), as well as AGN. CVs and AGN can also show harder spectra, if they show internal absorption (e.g., they are seen edge-on through their accretion discs). Consistency with a photon index between 2 and 4 is typical of fainter ($L_X < 10^{31}$ erg s $^{-1}$) MSPs, CVs, and (very common) ABs, and of quiescent LMXBs at any luminosity.

Source classification can be further complemented by investigation of X-ray/optical ratios. In Figure 4.5, we plot 0.5–2.5 keV X-ray luminosities vs. absolute V band magnitudes (M_V) for sources identified with optical counterparts. Bassa et al. (2004) found an empirical separatrix on this diagram that roughly distinguishes cluster ABs from CVs, given by $\log_{10} L_X [0.5 - 2.5 \text{ keV}] = -0.4M_V + 34$. CVs usually have higher ratios and locate above this separatrix, while ABs lie to the lower right in the $L_X - M_V$ plane.

Finally, temporal features, especially signs of variability, might also be useful in determining the source nature. Most classes of X-ray source show variability; the only classes that lack evidence of intrinsic variability (on timescales of minutes to days) are quiescent LMXBs and MSPs showing only thermal X-ray emission from their surfaces, or MSPs showing magnetospheric emission (note that redback MSPs showing shock-powered emission do vary).

4.3.8.2 Radio counterparts

Radio counterparts to X-ray sources can provide complementary information on the source nature. Indeed, multiple source classes are also expected to be radio emitters. An important feature is the radio spectral index (α ; as defined in $S_\nu \propto \nu^\alpha$, where S_ν is the specific flux density). In both NS (Migliari & Fender, 2006) and BH LMXBs (Gallo et al., 2014, 2018), radio emission has been observed to have flat ($-0.5 < \alpha < 0$) to slightly inverted ($\alpha > 0$) spectra, which are thought to be from relativistic jets; whereas MSPs commonly

exhibit steep radio spectra ($\alpha \approx -1.4$ with unit standard deviation; see Bates et al. 2013). Radio emission has also been observed in CVs (e.g., Coppejans et al., 2015, 2016; Barrett et al., 2017), which are usually fainter than LMXBs but could attain higher flux levels during occasional flares (e.g., Russell et al., 2016). ABs can also be radio sources, but even short bright flares, as bright as 10^{19} erg s $^{-1}$ Hz $^{-1}$ at centimeter wavelengths (see e.g., Drake et al., 1989; Osten et al., 2000), are too faint to be detected by our *VLA* observation considering the distance to M30. Finally, supermassive black holes in AGN are also active radio emitters; indeed, AGNs are the most common radio sources observed in the directions of GCs (Shishkovsky et al., 2020).

4.3.8.3 Chance coincidence

Optical counterparts that are positionally consistent with the X-ray error circles might be chance coincidences. This is significantly more likely in the dense cluster core. To estimate the average number of chance coincidences, we use the $UV_{275} - U_{336}$ CMD from the HUGS catalogue, plotted only for stars that are likely cluster members ($P_{\mu} \geq 90\%$). We then apply polygonal selection areas to roughly separate different subpopulations (Figure 4.6) using the GLUEVIZ software (Beaumont et al., 2015; Robitaille et al., 2017). There are a total of 21596 cluster members detected in the WFC3 field of view (FOV; $160'' \times 160''$), including 20256 main sequence stars, 744 evolved members, including 338 subgiants and 406 red giants, 163 blue stars ($UV_{275} - U_{336} \lesssim 0.72$), 151 red stars ($UV_{275} - U_{336} \gtrsim 0.58$), 49 blue stragglers (BSs) and 12 sub-subgiant stars (SSGs)¹².

To estimate numbers of chance coincidences for different subpopulations, we divide the cluster into a series of concentric annuli of the width of the core radius 0'.06. Stars of different subpopulations are assumed to be evenly distributed

¹²Stars that are lower than the subgiant branch but redder than the main sequence; see Leiner et al. (2017)

within each annulus, so the number of chance coincidences is roughly

$$N_{c,i} = N_{\text{tot},i} \times \frac{\overline{A_{\text{err}}}}{A_{\text{annu},i}}, \quad (4.2)$$

where $N_{c,i}$ is the number of chance coincidences within the i th annulus, $N_{\text{tot},i}$ is the corresponding total number of stars in one of the subpopulations, $\overline{A_{\text{err}}}$ is the averaged area of the 95% error region derived from the average error radius ($\approx 0.5''$) and $A_{\text{annu},i}$ is the area of the i th annulus. BS and SSG populations have small numbers of stars, so we only make the estimate over the whole WFC3 FOV, which yields $N_c \approx 1.5 \times 10^{-3}$ and $\approx 3.7 \times 10^{-4}$ for BSs and SSGs, respectively. N_c values for other populations are presented in Figure 4.7, and it is clear that N_c exhibits a general descending trend toward the cluster outskirts; specifically, N_c is roughly 10 times higher in the core than at the half-light radius for main sequence stars.

4.4 Results and Discussion

We found possible optical counterparts to 18 of the total 23 sources, of which two—MSP A and source 13—have *VLA* counterparts. In the following sections, we discuss these identifications in more details, incorporating information from multiple wavelengths for source classification.

4.4.1 A1—a qLMXB

A1, the brightest cluster source, was identified by Lugger et al. (2007) as a quiescent LMXB, due to the excellent fit of its X-ray spectrum to a hydrogen atmosphere NS model. The detailed spectral fitting of A1’s X-rays in Echiburú et al. (2020) indicates that a normal nsatmos fit gives a remarkably small radius, apparently inconsistent with current nuclear theory. Echiburú et al. (2020) suggest two possible solutions; a) the NS photosphere is composed of

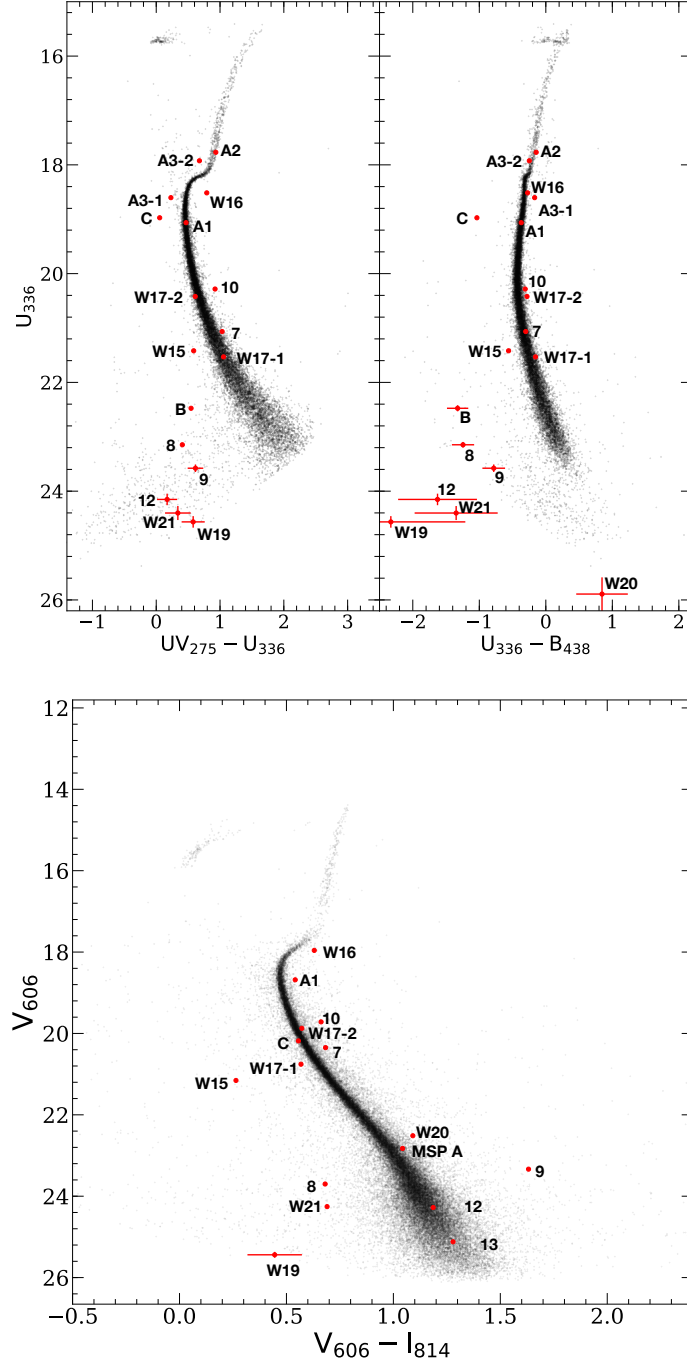


Figure 4.2: *Top*: $UV_{275} - U_{336}$ (top left) and $U_{336} - B_{438}$ (top right) CMDs plotted for stars with errors in magnitudes ≤ 0.1 (black). *Bottom*: $V_{606} - I_{814}$ CMD plotted for stars with errors in magnitudes ≤ 0.1 (black). The locations of the counterparts are marked with red dots. Counterparts with uncertainties in magnitudes greater than 0.1 (intrinsic error calculated by DOLPHOT) are plotted together with error bars.

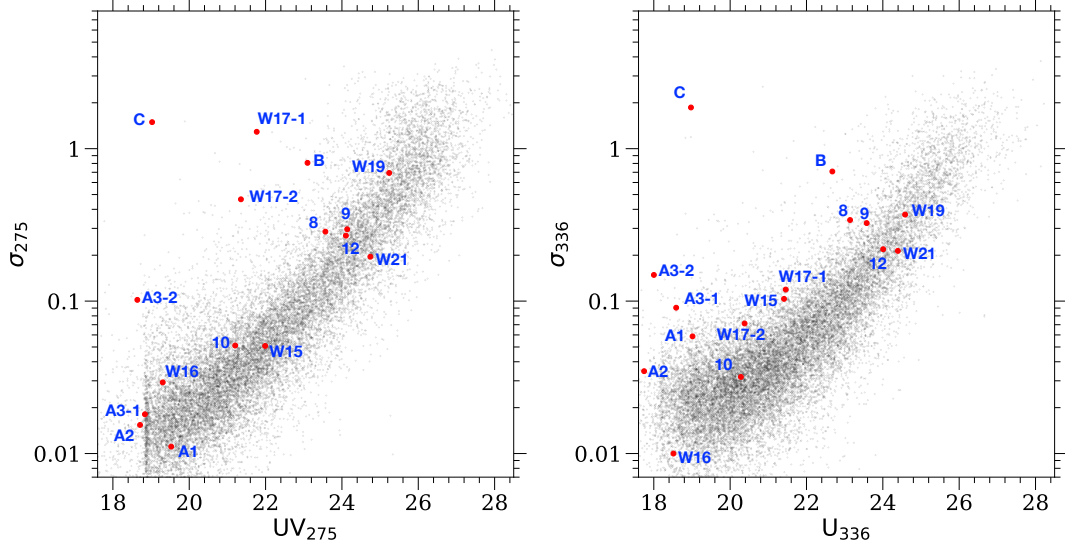


Figure 4.3: UV_{275} and U_{336} rms variability plotted against UV_{275} (left) and U_{336} (right) magnitudes. The locations of counterparts are indicated with filled red circles annotated with the corresponding source IDs. The majority of stars lie on a sequence, while stars with variability appear to be outliers.

helium (also a good spectral fit to the X-ray data), in which case the companion must be a He (or hybrid) WD; b) the NS has hot spots on its surface, which would alter the inferred NS radius (e.g. Elshamouty et al., 2016).

Lugger et al. (2007) suggested a potential counterpart to A1, which we measure to be $0.07''$ from the nominal X-ray position. It is consistent with the main sequence on the two UV CMDs, but is redwards of the main sequence in our HST/ACS $V_{606} - I_{814}$ CMD (Figure 4.2), although it is on the blue side of the main sequence in Lugger et al’s WFPC2 $V_{606} - I_{814}$ CMD. The location of A1 in the crowded core suggests that this star may be just a chance coincidence (Figure 4.7); however, the red excess in the ACS $V_{606} - I_{814}$ CMD may indicate an irradiated companion star, bloated by irradiation from the NS, or variability (compared to the WFPC2 $V_{606} - I_{814}$ CMD). Alternatively, the apparent red excess might be due to blending of a faint blue star (which is more likely to be the counterpart as suggested by Lugger et al. 2007) and a brighter unrelated star, though this would not explain the apparent change in the two $V_{606} - I_{814}$ CMDs.

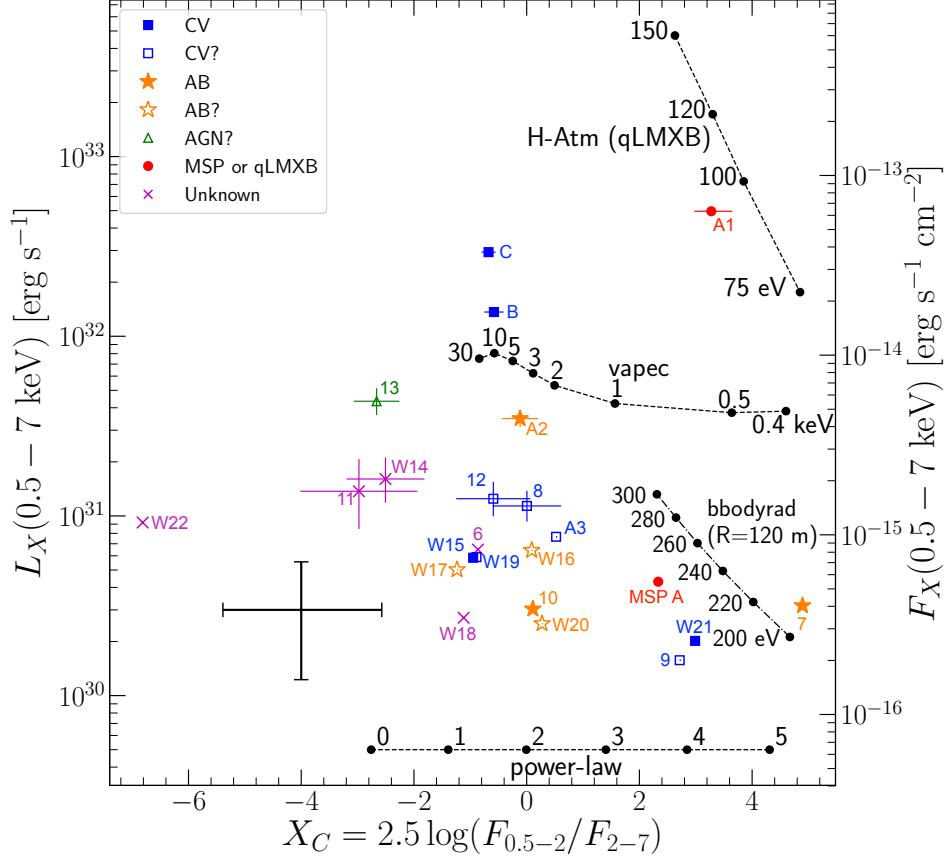


Figure 4.4: X-ray colour-magnitude diagram plotting X-ray hardness ratios defined in eq.(4.1) vs. unabsorbed model fluxes (luminosities calculated assuming the cluster distance of 8.1 kpc) from Table 4.4. Different source classes are indicated with different markers, and open markers are less certain identifications. The lines indicate locations on this plot derived from models: power-law, *vapec*, NS hydrogen atmosphere (H-Atm) of different temperatures (using a 12 km, $1.4 M_{\odot}$ NS while assuming emission from the whole NS), and blackbody *bbodyrad* of different temperatures assuming emission region of 120 m. For better readability, we only plot error bars for sources with $F(0.5 - 7 \text{ keV}) \gtrsim 1.3 \times 10^{-15} \text{ erg s}^{-1} \text{ cm}^{-2}$. Averaged uncertainties of the fainter sources are indicated by a capped error bar on the lower left of the plot. The fluxes of A1 are from the best-fitting atmospheric model in Echiburú et al. (2020).

The X-ray information can provide some constraints on the nature of the companion star. If the X-ray spectrum is indeed produced by a helium photosphere, then the companion star must be a He (or hybrid He/C-O) WD. This would exclude the suggested main sequence optical counterpart. However, if the X-ray spectrum is distorted by the presence of hot spots, then a MS com-

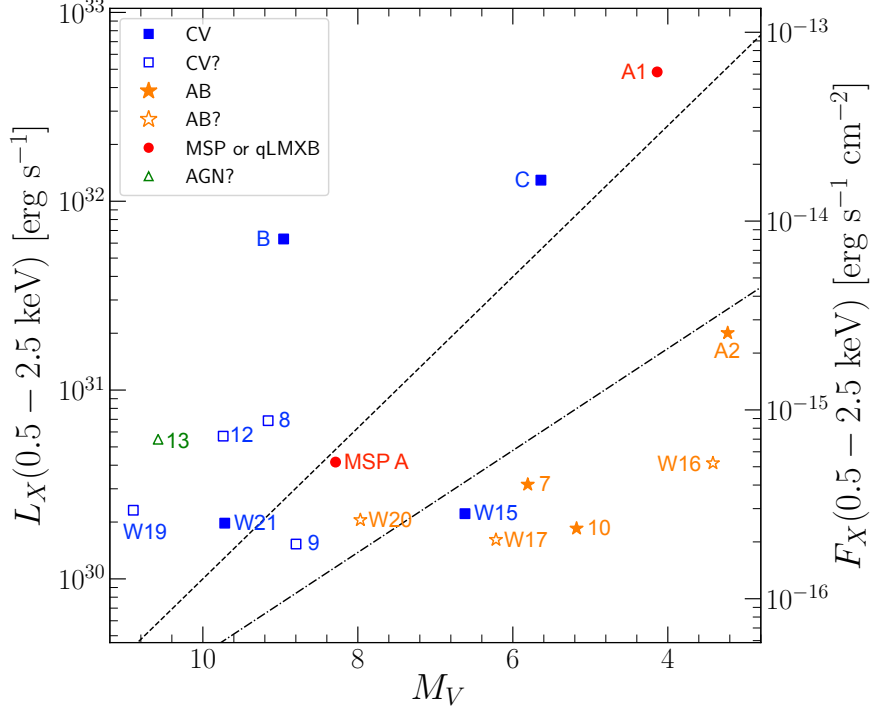


Figure 4.5: 0.5–2.5 keV X-ray luminosities vs. absolute V -band magnitudes (M_V), assuming an 8.1 kpc distance. Note that V_{555} magnitudes from Lugger et al. (2007) are used for A2 and B to derive M_V s. The short-dashed line indicates the separatrix $\log_{10} L_X[0.5 - 2.5 \text{ keV}] = -0.4M_V + 34$ from Bassa et al. (2004); the dashed-dotted line marks the upper limit of L_X for nearby ABs, which was derived by Verbunt et al. (2008) as $\log_{10} L_X[0.5 - 2.5 \text{ keV}] = 32.3 - 0.27M_V$. Open symbols are less certain identifications.

panion is possible. The similarity of this suggested companion to those of IGR J18245-2452 (Pallanca et al., 2013) and PSR J1740-5340 (Ferraro et al., 2001) raises the question of whether a transitional and/or redback MSP nature, as in those systems, is possible. Redback and transitional MSPs show hard X-ray emission, with photon index $\sim 1.0 - 1.5$, and $L_X \sim 10^{31-32} \text{ erg s}^{-1}$ (e.g. Archibald et al., 2010; Bogdanov et al., 2010; Roberts et al., 2014; Linares, 2014; Hui et al., 2014; Al Noori et al., 2018), thought to be produced by an intrabinary shock between the pulsar and companion wind (e.g. Bogdanov et al., 2005; Romani & Sanchez, 2016; Wadiasingh et al., 2018).

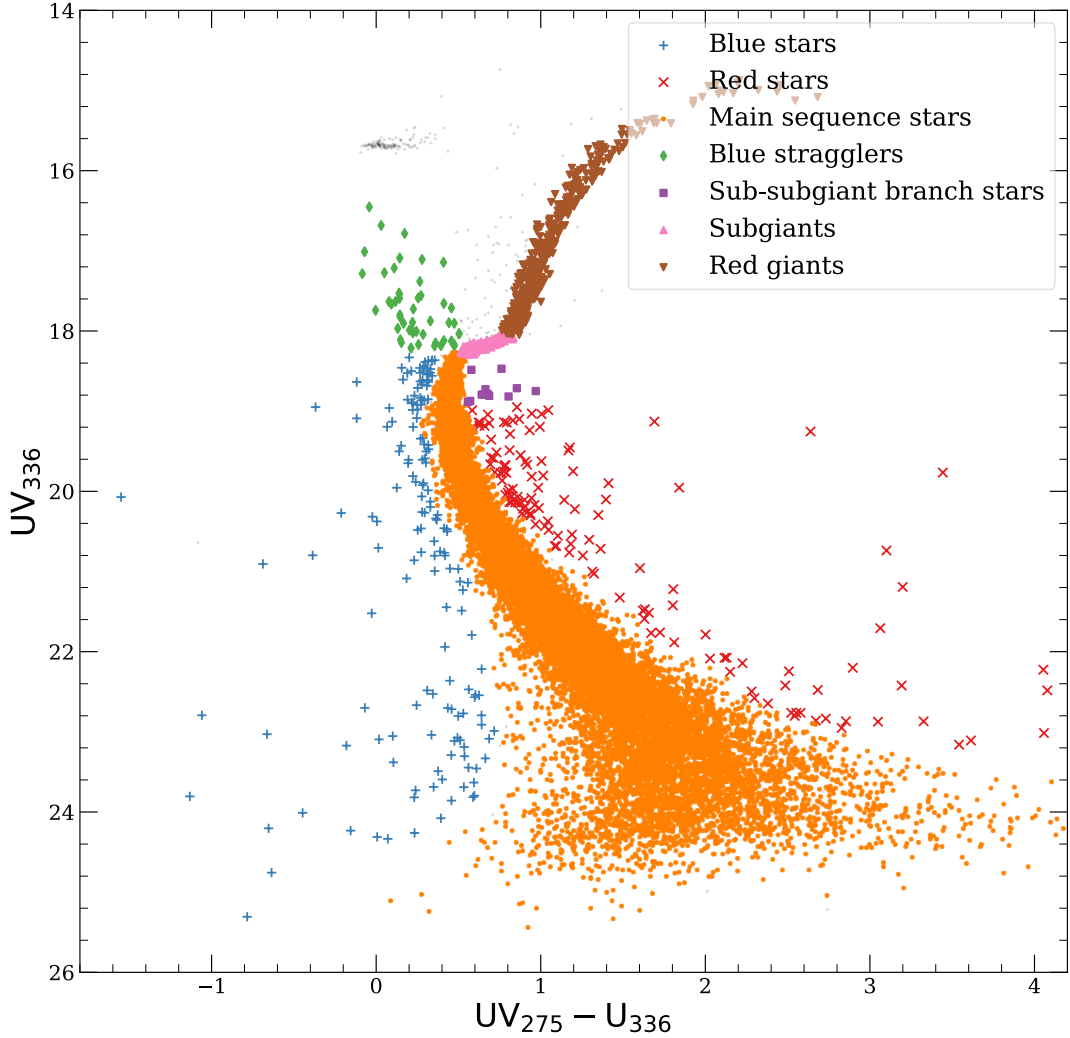


Figure 4.6: HUGS $UV_{275} - U_{336}$ CMD plotting U_{336} magnitudes vs. $U_{336} - UV_{275}$ colours for cluster members. Different subpopulations are plotted with different markers.

4.4.2 Known CVs: B and C

Both B and C were previously identified as bright CVs by Lugger et al. (2007). We confirmed the UV excesses in both $U_{336} - UV_{275}$ and $U_{336} - B_{438}$ (top panels of Figure 4.2) and found that both counterparts present significant UV variability (Figure 4.3). Spectroscopic MUSE observations (Göttgens et al., 2019, G19 hereafter) identified broad $H\alpha$ and $H\beta$ emission features from C, indicative of an accretion disc.

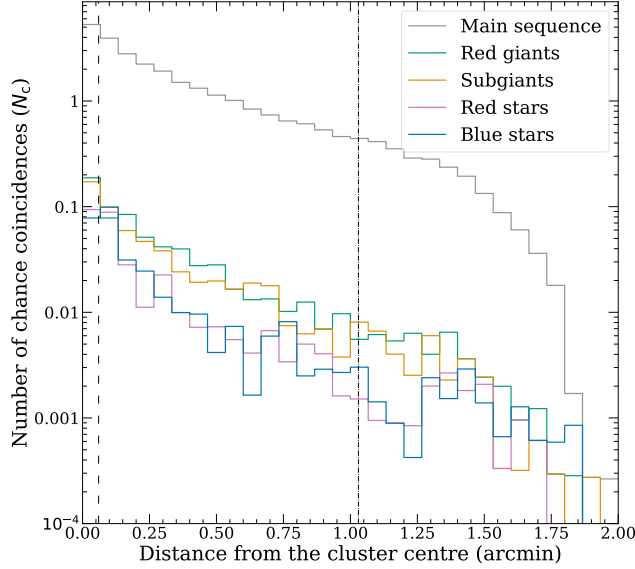


Figure 4.7: Number of chance coincidences (N_c) as defined in eq. (4.2) vs. distance from the cluster centre (in arcmin) for different subpopulations (Section 4.3.8.3). The vertical dashed and dashed-dotted lines indicate the core radius (r_c) and half-light radius (r_h). The probability of a chance coincidence with a main sequence star is significant throughout the half-light radius.

4.4.3 New faint CVs and candidates

4.4.3.1 A3

A bright potential UV counterpart, A3-1, lies $0.37''$ ($\approx 0.87P_{\text{err}}$) off the X-ray position (Figure 6). The star simultaneously exhibits marked blue and red excess in the $UV_{275} - U_{336}$ and $U_{336} - B_{438}$ CMDs, respectively (top panels of Figure 4.2). We note that the unusual colour combination might have been affected by light from the nearby bright star south to this star (Figure 6). This bright source has a U_{336} magnitude of 15.58 and is so saturated in the V_{606} and I_{814} images that photometry in these filters is not available for fainter stars nearby. However, this bright star does not show any sign of variability (with $\text{RMS}(UV_{275}) = 0.01$ at $UV_{275} = 17.13$, while $\text{RMS}(U_{336}) = 0.02$ at $U_{336} = 15.58$); the variability observed in the two fainter counterparts might not be affected by this bright object, but the WFC3 magnitudes should be interpreted with caution. Adopting this counterpart could still point to a CV

scenario, where the UV excess is from an accretion disc and/or the WD surface, while the red excess could be partly ascribed to the companion star and/or to the moderate variability in U_{336} .

Another possible counterpart, designated A3-2, lies $0.19''$ ($\approx 0.45P_{\text{err}}$) northeast of the X-ray position. This star resides at an uncommon location on the $UV_{275} - U_{336}$ CMD such that it is above the subgiant branch or slightly bluer than the red giant branch (see top panels of Figure 4.2). Again, the anomalous colour could be a result of the bright nearby star, or partly accounted for by the variability we found in both UV_{275} and U_{336} (Figure 4.3).

4.4.3.2 Sources 8, 9, 12, W15, W19, and W21

The X-ray error circle for Source 8 encloses a faint counterpart $\approx 0.11''$ ($\approx 0.31P_{\text{err}}$) from the nominal X-ray position, which exhibits marked blue excesses in both the UV and $V_{606} - I_{814}$ CMDs. The UV variability analyses revealed only moderate U_{336} variability. If we adopt this counterpart, the X-ray/optical ratio will be higher than the upper limit defined for ABs (Figure 4.5), suggesting a CV nature. Although no membership information is available, we consider source 8 likely to be a cluster member based on its position not far from the cluster centre ($\approx 7.5r_c$).

We found a faint star (R0052331) in the error circle of source 9 that resides $\approx 0.23''$ ($\approx 0.54P_{\text{err}}$) from the X-ray position. DOLPHOT suggests that this star exhibits moderate blue excesses in the two UVIS CMDs (top panels of Figure 4.2), while showing a strong red excess in the $V_{606} - I_{814}$ CMD. However, the presence of the star in the UV_{275} image is not clear by visual inspection (Figure 6), which leads us to be suspicious of the validity of the corresponding magnitude. As mentioned in Section 4.3.7, DOLPHOT uses the source list generated from the drizzle-combined U_{336} image, where R0052331 is visible, so the UV_{275} magnitude might just reflect the high background (as a result of a bright horizontal branch star northeast to R0052331) at the nominal position.

The blue excess on the $U_{336} - B_{438}$ CMD is more robust, which leads us to our classification of source 9 as a CV candidate.

The very faint counterpart to source 12 has photometric properties suggestive of a CV nature—it shows blue excesses in the UV (top panels of Figure 4.2) while being consistent with the main sequence in the optical (bottom panel of Figure 4.2). However, source 12 could be a background source, as it is 1.14' from the cluster centre, and lacks any cluster membership information. We tentatively classify source 12 as a likely CV.

We found a faint ($V_{606} = 21.16$) blue star in the error circle of W15, which shows blue excesses in all three CMDs (Figure 4.2). This counterpart has a well-determined cluster membership ($P_{\mu} = 96.7\%$), so we consider it a new confident cluster CV.

Similarly, W19 is consistent with a blue and UV bright object, which could indicate a CV nature. However, the membership is not determined through P_{μ} , so W19 could also be a background AGN. We therefore classify W19 a likely CV.

Finally, the counterpart to W21 shows blue excesses on all three CMDs (Figure 4.2) and has a well-determined cluster membership ($P_{\mu} = 95.3\%$). We thus classify it as a confident cluster CV.

4.4.4 Previously suggested ABs: sources 7 and 10

The counterpart to source 7 lies on the red side of the $UV_{275} - U_{336}$ main sequence and exhibits a red excess on the $V_{606} - I_{814}$ CMD (Figure 4.2), consistent with the binary sequence. The counterpart has a well-determined cluster membership ($P_{\mu} = 96.8\%$). Similarly, source 10's counterpart is above the main sequence in both $UV_{275} - U_{336}$ and $V_{606} - I_{814}$ CMDs, also a cluster member ($P_{\mu} = 98.1\%$). Both sources were classified as cluster AB candidates by Lugger et al. (2007); now with confirmed association with the cluster, we classify them as more confident ABs.

4.4.5 New ABs and candidates

4.4.5.1 A2

The counterpart suggested by Lugger et al. (2007) is a bright star that exhibits definite blue excesses on both $U - V$ and $V - I$ CMDs, $0.25''$ ($\approx 0.78P_{\text{err}}$) southeast of the nominal X-ray position (Figure 6). However, the VLT/MUSE spectroscopic study by G19 suggest another star that shows variable $\text{H}\alpha$ emission feature as the counterpart. This star lies 3 times closer ($\approx 0.09''$ or $\approx 0.27P_{\text{err}}$) to the X-ray position (Figure 6), and is photometrically consistent with a slightly evolved red giant in the $UV_{275} - U_{336}$ CMD (top panels of Figure 4.2). If we adopt this as the counterpart, the locus of A2 on the $L_X - M_V$ plane is below the separatrix (Figure 4.5), viz. X-ray fainter but optically brighter than cluster CVs, indicating an RS CVn nature. The position of A2 in the core would give rise to a moderate average number of chance coincidences with red giants (≈ 0.2 ; see Figure 4.6); however, red giants with a variable $\text{H}\alpha$ emission feature are rare. We thus keep this star as the counterpart and conclude that A2 is an RS CVn type of AB.

4.4.5.2 W16

The counterpart to W16 is consistent with a cluster ($P_\mu = 97.5\%$) sub-subgiant in $UV_{275} - U_{336}$ and $V_{606} - I_{814}$. Sub-subgiants are rare, so this counterpart is very unlikely to be a chance coincidence (Section 4.3.8). Moreover, G19 noted a variable $\text{H}\alpha$ absorption feature from this sub-subgiant, which further corroborates it as the actual counterpart.

Sub-subgiants are typically X-ray sources with 0.5–2.5 keV X-ray luminosity of $\sim 10^{30-31}$ erg s $^{-1}$ (Geller et al., 2017b). Corresponding to the high stellar densities in the core, GC sub-subgiants are thought to be products of binary evolution or close encounters (Albrow et al., 2001; Geller et al., 2017a). Indeed, they have been seen in multiple source classes. For example, the MSP PSR

J1740–5340 in the GC NGC 6397 has a well-determined sub-subgiant counterpart that exhibits clear $H\alpha$ variability (Sabbi et al., 2003). Shishkovsky et al. (2018) found a sub-subgiant counterpart (on their $UV_{275} - U_{336}$ CMD) with double-peaked $H\alpha$ emission lines to an X-ray source in M10, also associated with a flat-to-inverted radio source. This object was considered to be a candidate accreting BH, or other exotic binary source. For W16, a BH interpretation is not likely with the absence of radio counterpart; absorption instead of emission features argue against the presence of a disc, and the lack of UV excess (top panels of Figure 4.2) contradicts a CV nature. Among the common source classes in GCs, W16 is more likely an RS CVn type of AB.

4.4.5.3 W17

The two possible counterparts to W17 (W17-1 and W17-2) were selected based on their marked UV_{275} variability (Figure 4.3). These two sources are located close to each other, with W17-2 brighter in all bands (Table 4.6) and closer to the X-ray position ($0.12''$ vs. $0.19''$). W17-1 appears to be consistent with the main sequence in the UVIS CMDs but shows a moderate blue excess in the $V_{606} - I_{814}$ CMD (Figure 4.2), while W17-2 shows a slight red excess in the $U_{336} - B_{438}$ and $V_{606} - I_{814}$ CMDs. In the individual UV_{275} images, most of W17-1’s PSF overlaps the chip gap in the third exposure, so its apparent variability may be spurious.

Given the uncertainty in the UV variability of W17-1 and W17-2, we have investigated the optical variability of these objects, using the WFPC2 V_{555} images from the GO-7379 dataset. There are a total of 48 images, of which 33 are 23s exposures, 4 are 100s exposures, and 11 are 3s exposures. The two stars can be seen in the 23s and 100s exposures, but are not visible in the 3s exposures. We used FIND and PHOT in DAOPHOT II to do aperture photometry on the 23s and 100s exposures. While FIND is able to detect W17-2 in the 23s exposures, it does not detect W17-1. Thus, we added W17-1 into

the object lists based on its spatial offset from W17-2. We used DAOMATCH and DAOMASTER to correlate the photometry from the 33 23s exposures and to compute the mean magnitude and σ for each object. Similar to Figure 4.3, in Figure 4.8, we present a plot of σ vs. mean V_{555} magnitude, which gives a measure of variability. Both W17-1 and W17-2 show a deviation from the mean σ -magnitude relation, indicating variability, with the signal stronger for W17-2. The mild blue excess in the $V_{606} - I_{814}$ CMD might therefore be a result of this variability.

The lack of blue excess in the UV CMDs and the main sequence counterpart together hint at an AB nature for W17. We argue that W17 is likely a BY Dra system with variability caused by orbital motion.

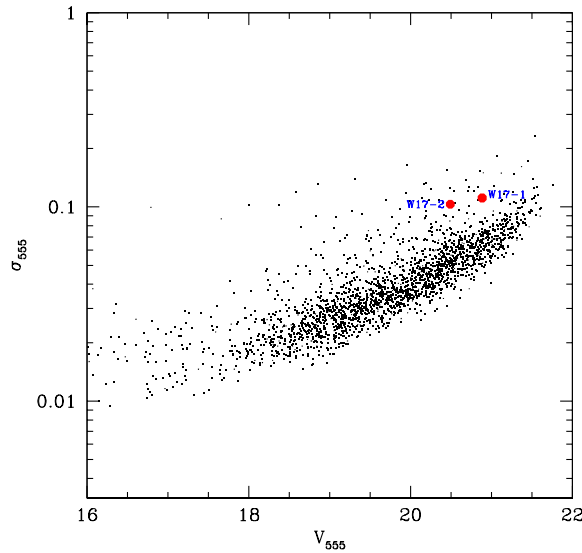


Figure 4.8: WFPC2 V_{555} rms plotted versus V_{555} magnitudes. W17-1 and W17-2 are apparently outliers to the bulk of stars, indicating marked variability.

4.4.5.4 W20

W20 lies above the main sequence on the $V_{606} - I_{814}$ CMD, but does not have a confirmed membership, so it is also possible to be a faint foreground star. We thus classify W20 as an AB candidate.

4.4.6 MSP A

MSP A (PSR J2140–2310A) is an eclipsing pulsar with a spin period of 11 ms, a 4-hour orbit, and a 0.1–0.2 M_{\odot} companion, discovered at 1.4 GHz by the *Green Bank Telescope*; *GBT* (Ransom et al. 2004; R04 hereafter). Our 4.9 GHz *VLA* observation detected a point source (ID: VLA 44) which is 0.12'' south of the *GBT* timing position, with displacements ($VLA - GBT$) in RA and DEC of $-0.016 \pm 0.028''$ and $0.116 \pm 0.051''$, respectively (uncertainties are calculated by adding the errors from the *VLA* and *GBT* in quadrature). The two observations are separated by roughly 13.7 yr, so the inconsistency of source positions might be a result of proper motion. Indeed, the displacements correspond to velocities, in RA and DEC, of -1.18 ± 2.03 mas yr $^{-1}$ and -8.44 ± 3.71 mas yr $^{-1}$, respectively. These are consistent with the GAIA-measured PM of the cluster ($\mu_{\alpha} = -0.7017 \pm 0.0063$ mas yr $^{-1}$, and $\mu_{\delta} = -7.2218 \pm 0.0055$ mas yr $^{-1}$; see Gaia Collaboration et al. 2018b).

The 4.9 GHz $S_{\nu} = 11.3$ μ Jy, but the source was not detected in the 7 GHz band ($S_{\nu} < 4.8$ μ Jy, at the 3 σ level), so we only get a very rough constraint on the spectral index: $\alpha < 0$.

We also detect 25 counts from an X-ray source 0.23'' from the *VLA* position (previously suggested by R04 on the basis of 5 counts). The X-ray spectrum can be modelled with an absorbed `bbbodyrad` or `pow` model. The former yields a temperature of 0.3 ± 0.1 keV but an unconstrained emission radius; the `pow` model results in a photon index $\Gamma = 2.9 \pm 0.9$, consistent with the photon index range observed in faint MSPs (Table 4.4).

Indeed, either model should be physically possible as we expect both thermal emission from the NS surface, and non-thermal emission resulting from accelerated particles between the interacting pulsar and companion winds (see e.g., Harding & Gaisser, 1990; Arons & Tavani, 1993; Romani & Sanchez, 2016). The inferred blackbody parameters, and 0.5–10 keV L_X of 4×10^{30} erg s $^{-1}$, are consistent with thermal emission from MSPs in other GCs (Bogdanov et al.,

2006; Forestell et al., 2014).

R04 inspected 1676 s WFPC2 observations (GO-7379) and reported V_{555} detections and I_{814} nondetections of a faint counterpart, indicating that the object is either on or bluer than the main sequence. We re-examined the co-added WFPC images, where the faint counterpart is only visible by visual inspection, so our DAOPHOT routine (Section 4.4.5.3) did not measure its magnitudes. We therefore manually run aperture photometry on the faint star, finding $V_{555} - I_{814} = 0.8 \pm 0.6$. This is consistent with the ACS result.

4.4.7 Unclassified sources and likely AGN

The sources that do not have a likely counterpart are 6, 11, W14, W18, and W22. These sources only have stars that are consistent with the main sequence in one or multiple CMDs. We leave them unclassified in our catalogue but tentatively discuss their possible nature in this section.

The two main sequence stars in source 6’s error circle may be chance coincidences, considering the relatively high number of chance coincidences (≈ 2) expected near the cluster centre (Figure 4.7). Fitting an `apec` model to source 6’s X-ray spectrum does not constrain N_{H} , so we fixed it to the cluster value (Section 4.3). We note a likely emission feature at ~ 1.9 keV (Figure 4.9), which does not match any emission feature at the cluster abundances. One possible explanation is that source 6 is extragalactic, so this line could be a redshifted Fe K- α emission line.

Compared to source 6, W18 and W22 are farther from the cluster core, so their main sequence counterparts are less likely to be chance coincidences ($N_{\text{c}} \approx 0.7$ and ≈ 1 for W18 and W22, respectively). There are three sources in W18’s error circle, two blended together, all of which are consistent with the main sequence. If the two stars were associated, we might further classify W18 a likely BY Dra type of AB.

The 3 stars in W22’s error circle are also consistent with the main sequence.

However, unlike W18, W22 has a very hard X-ray spectrum (no counts in 0.5–2 keV; Figure 4.4) which is not seen in faint cluster ABs. We thus suspect that none of the main sequence stars are the true counterpart, and consider W22 a likely AGN. Sources 11 and W14 are also rather spectrally hard (Figure 4.4), suggesting enhanced absorption and thus likely an extragalactic nature.

There is a more definite AGN candidate—source 13—which has a steep-spectrum ($\alpha = -1.44_{-0.17}^{+0.16}$) radio counterpart (VLA6) and, like sources 11, W14 and W22, shows a very hard X-ray spectrum. There is a very faint optical counterpart (within the radio error circle) that is marginally detected in the V_{606} and I_{814} bands (Figure 6). Another nearby radio source, VLA29, lies $1.6''$ ($\approx 1.7P_{\text{err}}$) southwest of source 13’s X-ray position. VLA29 may also be associated with X-ray source 13 and VLA6, such as a radio lobe from a central AGN. The optical source appears to be consistent with the main sequence (bottom panel of Figure 4.2); however, the radio-optical match with a tiny radio error circle suggests that this counterpart is very unlikely to be a chance coincidence. Overall, the hard X-ray spectrum, large offset from the cluster center, and radio counterpart together hint at an extragalactic nature of source 13.

Finally, we can estimate the predicted number of AGN in our field, and compare it with the number of likely AGN we see. We apply a 0.5–2 keV flux limit of 1.1×10^{-16} erg s $^{-1}$ cm $^{-2}$ (from the faintest source detectable by `wavdetect` on the 0.5–2 keV image given the threshold parameter in Section 4.3). The expected number of AGN within a radius of 1.15’ (our search radius) is 4_{-2}^{+4} according to the empirical formula from Mateos et al. (2008)¹³; this number is consistent with the number of likely AGN (6, 11, 13, W14, and W22) we have found in our catalogue.

¹³The errors correspond to 90% confidence levels, according to Gehrels (1986).

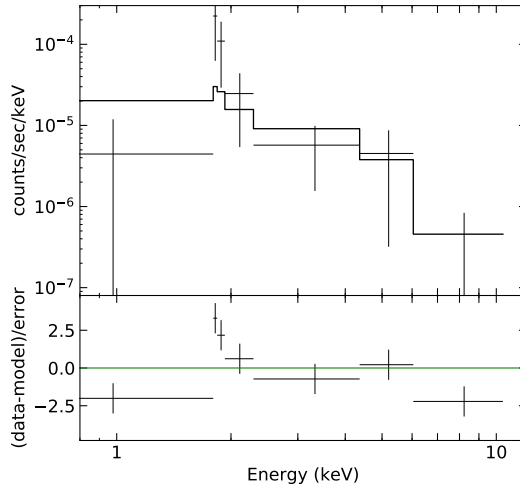


Figure 4.9: *Top*: X-ray spectrum of source 6 fitted with a `vpec` model (the spectrum is rebinned for better readability). *Bottom*: fitting residuals; a likely emission feature is present around 1.9 keV.

4.4.8 Spatial distribution of different source classes

In order to study the spatial distribution of the *Chandra* sources detected in M30, we followed the analysis methods of Cohn et al. (2010) and Lugger et al. (2017). We first fit a “generalised King model” (also known as a cored power law) of the form,

$$S(r) = S_0 \left[1 + \left(\frac{r}{r_0} \right)^2 \right]^{\alpha/2}, \quad (4.3)$$

to a main sequence turnoff (MSTO) sample, defined as stars in the HUGS database within 0.5 mag in V_{606} of the MSTO magnitude. We adopted the HUGS determination of the cluster centre. We chose the HUGS star counts for this analysis given their greater apparent completeness, relative to the DOLPHOT counts, near the cluster centre. While we fit the unbinned star counts, we have visualised the binned radial profile with the model fit in Figure 4.10. The central cusp in the profile is visible as a correlated deviation from the model fit within about $20''$ of the cluster centre. Nonetheless, the model gives a reasonable approximation to the profile within the half-light radius and provides a basis for comparison with other object groups.

We next considered several different source samples including all CVs plus the qLMXB A1, bright CVs, faint CVs, and ABs, in order to determine the characteristic masses for these samples. In defining the bright and faint samples, we may either use the optical magnitude or the X-ray flux. We have chosen the former in our previous work on NGC 6397 and NGC 6752 (Cohn et al., 2010; Lugger et al., 2017). Doing so resulted in two well-defined samples in each cluster. We note that the identifications in M30 of A1 (the qLMXB) and A3 with bright optical objects are less certain than the other identifications. In any case, these two objects have high X-ray fluxes, so would be placed in the bright group if the selection were alternatively based on X-ray flux. Using B_{438} magnitude, the bright CV group is comprised of A1, A3-1, C, and W15, and the faint CV group is comprised of B, 8, 9, W19, and W21. We note that we excluded W12, since it lies outside of the half-light radius and thus has a higher likelihood of being an AGN. As can be seen in Figure 4.11, the bright CVs have a more centrally concentrated distribution than the MSTO sample, whereas the other groups are not more centrally concentrated. This is quantified by Kolmogorov-Smirnov (K-S) comparisons of the samples to the MSTO sample which are listed in Table 4.7. Only the bright CV group differs from the MSTO sample at a significant level, $p < 1\%$. A direct K-S comparison of the bright and faint CV samples indicates that they are inconsistent at the 5.3% level, which is marginally significant.

To estimate the characteristic masses of the individual groups, we fit each group with a surface density profile of the form,

$$S(r) = S_0 \left[1 + \left(\frac{r}{r_0} \right)^2 \right]^{[q(\alpha_{\text{to}}-1)+1]/2}, \quad (4.4)$$

by maximising the likelihood over $q = m/m_{\text{to}}$, where $m_{\text{to}} = 0.80 M_{\odot}$ is the assumed MSTO mass (Lugger et al., 2007), and r_0 and α_{to} are determined by the previous fit to the MSTO group. The results of the fits are given in

Table 4.7. The q values for the all CV, bright CV, and AB groups exceed unity, with the significance ratio expressed in σ . The q value excess above unity is significant only for the bright CV sample, at the 2σ level. For the faint CV group, q is less than unity, although not at a significant level.

As we found for NGC 6397 (Cohn et al., 2010) and NGC 6752 (Lugger et al., 2017), the bright CVs in M30 (in this case including one qLMXB) are more centrally concentrated than the MSTO stars, while the faint CVs and ABs are not. The implied mass for the bright CVs in M30, $1.5 \pm 0.3 M_{\odot}$, is consistent with what we found for these other two clusters. We note that the determination, in Heinke et al. (2003b), of the mean mass of 20 qLMXBs in seven clusters resulted in a value of $1.5 \pm 0.2 M_{\odot}$. Thus, the inclusion of the qLMXB A1 in the bright CV sample for M30 should not bias the determination of the typical bright CV mass. Indeed, if A1 is excluded from the bright CV sample, the mean mass is found to be $1.3 \pm 0.3 M_{\odot}$, with a mass excess above the MSTO mass significant at the 1.9σ level.

As we have discussed for NGC 6397 and NGC 6752, the finding that the bright CVs are more centrally concentrated than the faint CVs is consistent with the bright CVs representing a recently formed population that is produced by dynamical interactions near the cluster centre (Cohn et al., 2010; Lugger et al., 2017). As recently formed CVs age, the mass of the secondary decreases and the accretion rate declines, leading to a reduction in both the optical and X-ray luminosity (Howell et al., 2001). The observation of a double blue straggler sequence in M30 provides independent evidence for a recent core collapse event that has resulted in the production of dynamically formed populations (Ferraro et al., 2009). However, Belloni et al. (2019) argue that their simulations of CVs in GCs push CVs out of the core in the dynamical interaction that forms them, and prefer a mass segregation argument for the higher concentration of bright CVs.

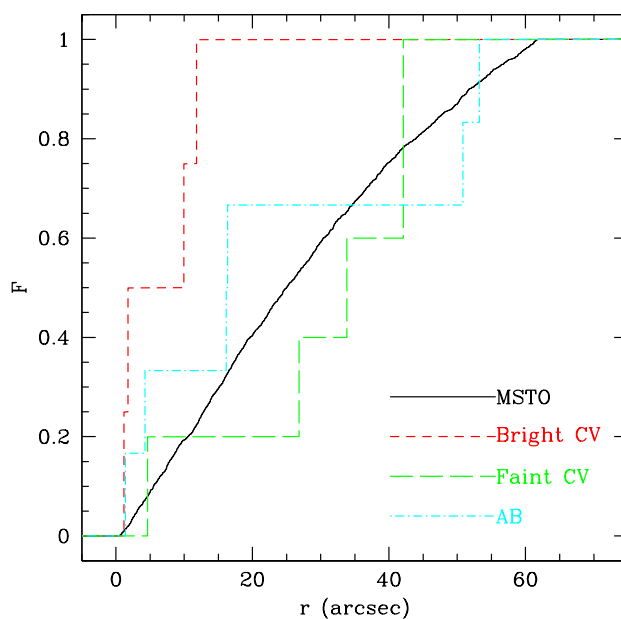


Figure 4.10: Binned radial profile of MSTO sample with a cored power law fit out to the half-light radius.

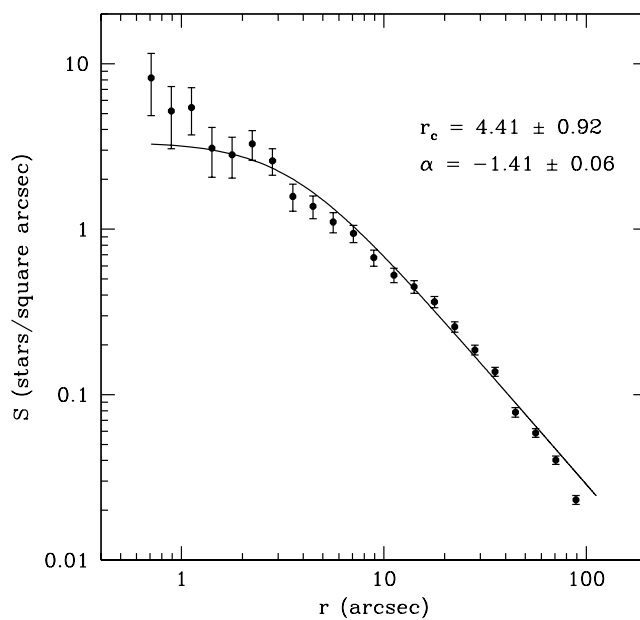


Figure 4.11: Cumulative radial distributions for selected stellar groups. Fitting information and K-S sample comparisons for these stellar groups are given in Table 4.7.

4.5 Conclusions

Our deep X-ray observation revealed a total of 10 new X-ray sources within the half-light radius, extending the original catalogue of Lugger et al. (2007) to 23 X-ray sources. Comparing X-ray positions with UV, V, and I band *HST* observations, we found optical counterparts to 18 of the 23 sources, identifying 2 new CVs (W15 and W21), 5 new CV candidates (A3, 8, 9, 12, W19), two RS CVn candidates (A2 and W16), and 2 new BY Dra candidates (W17 and W20). Cross-matching the *VLA* catalogue with our *Chandra* catalogue revealed two matches—MSP A and 13—which also match with their optical counterparts. The counterpart to MSP A lies slightly redward of the main sequence, which we interpret as a result of stripped mass from the companion star. The radio counterpart to source 13 matches a faint optical source consistent with the main sequence; but we classify 13 as a likely AGN based on its hard X-ray spectrum. The remaining 5 sources (6, 11, W14, W18, and W22) do not have definite optical counterparts, so we tentatively classify them to be extragalactic (6, 11, W14, and W22), or a faint cluster AB (W18).

Based on our classification, we performed a K-S comparison of the radial profiles of bright and faint populations. We found that bright CVs are more centrally concentrated than faint CVs. This is consistent with other core-collapsed GCs.

Table 4.3: M30 X-ray source catalogue.

ID	α (ICRS) (hh:mm:ss)	δ (ICRS) (°:′:″)	P_{err}^a (″)	Offset ^b (′)	0.5–2 keV Counts ^c	2–7 keV Counts ^c	Flux (0.5–7 keV) ^d ($\times 10^{-16}$ erg s ⁻¹ cm ⁻²)	Type ^e
A1	21:40:22.161	-23:10:46.05	0.29	0.03	2452.3 ^{+81.7} _{-81.2}	90.9 ^{+18.7} _{-13.5}	540.0 ^{+19.3} _{-18.6}	qLMBX
A2	21:40:22.213	-23:10:47.67	0.32	0.03	216.3 ^{+26.5} _{-22.4}	42.0 ^{+13.2} _{-9.0}	68.0 ^{+9.2} _{-7.0}	RS CVn?
A3	21:40:22.026	-23:10:47.62	0.42	0.02	45.6 ^{+14.3} _{-9.1}	10.3 ^{+8.5} _{-3.8}	22.2 ^{+8.0} _{-4.9}	CV?
B	21:40:22.181	-23:10:52.20	0.30	0.08	300.9 ^{+30.7} _{-27.3}	199.2 ^{+25.8} _{-21.4}	153.0 ^{+14.0} _{-11.7}	CV
C	21:40:22.954	-23:10:49.75	0.30	0.20	433.6 ^{+35.6} _{-33.2}	314.4 ^{+31.1} _{-27.6}	232.0 ^{+17.1} _{-15.2}	CV
6	21:40:21.506	-23:10:55.13	0.41	0.19	10.5 ^{+7.7} _{-4.0}	6.1 ^{+6.7} _{-2.8}	4.2 ^{+3.8} _{-1.7}	Unknown
7	21:40:21.598	-23:10:33.14	0.47	0.27	9.7 ^{+7.4} _{-3.8}	1.6 ^{+4.1} _{-1.2}	6.0 ^{+9.7} _{-2.9}	AB
8	21:40:22.123	-23:11:14.48	0.35	0.45	33.8 ^{+12.7} _{-7.6}	15.9 ^{+9.4} _{-5.0}	14.3 ^{+5.3} _{-3.0}	CV?
9	21:40:20.438	-23:10:22.95	0.42	0.56	3.6 ^{+4.9} _{-2.2}	1.9 ^{+4.1} _{-1.3}	1.5 ^{+2.6} _{-0.8}	CV?
10	21:40:23.237	-23:09:59.25	0.53	0.85	5.8 ^{+5.6} _{-3.0}	1.5 ^{+4.2} _{-1.1}	1.0 ^{+1.2} _{-0.4}	AB
11	21:40:19.384	-23:11:24.71	0.41	0.88	6.5 ^{+6.7} _{-2.9}	10.2 ^{+8.3} _{-3.7}	8.3 ^{+7.1} _{-2.9}	Unknown
12	21:40:27.029	-23:10:39.24	1.09	1.14	18.9 ^{+10.8} _{-5.2}	14.2 ^{+9.4} _{-4.4}	13.4 ^{+7.1} _{-3.5}	CV?
13	21:40:26.569	-23:11:18.81	0.97	1.15	17.0 ^{+9.9} _{-5.1}	65.1 ^{+16.4} _{-11.2}	49.1 ^{+11.8} _{-8.1}	AGN?
MSP A	21:40:22.403	-23:10:48.68	0.43	0.07	21.7 ^{+10.9} _{-5.9}	3.3 ^{+5.8} _{-1.6}	6.7 ^{+4.4} _{-1.8}	MSP
W14	21:40:25.505	-23:11:18.55	0.37	0.94	5.2 ^{+6.8} _{-2.3}	25.7 ^{+11.6} _{-6.4}	15.1 ^{+6.6} _{-3.7}	Unknown
W15	21:40:22.833	-23:10:47.50	0.43	0.17	4.0 ^{+6.0} _{-2.1}	9.5 ^{+8.0} _{-3.6}	5.3 ^{+4.8} _{-1.9}	CV
W16	21:40:20.963	-23:10:43.51	0.44	0.27	10.1 ^{+8.0} _{-3.8}	7.3 ^{+6.6} _{-3.3}	9.6 ^{+6.8} _{-3.4}	RS CVn?
W17	21:40:22.182	-23:10:43.53	0.46	0.07	17.6 ^{+10.3} _{-5.0}	10.1 ^{+8.3} _{-3.6}	12.7 ^{+6.9} _{-3.4}	AB?

Table 4.3: (Continued) M30 X-ray source catalogue.

ID	α (ICRS) (hh:mm:ss)	δ (ICRS) (°:':")	P_{err}^a (")	Offset ^b (')	Counts ^c 0.5–2 keV	Counts ^c 2–7 keV	Flux (0.5–7 keV) ^d ($\times 10^{-16}$ erg s ⁻¹ cm ⁻²)	Type ^e
W18	21:40:18.213	-23:10:39.10	0.59	0.91	1.6 ^{+4.1} _{-1.1}	3.8 ^{+6.1} _{-2.0}	1.5 ^{+2.4} _{-0.8}	Unknown
W19	21:40:23.932	-23:10:13.85	0.48	0.70	11.1 ^{+8.5} _{-3.9}	6.0 ^{+6.7} _{-2.7}	4.9 ^{+3.7} _{-1.6}	CV?
W20	21:40:24.098	-23:11:33.31	0.78	0.89	2.8 ^{+4.0} _{-2.1}	3.4 ^{+5.8} _{-1.7}	2.1 ^{+3.0} _{-0.9}	AB?
W21	21:40:25.035	-23:10:35.59	0.53	0.70	8.3 ^{+7.5} _{-3.3}	0.7 ^{+3.0} _{-0.7}	3.6 ^{+6.4} _{-2.0}	CV
W22	21:40:22.234	-23:09:50.95	0.70	0.94	< 2.3	5.4 ^{+6.4} _{-2.5}	4.5 ^{+5.8} _{-2.3}	Unknown

^a95% error radii calculated according to Hong et al. (2005).

^bOffsets from the cluster centre.

^cSource counts as calculated by `srcflux`; the errors are at the 90% confidence level.

The 90% upper limits are calculated according to Gehrels (1986).

^dModel-independent fluxes as calculated by `srcflux`; the errors are at the 90% confidence level.

^eBold texts indicate new classifications compared to Luggner et al. (2007).

Table 4.4: Results of spectral fitting to the Cycle 18 spectra.

ID	Model	N_{H}	kT^a	Γ or R_{bb}^b	$F_X(0.5-2 \text{ keV})^c$	$F_X(2-7 \text{ keV})^d$	$\chi^2_{\nu}(\text{dof})$ or Goodness
		10^{20} cm^{-2}	keV		$10^{-16} \text{ erg s}^{-1} \text{ cm}^{-2}$	$10^{-16} \text{ erg s}^{-1} \text{ cm}^{-2}$	
	XSPEC						
A2	vaptec	$< 8.0^*$	$4.1^{+4.4}_{-2.2}$	-	$21.0^{+3.1}_{-3.1}$	$23.4^{+3.5}_{-3.5}$	1.20 (11)
A3	vaptec	2.6^\dagger	$2.0^{+2.9}_{-1.0}$	-	$6.0^{+2.1}_{-1.7}$	$3.7^{+1.3}_{-1.0}$	65.40%
B	vaptec	$< 12^*$	$10.2^{+9.8}_{-4.6}$	-	$64.2^{+5.1}_{-5.1}$	$109.6^{+8.6}_{-8.6}$	0.98 (44)
C	vaptec	$18.9^{+10.5}_{-8.5}$	$13.2^{+13.1}_{-5.2}$	-	$130.7^{+7.5}_{-7.5}$	$243.7^{+13.9}_{-13.9}$	0.85 (74)
6	vaptec	2.6^\dagger	> 2.6	-	$2.6^{+1.4}_{-1.1}$	$5.7^{+3.1}_{-2.4}$	9.30%
7	vaptec	2.6^\dagger	$0.4^{+0.5}_{-0.2}$	-	$4.0^{+3.7}_{-2.3}$	$0.04^{+0.04}_{-0.03}$	64.40%
8	vaptec	2.6^\dagger	$3.4^{+11.2}_{-1.7}$	-	$7.3^{+2.2}_{-1.9}$	$7.2^{+2.2}_{-1.8}$	40.50%
9	vaptec	2.6^\dagger	$0.7^{+44.8}_{-0.4}$	-	$1.9^{+1.8}_{-1.2}$	$0.2^{+0.2}_{-0.1}$	37.30%
10	pow	2.6^\dagger	-	2^\ddagger	$2.0^{+1.6}_{-1.1}$	$1.8^{+1.5}_{-1.0}$	25.60%
11	pow	2.6^\dagger	-	$-0.2^{+0.9}_{-1.0}$	$1.1^{+0.6}_{-0.4}$	$16.4^{+8.9}_{-6.7}$	29.00%
12	vaptec	2.6^\dagger	$> 3.4^*$	-	$5.8^{+1.9}_{-1.6}$	$10.1^{+3.3}_{-2.8}$	65.10%
13	pow	2.6^\dagger	-	$0.0^{+0.3}_{-0.4}$	$4.4^{+0.9}_{-0.8}$	$51.0^{+10.0}_{-8.9}$	43.00%
MSP A	bbodyrad	2.6^\dagger	$0.3^{+0.1}_{-0.1}$	70^*	$4.9^{+2.1}_{-1.7}$	$0.6^{+0.2}_{-0.2}$	27.00%
MSP A	pow	2.6^\dagger	-	$2.9^{+0.9}_{-0.9}$	$6.2^{+2.6}_{-2.1}$	$1.8^{+0.7}_{-0.6}$	72.60%
W14	pow	2.6^\dagger	-	$0.2^{+0.6}_{-0.6}$	$1.9^{+0.6}_{-0.5}$	$18.6^{+6.5}_{-5.3}$	51.80%
W15	vaptec	2.6^\dagger	$> 6.6^*$	-	$2.2^{+1.2}_{-0.9}$	$5.3^{+2.8}_{-2.1}$	40.30%
W16	vaptec	2.6^\dagger	$> 1.0^*$	-	$4.3^{+1.9}_{-1.5}$	$3.9^{+1.7}_{-1.4}$	49.30%
W17	pow	2.6^\dagger	-	$1.1^{+0.9}_{-0.9}$	$1.6^{+0.9}_{-0.7}$	$4.8^{+2.8}_{-2.1}$	64.40%

Table 4.4: (Continued) Results of spectral fitting to the Cycle 18 spectra.

ID	Model	N_{H}	kT^a	Γ or R_{bb}^b	$F_{\text{X}}(0.5\text{--}2 \text{ keV})^c$	$F_{\text{X}}(2\text{--}7 \text{ keV})^d$	$\chi^2_{\nu}(\text{dof})$ or Goodness
	XSPEC	10^{20} cm^{-2}	keV		$10^{-16} \text{ erg s}^{-1} \text{ cm}^{-2}$	$10^{-16} \text{ erg s}^{-1} \text{ cm}^{-2}$	
W18	pow	2.6^{\dagger}	-	2^{\dagger}	$0.9^{+1.4}_{-0.8}$	$2.5^{+2.9}_{-1.7}$	88.40%
W19	vapec	2.6^{\dagger}	$> 2.0^*$	-	$2.3^{+1.1}_{-0.9}$	$5.2^{+2.6}_{-2.0}$	55.90%
W20	pow	2.6^{\dagger}	-	2^{\dagger}	$1.8^{+2.2}_{-1.2}$	$1.4^{+2.4}_{-1.2}$	52.80%
W21	vapec	2.6^{\dagger}	$0.6^{+3.9}_{-0.3}$	-	$2.4^{+2.1}_{-1.1}$	$0.2^{+0.1}_{-0.1}$	10.50%
W22	pow	2.6^{\dagger}	-	$-3.0^{+1.9}_{-2.6}$	$0.02^{+0.02}_{-0.01}$	$11.7^{+8.8}_{-6.1}$	67.00%

^aPlasma temperature (of the vapec) model or blackbody temperature (of the bbodyrad) model.

^b R_{bb} is the radius of the emission region (in m) derived from the bbodyrad model.

^{c,d}Unabsorbed model fluxes.

* superscripts indicate that either the upper or lower limit (or both) of the parameter is (are) unconstrained.

[†] superscripts mark parameters fixed during the fit.

Table 4.5: Parameters used in DOLPHOT.

Name	Value		Notes
	WFC3	ACS	
img_RAper	8	8	Photometry apertures
img_RSky	9, 14	9, 14	Radii of sky annulus
img_RPSF	15	15	PSF radius
img_aprad	15	10	Radius for aperture correction
SigFind	3	3	Detection threshold (σ)
UseWCS	1	1	Use WCS in alignment
Align	1	1	Offsets and re-scaling
ACSpsfType	0	1	Use Anderson PSF cores for ACS
WFC3UVISpsfType	1	0	Use Anderson PSF cores for WFC3

Table 4.6: Optical counterparts

Source ID	HUGS ID	α (ICRS)	δ (ICRS)	UV ₂₇₅	U ₃₃₆	B ₄₃₈	V ₆₀₆	I ₈₁₄	P _{μ} ^a	Comments
A1	R0002625	21:40:22.158	-23:10:46.106	19.53	19.06	19.43	18.68 [†]	18.14 [†]	72.7%	Moderate red excess in V ₆₀₆ - I ₈₁₄
A2	-	21:40:22.217	-23:10:47.603	18.70	17.77	17.91	-	-	-	Giant branch, variable H α emission (G19)
A3-1	-	21:40:22.044	-23:10:47.348	18.83	18.60	18.77	-	-	-	Blue in UV ₂₇₅ -U ₃₃₆ , red in U ₃₃₆ -B ₄₃₈
A3-2	-	21:40:22.031	-23:10:47.439	18.60	17.93	18.17	-	-	-	Bluer than the red giant branch
B	-	21:40:22.181	-23:10:52.208	23.02	22.48	23.80	-	-	-	Moderate blue excesses in UV CMDs
C	R0039782	21:40:22.956	-23:10:49.744	19.03	18.97	20.01	20.18	19.63	94.3%	Blue excesses in the UV CMDs
6	-	-	-	-	-	-	-	-	-	Only MS stars found in the error circle
7	R0047985	21:40:21.597	-23:10:33.107	22.10	21.07	21.37	20.35	19.67	96.8%	Slight red excess in V ₆₀₆ - I ₈₁₄
8	-	21:40:22.117	-23:11:14.406	23.56	23.15	24.39	23.70	23.02	-	Blue excesses in all CMDs
9	R0052331	21:40:20.434	-23:10:22.722	24.19	23.58	24.36	23.34	21.70	-	Blue excesses on the UV CMDs; red excess in V ₆₀₆ - I ₈₁₄

Table 4.6: Optical counterparts

Source ID	HUGS ID	α (ICRS)	δ (ICRS)	UV ₂₇₅	U ₃₃₆	B ₄₃₈	V ₆₀₆	I ₈₁₄	P _{μ} ^a	Comments
10	R0061582	21:40:23.227	-23:09:58.998	21.21	20.28	20.59	19.72	19.05	98.1%	Red excess in V ₆₀₆ - I ₈₁₄ and UV ₂₇₅ -U ₃₃₆
11	-	-	-	-	-	-	-	-	-	Only MS stars found in the error circle
12	R0044536	21:40:27.037	-23:10:39.176	24.32	24.15	25.78	24.28	23.09	-	Blue in UV CMDs, on MS in V ₆₀₆ -I ₈₁₄
13	R0022851	21:40:26.573	-23:11:18.828	-	-	-	25.12	23.84	-	MS counterpart consistent with the <i>VLA</i> position
MSP A	R0040403	21:40:22.404	-23:10:48.957	-	-	-	22.83 [†]	21.78 [†]	-	MS counterpart consistent with the <i>VLA</i> position
W14	-	-	-	-	-	-	-	-	-	Only MS stars found in the error circle
W15	R0039800	21:40:22.834	-23:10:47.624	22.01	21.42	21.98	21.16 [†]	20.89 [†]	96.7%	Blue excesses in all CMDs
W16	R0002852	21:40:20.965	-23:10:43.414	19.31	18.52	18.79	17.96	17.33	97.5%	A sub-subgiant
W17-1	R0043137	21:40:22.177	-23:10:43.350	22.59	21.53	21.69	20.76 [†]	20.19 [†]	91.3%	Slightly blue in V ₆₀₆ - I ₈₁₄ , MS in UV CMDs
W17-2	R0043073	21:40:22.174	-23:10:43.470	21.03	20.42	20.70	19.87 [†]	19.30 [†]	98.1%	MS in all CMDs; variable in UV
W18	-	-	-	-	-	-	-	-	-	Blended source consisting of two faint MS stars
W19	-	21:40:23.932	-23:10:13.755	25.14	24.57	26.90	25.44	25.00	-	A faint star with blue excess on all CMDs; large photometric errors

Table 4.6: Optical counterparts

Source ID	HUGS ID	α (ICRS)	δ (ICRS)	UV ₂₇₅	U ₃₃₆	B ₄₃₈	V ₆₀₆	I ₈₁₄	P $_{\mu}^a$	Comments
W20	R0017878	21:40:24.143	-23:11:33.304	-	25.89	25.05	22.51	21.42	-	Moderate red excess in V ₆₀₆ - I ₈₁₄
W21	R0046432	21:40:25.026	-23:10:35.644	24.74	24.40	25.75	24.26	23.57	95.3%	Blue excesses in all CMDs
W22	-	-	-	-	-	-	-	-	-	Only MS stars found in the error circle

^aMembership probabilities from the HUGS catalogue.

† indicates magnitudes from the HUGS catalogue that are calibrated to our DOLPHOT photometry.

Table 4.7: Cored-Power-Law Model Fit Results

Sample	N^a	q	$r_c (")$	α	$m (M_\odot)$	σ^b	K-S prob ^c
MSTO	1881	1.0	4.4 ± 0.9	-1.41 ± 0.06	0.80 ± 0.05
all CV	9	1.28 ± 0.19	3.3 ± 0.5	-2.09 ± 0.47	1.02 ± 0.15	1.5	10%
bright CV	4	1.85 ± 0.42	2.4 ± 0.4	-3.45 ± 1.01	1.48 ± 0.34	2.0	0.68%
faint CV	5	0.90 ± 0.27	5.2 ± 4.9	-1.16 ± 0.65	0.72 ± 0.22	-0.4	55%
AB	6	1.20 ± 0.24	3.6 ± 0.9	-1.89 ± 0.58	0.96 ± 0.19	0.8	42%

^aSize of sample within $61''8$ of cluster centre

^bSignificance of mass excess above MSTO mass in sigmas

^cK-S probability of consistency with MSTO group

Chapter 5

The MAVERIC Survey: Dynamical Origin of Radio Sources in Galactic Globular Clusters

Yue Zhao¹, Craig O. Heinke¹, Laura Shishkovsky², Jay Strader², Laura Chomiuk², Thomas J. Maccarone³, Arash Bahramian⁴, Gregory R. Sivakoff¹, James C. A. Miller-Jones⁴, Evangelia Tremou⁵,

¹Department of Physics, University of Alberta, CCIS 4-183, Edmonton, AB T6G 2E1, Canada ²Center for Data Intensive and Time Domain Astronomy, Department of Physics and Astronomy, Michigan State University, East Lansing, MI 48824, USA ³Department of Physics & Astronomy, Texas Tech University, Box 41051, Lubbock, TX 79409-1051, USA ⁴International Centre for Radio Astronomy Research-Curtin University, GPO Box U1987, Perth, WA 6845, Australia ⁵LESIA, Observatoire de Paris, CNRS, PSL, SU/UPD, Meudon, France

This chapter details the work published in Zhao et al. 2021b, titled “The

MAVERIC Survey: Dynamical Origin of Radio Sources in Galactic Globular Clusters”, *ApJ*, 914, 7, DOI: 10.3847/1538-4357/abfc58, where we take census of background-corrected numbers of radio sources in different globular clusters, and investigate how radio source counts are dependent on globular cluster parameters.

Abstract

We investigate potential correlations between radio source counts (after background corrections) of 22 Galactic globular clusters (GCs) from the MAVERIC survey, and stellar encounter rates (Γ) and masses (M) of the GCs. Applying a radio luminosity limit of $L_{\text{lim}} = 5.0 \times 10^{27} \text{ erg s}^{-1}$, we take a census of radio sources in the core and those within the half-light radius, of each cluster. By following a maximum likelihood method and adopting a simplified linear model, we find an unambiguous dependence of core radio source counts on Γ and/or M at 90% confidence, but no clear dependence of source counts within the half-light radius on either Γ or M . Five of the identified radio sources in GC cores above our adopted limit are millisecond pulsars or neutron star X-ray binaries (XRBs), the dependence of which on Γ is well-known, but another is a published black hole (BH) XRB candidate, and ten others are not identified; Accounting for these verified cluster members increases the significance of correlation with M and/or Γ (to 99% confidence), for fits to core and half-light region source counts, while excluding a dependence on Γ alone at 90% (core) and 68% (half-light) confidence. This is consistent with published dynamical simulations of GC BH interactions that argue Γ will be a poor predictor of the distribution of accreting BHs in GCs. Future multiwavelength follow-up to verify cluster membership will enable stronger constraints on the dependence of radio source classes on cluster properties, promising a new view on the dynamics of BHs in GCs.

5.1 Introduction

Since the launch of early X-ray missions like *Uhuru* and *OSO-7*, it has been known that Galactic globular clusters (GCs) host an overabundance of X-ray sources (Katz, 1975). These X-ray sources are ascribed to close binaries of various kinds, whose origin is closely related to the dynamically active cores of GCs. Specifically, the very dense cores of GCs facilitate many close dynamical encounters, producing close binaries through multiple possible channels (Clark et al., 1975; Fabian et al., 1975; Sutantyo, 1975; Hills, 1976). The most well-studied population is comprised of low-mass X-ray binaries (LMXBs), where neutron stars (NSs) or black holes (BHs) accrete matter from (usually) a (near) main-sequence donor star (Lewin & Joss, 1983; Grindlay et al., 1984). LMXBs were discovered to dominate the bright X-ray source population, with typical X-ray luminosities $L_X \sim 10^{36-38} \text{ erg s}^{-1}$ (Giacconi et al., 1974; Clark et al., 1975; Canizares & Neighbours, 1975).

With the advent of the *Chandra X-ray Observatory's* superior sensitivity and angular resolution, a plethora of faint ($L_X \lesssim 10^{33} \text{ erg s}^{-1}$) sources were detected in many GCs (e.g., Grindlay et al., 2001a,b; Pooley et al., 2002a,b; Bassa et al., 2004; Heinke et al., 2005b, 2006; Bassa et al., 2008; Lu et al., 2009; Zhao et al., 2019). Some of these faint sources are thought to be quiescent LMXBs (qLMXBs), which are generally $\lesssim 10^4$ times fainter than actively accreting LMXBs (e.g., Campana et al., 1998; Rutledge et al., 2002; Heinke et al., 2003a). Closely related to LMXBs are the millisecond pulsars (MSPs); these are fast-spinning radio pulsars spun up by accreted matter from donor stars during a prior LMXB phase (Bhattacharya & van den Heuvel, 1991). MSPs emit thermal or non-thermal X-rays, and also contribute to the faint source population, especially below $10^{31} \text{ erg s}^{-1}$ (Saito et al., 1997; Bogdanov et al., 2006). A majority of the faint X-ray population between $10^{31} < L_X < 10^{32} \text{ erg s}^{-1}$ is comprised of cataclysmic variables (CVs), which are accreting white

dwarfs in close orbit with normal stars (Hertz & Grindlay, 1983b; Cool et al., 1995; Pooley et al., 2002a; Cohn et al., 2010; Rivera Sandoval et al., 2018). Finally, chromospherically active binaries (ABs), which are tidally-locked close binaries of normal or evolved stars, are very common in GCs below 10^{31} erg s⁻¹ (Bailyn et al., 1990; Dempsey et al., 1993; Grindlay et al., 2001a; Bassa et al., 2004; Heinke et al., 2005b). The LMXB and MSP populations, along with the brighter CVs, are closely correlated with the frequency of dynamical encounters, quantified by the stellar encounter rate (Verbunt & Hut, 1987; Johnston et al., 1992; Verbunt, 2003; Pooley et al., 2003; Heinke et al., 2003a; Pooley & Hut, 2006; Hui et al., 2010; Bahramian et al., 2013; Heinke et al., 2020). However, other X-ray sources are not of dynamical origin; most ABs descend from primordial binaries (Bassa et al., 2004, 2008; Huang et al., 2010; Cheng et al., 2018), as do many CVs (Davies, 1997; Kong et al., 2006; Ivanova et al., 2006; Belloni et al., 2019).

Binaries containing BHs may not be distributed in the same way as those containing NSs, as the numbers of BHs remaining in different GCs, and their level of mixture with other stars, may vary in complicated ways. Early theoretical calculations suggested that dynamical interactions involving BHs would quickly expel all, or nearly all, BHs from GCs (Sigurdsson & Hernquist, 1993; Kulkarni et al., 1993). However, observations of candidate BH X-ray binaries in extragalactic (Maccarone et al., 2007) and Galactic GCs (Strader et al., 2012), along with GC simulations that left numerous BHs in clusters (Morscher et al., 2013; Sippel & Hurley, 2013; Heggie & Giersz, 2014; Morscher et al., 2015), changed the prevailing wisdom. There is now solid dynamical evidence of three (noninteracting) BH binaries in the GC NGC 3201 (Giesers et al., 2018, 2019). Current GC simulations predict large numbers of BHs in clusters with relatively little mass segregation (Peuten et al., 2016; Askar et al., 2018; Weatherford et al., 2018, 2020), though the number of detectable BHs in binary systems with other stars is not predicted to correlate with the total number of BHs in

the clusters (Kremer et al., 2018; Arca Sedda et al., 2018; Askar et al., 2018).

The MAVERIC (*Milky way ATCA and VLA Exploration of Radio sources In Clusters*) survey involves deep radio imaging of 50 Galactic GCs (see Tremou et al. 2018, Shishkovsky et al. 2020, Sh20 hereafter, and Tudor et al. in prep.), dedicated to discovery of potential BH LMXBs and other exotic radio sources. The key motivation is that accreting BHs are more radio-luminous for a given X-ray luminosity than other systems (Maccarone, 2005; Migliari & Fender, 2006), making deep radio surveys an excellent method to find candidate BHs. Thanks to the superior sensitivity and sub-arcsecond resolving power of the *Karl G. Jansky Very Large Array (VLA)* and the *Australia Telescope Compact Array (ATCA)*, it has led to fruitful revelations of faint radio sources that are strong candidate BH LMXBs (Strader et al., 2012; Chomiuk et al., 2013; Miller-Jones et al., 2015; Bahramian et al., 2017; Shishkovsky et al., 2018; Bahramian et al., 2020), and strong candidates for MSPs not yet detected via radio pulsations (Bahramian et al., 2018; Zhao et al., 2020a; Urquhart et al., 2020). The 5σ detection limit of the observations reaches as low as $S_\nu \sim 10 \mu\text{Jy beam}^{-1}$ (S_ν is the flux density), covering different kinds of radio emitting objects in the fields of the GCs.

Of the detected radio sources, we expect a considerable fraction to be background sources (e.g., active galactic nuclei), while the sources that are actually associated with the clusters are mostly BH or NS LMXBs and MSPs. Radio emission has been observed in both NS (Migliari & Fender, 2006) and BH (Gallo et al., 2014, 2018) LMXBs, characterized by flat ($-0.5 < \alpha < 0$)¹ to inverted ($\alpha > 0$) radio spectra, while MSPs are generally steep-spectrum radio sources (Bates et al., 2013, $\alpha \approx -1.4$ with unit standard deviation). CVs and ABs may also be active radio emitters. For example, radio emission has been observed from both non-magnetic (e.g., Coppejans et al., 2015, 2016) and magnetic CVs (e.g., Barrett et al., 2017), generally fainter than from LMXBs, but

¹ α is the radio spectral index (α) defined by $S_\nu \propto \nu^\alpha$

visible at GC distances (typically a few kpc’s) during the peaks of outbursts (e.g., Mooley et al., 2017). ABs have also been observed in the radio; typically only visible at kpc distances during flares (e.g., Osten et al., 2000). One abnormal radio-emitting binary observed in the GC M10 with a low measured mass function is possibly a RS CVn type of AB, or an unusual CV, or a face-on BH LMXB (Shishkovsky et al., 2018).

It is then intriguing to investigate if there exists a dependence, similar to that revealed by X-ray observations, of radio source populations on GC dynamical parameters. In this work, we compare radio source counts of different GCs at the same luminosity cutoff, searching for correlations between the number of radio sources vs. stellar encounter rate (Γ) and/or GC mass (M). The paper is organized as follows: in §5.2, we describe the MAVERIC observations involved in this work, presenting the method we used to fit the data; in §5.3 we present results and discussions based on the results, and in §5.4, we draw conclusions.

5.2 Observations and Method

We use the *VLA* catalog of 5σ radio point sources from the MAVERIC survey (Sh20). The catalog compiles radio point sources for 25 GCs, reporting source coordinates and radio flux densities in low and high frequency bands at 5 GHz (S_{low}) and 7.2 GHz (S_{high})², respectively. For each GC, we count the numbers of radio sources within the core radius (r_c) and the half-light radius (r_h). A radio source is selected if its 5 GHz radio luminosity (L_{low}) at the host cluster distance is higher than a limiting luminosity (L_{lim}). We set $L_{\text{lim}} = 5.0 \times 10^{27}$ erg s⁻¹ to include most relatively bright radio sources, excluding only the distant GCs M2, M3, and M54, as L_{lim} converts to a limiting flux (S_{lim}) below the $< 5\sigma$ detection limit of the catalog for those clusters. The source counts and relevant

²Note that these frequencies are average central frequencies; the actual values may be slightly different between clusters.

GC parameters are summarized in Table 5.1.

To fit the data, we follow the maximum likelihood method described in Verbunt et al. (2008, V08 hereafter). We briefly outline the method here.

The number of radio sources observed within the core or half-light radius of a GC follows a Poisson distribution:

$$P(N, \mu) = \frac{\mu^N}{N!} e^{-\mu}, \quad (5.1)$$

where μ is the expected number of sources, and N is the observed number of sources. This formula applies to both the number of actual cluster members (N_c) and the number of background sources (N_b), with μ_c members or μ_b background sources expected³. μ_b is calculated for each cluster using the normalized source counts from Sh20 (see table 4 of Sh20), given in differential form $S_\nu^{2.5} dN/dS_\nu$, while applying the S_{lim} of each cluster as the lower bound of our integration. We assume that the expected number of cluster members, μ_c , is determined by Γ and cluster mass (M). Given the low numbers of sources (Table 5.1) at our designated luminosity cutoff (L_{lim}), we follow a simplified linear model as in V08, viz.

$$\mu_c = a\Gamma + bM, \quad (5.2)$$

where a and b are positive coefficients, while for convenience, we re-normalized Γ and M , taken from Table 5.1, to fractions of the Γ of M62 and the M of M14. The form of the model is based on the assumption that one expects more LMXBs and MSPs in GCs with higher Γ and/or M . The positive correlation with Γ has been tested by using census of X-ray sources from archival observations (e.g., Pooley & Hut, 2006) and radio timing surveys (Hui et al.,

³Note that here μ_c and μ_b are shorthands for the expected numbers of members and background sources; in our application, they can represent the numbers in the core (indicated by a “core” subscript) or within the half-light region (indicated by a “half” subscript) as listed in Table 5.1.

2010).

The likelihood function is then the multiplication of the joint probability, $P(N_c, \mu_c) P(N_b, \mu_b)$, over all GCs in our sample, i.e.,

$$\mathcal{L} = \prod_i P(N_{c,i}, \mu_{c,i}) P(N_{b,i}, \mu_{b,i}), \quad (5.3)$$

where i indexes the GCs. The best-fitting model is given by a combination of a and b that maximizes \mathcal{L} .

We set up a grid of a and b values ranging from 0 to 4, with a spacing of 0.02 in both a and b , and for each pair of a and b , we generate 1000 random Poisson realizations. Each realization draws a random integer as per a Poisson distribution given μ_c , which is assigned to N_c ; N_b is then calculated by subtracting N_c from the observed number of radio sources as listed in the 6th and the 7th column of Table 5.1. To use the Poisson probabilities, we keep N_c below the observed number of sources (N_{core} or N_{half}), avoiding negative N_b values; this is done by setting probability $P(N_b, \mu_b) = 0$ when N_b is negative, while keeping the total number of realizations (1000) for each pair of a and b unchanged. Zero probability leads to zero likelihood, so equivalently these realizations are excluded from the maximization of the combined likelihood (\mathcal{L}

We also perform a somewhat more constrained fit by keeping N_c to be at least the number of confirmed members in the cores ($N_{\text{m,core}}$, the 8th column in Table 5.1) or half-light regions ($N_{\text{m,half}}$, the 9th column of Table 5.1). The members include confirmed core MSPs and LMXBs listed in Table 5.2, and PSR J1701–3006A in M62, which is outside the core (Lynch et al., 2012). Similarly, realizations with $N_c < N_{\text{m,core}}$ or $N_{\text{m,half}}$ are excluded from the fit by setting $P(N_c, \mu_c) = 0$. For simplicity, this fit is referred to as the “constrained fit”—to differentiate it from the “unconstrained fit” where we only apply upper bounds on N_c (N_c less than or equal to the observed number of sources).

To plot the result and compute confidence contours, we follow the definition

of Z in V08 that

$$Z \equiv -2 [\log(\mathcal{L}) - \log(\mathcal{L})_{\max}]. \quad (5.4)$$

Confidence contours are calculated assuming that Z follows a χ^2 distribution with one degree of freedom, so the best fit ($\mathcal{L} = \mathcal{L}_{\max}$) corresponds to $Z = 0$, while the 68%, 90%, and 99% confidence intervals are where $\Delta Z = 1.00$, 2.71, and 6.63, respectively.

5.3 Results and Discussion

The resulting distributions of Z for unconstrained and constrained fits are presented in Figure 5.1 and 5.2, overplotted with confidence contours. The unconstrained fit to source counts in the core gives the best-fitting $a = 0.52$ and $b = 0.58$, excluding non-correlation ($a = b = 0$) at the 90% confidence level; whereas the best fit to source counts within the half-light region suggests no correlation: $a = b = 0$.

The constrained fit to source counts in the core consistently favors a correlation (best fit: $a = 0.10$ and $b = 1.09$), now at the 99% confidence level. Furthermore, the entire a -axis lies outside the 90% confidence contour, indicating a dependence of source counts on GC mass ($b \neq 0$) at 90% confidence. We note that the constrained fit to source counts within the half-light region (best fit: $a = 0.86$, and $b = 0.56$) also excludes non-correlation at 99% confidence, in contrast to the unconstrained fit; while it rules out the Γ -only dependence ($b = 0$) at a lower (68%) confidence level.

For both the constrained and unconstrained fits, we generate 1000 random data sets based on the best-fitting a and b and calculate the corresponding combined likelihood \mathcal{L} for each data set. We note that the maximum likelihoods corresponding to the best fits are greater than those for all random data sets; the best fits are therefore appropriate for modelling the radio source counts.

Looking at Table 5.1, we note that a few GCs (indicated with an *) show sig-

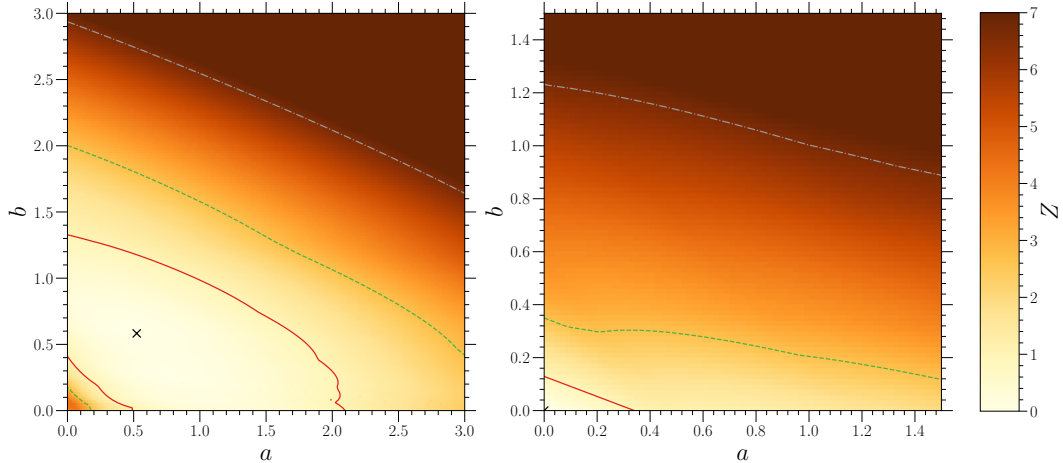


Figure 5.1: 68% (solid red), 90% (dashed green), and 99% (dashed-dotted grey) contours in the ab plane for fits to radio source counts in cluster cores (left) and half-light regions (right). The best-fitting values of a and b are indicated with a black cross in each panel. The colorbar presents intensity of Z . For source counts in the core, $a \neq 0$ or $b \neq 0$ at the 90% level, while $a = b = 0$ is consistent with the data for sources within the half-light regions.

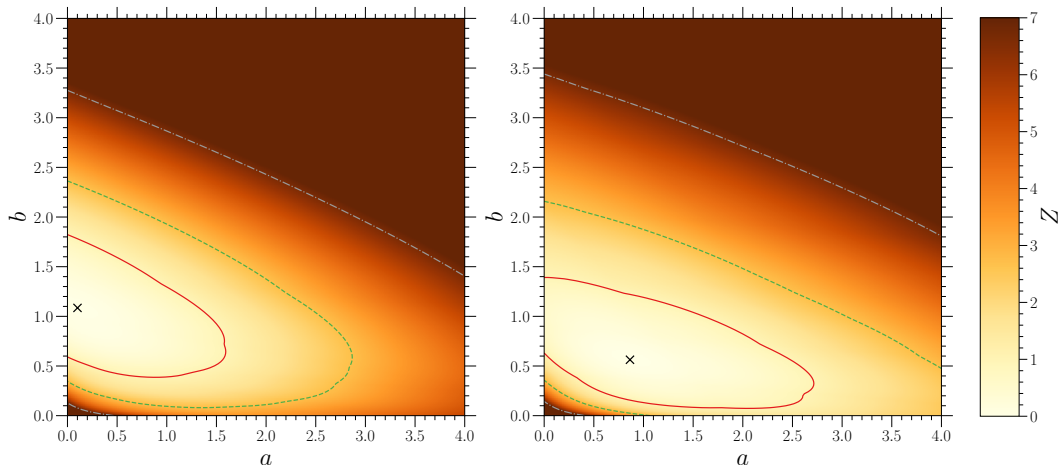


Figure 5.2: The marker and the contours are the same as those of Figure 5.1, but this fit required N_c to be equal to or greater than the number of confirmed members in the core (left) or within the half-light region (right).

nificant core source excesses over the predicted numbers of background sources (6th column vs. 10th column). Statistically, the probability of observing 1 while expecting 0.04 – 0.07 background sources (Table 5.1) is around 4% – 7% (eq. 5.1), so the excess is not very likely given by background sources. In Figure 5.3, we plot the model predicted counts using the best-fitting parameters

vs. the observed counts in the core for each GC. We also overplot error bars that indicate uncertainties propagated from the fitting parameters (a and/or b) and from the corresponding GC parameters (Γ and/or M).

Source counts within the half-light region have no clear dependence on either Γ or M (with the best-fitting a and $b = 0$), when N_c is only limited by N_{half} . However, when confirmed members are specified, the result excludes non-dependence ($a = b = 0$) at 99% confidence. Of the 6 GCs that have confirmed members, three (M62, NGC 6440, and M28) are large in both Γ and M (Table 5.1); specifying confirmed members for these GCs favors a positive correlation between μ_c and Γ and/or M , although the observed source counts (N_{half}) are generally consistent with the predicted numbers of background sources ($\mu_{b,\text{half}}$), within the 90% confidence level derived for Poisson statistics (Gehrels upper and lower limits; see Gehrels, 1986).

One exception is M14—the observed half-light region source count (14) is consistent with the background estimate (5.71) at a higher, 98%, confidence level, considering the Gehrels upper limit. We note that M14 has the lowest S_{lim} of $\approx 9.2 \mu\text{Jy}$, and for all GCs but M14, S_{lim} is above the very first flux bin of Sh20’s radio source counts (between $7.90 \mu\text{Jy}$ and $10.61 \mu\text{Jy}$; see table 4 of Sh20). For M14, part of this bin goes below the 5σ flux limit of the observation ($\approx 9 \mu\text{Jy}$). Including this flux bin in the integration will incorporate faint sources, between 9 and $10.61 \mu\text{Jy}$, so gives a somewhat higher background estimate (7.82) for M14. However, the first flux bin also misses faint sources between $7.9 \mu\text{Jy}$ and $9 \mu\text{Jy}$. It is hence clear that the expected number of background sources ($\mu_{b,\text{half}}$) might have been underestimated for M14 even when the first flux bin is considered. We run our constrained fits without M14 and note that the best fit to core radio source counts consistently excludes $a = b = 0$ at 99% confidence, with the maximum likelihood at $a = 0.08$ and $b = 1.03$; and the best fit to the half-light region counts also excludes $a = b = 0$ at 99% confidence, giving $a = 0.93$ and $b = 0.46$.

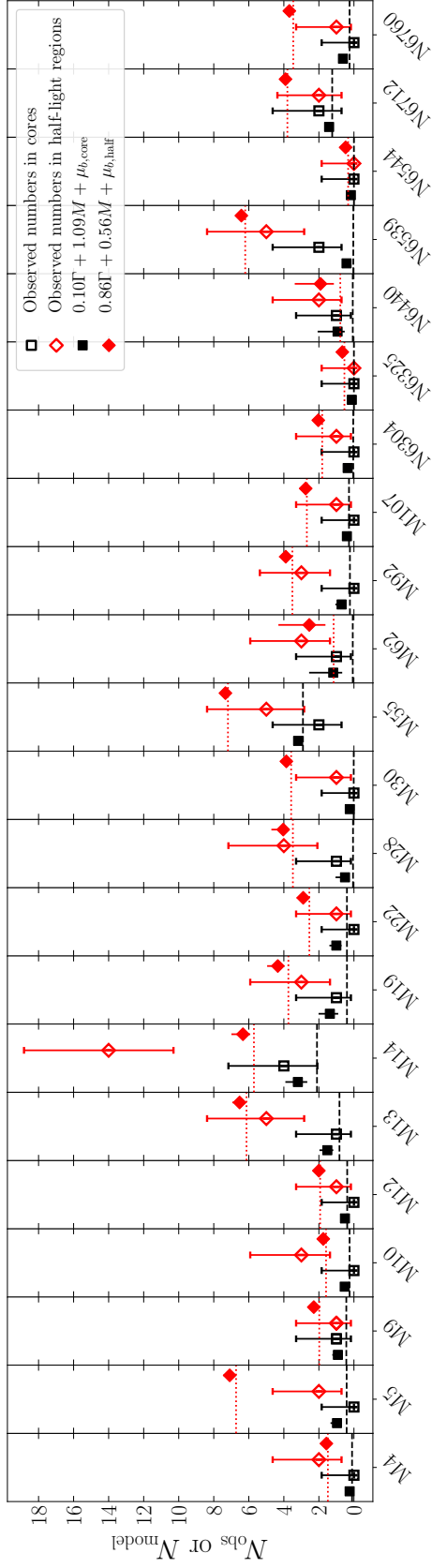


Figure 5.3: Observed core source counts (black empty squares) and observed half-light region source counts (red empty diamonds) vs. predicted source counts in the core (black filled squares) and in the half-light region (red filled diamonds) based on the constrained fits plotted for all 22 GCs. The error bars on the observed numbers indicate 84% confidence upper and lower limits (Gehrels, 1986); for GCs with zero counts, we only plot the upper bar. The uncertainties in predicted numbers are propagated from uncertainties in Γ and M , and the 68% confidence ranges of a and b . The black dashed and red dotted lines in each panel marks the number of expected background sources in the core ($\mu_{b,\text{core}}$) and in the half-light region ($\mu_{b,\text{halif}}$), respectively.

The 22 GCs listed in Table 5.1 host a total of 16 sources in their cores. We further investigate all these sources by matching their radio positions to those measured by timing observations (Table 5.2, and references therein). We find 4 known MSPs, three of which are in M28, NGC 6440, and NGC 6539, GCs that have core source excesses over the background (Table 5.1), and one in M13, which is marginally above L_{lim} (Table 5.2). Two more sources are known cluster members; a BH candidate in M62 (Chomiuk et al., 2013) and a NS LMXB in NGC 6712 (Swank et al., 1976).

These sources are all confirmed cluster members, with 4 hosted by GCs that have a core radio source excess, namely M28, M62, NGC 6440, and NGC 6539. Three of these are GCs with high mass and Γ (Table 5.1), in agreement with the positive correlation shown by the fit.

NGC 6539 possesses a clear core source excess (2 observed vs. 0.04 expected), while having a low Γ of 42 and an intermediate M ($= 2.6 \times 10^5 M_{\odot}$ vs. median mass of $2.8 \times 10^5 M_{\odot}$). There are two core sources, VLA11 and VLA12. VLA11 is positionally consistent with the known MSP, PSR B1745–20 (D’Amico et al., 1993), while VLA12 has an inverted-to-steep index ($\alpha = -0.4 \pm 0.7$, Table. 5.2), which can overlap with multiple scenarios. The probability of finding a background source in the core is $\approx 8\%$, not very likely but not ruled out. Considering the low Γ , it is possible that VLA12 is a primordial cluster member. For example, short (\sim hours) flares observed in some short-period RS CVn ABs can be detected in the radio at kpc distances (e.g., Osten et al., 2000).

MSPs in cluster cores are expected to scale directly with Γ , as they are produced by LMXBs that scale with stellar encounter rate (e.g. Heinke et al., 2003a; Pooley & Hut, 2006; Hui et al., 2010; Bahramian et al., 2013). The presence of four confirmed MSPs among the cluster radio sources indicates that at least some cluster radio sources must be dynamically formed. However, our analysis including known cluster members requires a contribution from

cluster mass, not just stellar encounter rate. It is therefore of great interest that the relative numbers of radio-emitting BH LMXBs are not predicted to scale directly with relative stellar encounter rates Γ (which are calculated for visible stars, not the BH subsystems). The numbers of these BH binaries are instead predicted to depend in complicated ways on the total number of BHs in each cluster, and on the interactions of these BH populations with other cluster stars (Weatherford et al., 2018; Arca Sedda et al., 2018). Thus, our work gives tentative support to the idea that a portion of the cluster radio sources are BH LMXBs, distributed in a complicated way among clusters, although we cannot rule out a contribution by other kinds of sources.

Another interesting test involves comparing the radio spectral indices of our sample with the known distribution of spectral indices of MSPs. In Figure 5.4, we present normalized histograms of spectral indices (α) for pulsars from the ATNF catalog (Manchester et al., 2005, and references therein); sources from the MAVERIC catalog that are outside of the half-light radii and thus are mostly background active galactic nuclei (AGNs); and for radio sources in Table 5.2 (excluding sources with unconstrained α values). We first compare equal-size samples of MSPs ($P \leq 20$ ms) and normal pulsars from the ATNF catalog, and note that there is no significant difference between the distribution of their spectral indices (p-value of 0.25 for a two-sample Anderson-Darling test). We can therefore randomly draw pulsars from the whole ATNF catalog to form a sample the same size as that of the AGNs. The core sources seem to follow a bimodal distribution, containing a group of steep ($-2.5 \lesssim \alpha \lesssim -1.2$) sources, and a group of relatively flatter ($-0.8 \lesssim \alpha \lesssim 0.2$) sources. The latter significantly deviates from the observed pulsar distribution, and exceeds the AGN distribution around $-0.5 \lesssim \alpha \lesssim -0.2$, which could be partially contributed by LMXBs. We performed a 2-sample Anderson-Darling test (Scholz & Stephens, 1987) comparing the core source distribution with that of the ATNF pulsars and that of AGNs. A test comparing the core sources with

ATNF pulsars rejects the null hypothesis that the core sources and ATNF pulsars are drawn from the same population at a level more significant than 0.1%. A test comparing core sources with the AGN sample rejects the null hypothesis at 3% significance. Finally, a test comparing the core sources with the AGN and pulsar samples combined rejects the null hypothesis at a level more significant than 0.1%. In fact, the flatter group contains 6 sources, of which one is a NS LMXB, one is the known BH candidate in M62, and one is the known MSP in NGC 6539; the other 3 sources could be either background AGNs or cluster members.

Our analyses have shown that additional membership information results in tighter constraints on the parameters for both source counts in the core and those in the half-light region. In this regard, future careful multiwavelength follow-up will therefore be necessary to separate background sources from cluster members, allowing investigation of radial trends in the radio source properties. For example, proper motion analysis of potential optical counterparts, or with radio VLBI (Tetarenko et al., 2016), can be effective in excluding background sources. Detailed investigation at other wavelengths is beyond the scope of this paper, but will be addressed in future work.

There are several potential factors that could affect our final results; uncertainties in Γ or mass of clusters, differences in sensitivity to radio sources across the cluster cores, and unusual cluster histories. Uncertainties in Γ can be up to 70% of the central values (Bahramian et al., 2013), but are not included in our aforementioned fits. To address this, we fit a and b simultaneously to the same observed counts but with Γ and M randomly drawn from the error ranges for each cluster, and observe the distribution of the best-fitting values and the corresponding confidence contours. We ran a total of 50 random constrained fits and find the point $a = b = 0$ is outside of the 99% confidence contour in all of the fits; running 50 random constrained fits for source counts in the half-light regions also excludes $a = b = 0$ at 99% confidence, so the correlation holds for

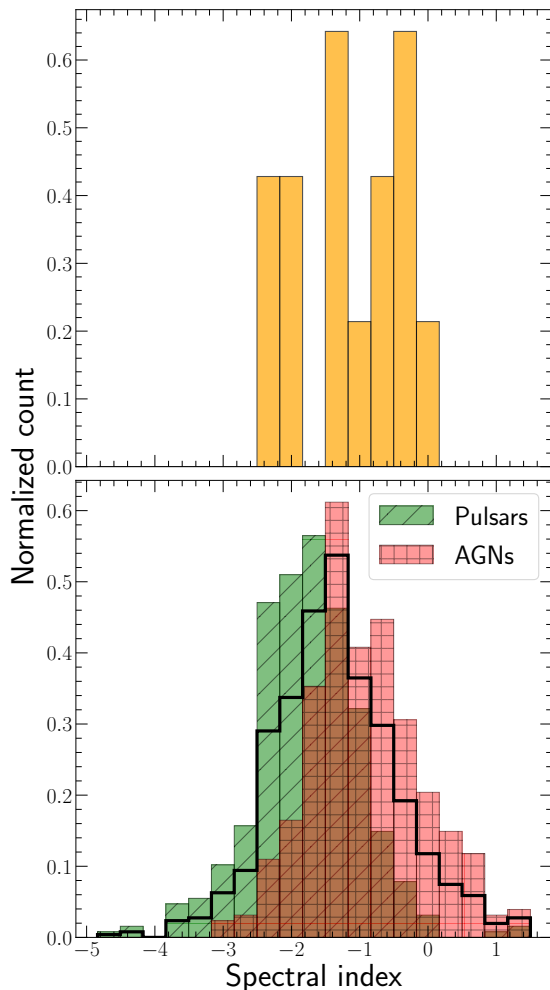


Figure 5.4: *Top*: A histogram showing distribution of spectral index (α) for core radio sources with constrained α values as listed in Table 5.2 (orange). *Bottom*: Histograms of α for pulsars from the ATNF catalog (hatched green), AGNs (hatched red), pulsar and AGN combined (solid black contour). The counts in each bin is normalized by dividing the total counts of each sample and the bin width. The core sources divide into steep-index and flatter-index groups; the flatter group is more numerous than expected from a pulsar-only distribution. Despite that the AGNs can partly account for the flatter group, there is an overabundance of core sources around $-0.5 \lesssim \alpha \lesssim -0.2$.

both core and half-light region source counts, regardless of uncertainties in Γ and M .

Another factor to consider is the increase in noise in the radio images with increasing off-axis distance. To first order, the RMS noise scales as the reciprocal of the primary beam sensitivity. As a result, sources at the edges of

the beam might have a flux above the average 5σ level, but might have been missed because they are below the local 5σ level. This effect is expected to be minor on our analyses of the core sources, as most of the clusters have core sizes much smaller than the half-power primary beam size ($\approx 8.2'$ at 5.5 GHz). The largest core, in the cluster M55, is $1.8'$ in radius. If we made the assumption that all of our core sources (Table 5.2) are located $1.8'$ from the beam center, we would expect the sensitivity to drop to $\approx 88\%$ of the center value (assuming the primary beam follows a Gaussian sensitivity curve); this corresponds to an increase in noise by a factor of ≈ 1.1 , so the detection procedure might miss sources between 5 and 5.5σ . Only one (of 16) of our core sources, M19-VLA34, falls in this flux range; we thus estimate that $< 6\%$ of the core sources above our stated flux limit might have been missed by our observations. Each GC has 1–3 core sources, corresponding to 0.1–0.2 missing sources. Therefore, the effect of noise variation is minor on our analyses.

A final concern is whether unusual histories of these GCs could mean that the current mass and stellar interaction rate do not represent their values during the period in which X-ray binaries or MSPs were formed. The prototype for this argument is the GC NGC 6712, which was shown to have lost $> 99\%$ of its mass, leaving preferentially high-mass stars and binaries in the core (de Marchi et al., 1999; Andreuzzi et al., 2001). This cluster was probably much more massive and dense when the two detected radio sources (one a known NS LMXB) were formed, explaining their presence in an apparently low-mass, low-density cluster (see Ferraro et al., 2000). However, running our fits excluding NGC 6712 gives best-fitting $a = 0.32$ and $b = 0.78$ for the core source counts, and $a = 0.97$, $b = 0.42$ for the half-light region counts, while both fits consistently exclude $a = b = 0$ at 99% confidence (when lower limits on N_c are included). Although similar cluster mass loss is likely to have affected other clusters (see e.g. Moreno et al., 2014), this effect has not removed the detectable correlation of stellar interactions on X-ray sources (Pooley & Hut, 2006; Bahramian et al., 2013),

and therefore we suspect its effects on radio sources are likely also modest.

5.4 Conclusion

We investigate linear correlations of radio source counts with the encounter rate (Γ) and mass (M) for a total of 22 GCs from the MAVERIC survey. Including information about confirmed cluster members in our analysis, the fit to source counts in the core rules out no correlation with M or Γ at 99% confidence, and excludes a dependence on Γ alone at 90% confidence. The fit to source counts in the half-light region also rules out no correlation at 99% confidence, but just excludes a Γ -only dependence at 68% confidence.

The histogram of spectral indices of our radio sources are inconsistent with that of pulsars and/or AGN alone, indicating another component with flatter spectra is present. Our findings are intriguingly consistent with the expectations that of detectable radio sources, some will be MSPs (produced dynamically, and thus correlated with Γ), and some may be BH LMXBs, the numbers of which are unlikely to be directly correlated with Γ (Kremer et al., 2018; Arca Sedda et al., 2018).

Our analyses also suggest that membership information can lead to significantly tighter constraints on the parameters. Future secure determinations of the nature of individual systems, obtained with careful follow-up, will therefore allow us to test predictions of the distribution of BH binaries in globular clusters in more detail. More detailed analyses will also use the full luminosity range of detected radio sources in each cluster, and (with sufficient follow-up efforts) will study their radial distributions.

Table 5.1: Radio source counts in different GCs.

GC Name	Distance (kpc)	r_c (')	r_h (')	S_{lim} (μJy)	N_{core}	N_{half}	$N_{\text{m,core}}$	$N_{\text{m,half}}$	$\mu_{b,\text{core}}$	$\mu_{b,\text{half}}$	Γ	M ($\times 10^5 M_{\odot}$)
M62*	6.7	0.22	0.92	18.6	1	3	1	2	0.07	1.16	1670^{+710}_{-570}	6.90 ± 0.05
NGC 6440*	8.5	0.14	0.48	11.6	1	2	1	1	0.07	0.78	1400^{+630}_{-477}	5.33 ± 0.65
M28*	5.5	0.24	1.97	27.6	1	4	1	1	0.05	3.48	648^{+85}_{-91}	2.84 ± 0.15
M30	8.6	0.06	1.03	11.3	0	1	0	0	0.01	3.58	324^{+124}_{-81}	1.39 ± 0.06
M92	8.9	0.26	1.02	10.6	0	3	0	0	0.23	3.51	270^{+30}_{-29}	3.12 ± 0.04
M19	8.2	0.43	1.32	12.4	1	3	0	0	0.40	3.74	200^{+67}_{-39}	6.57 ± 0.33
M5	7.7	0.44	1.77	14.1	0	2	0	0	0.42	6.73	164^{+39}_{-30}	3.68 ± 0.06
M9	7.8	0.45	0.96	13.7	1	1	0	0	0.43	1.98	131^{+59}_{-42}	3.21 ± 0.25
M14	9.3	0.79	1.30	9.7	4	14	0	0	2.11	5.71	124^{+32}_{-30}	7.39 ± 0.37
NGC 6304	5.9	0.21	1.42	24.0	0	1	0	0	0.04	1.81	123^{+54}_{-22}	2.11 ± 0.18
NGC 6325	6.5	0.03	0.63	19.8	0	0	0	0	0.001	0.54	118^{+45}_{-46}	0.76 ± 0.13
NGC 6544	3.0	0.05	1.21	92.9	0	0	0	0	0.00	0.33	111^{+68}_{-36}	1.15 ± 0.11
M22	3.1	1.33	3.36	86.9	0	1	0	0	0.40	2.54	78^{+31}_{-26}	4.09 ± 0.04
M13	7.6	0.62	1.69	14.5	1	5	1	1	0.83	6.13	69^{+18}_{-15}	4.69 ± 0.20
NGC 6760	7.4	0.34	1.27	15.3	0	1	0	0	0.25	3.46	57^{+27}_{-19}	2.55 ± 0.30
NGC 6539*	7.8	0.38	1.70	13.7	2	5	1	1	0.04	6.20	42^{+29}_{-15}	2.61 ± 0.31
M10	4.4	0.77	1.95	43.1	0	3	0	0	0.25	1.59	31^{+5}_{-4}	1.89 ± 0.04

Table 5.1: (Continued) Radio source counts in different GCs.

GC Name	Distance (kpc)	r_c (')	r_h (')	S_{lim} (μJy)	N_{core}	N_{half}	$N_{\text{m,core}}$	$N_{\text{m,half}}$	$\mu_{b,\text{core}}$	$\mu_{b,\text{half}}$	Γ	M ($\times 10^5 M_{\odot}$)
NGC 6712	8.0	0.76	1.33	13.1	2	2	1	1	1.24	3.80	31_{-7}^{+5}	1.19 ± 0.08
M4	1.8	1.16	4.33	258.0	0	2	0	0	0.11	1.49	27_{-10}^{+12}	0.93 ± 0.02
M12	5.2	0.79	1.77	30.9	0	1	0	0	0.38	1.93	13_{-4}^{+5}	0.87 ± 0.03
M107	6.1	0.56	1.73	22.5	0	1	0	0	0.28	2.69	$6.8_{-1.7}^{+2.3}$	0.81 ± 0.05
M55	5.7	1.80	2.83	25.7	2	5	0	0	2.91	7.19	$3.2_{-1.0}^{+1.4}$	1.88 ± 0.07

The distances are from Tremou et al. (2018); core radii (r_c), half-light radii (r_h) are from Harris (1996) (2010 edition); the Γ 's are from Bahramian et al. (2013); the GC masses (M) are from Baumgardt & Hilker (2018) (2nd version)⁴. N_{core} and N_{half} are the observed numbers of radio sources within the core and the half-light region, with $L > 5 \times 10^{27}$ erg s⁻¹. $N_{\text{m,core}}$ and $N_{\text{m,half}}$ are numbers of confirmed members within the core radius and the half-light radius. GCs indicated with * have a significant radio source excess in the core over the expected background.

Table 5.2: Radio sources in the core with $L_{\text{low}} > 5 \times 10^{27} \text{ erg s}^{-1}$.

Source ID	L_{low} ($\times 10^{27} \text{ erg s}^{-1}$)	$S_{\text{low}}/\text{RMS}$ (σ)	α ($S_{\nu} \propto \nu^{\alpha}$)	Notes	References
M9-VLA24	5.4 ± 0.6	8.6	$-0.9^{+0.6}_{-0.6}$	-	-
M13-VLA21	5.0 ± 0.7	7.3	$-1.3^{+0.7}_{-0.8}$	PSR B1639+36A	K91, W20
M14-VLA11	20.0 ± 1.0	21.4	$-1.2^{+0.3}_{-0.3}$	-	-
M14-VLA15	18.6 ± 1.0	20.0	$-0.2^{+0.2}_{-0.2}$	-	-
M14-VLA45	6.3 ± 1.0	6.8	< 0.0	-	-
M19-VLA34	5.1 ± 0.9	5.5	< 0.6	-	-
M28-VLA3	24.3 ± 0.5	53.7	$-2.2^{+0.1}_{-0.1}$	PSR B1821-24A	L87, F88, C04, R04, B11, J13
M55-VLA6	8.7 ± 0.4	19.6	$-1.2^{+0.3}_{-0.3}$	-	-
M55-VLA15	5.1 ± 0.5	11.3	$-2.3^{+0.7}_{-0.7}$	-	-
M62-VLA1	6.0 ± 1.0	7.0	$-0.4^{+0.6}_{-0.5}$	A BH candidate	C13
NGC 6440-VLA6	33.2 ± 1.3	28.4	$-2.0^{+0.2}_{-0.2}$	PSR B1745-20	L96, F08
NGC 6539-VLA11	9.4 ± 0.7	9.4	$-0.7^{+0.7}_{-0.8}$	PSR B1802-07	D93, T93, T99
NGC 6539-VLA12	5.2 ± 0.6	8.5	$-0.4^{+0.7}_{-0.7}$	-	-
NGC 6712-VLA7	33.8 ± 0.9	38.4	$0.1^{+0.1}_{-0.1}$	4U 1850-087	S76, A93, H96, S06
NGC 6712-VLA9	25.0 ± 0.9	28.3	$-0.6^{+0.1}_{-0.1}$	-	-

RMS noises are adapted from Sh20. α is the spectral index from Sh20. References: A93: Anderson et al. (1993), B11: Bogdanov et al. (2011), C04: Cognard & Backer (2004), C13: Chomiuk et al. (2013), D93: D’Amico et al. (1993), F88: Foster et al. (1988), F08: Freire et al. (2008), H96: Homer et al. (1996), J13: Johnson et al. (2013), K91: Kulkarni et al. (1991), L87: Lyne et al. (1987), L96: Lyne et al. (1996), R04: Rutledge et al. (2004), S76: Swank et al. (1976), S06: Sidoli et al. (2006), T93: Thorsett et al. (1993), T99: Thorsett & Chakrabarty (1999), W20: Wang et al. (2020).

Chapter 6

Conclusions

This thesis presents identification of exotic binaries in globular clusters (GCs) using optical/UV, X-ray, and radio observations (Chapter 2, 3, 4), and a study of how exotic binary populations are dependent on cluster structural and dynamical parameters (Chapter 5).

In Chapter 2, we present a catalogue of 16 faint X-ray sources in the globular cluster (GC) M3 and report counterparts to 10 of the 16 sources. This includes a known supersoft X-ray source, 1E1339, a quiescent low-mass X-ray binary (qLMXB) candidate, two likely CVs, four CV candidates, and two likely RS CVn systems. Our optical spectral-energy distribution (SED) modelling of 1E1339 suggests a blue spectral component from an accretion disk and a red component that arises from the companion star. CX2 has a blackbody-like soft X-ray spectrum and is likely a qLMXB candidate. However, due to the limited counting statistics and the deteriorating low-energy sensitivity of the *Chandra*/ACIS camera, related spectral parameters are not well-constrained, and the best fit cannot unambiguously distinguish between a neutron star atmosphere model and a thermal plasma model. To better verify CX2's qLMXB nature, we have proposed an *XMM-Newton* observation (accepted for AO20) for more spectral counts. This observation will also help to characterise the soft spectral component of 1E1339, search for possible temporal features, and

confirm its nature.

Chapter 3 reports the discovery of a “hidden” pulsar in the second closest GC NGC 6397 through incorporating radio imaging observations. This X-ray source, U18, was previously suggested to be the second pulsar because it has a similar sub-subgiant counterpart and X-ray temporal features to that of the known pulsar PSR J1740–5340. Radio continuum imaging observations from the MAVERIC survey identify U18 with a steep-spectrum radio counterpart which further confirms its pulsar nature. In the recent work by Pichardo Marcano et al. (2021), we have identified a 2-day orbital period of the binary using *HST* imaging series, while the pulsar nature can be further confirmed by future timing searches of NGC 6397. We also find a radio counterpart to the X-ray source U97, the optical counterpart of which exhibits $H\alpha$ variability. U97’s position on the $L_R - L_X$ plot (Figure 3.4) suggests a BH LMXB nature, which can only be confidently confirmed with future measurement of the primary mass (e.g., through binary radial velocity observations). Chapter 3 also reports an extended X-ray source catalogue (revealing 23 new sources) with updated astrometry, for which we perform tentative identifications using *Gaia* DR2 photometric data. We expect more pulsar candidates like U18 to be identified with deep radio imaging observations. Therefore, my future work will focus on exploring the full MAVERIC survey data to discover more pulsar candidates, complementing radio timing observations of GC pulsars.

Chapter 4 reports analyses of a deep X-ray observation of the core-collapsed GC M30. We compile an X-ray catalogue of 23 sources (10 new sources) and use existing UV, optical, and near-IR observations to identify these sources. We found UV/optical counterparts to 18 of the 23 sources, identifying 2 new CVs, 5 new CV candidates, two likely RS CVn systems, and 2 new BY Dra candidates. We also incorporate radio imaging observations from the MAVERIC survey, which reveals radio counterparts to two of the X-ray sources — including the known pulsar PSR J2140–2310A. We also investigate the radial distribution

of the bright and faint X-ray populations and find that bright sources are more centrally concentrated than the faint sources. The significant difference between the bright and faint source distributions can be the result of mass segregation, and has been observed in several core-collapsed GCs.

Finally, in Chapter 5, we take a census of radio sources in 22 GCs from the MAVERIC survey and investigate the possible dependence of radio source counts on cluster stellar encounter rate (Γ) and cluster mass (M). We adopt a simplified linear model, and use a maximum likelihood method to fit the model to radio source counts in GCs. We note that non-dependence on both Γ and M is excluded at 90% confidence when fitting the model to source counts in cluster cores, while no statistically significant dependence on neither Γ nor M for source counts within the half-light radii. The dependence is much more significant when known cluster members are specified: core source counts are dependent on Γ and/or M at 99% confidence, and source counts within the half-light radii depend on Γ and/or M also at 99% confidence. Furthermore, the best fits also exclude a dependence on Γ alone at 90% confidence for source counts in cluster cores, or at 68% confidence for source counts within half-light radii. It has been suggested that cluster NS LMXBs and MSPs scale with Γ , but BH LMXBs, which are thought to constitute a fraction of the core radio sources, might have a more complicated dependence on cluster parameters. Future observations (e.g., high angular resolution VLBA observations) that can confirm or exclude radio source membership will significantly increase the constraints on the fitting parameters.

Bibliography

- Abada-Simon, M., Lecacheux, A., Bastian, T. S., Bookbinder, J. A., & Dulk, G. A. 1993, *ApJ*, 406, 692
- Al Noori, H., Roberts, M. S. E., Torres, R. A., et al. 2018, *ApJ*, 861, 89
- Albrow, M. D., Gilliland, R. L., Brown, T. M., et al. 2001, *ApJ*, 559, 1060
- Andersen, B. C., & Ransom, S. M. 2018, *ApJL*, 863, L13
- Anderson, J., Sarajedini, A., Bedin, L. R., et al. 2008, *AJ*, 135, 2055
- Anderson, S. F., Margon, B., Deutsch, E. W., & Downes, R. A. 1993, *AJ*, 106, 1049
- Andreuzzi, G., De Marchi, G., Ferraro, F. R., et al. 2001, *A&A*, 372, 851
- Arca Sedda, M., Askar, A., & Giersz, M. 2018, *MNRAS*, 479, 4652
- Archibald, A. M., Kaspi, V. M., Bogdanov, S., et al. 2010, *ApJ*, 722, 88
- Archibald, A. M., Stairs, I. H., Ransom, S. M., et al. 2009, *Science*, 324, 1411
- Arnaud, K. A. 1996, *Astronomical Society of the Pacific Conference Series*, Vol. 101, *XSPEC: The First Ten Years*, ed. G. H. Jacoby & J. Barnes, 17
- Arons, J., & Tavani, M. 1993, *ApJ*, 403, 249
- Askar, A., Arca Sedda, M., & Giersz, M. 2018, *MNRAS*, 478, 1844

- Bahramian, A., Heinke, C. O., Degenaar, N., et al. 2015, *MNRAS*, 452, 3475
- Bahramian, A., Heinke, C. O., Sivakoff, G. R., & Gladstone, J. C. 2013, *ApJ*, 766, 136
- Bahramian, A., Heinke, C. O., Tudor, V., et al. 2017, *MNRAS*, 467, 2199
- Bahramian, A., Miller-Jones, J., Strader, J., et al. 2018, Radio/X-ray correlation database for X-ray binaries, , , doi:10.5281/zenodo.1252036. <https://doi.org/10.5281/zenodo.1252036>
- Bahramian, A., Strader, J., Miller-Jones, J. C. A., et al. 2020, *ApJ*, 901, 57
- Bailer-Jones, C. A. L., Rybizki, J., Fouesneau, M., Mantelet, G., & Andrae, R. 2018, *AJ*, 156, 58
- Bailyn, C. D., Grindlay, J. E., & Garcia, M. R. 1990, *ApJL*, 357, L35
- Barrett, P. E., Dieck, C., Beasley, A. J., Singh, K. P., & Mason, P. A. 2017, *AJ*, 154, 252
- Bassa, C., Pooley, D., Homer, L., et al. 2004, *ApJ*, 609, 755
- Bassa, C. G., Pooley, D., Verbunt, F., et al. 2008, *A&A*, 488, 921
- Bassa, C. G., Patruno, A., Hessels, J. W. T., et al. 2014, *MNRAS*, 441, 1825
- Bates, S. D., Lorimer, D. R., & Verbiest, J. P. W. 2013, *MNRAS*, 431, 1352
- Baumgardt, H., & Hilker, M. 2018, *MNRAS*, 478, 1520
- Beaumont, C., Goodman, A., & Greenfield, P. 2015, *Astronomical Society of the Pacific Conference Series*, Vol. 495, *Hackable User Interfaces In Astronomy with Glue*, ed. A. R. Taylor & E. Rosolowsky, 101
- Bégin, S. 2006, Master's thesis, University of British Columbia

- Belloni, D., Giersz, M., Rivera Sandoval, L. E., Askar, A., & Ciecieląg, P. 2019, MNRAS, 483, 315
- Belloni, T., Verbunt, F., & Mathieu, R. D. 1998, A&A, 339, 431
- Benz, A. O., Fuerst, E., & Kiplinger, A. L. 1983, Nature, 302, 45
- Bhattacharya, D., & van den Heuvel, E. P. J. 1991, PhR, 203, 1
- Bhattacharya, S., Heinke, C. O., Chugunov, A. I., et al. 2017, MNRAS, 472, 3706
- Blandford, R. D., & Begelman, M. C. 1999, MNRAS, 303, L1
- Bogdanov, S., Bahramian, A., Heinke, C. O., & Ransom, S. M. 2020, arXiv e-prints, arXiv:2012.12944
- Bogdanov, S., Esposito, P., Crawford, Fronefield, I., et al. 2014, ApJ, 781, 6
- Bogdanov, S., Grindlay, J. E., Heinke, C. O., et al. 2006, ApJ, 646, 1104
- Bogdanov, S., Grindlay, J. E., & van den Berg, M. 2005, ApJ, 630, 1029
- Bogdanov, S., van den Berg, M., Heinke, C. O., et al. 2010, ApJ, 709, 241
- Bogdanov, S., van den Berg, M., Servillat, M., et al. 2011, ApJ, 730, 81
- Bogdanov, S., Deller, A. T., Miller-Jones, J. C. A., et al. 2018, ApJ, 856, 54
- Britt, C. T., Hynes, R. I., Johnson, C. B., et al. 2014, ApJS, 214, 10
- Broderick, J. W., Fender, R. P., Breton, R. P., & et al. 2016, MNRAS, 459, 2681
- Cadelano, M., Ransom, S. M., Freire, P. C. C., et al. 2018, ApJ, 855, 125
- Camilo, F., Lorimer, D. R., Freire, P., Lyne, A. G., & Manchester, R. N. 2000, ApJ, 535, 975

- Camilo, F., & Rasio, F. A. 2005, in *Astronomical Society of the Pacific Conference Series*, Vol. 328, *Binary Radio Pulsars*, ed. F. A. Rasio & I. H. Stairs, 147
- Campana, S., Stella, L., Mereghetti, S., et al. 1998, *ApJL*, 499, L65
- Canizares, C. R., & Neighbours, J. E. 1975, *ApJL*, 199, L97
- Cash, W. 1979, *ApJ*, 228, 939
- Chakrabarty, D., Tomsick, J. A., Grefenstette, B. W., et al. 2014, *ApJ*, 797, 92
- Chambers, K. C., Magnier, E. A., Metcalfe, N., et al. 2016, arXiv e-prints, arXiv:1612.05560
- Chanmugam, G. 1987, *Ap&SS*, 130, 53
- Cheng, Z., Li, Z., Xu, X., & Li, X. 2018, *ApJ*, 858, 33
- Chomiuk, L., Strader, J., Maccarone, T. J., et al. 2013, *ApJ*, 777, 69
- Chugainov, P. F. 1966, *Information Bulletin on Variable Stars*, 122, 1
- Clark, C. J., Pletsch, H. J., Wu, J., Guillemot, L., & et al. 2018, *Science Advances*, 4, eaao7228
- Clark, G. W. 1975, *ApJL*, 199, L143
- Clark, G. W., Markert, T. H., & Li, F. K. 1975, *ApJL*, 199, L93
- Cognard, I., & Backer, D. C. 2004, *ApJL*, 612, L125
- Cohn, H. N., Lugger, P. M., Couch, S. M., et al. 2010, *ApJ*, 722, 20
- Colpi, M., Possenti, A., & Gualandris, A. 2002, *ApJL*, 570, L85

- Cool, A. M., Grindlay, J. E., Cohn, H. N., Lugger, P. M., & Bailyn, C. D. 1998, *ApJL*, 508, L75
- Cool, A. M., Grindlay, J. E., Cohn, H. N., Lugger, P. M., & Slavin, S. D. 1995, *ApJ*, 439, 695
- Cool, A. M., Haggard, D., Arias, T., et al. 2013, *ApJ*, 763, 126
- Coppejans, D. L., Körding, E. G., Miller-Jones, J. C. A., et al. 2015, *MNRAS*, 451, 3801
- Coppejans, R., Frey, S., Cseh, D., et al. 2016, *MNRAS*, 463, 3260
- Corbel, S., Coriat, M., Brocksopp, C., et al. 2013, *MNRAS*, 428, 2500
- Corbel, S., Koerding, E., & Kaaret, P. 2008, *MNRAS*, 389, 1697
- Corbel, S., Tomsick, J. A., & Kaaret, P. 2006, *ApJ*, 636, 971
- Cox, A. N. 2000, *Allen's astrophysical quantities*
- Cropper, M. 1990, *SSRv*, 54, 195
- D'Amico, N., Bailes, M., Lyne, A. G., et al. 1993, *MNRAS*, 260, L7
- D'Amico, N., Lyne, A. G., Manchester, R. N., Possenti, A., & Camilo, F. 2001a, *ApJL*, 548, L171
- D'Amico, N., Possenti, A., Manchester, R. N., et al. 2001b, *ApJL*, 561, L89
- Davies, M. B. 1997, *MNRAS*, 288, 117
- de Marchi, G., Leibundgut, B., Paresce, F., & Pulone, L. 1999, *A&A*, 343, L9
- de Martino, D., Papitto, A., Belloni, T., et al. 2015, *MNRAS*, 454, 2190
- Deller, A. T., Moldon, J., Miller-Jones, J. C. A., et al. 2015, *ApJ*, 809, 13

- Dempsey, R. C., Linsky, J. L., Fleming, T. A., & Schmitt, J. H. M. M. 1993, *ApJS*, 86, 599
- Deustua, S. e. 2016, *WFC3 Data Handbook, Version 3.0* (Baltimore, MD: STScI)
- Dieball, A., Long, K. S., Knigge, C., Thomson, G. S., & Zurek, D. R. 2010, *ApJ*, 710, 332
- Dieball, A., Rasekh, A., Knigge, C., Shara, M., & Zurek, D. 2017, *MNRAS*, 469, 267
- Djorgovski, S., & King, I. R. 1986, *ApJL*, 305, L61
- Dolphin, A. E. 2000, *PASP*, 112, 1383
- Done, C., Gierliński, M., & Kubota, A. 2007, *A&A Rv*, 15, 1
- Dotani, T., Asai, K., & Greiner, J. 1999, *PASJ*, 51, 519
- Drake, S. A., Simon, T., & Linsky, J. L. 1989, *ApJS*, 71, 905
- Echiburú, C. S., Guillot, S., Zhao, Y., et al. 2020, *MNRAS*, arXiv:2005.11345
- Edmonds, P. D., Gilliland, R. L., Heinke, C. O., & Grindlay, J. E. 2003a, *ApJ*, 596, 1177
- . 2003b, *ApJ*, 596, 1197
- Edmonds, P. D., Kahabka, P., & Heinke, C. O. 2004, *ApJ*, 611, 413
- Elshamouty, K. G., Heinke, C. O., Morsink, S. M., Bogdanov, S., & Stevens, A. L. 2016, *ApJ*, 826, 162
- Eracleous, M., Halpern, J., & Patterson, J. 1991, *ApJ*, 382, 290
- Eracleous, M., & Horne, K. 1996, *ApJ*, 471, 427

- Fabian, A. C., Pringle, J. E., & Rees, M. J. 1975, *MNRAS*, 172, 15
- Feldman, P. A. 1983, in *Astrophysics and Space Science Library*, Vol. 102, IAU Colloq. 71: Activity in Red-Dwarf Stars, ed. P. B. Byrne & M. Rodono, 429–436
- Fender, R. P., Gallo, E., & Jonker, P. G. 2003, *MNRAS*, 343, L99
- Ferraro, F. R., Paltrinieri, B., Paresce, F., & De Marchi, G. 2000, *ApJL*, 542, L29
- Ferraro, F. R., Possenti, A., D’Amico, N., & Sabbi, E. 2001, *ApJL*, 561, L93
- Ferraro, F. R., Sabbi, E., Gratton, R., et al. 2003, *ApJL*, 584, L13
- Ferraro, F. R., Beccari, G., Dalessandro, E., et al. 2009, *Nature*, 462, 1028
- Forestell, L. M., Heinke, C. O., Cohn, H. N., et al. 2014, *MNRAS*, 441, 757
- Foster, R. S., Backer, D. C., Taylor, J. H., & Goss, W. M. 1988, *ApJL*, 326, L13
- Fragione, G., Loeb, A., & Rasio, F. A. 2020, *ApJL*, 902, L26
- Frank, J., King, A., & Raine, D. 1992, *Accretion power in astrophysics.*, Vol. 21
- Freeman, P. E., Kashyap, V., Rosner, R., & Lamb, D. Q. 2002, *The Astrophysical Journal Supplement Series*, 138, 185
- Freire, P. C. C. 2005, in *Astronomical Society of the Pacific Conference Series*, Vol. 328, Binary Radio Pulsars, ed. F. A. Rasio & I. H. Stairs, 405
- Freire, P. C. C., Ransom, S. M., Bégin, S., et al. 2008, *ApJ*, 675, 670
- Freire, P. C. C., Ridolfi, A., Kramer, M., et al. 2017, *MNRAS*, 471, 857
- Fruchter, A. S., & Goss, W. M. 1992, *ApJL*, 384, L47

- . 2000, *ApJ*, 536, 865
- Fruchter, A. S., Stinebring, D. R., & Taylor, J. H. 1988, *Nature*, 333, 237
- Fruscione, A., McDowell, J. C., Allen, G. E., et al. 2006, *Society of Photo-Optical Instrumentation Engineers (SPIE) Conference Series*, Vol. 6270, CIAO: Chandra’s data analysis system, 62701V
- Gaia Collaboration, Prusti, T., de Bruijne, J. H. J., et al. 2016, *A&A*, 595, A1
- Gaia Collaboration, Brown, A. G. A., Vallenari, A., et al. 2018a, *A&A*, 616, A1
- Gaia Collaboration, Helmi, A., van Leeuwen, F., et al. 2018b, *A&A*, 616, A12
- Gallo, E., Degenaar, N., & van den Eijnden, J. 2018, *MNRAS*, 478, L132
- Gallo, E., Migliari, S., Markoff, S., et al. 2007, *ApJ*, 670, 600
- Gallo, E., Miller, B. P., & Fender, R. 2012, *MNRAS*, 423, 590
- Gallo, E., Miller-Jones, J. C. A., Russell, D. M., et al. 2014, *MNRAS*, 445, 290
- Galloway, D. K., & Keek, L. 2017, *arXiv e-prints*, arXiv:1712.06227
- García-Sánchez, J., Paredes, J. M., & Ribó, M. 2003, *A&A*, 403, 613
- Gehrels, N. 1986, *ApJ*, 303, 336
- Geller, A. M., Leiner, E. M., Chatterjee, S., et al. 2017a, *ApJ*, 842, 1
- Geller, A. M., Leiner, E. M., Bellini, A., et al. 2017b, *ApJ*, 840, 66
- Giacconi, R., Murray, S., Gursky, H., et al. 1974, *ApJS*, 27, 37
- Giesers, B., Dreizler, S., Husser, T.-O., et al. 2018, *MNRAS*, 475, L15
- Giesers, B., Kamann, S., Dreizler, S., et al. 2019, *A&A*, 632, A3

Gnedin, O. Y., Zhao, H., Pringle, J. E., et al. 2002, *ApJL*, 568, L23

Göttgens, F., Husser, T.-O., Kamann, S., et al. 2019, *A&A*, 631, A118

Gregory, P. C., & Lored, T. J. 1992, *ApJ*, 398, 146

Greisen, E. W. 2003, *Astrophysics and Space Science Library*, Vol. 285, AIPS, the VLA, and the VLBA, ed. A. Heck, 109

Grindlay, J. E., Heinke, C., Edmonds, P. D., & Murray, S. S. 2001a, *Science*, 292, 2290

Grindlay, J. E., Heinke, C. O., Edmonds, P. D., Murray, S. S., & Cool, A. M. 2001b, *ApJL*, 563, L53

Grindlay, J. E., Hertz, P., Steiner, J. E., Murray, S. S., & Lightman, A. P. 1984, *APJL*, 282, L13

Gudel, M. 1992, *A&A*, 264, L31

Guedel, M., & Benz, A. O. 1993, *ApJL*, 405, L63

Guillot, S., Rutledge, R. E., & Brown, E. F. 2011, *ApJ*, 732, 88

Gusinskaia, N. V., Hessels, J. W. T., Degenaar, N., et al. 2020, *MNRAS*, 492, 2858

Haggard, D., Cool, A. M., & Davies, M. B. 2009, *ApJ*, 697, 224

Hamilton, T. T., Helfand, D. J., & Becker, R. H. 1985, *AJ*, 90, 606

Harding, A. K., & Gaisser, T. K. 1990, *ApJ*, 358, 561

Harris, W. E. 1996, *AJ*, 112, 1487

Heggie, D. C., & Giersz, M. 2014, *MNRAS*, 439, 2459

Heinke, C. O., Grindlay, J. E., & Edmonds, P. D. 2005a, *ApJ*, 622, 556

- Heinke, C. O., Grindlay, J. E., Edmonds, P. D., et al. 2005b, *ApJ*, 625, 796
- . 2003a, *ApJ*, 598, 516
- Heinke, C. O., Grindlay, J. E., Lugger, P. M., et al. 2003b, *ApJ*, 598, 501
- Heinke, C. O., Wijnands, R., Cohn, H. N., et al. 2006, *ApJL*, 651, 1098
- Heinke, C. O., Altamirano, D., Cohn, H. N., et al. 2010, *ApJ*, 714, 894
- Heinke, C. O., Cohn, H. N., Lugger, P. M., et al. 2014, *MNRAS*, 444, 443
- Heinke, C. O., Ivanov, M. G., Koch, E. W., et al. 2020, *MNRAS*, 492, 5684
- Henze, M., Pietsch, W., Haberl, F., et al. 2009, *A&A*, 500, 769
- . 2011, *A&A*, 533, A52
- . 2013, *A&A*, 549, A120
- Hertz, P., & Grindlay, J. E. 1983a, *ApJL*, 267, L83
- . 1983b, *ApJ*, 275, 105
- Hessels, J. W. T., Ransom, S. M., Stairs, I. H., Kaspi, V. M., & Freire, P. C. C. 2007, *ApJ*, 670, 363
- Hill, A. B., Szostek, A., Corbel, S., et al. 2011, *MNRAS*, 415, 235
- Hills, J. G. 1976, *MNRAS*, 175, 1P
- Hjellming, R. M., & Gibson, D. M. 1980, in *IAU Symposium*, Vol. 86, *Radio Physics of the Sun*, ed. M. R. Kundu & T. E. Gergely, 209–220
- Homer, L., Charles, P. A., Naylor, T., et al. 1996, *MNRAS*, 282, L37
- Hong, J., van den Berg, M., Schlegel, E. M., et al. 2005, *ApJ*, 635, 907
- Howell, S. B., Nelson, L. A., & Rappaport, S. 2001, *ApJ*, 550, 897

- Huang, R. H. H., Becker, W., Edmonds, P. D., et al. 2010, *A&A*, 513, A16
- Huang, R. H. H., Kong, A. K. H., Takata, J., et al. 2012, *ApJ*, 760, 92
- Hui, C. Y., Cheng, K. S., & Taam, R. E. 2010, *ApJ*, 714, 1149
- Hui, C. Y., Tam, P. H. T., Takata, J., et al. 2014, *ApJL*, 781, L21
- Hui, C. Y., Hu, C. P., Park, S. M., et al. 2015, *ApJL*, 801, L27
- Hulse, R. A., & Taylor, J. H. 1975, *ApJL*, 195, L51
- Ivanova, N., da Rocha, C. A., Van, K. X., & Nandez, J. L. A. 2017, *ApJL*, 843, L30
- Ivanova, N., Heinke, C. O., Rasio, F. A., Belczynski, K., & Fregeau, J. M. 2008, *MNRAS*, 386, 553
- Ivanova, N., Heinke, C. O., Rasio, F. A., et al. 2006, *MNRAS*, 372, 1043
- Johnson, T. J., Guillemot, L., Kerr, M., et al. 2013, *ApJ*, 778, 106
- Johnston, H. M., Kulkarni, S. R., & Phinney, E. S. 1992, in *X-Ray Binaries and the Formation of Binary and Millisecond Radio Pulsars*, 349–364
- Jonker, P. G., Bassa, C. G., Nelemans, G., et al. 2011, *ApJS*, 194, 18
- Jordán, A., Côté, P., Ferrarese, L., et al. 2004, *ApJ*, 613, 279
- Jordán, A., Sivakoff, G. R., McLaughlin, D. E., et al. 2007, *ApJL*, 671, L117
- Kaluzny, J., Rucinski, S. M., & Thompson, I. B. 2003, *AJ*, 125, 1546
- Kandel, D., Romani, R. W., & An, H. 2019, *ApJ*, 879, 73
- Katz, J. I. 1975, *Nature*, 253, 698
- Kellermann, K. I., Fomalont, E. B., Mainieri, V., et al. 2008, *ApJS*, 179, 71

- Kelly, B. C., Bechtold, J., & Siemiginowska, A. 2009, *ApJ*, 698, 895
- Kiel, P. D., & Hurley, J. R. 2006, *MNRAS*, 369, 1152
- Knigge, C., Baraffe, I., & Patterson, J. 2011, *ApJS*, 194, 28
- Knigge, C., Zurek, D. R., Shara, M. M., & Long, K. S. 2002, *Apj*, 579, 752
- Kong, A. K. H., Bassa, C., Pooley, D., et al. 2006, *ApJ*, 647, 1065
- Kong, A. K. H., McClintock, J. E., Garcia, M. R., Murray, S. S., & Barret, D. 2002, *ApJ*, 570, 277
- Körding, E., Rupen, M., Knigge, C., et al. 2008, *Science*, 320, 1318
- Kramer, M., Lange, C., Lorimer, D. R., et al. 1999, *ApJ*, 526, 957
- Kremer, K., Chatterjee, S., Rodriguez, C. L., & Rasio, F. A. 2018, *ApJ*, 852, 29
- Kulkarni, S. R., Anderson, S. B., Prince, T. A., & Wolszczan, A. 1991, *Nature*, 349, 47
- Kulkarni, S. R., Hut, P., & McMillan, S. 1993, *Nature*, 364, 421
- Kundu, M. R., & Shevgaonkar, R. K. 1985, *ApJ*, 297, 644
- Kurbatov, E. P., Zhilkin, A. G., & Bisikalo, D. V. 2019, *Astronomy Reports*, 63, 25
- Leiner, E., Mathieu, R. D., & Geller, A. M. 2017, *ApJ*, 840, 67
- Lewin, W. H. G., & Joss, P. C. 1981, *SSRv*, 28, 3
- Lewin, W. H. G., & Joss, P. C. 1983, in *Accretion-Driven Stellar X-ray Sources*, ed. W. H. G. Lewin & E. P. J. van den Heuvel, 41
- Li, D., Lin, F. X., Main, R., et al. 2019, *MNRAS*, 484, 5723

- Li, J., Kastner, J. H., Prigozhin, G. Y., et al. 2004, *ApJ*, 610, 1204
- Linares, M. 2014, *ApJ*, 795, 72
- Lorimer, D. R., Yates, J. A., Lyne, A. G., & Gould, D. M. 1995, *MNRAS*, 273, 411
- Lu, T.-N., Kong, A. K. H., Bassa, C., et al. 2009, *ApJ*, 705, 175
- Lucas, R. e. a. 2016, *ACS Data Handbook, Version 8.0* (Baltimore, MD: STScI)
- Ludlam, R., Miller, J. M., Miller-Jones, J., & Reynolds, M. 2017, *The Astronomer's Telegram*, 10690, 1
- Lugger, P. M., Cohn, H. N., Cool, A. M., Heinke, C. O., & Anderson, J. 2017, *ApJ*, 841, 53
- Lugger, P. M., Cohn, H. N., & Grindlay, J. E. 1995, *ApJ*, 439, 191
- Lugger, P. M., Cohn, H. N., Heinke, C. O., Grindlay, J. E., & Edmonds, P. D. 2007, *ApJ*, 657, 286
- Lynch, R. S., Freire, P. C. C., Ransom, S. M., & Jacoby, B. A. 2012, *ApJ*, 745, 109
- Lyne, A. G., Brinklow, A., Middleditch, J., Kulkarni, S. R., & Backer, D. C. 1987, *Nature*, 328, 399
- Lyne, A. G., Manchester, R. N., & D'Amico, N. 1996, *ApJL*, 460, L41
- Lyne, A. G., Mankelow, S. H., Bell, J. F., & Manchester, R. N. 2000, *MNRAS*, 316, 491
- Lyne, A. G., Manchester, R. N., D'Amico, N., et al. 1990, *Nature*, 347, 650
- Maccarone, T. J. 2005, *MNRAS*, 360, L30

- Maccarone, T. J., Kundu, A., Zepf, S. E., & Rhode, K. L. 2007, *Nature*, 445, 183
- Manchester, R. N. 2017, *Journal of Astrophysics and Astronomy*, 38, 42
- Manchester, R. N., Hobbs, G. B., Teoh, A., & Hobbs, M. 2005, *AJ*, 129, 1993
- Markoff, S., Nowak, M., Corbel, S., Fender, R., & Falcke, H. 2003, *A&A*, 397, 645
- Markoff, S., Nowak, M. A., & Wilms, J. 2005, *ApJ*, 635, 1203
- Marsh, T. R., Gänsicke, B. T., Hümmerich, S., et al. 2016, *Nature*, 537, 374
- Mason, P. A., & Gray, C. L. 2007, *ApJ*, 660, 662
- Mateos, S., Warwick, R. S., Carrera, F. J., et al. 2008, *A&A*, 492, 51
- Mathieu, R. D., van den Berg, M., Torres, G., et al. 2003, *AJ*, 125, 246
- McConnell, D., Deacon, R., & Ables, J. G. 2001, *PASA*, 18, 136
- McHardy, I. M., Koerding, E., Knigge, C., Uttley, P., & Fender, R. P. 2006, *Nature*, 444, 730
- McMullin, J. P., Waters, B., Schiebel, D., Young, W., & Golap, K. 2007, *Astronomical Society of the Pacific Conference Series*, Vol. 376, *CASA Architecture and Applications*, ed. R. A. Shaw, F. Hill, & D. J. Bell, 127
- Meintjes, P. J., & Venter, L. A. 2005, *MNRAS*, 360, 573
- Migliari, S., & Fender, R. P. 2006, *MNRAS*, 366, 79
- Miller-Jones, J. C. A., Jonker, P. G., Maccarone, T. J., Nelemans, G., & Calvelo, D. E. 2011, *ApJL*, 739, L18
- Miller-Jones, J. C. A., Sivakoff, G. R., Knigge, C., et al. 2013, *Science*, 340, 950

- Miller-Jones, J. C. A., Strader, J., Heinke, C. O., et al. 2015, *MNRAS*, 453, 3918
- Moehler, S., Koester, D., Zoccali, M., et al. 2004, *A&A*, 420, 515
- Mooley, K. P., Miller-Jones, J. C. A., Fender, R. P., et al. 2017, *MNRAS*, 467, L31
- Moreno, E., Pichardo, B., & Velázquez, H. 2014, *ApJ*, 793, 110
- Morscher, M., Pattabiraman, B., Rodriguez, C., Rasio, F. A., & Umbreit, S. 2015, *ApJ*, 800, 9
- Morscher, M., Umbreit, S., Farr, W. M., & Rasio, F. A. 2013, *ApJL*, 763, L15
- Mucciarelli, A., Salaris, M., Lanzoni, B., et al. 2013, *ApJL*, 772, L27
- Narayan, R., & McClintock, J. E. 2008, *Nature*, 51, 733
- Narayan, R., & Yi, I. 1994, *ApJL*, 428, L13
- . 1995a, *ApJ*, 444, 231
- . 1995b, *ApJ*, 452, 710
- Nardiello, D., Libralato, M., Piotto, G., et al. 2018, *ArXiv e-prints*, arXiv:1809.04300
- Orosz, J. A., & van Kerkwijk, M. H. 2003, *A&A*, 397, 237
- Osten, R. A., Brown, A., Ayres, T. R., et al. 2000, *ApJ*, 544, 953
- Padovani, P., Mainieri, V., Tozzi, P., et al. 2009, *ApJ*, 694, 235
- Pallanca, C., Dalessandro, E., Ferraro, F. R., Lanzoni, B., & Beccari, G. 2013, *ApJ*, 773, 122
- Pallavicini, R., Golub, L., Rosner, R., et al. 1981, *ApJ*, 248, 279

Pan, Z., Hobbs, G., Li, D., et al. 2016, MNRAS, 459, L26

Papitto, A., Ferrigno, C., Bozzo, E., et al. 2013, Nature, 501, 517

Patterson, J., & Skillman, D. R. 1994, PASP, 106, 1141

Peacock, M. B., Maccarone, T. J., Waters, C. Z., et al. 2009, MNRAS, 392, L55

Pecaut, M. J., & Mamajek, E. E. 2013, ApJS, 208, 9

Peuten, M., Zocchi, A., Gieles, M., Gualandris, A., & Hénault-Brunet, V. 2016, MNRAS, 462, 2333

Pfahl, E., Rappaport, S., & Podsiadlowski, P. 2003, ApJ, 597, 1036

Pichardo Marcano, M., Rivera Sandoval, L. E., Maccarone, T. J., Zhao, Y., & Heinke, C. O. 2021, MNRAS, arXiv:2103.03989

Pickles, A. J. 1998, PASP, 110, 863

Piotto, G., Milone, A. P., Bedin, L. R., et al. 2015, AJ, 149, 91

Pletsch, H. J., Guillemot, L., Fehrmann, H., et al. 2012, Science, 338, 1314

Plotkin, R. M., Gallo, E., & Jonker, P. G. 2013, ApJ, 773, 59

Plotkin, R. M., Markoff, S., Kelly, B. C., K rding, E., & Anderson, S. F. 2012, MNRAS, 419, 267

Plotkin, R. M., Miller-Jones, J. C. A., Chomiuk, L., et al. 2019a, ApJ, 874, 13

— . 2019b, ApJ, 874, 13

Plotkin, R. M., Miller-Jones, J. C. A., Gallo, E., et al. 2017, ApJ, 834, 104

Polzin, E. J., Breton, R. P., Stappers, B. W., et al. 2019, MNRAS, 490, 889

Polzin, E. J., Breton, R. P., Clarke, A. O., et al. 2018, MNRAS, 476, 1968

- Pooley, D., & Hut, P. 2006, *ApJL*, 646, L143
- Pooley, D., Lewin, W. H. G., Homer, L., et al. 2002a, *ApJ*, 569, 405
- Pooley, D., Lewin, W. H. G., Verbunt, F., et al. 2002b, *ApJ*, 573, 184
- Pooley, D., Lewin, W. H. G., Anderson, S. F., et al. 2003, *ApJL*, 591, L131
- Prager, B. J., Ransom, S. M., Freire, P. C. C., et al. 2017, *ApJ*, 845, 148
- Ransom, S. M., Hessels, J. W. T., Stairs, I. H., et al. 2005, *Science*, 307, 892
- Ransom, S. M., Stairs, I. H., Backer, D. C., et al. 2004, *ApJ*, 604, 328
- Rasio, F. A., & Shapiro, S. L. 1991, *ApJ*, 377, 559
- Ratti, E. M., Jonker, P. G., Miller-Jones, J. C. A., et al. 2012, *MNRAS*, 423, 2656
- Reynolds, M. T., Reis, R. C., Miller, J. M., Cackett, E. M., & Degenaar, N. 2014, *MNRAS*, 441, 3656
- Ridolfi, A., Freire, P. C. C., Torne, P., et al. 2016, *MNRAS*, 462, 2918
- Ridolfi, A., Gautam, T., Freire, P. C. C., et al. 2021, *MNRAS*, arXiv:2103.04800
- Rivera Sandoval, L. E., van den Berg, M., Heinke, C. O., et al. 2018, *MNRAS*, 475, 4841
- Roberts, M. S. E. 2013, in *IAU Symposium, Vol. 291, Neutron Stars and Pulsars: Challenges and Opportunities after 80 years*, ed. J. van Leeuwen, 127–132
- Roberts, M. S. E., Mclaughlin, M. A., Gentile, P., et al. 2014, *Astronomische Nachrichten*, 335, 313

- Robitaille, T., Beaumont, C., Qian, P., Borkin, M., & Goodman, A. 2017, glueviz v0.13.1: multidimensional data exploration, v0.13.1, Zenodo, doi:10.5281/zenodo.1237692
- Romani, R. W. 2012, *ApJL*, 754, L25
- Romani, R. W., & Sanchez, N. 2016, *ApJ*, 828, 7
- Romani, R. W., & Shaw, M. S. 2011, *ApJL*, 743, L26
- Roy, J., Ray, P. S., Bhattacharyya, B., et al. 2015, *ApJL*, 800, L12
- Rushton, A. P., Shaw, A. W., Fender, R. P., et al. 2016, *MNRAS*, 463, 628
- Russell, T. D., Miller-Jones, J. C. A., Sivakoff, G. R., et al. 2016, *MNRAS*, 460, 3720
- Rutledge, R. E., Bildsten, L., Brown, E. F., Pavlov, G. G., & Zavlin, V. E. 2002, *ApJ*, 578, 405
- Rutledge, R. E., Fox, D. W., Kulkarni, S. R., et al. 2004, *ApJ*, 613, 522
- Sabbi, E., Gratton, R., Ferraro, F. R., et al. 2003, *ApJL*, 589, L41
- Saito, Y., Kawai, N., Kamae, T., et al. 1997, *ApJL*, 477, L37
- Sarajedini, A., Bedin, L. R., Chaboyer, B., et al. 2007, *AJ*, 133, 1658
- Sault, R. J., Teuben, P. J., & Wright, M. C. H. 1995, in *Astronomical Society of the Pacific Conference Series, Vol. 77, Astronomical Data Analysis Software and Systems IV*, ed. R. A. Shaw, H. E. Payne, & J. J. E. Hayes, 433
- Scholz, F. W., & Stephens, M. A. 1987, *Journal of the American Statistical Association*, 82, 918. <https://doi.org/10.1080/01621459.1987.10478517>
- Shishkovsky, L., Strader, J., Chomiuk, L., et al. 2018, *ApJ*, 855, 55
- . 2020, *ApJ*, 903, 73

- Sidoli, L., Paizis, A., Bazzano, A., & Mereghetti, S. 2006, *A&A*, 460, 229
- Sieber, W. 1973, *A&A*, 28, 237
- Sigurdsson, S., & Hernquist, L. 1993, *Nature*, 364, 423
- Sippel, A. C., & Hurley, J. R. 2013, *MNRAS*, 430, L30
- Sirianni, M., Jee, M. J., Benítez, N., et al. 2005, *PASP*, 117, 1049
- Sivakoff, G. R., Jordán, A., Sarazin, C. L., et al. 2007, *ApJ*, 660, 1246
- Soleri, P., Fender, R., Tudose, V., et al. 2010, *MNRAS*, 406, 1471
- Soto, M., Bellini, A., Anderson, J., et al. 2017, *AJ*, 153, 19
- Stacey, W. S., Heinke, C. O., Elsner, R. F., et al. 2011, *ApJ*, 732, 46
- Stappers, B. W., Bailes, M., Lyne, A. G., et al. 2001, *MNRAS*, 321, 576
- Stetson, P. B. 1987, *PASP*, 99, 191
- Stovall, K., Lynch, R. S., Ransom, S. M., et al. 2014, *ApJ*, 791, 67
- Strader, J., Chomiuk, L., Maccarone, T. J., Miller-Jones, J. C. A., & Seth, A. C. 2012, *Nature*, 490, 71
- Strader, J., Swihart, S., Chomiuk, L., et al. 2019, *ApJ*, 872, 42
- Sutantyo, W. 1975, *A&A*, 44, 227
- Swank, J. H., Becker, R. H., Pravdo, S. H., Saba, J. R., & Serlemitsos, P. J. 1976, *IAUC*, 3010, 1
- Tavani, M. 1991, *ApJL*, 379, L69
- Tetarenko, B. E., Bahramian, A., Arnason, R. M., et al. 2016, *ApJ*, 825, 10

- Thompson, C., Blandford, R. D., Evans, C. R., & Phinney, E. S. 1994, *ApJ*, 422, 304
- Thomson, G. S., Knigge, C., Dieball, A., et al. 2012, *MNRAS*, 423, 2901
- Thorsett, S. E., Arzoumanian, Z., McKinnon, M. M., & Taylor, J. H. 1993, *ApJL*, 405, L29
- Thorsett, S. E., & Chakrabarty, D. 1999, *ApJL*, 512, 288
- Tomsick, J. A., Corbel, S., & Kaaret, P. 2001, *ApJ*, 563, 229
- Tremou, E., Strader, J., Chomiuk, L., et al. 2018, *ApJ*, 862, 16
- Tudor, V., Miller-Jones, J. C. A., Patruno, A., et al. 2017, *MNRAS*, 470, 324
- Tudor, V., Miller-Jones, J. C. A., Knigge, C., et al. 2018, *MNRAS*, 476, 1889
- Urquhart, R., Bahramian, A., Strader, J., et al. 2020, *ApJ*, 904, 147
- van Staden, A. D., & Antoniadis, J. 2016, *ApJL*, 833, L12
- VandenBerg, D. A., Brogaard, K., Leaman, R., & Casagrande, L. 2013, *ApJ*, 775, 134
- Verbunt, F. 2001, *A&A*, 368, 137
- Verbunt, F. 2003, in *Astronomical Society of the Pacific Conference Series*, Vol. 296, *New Horizons in Globular Cluster Astronomy*, ed. G. Piotto, G. Meylan, S. G. Djorgovski, & M. Riello, 245
- Verbunt, F., Bunk, W., Hasinger, G., & Johnston, H. M. 1995, *A&A*, 300, 732
- Verbunt, F., & Hut, P. 1987, in *IAU Symposium*, Vol. 125, *The Origin and Evolution of Neutron Stars*, ed. D. J. Helfand & J.-H. Huang, 187
- Verbunt, F., & Lewin, W. H. G. 2006, *Globular cluster X-ray sources*, ed. W. H. G. Lewin & M. van der Klis, 341–379

- Verbunt, F., & Meylan, G. 1988, *A&A*, 203, 297
- Verbunt, F., Pooley, D., & Bassa, C. 2008, in *IAU Symposium*, Vol. 246, *Dynamical Evolution of Dense Stellar Systems*, ed. E. Vesperini, M. Giersz, & A. Sills, 301–310
- Wadiasingh, Z., Harding, A. K., Venter, C., Böttcher, M., & Baring, M. G. 2017, *ApJ*, 839, 80
- Wadiasingh, Z., Venter, C., Harding, A. K., Böttcher, M., & Kilian, P. 2018, *ApJ*, 869, 120
- Wang, L., Peng, B., Stappers, B. W., et al. 2020, *ApJ*, 892, 43
- Warner, B. 1995, *Cataclysmic variable stars*, Vol. 28
- Watkins, L. L., van der Marel, R. P., Bellini, A., & Anderson, J. 2015, *ApJ*, 812, 149
- Weatherford, N. C., Chatterjee, S., Kremer, K., & Rasio, F. A. 2020, *ApJ*, 898, 162
- Weatherford, N. C., Chatterjee, S., Rodriguez, C. L., & Rasio, F. A. 2018, *ApJ*, 864, 13
- Weisberg, J. M., & Taylor, J. H. 2005, in *Astronomical Society of the Pacific Conference Series*, Vol. 328, *Binary Radio Pulsars*, ed. F. A. Rasio & I. H. Stairs, 25
- Wijnands, R., Degenaar, N., Armas Padilla, M., et al. 2015, *MNRAS*, 454, 1371
- Wilms, J., Allen, A., & McCray, R. 2000, *ApJ*, 542, 914
- Wynn, G. A., King, A. R., & Horne, K. 1997, *MNRAS*, 286, 436
- Yuan, F., & Cui, W. 2005, *ApJ*, 629, 408

- Yuan, F., & Narayan, R. 2014, ARA&A, 52, 529
- Zavlin, V. E., Pavlov, G. G., Sanwal, D., et al. 2002, ApJ, 569, 894
- Zhao, J., Zhao, Y., & Heinke, C. O. 2021a, MNRAS, 502, 1596
- Zhao, Y., Heinke, C. O., Cohn, H. N., Lugger, P. M., & Cool, A. M. 2019, MNRAS, 483, 4560
- Zhao, Y., Heinke, C. O., Tudor, V., et al. 2020a, MNRAS, 493, 6033
- Zhao, Y., Heinke, C. O., Cohn, H. N., et al. 2020b, MNRAS, 499, 3338
- Zhao, Y., Heinke, C. O., Shishkovsky, L., et al. 2021b, ApJ, 914, 77

Appendices

A Renormalization of SED models with χ^2 minimization method

For a single component model, the χ^2 is defined as

$$\chi^2 = \sum_i \left[\frac{(\alpha M_i - D_i)}{\sigma_i} \right]^2, \quad (1)$$

where M_i and D_i are the model value and the data value at x_i , respectively, and α is a normalization factor. We want to find α such that

$$\frac{\partial \chi^2}{\partial \alpha} = 0. \quad (2)$$

Plugging eq.(1), one can solve for α and find that

$$\alpha = \frac{\sum_i \frac{M_i D_i}{\sigma_i^2}}{\sum_i \frac{M_i^2}{\sigma_i^2}}. \quad (3)$$

For the case of an composite model with two additive components, i.e.

$$M = \alpha M_1 + \beta M_2, \quad (4)$$

one can use similar method to find that

$$\begin{aligned}
\alpha &= -\frac{\left(\sum_i \frac{M_{2,i}^2}{\sigma_i^2}\right) \left(\sum_i \frac{D_i M_{1,i}}{\sigma_i^2}\right) - \left(\sum_i \frac{M_{1,i} M_{2,i}}{\sigma_i^2}\right) \left(\sum_i \frac{D_i M_{2,i}}{\sigma_i^2}\right)}{\left(\sum_i \frac{M_{1,i} M_{2,i}}{\sigma_i^2}\right) - \left(\sum_i \frac{M_{1,i}^2}{\sigma_i^2}\right) \left(\sum_i \frac{M_{2,i}^2}{\sigma_i^2}\right)} \\
\beta &= -\frac{\left(\sum_i \frac{M_{1,i}^2}{\sigma_i^2}\right) \left(\sum_i \frac{D_i M_{2,i}}{\sigma_i^2}\right) - \left(\sum_i \frac{M_{1,i} M_{2,i}}{\sigma_i^2}\right) \left(\sum_i \frac{D_i M_{1,i}}{\sigma_i^2}\right)}{\left(\sum_i \frac{M_{1,i} M_{2,i}}{\sigma_i^2}\right) - \left(\sum_i \frac{M_{1,i}^2}{\sigma_i^2}\right) \left(\sum_i \frac{M_{2,i}^2}{\sigma_i^2}\right)}.
\end{aligned} \tag{5}$$

B An updated X-ray source catalogue and tentative identification of new sources in NGC 6397

Our X-ray catalogue (Tab. 1) includes sources within the $2'.9$ half-light radius (r_h , as updated by Harris 1996, 2010 revision; note that Bogdanov et al. 2010 used a previous Harris catalog version with $r_h = 2.33'$ to search for sources) and source positions with updated astrometry from *Gaia* DR2. We adopt source counts from Bogdanov et al. (2010) and calculate counts in the same bands using the CIAO `srcflux` tool, for the new sources (Sec. 3.2.2). Most of these sources are outside the *HST* field of view, so direct photometric identification might be hard. However, tenuous classification is still possible solely based on the X-ray hardness. For this purpose, we define an X-ray hardness ratio

$$X_C \equiv 2.5 \log_{10} \left(\frac{C_{0.5-1.5 \text{ keV}}}{C_{1.5-6 \text{ keV}}} \right), \tag{6}$$

where $C_{0.5-1.5 \text{ keV}}$ and $C_{1.5-6 \text{ keV}}$ are X-ray counts in 0.5-1.5 keV and 1.5-6 keV, respectively. The distribution of X_C is shown in Fig. 1, which plots 0.5-6 keV fluxes vs. X_C for known and new sources.

In principle, most of the very hard ($X_C \lesssim 0$) sources that lack soft counts are very likely background sources (e.g., AGNs) with high values of N_H . This

includes W127, W129, W135, W141 and W142. A typical example is W129, which is heavily absorbed and has zero counts in the 0.5-1.5 keV band. The best-fitting power-law model (Fig. 2) suggests an $N_{\text{H}} = 11.8_{-4.7}^{+6.6} \times 10^{22} \text{ cm}^{-2}$, which is clearly above the cluster value of $N_{\text{H}} = 1.57 \times 10^{21} \text{ cm}^{-2}$. Moreover, clear detections in the radio bands (Sec. 3.3.5) further corroborate their AGN nature.

The soft sources ($X_C \gtrsim 1.8$), including W126, W132, W136, W139, W143, W144, W145 and W146, are likely faint ABs or CVs, whose spectra can be fairly reproduced by either a blackbody with kT_{bb} between 0.1-0.3 keV, or a thermal plasma model (e.g., `vmekal` in XSPEC) with typical plasma temperature $\lesssim 2$ keV. Blackbody fits give kT_{bb} s and R_{bb} similar to those of MSPs, which seems reasonable since MSPs far from the cluster centre have been observed in other core-collapsed GCs (see e.g., Colpi et al. 2002; Forestell et al. 2014); however, we found the spectra are more likely reproduced by optically thin low-temperature plasma, as they possess evidence of emission features at low energies (e.g., emission line at ~ 0.8 -1 keV that overlaps the Fe L-shell emission), which is more common among faint ABs or CVs. As an example, we show the spectrum of W145 fitted with a `vmekal` model in Fig. 2, with a clear emission feature at ~ 1 keV.

Finally, sources with somewhat more balanced spectra, including W124, W125, W128, W130, W131, W133, W134, W137, W138, W140, could be either background AGNs or faint CVs.

We tried to search for optical counterparts with searching radii up to $2P_{\text{err}}$ for these new sources, using the *Gaia* DR2 archive (Gaia Collaboration et al., 2016, 2018a). Limited by the low stellar density at the cluster outskirts, detecting multiple objects in the sub-arcsecond error circles might be rare. Indeed, in all searching radii, we found at most 1 *Gaia* source (Tab. 2); however, these unique objects are not necessarily real counterparts, as fainter objects within the searching radii might have magnitudes above the *Gaia* limit (G-band limit-

ing magnitude ≈ 21). Nevertheless, non-detections might still indicate a distant nature for the source. In fact, all of the heavily absorbed sources mentioned above have empty searching regions, which further supports their nature as distant objects.

As complementary information, we check the photometric colours of these potential counterparts using the *Gaia* two-band (G_{BP} and G_{RP}) magnitudes. We show a *Gaia* $G_{\text{BP}} - G_{\text{RP}}$ CMD in Fig. 4 using stars within a $3'$ circular region centered on the cluster. We also make use of proper motion (PM) information from the *Gaia* database to confirm membership, only accepting sources that have PMs consistent with the cluster systematic PM ($\mu_{\alpha} = 3.2908 \pm 0.0026 \text{ mas yr}^{-1}$, $\mu_{\delta} = -17.5908 \pm 0.0025 \text{ mas yr}^{-1}$; see Gaia Collaboration et al. 2018b) at 5σ as cluster members.

There are five sources, W132, W133, W138, W143 and W146, that have clearly inconsistent PMs with the cluster. The red excesses in W132 and W143 (Fig. 4) are consistent with their foreground nature (as suggested by their distances in Tab. 2), while the counterparts to W133 and W146 appear to be bright stars with blue excesses. W132 has a more definite binarity with a *Gaia*-measured radial velocity of $|v_r| = 10.11 \pm 1.97 \text{ km s}^{-1}$. W133 has a PM clearly discordant with the cluster (Fig. 3). Intriguingly, W133 is a background source but the counterpart distance is just a few hundred parsecs greater than the cluster (Tab. 2). We suspect that W133 is either a halo object or a “runaway” close binary—likely a CV—ejected by dynamical encounters in the core. The stars found near W138 and W146 could be chance coincidences, as they are relatively far from the X-ray positions.

Three stars in the list are found to have PMs consistent with the cluster value. The PM-selected cluster member W136 has a red giant counterpart, so it could be an RS CVn system. W139 has a definite association with the cluster, but is so faint that no further photometric information is available. W145 has a counterpart consistent with the MS, but is likely to be a chance coincidence,

as it lies at $\sim 2P_{\text{err}}$ off the X-ray position.

Finally, W134 is within the *HST* field of view, so HUGS photometry is available. We found 3 stars (Fig. 5) with colours consistent with the main sequence (MS) in the $UV_{275} - U_{336}$ and $U_{336} - B_{438}$ CMDs, while in the $V_{606} - I_{814}$ CMD, there is one star (W134-2) that exhibits a very mild red excess relative to the MS (Fig. 3.2), which we think is more likely to be the counterpart. W134-2 has a definite cluster membership probability of 98.3% but is less likely a chance coincidence compared to the other two.

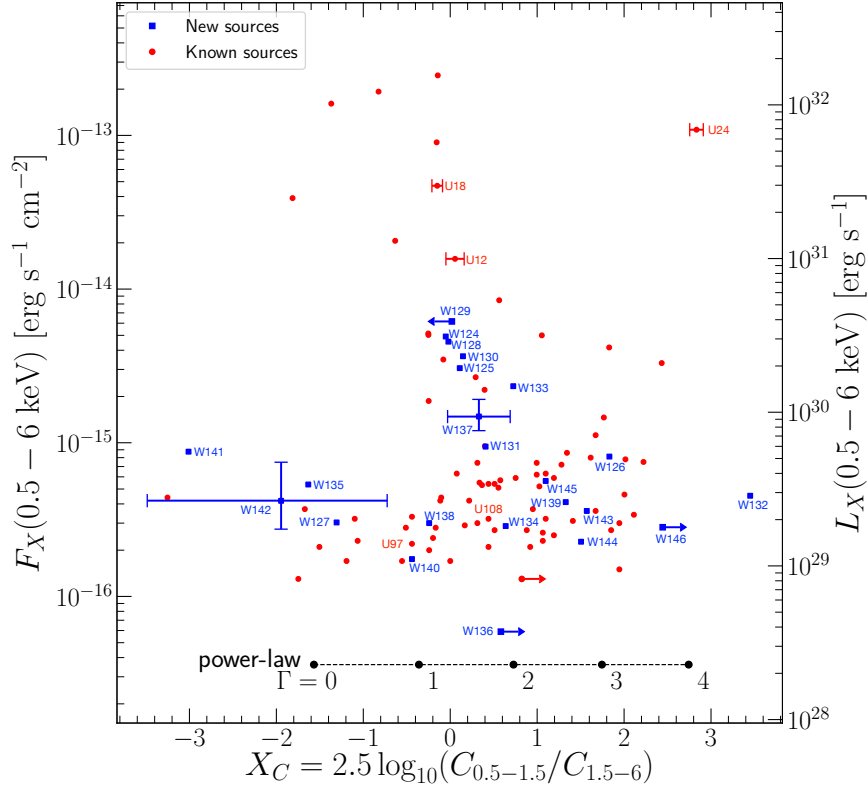


Figure 1: X-ray colour-magnitude diagram plotting 0.5-6 keV fluxes (left scale) and luminosities (right scale) vs. hardness ratio (X_C , defined in eq.(6)) for known (red) and new (blue) sources. X_C s and fluxes of the known sources are adapted from Bogdanov et al. (2010), while were calculated by `srcflux` (Sec. 3.2.2) for the new sources. For better readability, we only labelled the relevant known sources and the new sources, and put error bars on several sources to represent uncertainties at different flux levels. Upper/lower limits and errors in X_C are at the 90% confidence as derived according to methods in Gehrels (1986). We also indicate the locations of power-law models with different photon indices (Γ s).

Table 1: X-ray catalogue of source within the 2'9 half-light radius.

ID	RA	DEC (J2000)	P_{err}^a	Counts ^b		Flux ^c
				0.5-1.5 keV	1.5-6 keV	0.5-6.0 keV
U5	17:40:54.539	-53:40:44.912	0.33	167	31	41.7
U7	17:40:52.843	-53:41:22.170	0.32	252	150	84.6
U10	17:40:48.987	-53:39:48.986	0.29	283	1504	390.8
U11	17:40:45.786	-53:40:41.898	0.32	72	55	26.7
U12	17:40:44.627	-53:40:41.957	0.30	382	363	157.3
U13	17:40:44.093	-53:40:39.506	0.31	107	135	51.4
U14	17:40:43.340	-53:41:55.821	0.40	17	10	5.7
U15	17:40:42.923	-53:40:34.127	0.34	42	9	11.2
U16	17:40:42.659	-53:42:15.698	0.42	15	10	5.4
U17	17:40:42.659	-53:40:19.628	0.28	5358	6114	2458.0
U18	17:40:42.619	-53:40:27.964	0.29	995	1142	470.2
U19	17:40:42.317	-53:40:29.073	0.28	2777	5934	1927.3
U21	17:40:41.843	-53:40:21.740	0.29	1974	2279	901.4
U22	17:40:41.711	-53:40:29.380	0.31	104	131	50.3
U23	17:40:41.605	-53:40:19.624	0.28	1677	5915	1609.5
U24	17:40:41.481	-53:40:04.790	0.28	4797	353	1088.8
U25	17:40:41.248	-53:40:26.164	0.33	39	49	18.7
U28	17:40:38.915	-53:39:51.472	0.30	351	629	206.1
U31	17:40:34.213	-53:41:15.588	0.37	26	18	9.5
U41	17:40:45.015	-53:39:55.544	0.36	31	4	7.5
U42	17:40:43.064	-53:38:31.633	0.34	141	15	33.0
U43	17:40:40.556	-53:40:23.180	0.36	25	10	7.4
U60	17:40:47.825	-53:41:28.649	0.41	10	11	4.4
U61	17:40:45.231	-53:40:28.964	0.32	79	85	34.8
U62	17:40:30.426	-53:39:17.921	0.48	12	5	3.7
U63	17:40:31.680	-53:38:46.731	0.42	31	7	8.0
U65	17:40:37.578	-53:39:18.215	0.43	14	3	3.6
U66	17:40:38.952	-53:38:49.981	0.48	9	4	2.7
U67	17:40:40.074	-53:40:16.880	0.41	8	6	3.0
U68	17:40:40.694	-53:38:33.180	0.44	1	20	4.4
U69	17:40:40.880	-53:40:17.513	0.37	15	9	5.1
U70	17:40:41.705	-53:40:33.608	0.32	59	41	22.1
U73	17:40:42.692	-53:39:29.145	0.38	22	8	6.3
U75	17:40:43.662	-53:40:30.993	0.39	9	10	4.2
U76	17:40:43.827	-53:41:16.679	0.38	21	7	5.9
U77	17:40:44.140	-53:42:11.808	0.42	18	7	5.2
U79	17:40:46.415	-53:40:04.248	0.38	18	9	5.9
U80	17:40:46.445	-53:41:56.863	0.39	20	15	7.4
U81	17:40:46.482	-53:41:15.771	0.38	15	11	5.5
U82	17:40:48.549	-53:39:39.775	0.37	31	9	8.6
U83	17:40:49.636	-53:40:43.350	0.46	5	6	2.4
U84	17:40:54.815	-53:40:20.169	0.40	32	5	7.8

Table 1: (Continued) X-ray catalogue of sources within the 2'9 half-light radius.

ID	RA	DEC (J2000)	P_{err}	Counts		Flux
				0.5-1.5 keV	1.5-6 keV	0.5-6.0 keV
U86	17:40:37.483	-53:41:47.651	0.35	56	11	14.6
U87	17:40:42.888	-53:40:26.772	0.37	14	10	5.3
U88	17:40:42.848	-53:40:23.886	0.37	20	8	6.2
U89	17:40:43.651	-53:40:24.927	0.41	11	3	3.1
U90	17:40:41.808	-53:40:14.924	0.36	26	8	7.2
U91	17:40:42.422	-53:40:42.510	0.40	6	9	3.3
U92	17:40:43.923	-53:40:35.690	0.40	11	4	3.2
U93	17:40:42.361	-53:40:47.315	0.42	6	7	2.8
U94	17:40:42.893	-53:40:49.413	0.40	14	2	3.4
U95	17:40:40.334	-53:40:44.916	0.47	4	4	1.7
U96	17:40:39.090	-53:40:23.414	0.42	11	2	2.7
U97	17:40:43.916	-53:40:05.702	0.44	4	6	2.2
U98	17:40:41.006	-53:40:58.883	0.41	12	2	3.0
U99	17:40:46.439	-53:40:30.767	0.50	6	1	1.5
U100	17:40:38.212	-53:40:46.872	0.45	6	4	2.1
U101	17:40:45.412	-53:41:01.797	0.39	19	3	4.6
U102	17:40:38.877	-53:39:43.446	0.40	11	9	4.2
U103	17:40:35.718	-53:40:13.018	0.44	9	3	2.5
U104	17:40:43.138	-53:39:29.280	0.44	5	8	2.8
U105	17:40:36.535	-53:41:08.319	0.44	8	5	2.7
U106	17:40:43.768	-53:39:17.814	0.51	3	5	1.7
U107	17:40:34.119	-53:40:17.295	0.39	16	10	5.4
U108	17:40:52.105	-53:39:48.404	0.46	9	6	3.2
U109	17:40:52.755	-53:40:53.217	0.50	8	3	2.3
U110	17:40:33.455	-53:39:17.335	0.50	8	3	2.6
U111	17:40:29.884	-53:40:27.207	0.45	3	14	3.7
U112	17:40:50.385	-53:39:06.322	0.53	7	3	2.1
U113	17:40:42.764	-53:40:21.041	0.31	161	61	50.0
U114	17:40:43.480	-53:40:34.662	0.45	4	5	2.0
U116	17:40:42.247	-53:40:20.292	0.36	15	14	6.3
U117	17:40:42.164	-53:40:25.882	0.41	7	6	2.9
U118	17:40:41.587	-53:40:16.202	0.43	3	8	2.3
U119	17:40:41.272	-53:40:19.672	0.40	4	11	3.2
U120	17:40:46.528	-53:40:15.962	0.53	6	0	1.3
U121	17:40:33.642	-53:39:35.282	0.50	2	8	2.1
U122	17:40:47.914	-53:39:25.152	0.58	1	5	1.3
U123	17:40:49.632	-53:38:46.252	0.60	2	6	1.7
W124	17:40:30.511	-53:42:34.201	0.38	103	108	49.1
W125	17:40:27.976	-53:42:00.059	0.39	73	66	30.6
W126	17:40:59.672	-53:40:39.095	0.38	54	10	8.1
W127	17:40:58.559	-53:40:14.878	0.52	3	10	3.0
W128	17:40:56.736	-53:39:39.863	0.33	102	104	45.5
W129	17:40:56.204	-53:39:11.229	0.35	0	123	61.6

Table 1: (Continued) X-ray catalogue of source within the 2'9 half-light radius.

ID	RA	DEC	P_{err}^a	Counts ^b		Flux ^c
				0.5-1.5 keV	1.5-6 keV	0.5-6.0 keV
W130	17:40:50.597	-53:38:25.760	0.34	103	90	36.6
W131	17:40:37.690	-53:42:46.340	0.42	32	22	9.4
W132	17:40:36.503	-53:42:41.158	0.52	24	1	4.5
W133	17:40:58.337	-53:41:53.413	0.37	78	40	23.3
W134	17:40:42.036	-53:40:37.877	0.41	9	5	2.9
W135	17:40:48.754	-53:43:04.444	0.64	2	9	5.4
W136	17:40:53.157	-53:40:58.363	0.63	5	0	0.6
W137	17:40:58.548	-53:39:17.142	0.42	42	31	14.8
W138	17:40:50.710	-53:43:02.721	0.73	5	5	3.0
W139	17:40:29.296	-53:42:21.018	0.85	17	5	4.1
W140	17:40:53.868	-53:41:30.826	0.57	4	6	1.8
W141	17:40:26.669	-53:41:18.152	0.74	1	16	8.8
W142	17:41:00.896	-53:40:52.215	0.62	2	12	4.2
W143	17:40:22.994	-53:40:34.913	0.72	17	4	3.6
W144	17:40:33.992	-53:39:07.244	0.74	8	2	2.3
W145	17:40:27.889	-53:38:45.537	0.88	22	8	5.6
W146	17:40:57.386	-53:38:40.507	0.65	23	0	2.8

^{a,b} P_{err} (in ") and counts for U-sources are from Bogdanov et al. (2010). Counts of the W sources are calculated by `srcflux`.

^c Source fluxes are in units of 10^{-16} erg s⁻¹ cm⁻²; fluxes for all U sources are from Bogdanov et al. (2010), while fluxes for the W sources are model-independent fluxes calculated by `srcflux`.

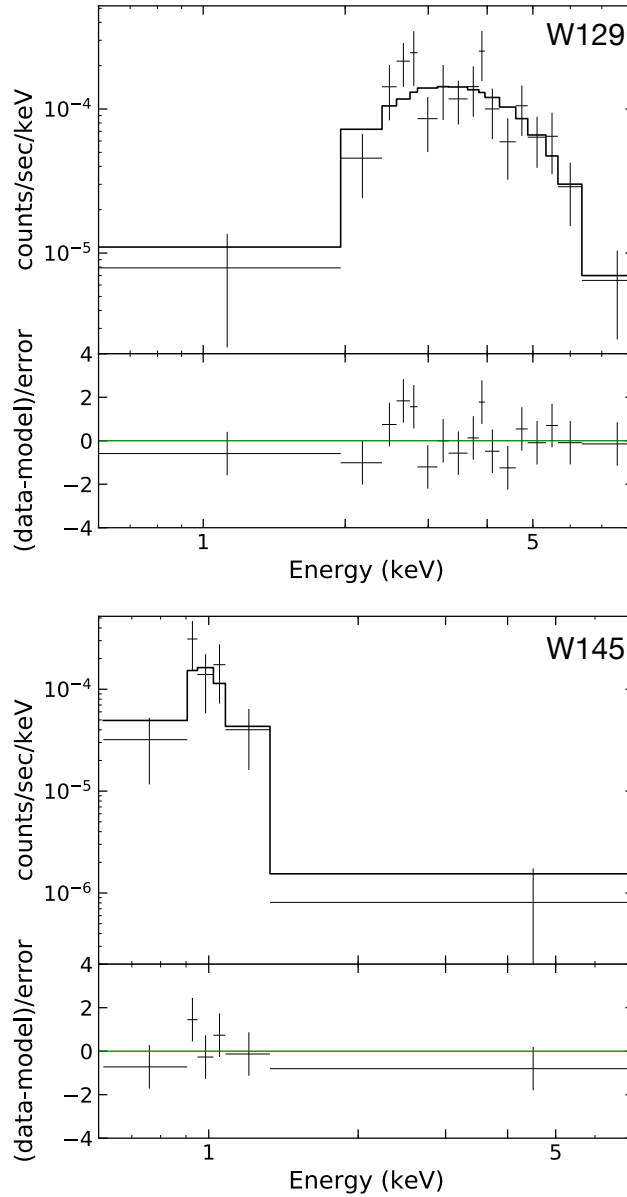


Figure 2: *Chandra* ACIS-S spectra of W129 (top) and W145 (bottom) overplotted with best-fitting power-law (W129) and *vmekal* (W145) model. The bottom panel of each plot shows the fitting residuals. The spectra are re-binned only for plotting purpose.

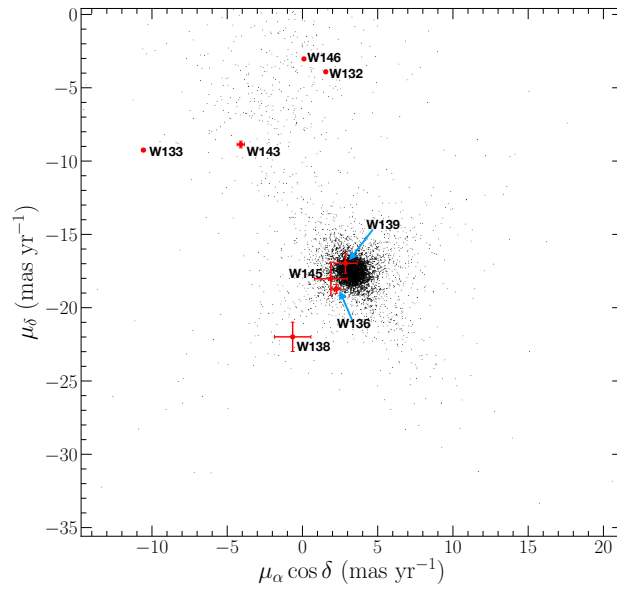


Figure 3: Proper motions (PMs) from *Gaia* DR2 of stars within a $3'$ searching radius. The plot is centered on the cluster proper motion at $\mu_\alpha = 3.2908 \pm 0.0026 \text{ mas yr}^{-1}$, $\mu_\delta = -17.5908 \pm 0.0025 \text{ mas yr}^{-1}$. PM of each counterpart is indicated with red dot and 1σ error bars.

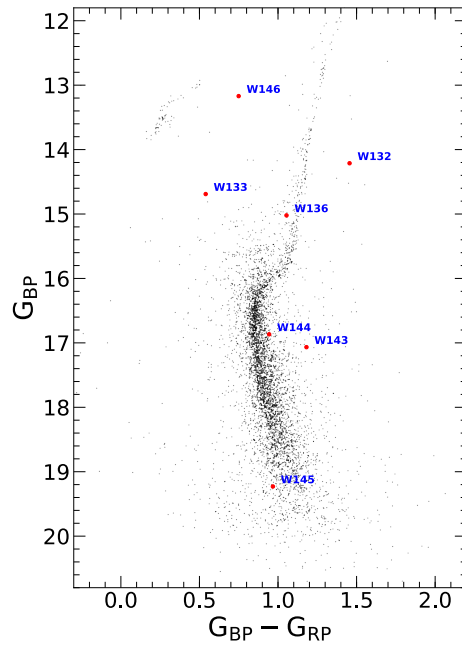


Figure 4: Gaia CMD plotting $G_{BP} - G_{RP}$ colours vs. G_{BP} band magnitudes. The counterparts are indicated with red filled circles.

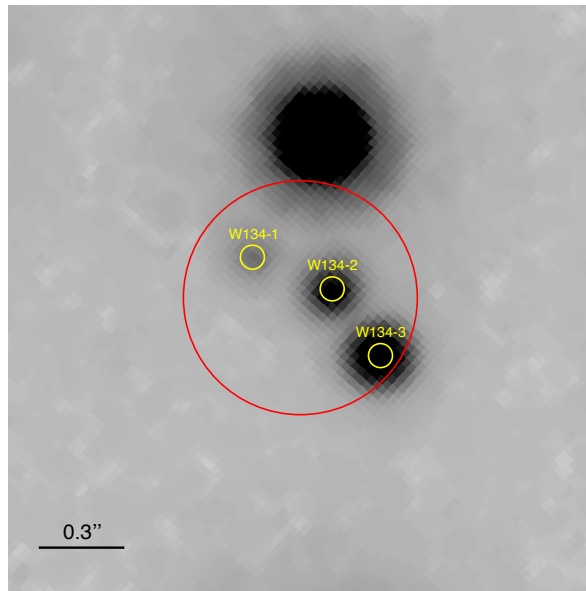


Figure 5: *HST/ACS* R625W finding chart for W134 showing a $2''.1 \times 2''.1$ region centered on the nominal X-ray position of W134, north is up and east is to the left. The red circle indicates the *Chandra* 95% error region while likely counterparts are indicated with yellow circles.

Table 2: Optical counterparts to the new sources.

ID	Optical position		Offset ^a		Magnitudes [†]		Membership ^b	Dist ^c (kpc)	Comments
	RA	DEC	($''$; P_{err})	G_{BP}	G_{RP}				
W126	17:40:59.662	-53:40:39.001	0.13; 0.34	-	-	-	-	-	Faint AB or CV?
W131	17:40:37.686	-53:42:46.324	0.04; 0.10	-	-	-	-	-	Faint AB or CV?
W132	17:40:36.481	-53:42:41.151	0.20; 0.38	14.21	12.76	Foreground	0.257 ^{+0.002} _{-0.002}	-	Foreground AB?
W133	17:40:58.332	-53:41:53.318	0.11; 0.29	14.69	14.15	Background	2.84 ^{+0.31} _{-0.26}	-	Runaway CV?
W134	17:40:42.024	-53:40:37.854	0.11; 0.27	20.30	19.10	Member	1.82 ^{+0.38} _{-0.27}	-	Faint AB or CV?
W136	17:40:53.174	-53:40:58.642	0.32; 0.51	15.02	13.97	Member	1.57 ^{+0.72} _{-0.38}	-	RS CVn?
W138	17:40:50.856	-53:43:03.335	1.43; 1.96	-	-	Foreground	0.58 ^{+0.21} _{-0.21}	-	-
W139	17:40:29.293	-53:42:21.196	0.18; 0.21	-	-	Member	3.59 ^{+3.32} _{-1.79}	-	Faint AB or CV?
W143	17:40:22.925	-53:40:34.066	1.04; 1.45	17.07	15.89	Foreground	1.36 ^{+0.40} _{-0.30}	-	Foreground AB?
W144	17:40:33.890	-53:39:08.198	1.32; 1.78	16.86	15.92	-	-	-	-
W145	17:40:27.722	-53:38:45.047	1.56; 1.78	19.23	18.26	Member	3.13 ^{+3.30} _{-1.83}	-	Faint AB or CV?
W146	17:40:57.314	-53:38:39.885	0.89; 1.37	13.17	12.42	Foreground	0.70 ^{+0.02} _{-0.02}	-	Faint AB or CV?

^aOffsets from the X-ray positions in terms of $''$ and P_{err}

^bCluster membership determinations based on *Gaia* proper motions and/or distances or, for W134, the membership probability from the HUGS data

^cDistance estimates according to Bailer-Jones et al. (2018). The reported errors are at the 68% confidence level

[†]Magnitudes in the *Gaia* G_{BP} and G_{RP} band passes; for W134, the first and second column corresponds to magnitudes at the *HST*/ACS *F606W* and *F814W* filter, respectively

C All finding charts for M30 X-ray sources

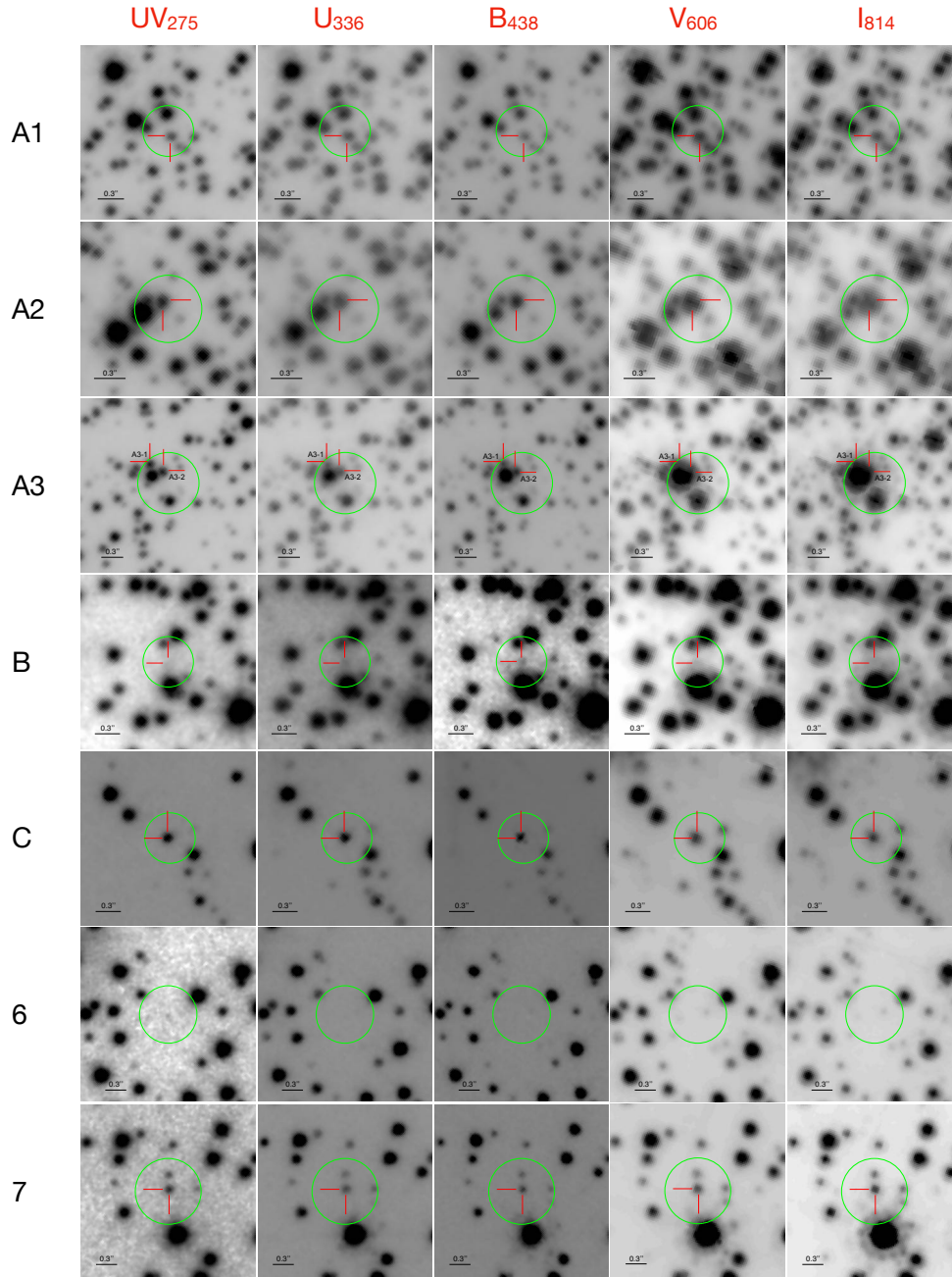


Figure 6: UV₂₇₅, U₃₃₆, B₄₃₈, V₆₀₆, and I₈₁₄ finding charts for 23 X-ray sources; north is up and east is to the left. The green circle in each finding chart marks the 95% *Chandra* error circle as per Hong et al. (2005), and identified counterparts are indicated with red cross hairs. In the charts for source 13 and MSP A, the ellipses in cyan marks the 1σ radio positional uncertainty.

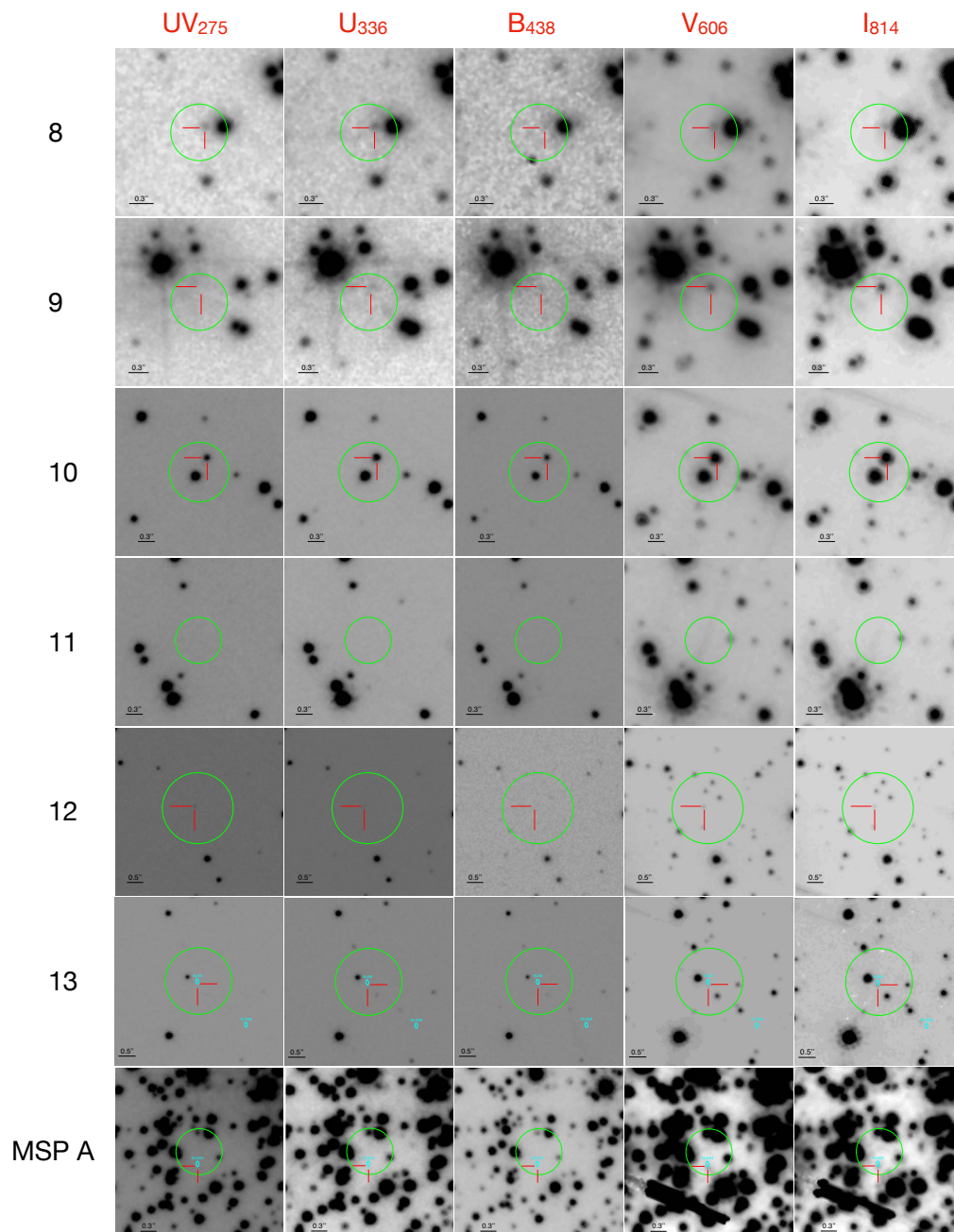


Figure 6: Continued

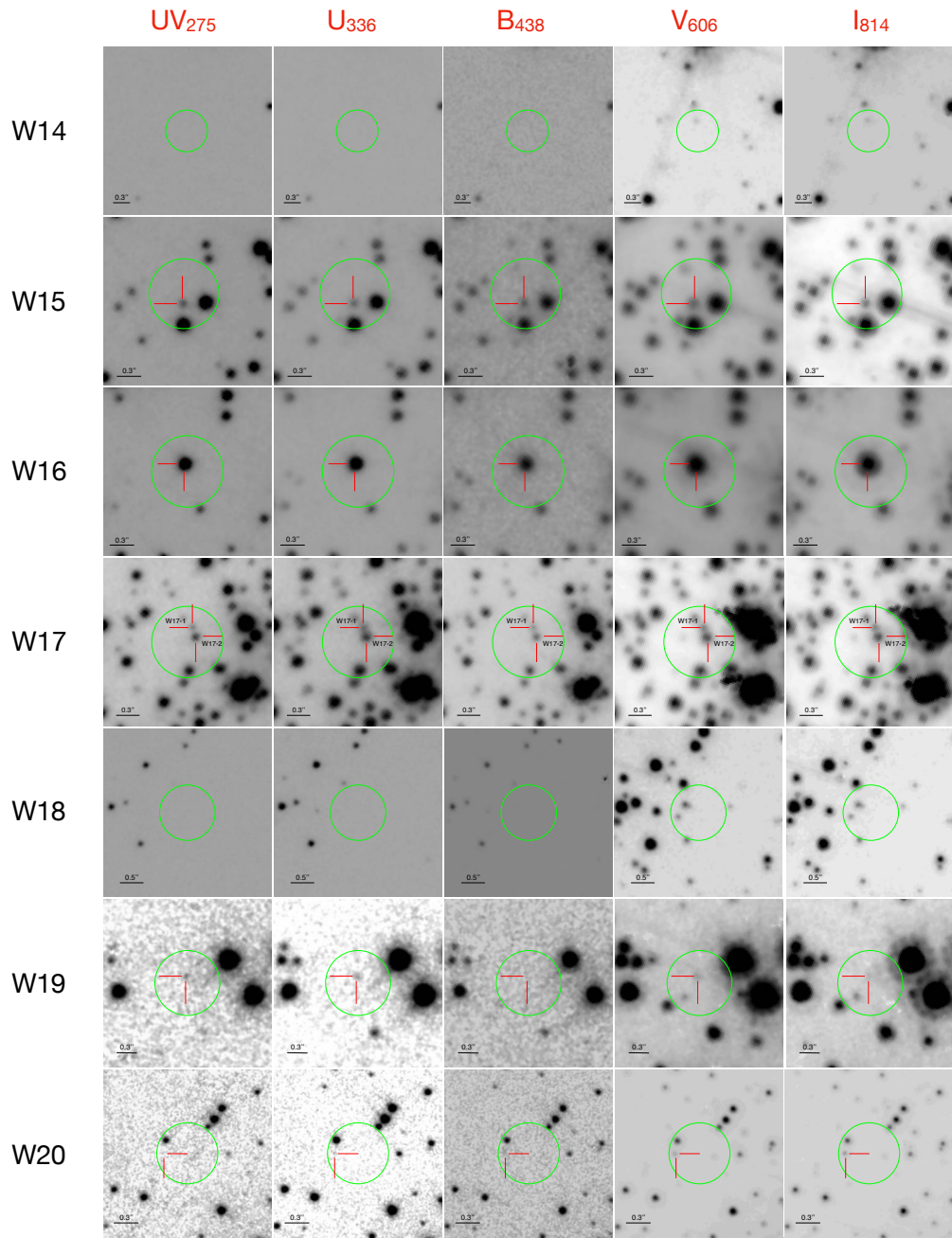


Figure 6: Continued

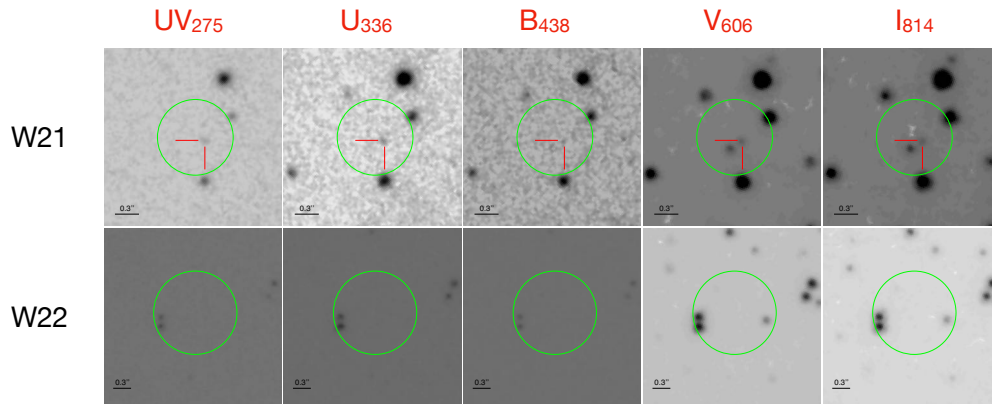


Figure 6: Continued